FOSSIL ENERGY

DOE/BC/15211-13
(OSTI ID: 781148)

INVESTIGATION OF MULTISCALE AND MULTIPHASE FLOW, TRANSPORT AND REACTION IN HEAVY OIL RECOVERY PROCESSES

Annual Report
May 6, 2000-May 5, 2001

By:
Yanis C. Yortsos

Date Published: May 2001

Work Performed Under Contract No. DE-AC26-99BC15211

University of Southern California
Los Angeles, California

National Energy Technology Laboratory
National Petroleum Technology Office
U.S. DEPARTMENT OF ENERGY
Tulsa, Oklahoma

DOE/BC/15211-13
Distribution Category UC-122

Investigation of Multiscale and Multiphase Flow, Transport and Reaction in Heavy Oil Recovery Processes

By
Yanis C. Yortsos

May 2001

Work Performed Under Contract DE-AC26-99BC15211

Prepared for
U.S. Department of Energy
Assistant Secretary for Fossil Energy

Tom Reid, Project Manager
National Petroleum Technology Office
P.O. Box 3628
Tulsa, OK 74101

Prepared by
Petroleum Engineering Program
Department of Chemical Engineering
University of Southern California
Los Angeles, CA 90089-1211

TABLE OF CONTENTS

ABSTRACT

This is the second annual report for contract DE-AC26-99BC15211. The report describes progress made in the various thrust areas of the project, which include internal drives for oil recovery, vapor-liquid flows, combustion and reaction processes, instabilities and upscaling and the flow of fluids with yield stress. The report is mainly a compilation of previous topical reports published in the second year of the project, which ended on May 5, 2001. Advances in multiple processes and at various scales are described.

In the area of internal drives, significant progress was made in the modeling of the nucleation and growth of the gas-phase driven by mass transfer, which particularly applies to foamy oil. A review of various issues in phase change in porous media is also presented. In the area of vapor-liquid flows, we describe the scaling of the rates of produced fluids in laboratory displacements in conjunction with gas-liquid flows. A report on the dynamics of concurrent gas-liquid flows is also given. In the area of combustion, we continue our investigation at two different scales, one involving pore-network scale modeling, and another involving the propagation of combustion fronts in porous media at the large scale. In the area of viscous instabilities, upscaling and identification, we report on three studies, one involving the upscaling of processes with fast kinetics, another on the upscaling of displacements in fractured systems and a third on the identification of the permeability heterogeneity in anisotropic systems, from the injection of a passive tracer. On-going work in the area of flow of fluids with yield stress is also reported.

EXECUTIVE SUMMARY

This is the second annual report of an investigation of the various multi-phase and multiscale transport and reaction processes associated with heavy oil recovery. The thrust areas of the project include the following: Internal drives, vapor-liquid flows, combustion and reaction processes, fluid displacements and the effect of instabilities and heterogeneities and the flow of fluids with yield stress. These find respective applications in foamy oils, the evolution of dissolved gas, internal steam drives, the mechanics of concurrent and countercurrent vapor-liquid flows, associated with thermal methods and steam injection, such as SAGD, the in-situ combustion, the upscaling of displacements in heterogeneous media and the flow of foams, Bingham plastics and heavy oils in porous media and the development of wormholes during cold production.

In many processes associated with heavy oil recovery, internal drives, namely these driven by applied supersaturation in dissolved gases or heat content, are common. The main result is the growth of a gas phase, which is driven by mass or heat transfer, depending on the kind of the applied supersaturation. We have conducted various studies of this multifaceted problem. In this report, we present results in two areas, one associated with the nucleation and growth of a gas phase from a supersaturated liquid, and another reviewing recent advances on phase change processes in porous media. The first study describes a mathematical model of the dynamics of gas evolution as a function of the rate of application of the supersaturation for solution gas drive. With simple changes in variables, it also finds application to the process of internal steam drive. The second study is a compilation of recent findings in general phase change problems in porous media. We review notable advances published in the year 1999 in the area of phase change and phase growth in porous media. The review identifies common processes at the various scales and points out important open problems.

The simultaneous flow of vapor and liquid phases is common to steam injection. Counter-current flows are encountered in Steam-Assisted-Gravity-Drainage (SAGD), and in steam injection in horizontal wells. Concurrent flows are found in typical

displacements, in solution gas-drives near wells, and various other contexts. In this section we report on two studies, one dealing with transient gas-liquid flows with an evaporating component, although at time scales where evaporation is not significant, and another on the dynamics of two-phase flows in heterogeneous media where capillarity induces a trapped phase. The first study shows how the flow rates of the produced fluids in laboratory displacements can be used to assess the exponent of the relative permeability of the flowing liquid. We propose a novel diagnostic technique to infer these properties, which allows for the mechanism of fluid flow to be uncovered. The second study is a new approach, based on what we term Darcian Dynamics, to describe the dynamics of the flow of a disconnected phase, in the form of ganglia, in the flow field of a displacing continuous phase. It is a computationally fast approach for the evaluation of quantities in concurrent and counter-current flows, such as the critical capillary number for mobilization, the subsequent movement of the mobilized phase, and its possible stranding and/or coalescence. The two studies do not address phase-change or heat transfer issues, which are currently under consideration.

A well-established method for the recovery of heavy oils is in-situ combustion. Two particular aspects are analyzed in this project: The description of the process at the pore-network scale, and its upscaling at the large scale for field applications. A detailed pore-network simulator is described in the first study. The simulator accounts for all relevant phenomena at the microscale, including mass transfer by convection and diffusion, viscous flow, heat transfer in the porespace and the solid matrix and chemical reactions. It predicts small-scale patterns, including particularly the structure of the combustion zone and associated instabilities. The simulator can be used to understand the combustion process from first principles and to delineate ignition, extinction and sustained propagation phenomena. In the second study, we continue our previous work using an asymptotic approach to describe the movement of combustion fronts in porous media. This approach is essential for the upscaling of the process at the field scale. The novel aspect of the present effort is the incorporation of the effect of heat losses in non-adiabatic combustion processes.

The effect of macroscale heterogeneity on displacements, including those of heavy oil is an important consideration. Key issues include the identification of the heterogeneity, and its upscaling. We report on two studies, one on the continuation of a previous effort on the identification of permeability using a passive tracer, and another on the development of a model equation to incorporate heterogeneity effects in both stable and unstable displacements. The work on the identification of permeability is an extension of our previous study for direct inversion to anisotropic porous media. This technique is the first, to our knowledge, that in principle allows one to identify the heterogeneity of permeability along the principal axes of anisotropy. The second study provides a new model equation to capture the effect of heterogeneity (noise) on large-scale front propagation, by proposing an extension of the so-called KPZ equation. We describe an approach, in which stable and unstable effects can be incorporated using a non-local formalism. The properties of this equation are examined in detail, both for stable and unstable processes.

ACKNOWLEDGEMENTS

This research was possible through the Department of Energy contract DE-AC26-99BC15211, the contribution of which is gratefully acknowledged. Partial support was also provided by Chevron Petroleum Company. The PI would like to express his gratitude to the NPTO Project officers in charge of the contract, Dr. Jerry Casteel and Mr. Thomas Reid for their help and support.

INTRODUCTION

This project is an investigation of various multi-phase and multiscale transport and reaction processes associated with heavy oil recovery. The thrust areas of the project include the following: Internal drives, vapor-liquid flows, combustion and reaction processes, fluid displacements and the effect of instabilities and heterogeneities and the flow of fluids with yield stress. These find respective applications in foamy oils, the evolution of dissolved gas, internal steam drives, the mechanics of concurrent and countercurrent vapor-liquid flows, associated with thermal methods and steam injection, such as SAGD, the in-situ combustion, the upscaling of displacements in heterogeneous media and the flow of foams, Bingham plastics and heavy oils in porous media and the development of wormholes during cold production. Funding of the project is for three years, from May 6, 1999 to May 5, 2002.

In this report, progress made in the various areas outlined above during the second year of the project is described. Work was conducted in all areas, with progress being greater in some areas compared to others, for a variety of circumstances. During the reporting period, a total of up to 8 students were supported by the project. A number of publications and 11 technical reports have resulted from this effort. The publications are listed below. The report is essentially, but not exclusively, a compilation of the topical reports.

This report is organized as follows: For each of the four first thrust areas, namely internal drives, vapor-liquid flows, combustion dynamics, and instabilities and heterogeneity, we provide a brief summary of the work performed, followed by two reports each. Work in the thrust area of fluids with yield stress will not be reported here. Although progress was made, the results obtained are preliminary and further work is required before they can become conclusive.

PUBLICATION LIST

Laroche, C., Chen, M., Yortsos, Y.C., and Kamath, J., "Time Scaling of the Rates of Produced Fluids in Laboratory Displacements", Water Res. Res., submitted (2001).

Yortsos, Y.C., and Stubos, A.K, "Phase Change in Porous Media", Current Opinions in Colloid and Interface Science, in press (2001).

Kechagia, P., Yortsos, Y.C. and Lichtner, P., "A Non-Local KPZ Equation to Model Interface Growth", Phys. Rev. E, in press (2001).

Zhan, L. and Yortsos, Y.C., "A Direct Method for the Identification of the Permeability Field of an Anisotropic Porous Medium", Water Res. Res., in press (2001).

Lajeunesse, E., Martin J., Rakotomalala, N., Salin, D., and Yortsos, Y.C., "The Threshold of Instability in Miscible Displacements in a Hele-Shaw Cell at High Rates", Phys. Fluids, in press (2001).

Yiotis, A.G., Stubos, A.K., Bountouvis, A., and Yortsos, Y.C., "A 2-D Pore-Network Model of the Drying of Single-Component Liquids in Porous Media", Adv. Water Res. **24**, 437-458 (2001).

Yortsos, Y.C., Xu, B., and Salin, D., "Delineation of Microscale Regimes in Fully Developed Drainage and Implications for Continuum Models", Comp. Geosc., submitted (2000).

Zhan, L. and Yortsos, Y.C., "The Shape of a Gravity Finger in a Rectangular Channel in a Homogeneous Porous Medium", Transport in Porous Media, submitted (2000).

Zhan, L. and Yortsos, Y.C., "A Note on the Use of Streamline Coordinates in Porous Media Displacements", Water Res. Res., submitted (2000).

Kechagia, P., Tsimpanogiannis, I.N., Yortsos, Y.C. and Lichtner, P., "On the Upscaling of Reaction-Transport Processes in Porous Media with Fast Kinetics", Chem. Eng. Sci., submitted (2000).

Shariati, M. and Yortsos, Y.C., "Stability of Miscible Displacements Across Stratified Porous Media", Phys. Fluids, submitted (2000).

Yortsos, Y.C., "The Permeability Variogram from Pressure Transients of Multiple Wells", in "Theory, Modeling, and Field Investigation in Hydrogeology: A Special Volume in Honor of Shlomo P. Neuman's 60th Birthday" (D. Zhang, and C.L. Winter, eds.), Geological Society of America Special Paper {\bf 348}, 19-23 (2000).

Yortsos, Y.C., "Physical Considerations in the Upscaling of Immiscible Displacements in a Fractured Medium", in "Dynamics of Fluids in Fractured Rock" (B. Faybisenko, P.A. Witherspoon and S.M. Benson, eds.), Geophysical Monograph Series {\bf 122}, American Geophysical Union, 235-251 (2000).

Zhan, L., and Yortsos, Y.C., "Identification of the Permeability Field of a Porous Media from the Injection of a Passive Tracer", Phys. Rev. E **62**, 863-879 (2000).

Tsimpanogiannis, I.N., Yortsos, Y.C., and Stubos, A.K., "Evaporation of a Stagnant Liquid", Ind. Eng. Chem. Res. **39**, 1505-1513 (2000).

Lu, C., and Yortsos, Y.C., "A Pore-Network Model of Combustion in Porous Media", paper SPE 69705 presented at the International Thermal Operations and Heavy Oil Symposium (ITOHOS), Margarita Island, Venezuela (March 12-14, 2001).

Akkutlu, I., and Yortsos, Y.C., "The Dynamics of Combustion Fronts in Porous Media", paper SPE 63225 proceedings of the 74th SPE Annual Fall Meeting, Dallas, TX (Oct. 1-4, 2000).

Zhan, L. and Yortsos, Y.C., "A Direct Method for the Identification of the Permeability Field of an Anisotropic Porous Medium", paper SPE 62976 proceedings of the 74th SPE Annual Fall Meeting, Dallas, TX (Oct. 1-4, 2000).

Lu, C. and Yortsos, Y.C., "The Dynamics of Combustion in Porous Media at the Pore-Network Scale", paper presented at the 7th European Conference on the Mathematics of Oil Recovery, Baveno, Lago Maggiore, Italy (Sept. 5-8, 2000).

Laroche, C., Yortsos, Y.C., and Kamath, J., "Time-Scaling of the Rates of Produced Fluids in Laboratory Displacements in Porous Media", paper presented at the 7th European Conference on the Mathematics of Oil Recovery, Baveno, Lago Maggiore, Italy (Sept. 5-8, 2000).

Lu, C., and Yortsos, Y.C., "A Pore-Network Model of Smoldering Combustion}, paper presented at the AIChE Fall Meeting, Los Angeles, CA (November 12-17, 2000).

Shariati, M., and Yortsos, Y.C., "A Study of Miscible Displacement in the Gap of a Hele-Shaw Cell with a Non-Monotonic Viscosity Profile", paper presented at the AIChE Fall Meeting, Los Angeles, CA (November 12-17, 2000).

Kechagia, P., Yortsos, Y.C. and Lichtner, P., "On the Constraint of Local Equilibrium in the Upscaling of Reaction and Transport Problems in Heterogeneous Porous Media", paper presented at the AIChE Fall Meeting, Los Angeles, CA (November 12-17, 2000).

Zhan, L., and Yortsos, Y.C., "Identification of Permeability Heterogeneity from Tracer Displacement: Sensitivity Analysis", proceedings of Conference Tracers and Modelling in Hydrogeology, Tram 2000, Liege, Belgium, pp. 63-73 (May 23-26, 2000).

Shariati, M., and Yortsos, Y.C., "The Effect of Heterogeneity on the Stability of Miscible Displacements in Porous Media", paper presented at the AGU Fall Meeting, San Francisco, CA (December 16, 1999).

Zhan, L., and Yortsos, Y.C., "The Identification of the Permeability Heterogeneity of Porous Media from the Displacement of a Passive Tracer", paper presented at the APS (DFD) Fall Meeting, New Orleans, LA (November 21-23, 1999).

Amili, P. and Yortsos, Y.C., "Stability of Heat Pipes in Vapor-Dominated Systems", paper presented at the ASME Fall Meeting, Nashville, TN (November 14-19, 1999).

Kechagia, P., and Yortsos, Y.C., "A Model Stochastic Equation for Convection-Diffusion Equation in Evolving Porous Media", paper presented at the AIChE Fall Meeting, Dallas, TX (November 1-5, 1999).

I. INTERNAL DRIVES

In many processes associated with heavy oil recovery, internal drives, namely these driven by applied supersaturation in dissolved gases or heat content, are common. These include, but are not limited to the evolution of gas in foamy oils, internal steam drives, the evaporation of volatile components during gas injection or the injection of steam, and other processes. The main result is the growth of a gas phase, which is driven by mass or heat transfer, depending on the kind of the applied supersaturation. We have conducted various studies of this multifaceted problem. In this report, we present results in two areas, one associated with the nucleation and growth of a gas phase from a supersaturated liquid, and another reviewing recent advances on phase change processes in porous media. The first study describes a mathematical model of the dynamics of gas evolution as a function of the rate of application of the supersaturation for solution gas drive. With simple changes in variables, it also finds application to the process of internal steam drive. The second study is a compilation of recent findings in general phase change problems in porous media. We review notable advances published in the year 1999 in the area of phase change and phase growth in porous media. Phase equilibria thermodynamics, particulary in micropores, and growth kinetics, emphasizing the pore-network structure, are highlighted. Advances reported include the effects of confinement in phase transitions in micropores, and of the pore microstructure in the growth and dissolution of gas and liquid phases with applications ranging from capillary condensation to drying to gas evolution to condensation. The review identifies common processes at the various scales and points out important open problems.

AN EFFECTIVE CONTINUUM MODEL FOR THE LIQUID-TO-GAS PHASE CHANGE AND GROWTH IN A POROUS MEDIUM DRIVEN BY SOLUTE DIFFUSION

By

Ioannis N. Tsimpanogiannis and Yanis C. Yortsos

I. INTRODUCTION

The liquid-to-gas phase change in a porous medium and the subsequent growth of the gas phase is a process encountered in many applications driven by mass or heat transfer. These span various fields of scientific interest and a range of length scales (Yortsos, 2001). Examples include the so-called solution gas-drive process for the recovery of oil from oil reservoirs (Sheng et al., 1999a, 1999b), boiling in porous media (Thome, 1990; Satik and Yortsos, 1996), thermal methods for oil recovery (Prats, 1982), nuclear waste disposal (Doughty and Pruess, 1990), soil remediation (Ho and Udell, 1995) and many others. In this chapter, we focus on the specific process of isothermal gas phase growth from a supersaturated, slightly compressible, binary liquid in a porous medium. This process is driven by mass transfer, the extent of which is controlled by the application of either a constant-rate decline of the system pressure or by the withdrawal of the liquid at a constant rate.

Consider the constant-rate removal of an initially supersaturated liquid from a porous medium of a fixed volume (Fig. 1). As the pressure continuously declines, due to liquid expansion, the bubble point of the liquid is eventually reached. Then, nucleation of a gas phase starts, at rates depending on the nucleation properties of the medium. Nucleation is manifested either in the form of the release of pre-existing gas bubbles, trapped in hydrophobic cavities, or in the form of heterogeneously nucleated nuclei. Emphasis in this chapter will be placed on the former mechanism, although a conventional model will also be discussed. Because of the competing processes of bubble growth, which depletes the solute from the liquid, thus reducing the supersaturation, and the liquid withdrawal, which reduces the pressure, thus increasing the supersaturation, a maximum in the supersaturation is attained, following which, nucleation terminates for all practical purposes. Identifying the maximum supersaturation and its dependence on process parameters is, therefore, a key issue. The subsequent evolution of the gas phase is controlled by the available supersaturation, the mass transfer of the solute from the liquid to the gas and by the capillary characteristics of the porous medium. The gas phase appears first in the form of small bubbles growing within the confines of single pores (Fig. 2a), but ultimately takes the form of large clusters,

spanning a number of pores (Fig. 2b). Competition for mass transfer between the growing bubbles or clusters, capillary effects at pore constrictions, viscous and gravity forces, and the possibility of coalescence or the snap-off of gas-liquid interfaces are important factors for determining the gas phase evolution.

Eventually, gas flows as a bulk phase out of the porous medium. The onset of flow is signaled when the gas pore-volume fraction, S_g, becomes equal to the so-called critical gas saturation, S_{gc}, a value which depends on the underlying growth and flow mechanisms. If viscous or gravity gradients are negligible, then bulk gas flow occurs for the first time when the various isolated gas clusters connect to form a sample-spanning (percolation) cluster (Yortsos and Parlar, 1989). If they are not, gas flow and production occur through the continuous motion of finite-size gas clusters, subject to various mechanisms of interaction, including coalescence. The simultaneous flow of gas and liquid can be quite complex, particularly under strong pressure gradients, as is the case with high-viscosity oils, where the interesting and yet to be fully explained "foamy" oil flow takes place (Smith, 1988; Maini, 1996, 1999; Pooladi-Darvish and Firoozabadi, 1999, Kumar et al., 2000, Renard et al., 2000). In this chapter, we will only consider the stage before the onset of gas flow, however, and in the absence of gravity or viscous gradients.

Due to the interest of the problem, a number of studies have been conducted. A review of the early literature can be found in Li and Yortsos (1995a, 1995b). Experimental work in consolidated porous media was reported Moulu and Longeron (1989), Firoozabadi et al., (1992), Scherpenisse et al., (1994), Firoozabadi and Aronson, (1999). These studies showed that the critical gas saturation is an increasing function of the liquid withdrawal rate, a finding explained by the increasing number of nucleation centers, from which gas clusters grow, at larger depletion rates. Scherpenisse et al., (1994) provided useful, but qualitative, scaling arguments showing that the maximum supersaturation and the critical gas saturation are power-law functions of the depletion rate. A theoretical analysis of bubble growth by solute diffusion, following nucleation, in which mass transfer and porous medium capillarity dominate, was provided by Li and Yortsos (1995a, 1995b). These authors conducted visualization experiments in glass micromodels and pore-network simulations to explain patterns and rates of growth of the gas phase at the pore-network scale. Along similar lines, Du and Yortsos (1999) focused on a pore-network analysis of the critical gas saturation, in the absence of gravity/viscous gradients. They confirmed the hypothesis of Yortsos and Parlar (1989) that the onset of critical gas saturation coincides with the percolation threshold of invasion percolation, originating from multiple nucleation centers, and showed that S_{gc} is a power law of the final nucleation fraction (defined more precisely below), f_{qf}, namely

$$S_{gc} = f_{qf}^{1-D_f/E} \tag{1}$$

Here, E (equal to 2 or 3) is the (Euclidian) dimension of the pore network and D_f is the mass fractal dimension of the percolation cluster (equal to 1.82 for 2-D Invasion Percolation (IP) with trapping, and 2.53 for 3-D IP with or without trapping (Feder, 1988)). The dependence shown in (1) was established regardless of the nucleation sequence (instantaneous or sequential) or the particular regime of bubble growth (global or local percolation, see Li and Yortsos, 1995a, 1995b).

Certainly, the presence of gradients will affect the above scaling. Pore-network simulations conducted by McDougal and Sorbie (1999) and Wang and Mohanty (1999) (in the related topic of gas condensation) showed that S_{gc} decreases as the hydrostatic pressure gradient increases, a trend also anticipated in Scherpenisse et al., (1994). In a parallel study (Tsimpanogiannis and Yortsos, 2001), we have analyzed the effect of gravity and/or viscous forces on S_{gc}, and developed scaling laws for the dependence of S_{gc} on both f_{qf} and the two respective dimensionless parameters, the Bond and capillary numbers, defined, respectively, as

$$B = \frac{\Delta\rho g k}{\gamma} \quad \text{and} \quad Ca = \frac{q\mu}{\gamma} \tag{2}$$

where $\Delta\rho$ is the density difference between liquid and gas, k is the medium permeability, γ the liquid-gas interfacial tension, q the liquid flow rate and μ is the liquid viscosity. We have found that S_{gc} is a function of f_{qf}, B and Ca, leading to power-law scalings in various limits, with equation (1) obtained in the limits $B \ll 1$ and $Ca \ll 1$, which are also the regions of interest in this chapter.

A modeling attempt to capture the gas phase growth in a depletion experiment was made by Firoozabadi and Kaschiev (1997). These authors used an effective continuum model with bubble growth driven by diffusion. The gas phase is modeled as a collection of effective bubbles, mass transfer to which is approximated by simple expressions. Although the chapter discusses rate-dependent nucleation using classical expressions (see also below), the nucleation issue is in fact bypassed, in that nucleation fraction, the maximum supersaturation, or the effect of depletion rate on the number of bubbles nucleated, are not actually predicted or calculated. Rather, the latter quantities are inferred from the experimental results, and are subsequently used as initial conditions for the gas phase growth following the nucleation period. Additional experiments on pressure depletion, particularly with heavy oils, were reported in Bora et al., (1997), Tang and Firoozabadi (1999), Bora et al., (2000), Andarcia et al., (2001), Arora and Kovscek (2001), Kamp et al., (2001a, 2001b), In some very recent studies, which appeared at the same time this work was being written, (Kamp et al., 2001a; Arora and Kovscek, 2001), presented effective continuum models to interpret the pressure depletion of heavy oils, focusing, in particular, on the foamy oil issue. Because of the high viscous forces in these experiments, these models must also account for two-phase flow, which

in these studies was done using conventional relative permeability functions. In the present context, these studies are of interest insofar as nucleation is concerned. The latter is incorporated in the form of rate-dependent nucleation in Kamp et al., (2001a), and in the form of activated cavities in Arora and Kovscek (2001). Nucleation parameters were estimated to match experimental data (see more discussion below).

The objective of this chapter is to provide a comprehensive model both of the nucleation and the gas-phase growth periods, until the onset of the critical gas saturation. For this purpose, an effective continuum model will be used. If used to model the later stages of bubble growth, where gas clusters occupy several pores and are influenced by the pore geometry, topology and capillarity (e.g. see Li and Yortsos, 1995a, 1995b), effective continuum models have obvious drawbacks. However, they may be adequate for describing nucleation and the early stages of bubble growth. The last two, and particularly the nucleation sequence, are the main areas of interest of this chapter. We focus on the effect of the nucleation characteristics of the porous medium on the maximum supersaturation, the nucleation fraction and the critical gas saturation, and provide an analysis of the effect of various parameters, such as rate, on these quantities. Results for the gas phase growth following the conclusion of nucleation are also presented.

The chapter is organized as follows: First, we formulate the problem and discuss the assumptions made. A scaling analysis allows to recast the problem in a more useful form, to be used for direct predictions. Then, the numerical results of the mathematical model are analyzed. It turns out that for their interpretation, a simplified model of the nucleation and growth periods can be developed. We use the simpler model to obtain expressions for the maximum supersaturation attained in the system as a function of the geometric, thermodynamic and process parameters. In turn, this permits to obtain useful predictive relations for the dependence of the final nucleation fraction and the critical gas saturation on the process parameters. For completeness, we consider two different cases, one corresponding to the decline of pressure at a constant rate, and another corresponding to the withdrawal of liquid at a constant rate. The results are then compared to various published experimental results.

II. MATHEMATICAL FORMULATION

We consider heterogeneous nucleation and growth of multiple bubbles from a binary liquid, within an effective porous medium. The process is driven by the continuous increase in the supersaturation of the system, $KC_\infty(t) - P_l(t)$, due to the slow flow of the liquid phase out of the porous medium. Here, we have assumed for simplicity linear thermodynamic equilibria using Henry's law

$$P_g = KC_\infty(t) \tag{3}$$

where K is the solubility constant, $C_\infty(t)$ is the time-varying mass concentration, P stands for pressure, and subscripts g and l denote gas and liquid, respectively. More complex thermodynamics can certainly be incorporated in the model, but the salient features are manifested with the simple model (3). As remarked, the change in supersaturation can be imposed in two different ways, one in which the pressure declines at a constant rate, and another in which the liquid is withdrawn at constant rate. In either of these, gravitational and/or viscous effects will not be included, with the corrolary that the pressure is spatially uniform. Instead, emphasis is placed on nucleation and on the effect of the increase of supersaturation on the growth of the gas phase.

a. Nucleation

As the liquid pressure declines, nucleation sets in. Yortsos and Parlar (1989) provided a comprehensive review of nucleation in a gas-liquid phase change in porous media driven by solute diffusion. They examined homogeneous and heterogeneous nucleation and concluded that heterogeneous nucleation is the most plausible mechanism in solution gas drives in porous media (see also the recent reviews on the nucleation problem by Laaksonen et al, 1995; Jones et al., 1999). In one particular mechanism considered, nucleation occurs when a gas bubble, either pre-existing or nucleated inside a hydrophobic cavity at the pore walls, becomes unstable and detaches or otherwise occupies the host pore body (Fig. 3a). This type of mechanism is in agreement with visual observations from micromodel experiments (Li and Yortsos, 1995a; El Yousfi et al., 1991; 1997; Bora et al., 2000). In the cavity model, the condition for the activation of a nucleation site is when capillary forces, which hold the bubble trapped inside the cavity, are overcome for the first time (Fig. 3a), namely when the following condition is satisfied between the radius of the nucleation cavity, r_c, and supersaturation,

$$\frac{2\gamma\cos\theta}{r_c} = KC_\infty(t) - P_l(t) \tag{4}$$

where θ is the contact angle ($0 < \theta < \pi/2$). We remark that the onset of nucleation is not kinetically related to the degree of supersaturation, as for example, in conventional approaches (Firoozabadi et al.), but rather depends on the size distribution $\alpha_c(r_c)$ of the nucleation cavities (Fig. 3b). Without loss in generality, we will assume in the following a zero contact angle, which is equivalent to redefining the interfacial tension term γ.

Consider, now, the activation of nucleation sites. With the decrease in the liquid pressure, the right-hand side of (4) increases, eventually becoming positive. Then, various cavities of size satisfying (4) become activated and their corresponding host pore bodies become occupied by gas. At any time, therefore, the current nucleation fraction, f_q, defined as the number fraction of pores that contain sizes which have been activated, is

$$f_q = \int_{r_c}^{\infty} \alpha_c(r) dr \tag{5}$$

where r_c is an implicit function of time, through (4). Equation (5) implies a zero nucleation fraction at zero supersaturation ($r_c \to \infty$) and a nucleation fraction of one at infinite supersaturation ($r_c \to 0$), as expected. Here, the cavity size distribution α_c pertains only to the largest cavity in any given pore (as this cavity will be activated first). The actual number of bubbles contained in a given pore may be larger. We will proceed using the assumption that a number of bubbles n_B are contained in each activated pore. The unknown parameter n_B will be taken equal to 1, for the cavity model (as this is strongly suggested in micromodel experiments), but will be kept arbitrary for the rate-dependent heterogeneous nucleation. We also remark that equation (5) slightly overestimates the true nucleation fraction, since pores containing sites to be activated later, may already be occupied by gas, due to the growth of gas clusters from neighboring pores. A more appropriate expression in such a case would be

$$\frac{df_q}{dt} = (1 - S_g) \frac{d}{dt} \left[\int_{r_c}^{\infty} \alpha_c(r) dr \right] \tag{6}$$

where S_g is the gas saturation (defined as the volume fraction of the pore space occupied by gas). However, in most cases, nucleation terminates well before gas bubble growth has occurred to any substantial degree ($S_g \ll 1$), thus (5) should be an excellent approximation.

It is interesting to illustrate the f_q dependence for various cavity size distributions. For a Rayleigh distribution of the form

$$\alpha_c(r) = \frac{\pi r}{2 r_c^{*2}} \exp\left(-\frac{\pi r^2}{4 r_c^{*2}} \right) \tag{7}$$

where r_c^* is a characteristic (here the mean) cavity size, equation (5) reads

$$f_q = \exp\left(-\frac{\pi r_c^2}{4 r_c^{*2}} \right) = \exp\left(-\frac{\pi \gamma^2}{4 r_c^{*2} (K C_\infty - P_l)^2} \right) \tag{8}$$

This exponential relation bears a superficial resemblance to classical nucleation (see below), a result, however, purely due to the assumption of Rayleigh distribution. Different distributions result in different functionals. For example, we will also consider stretched-exponential or log-normal distributions of the type

$$f_q = \exp\left(-\frac{r_c^n}{\sigma r_c^{*n}} \right) \quad \text{or} \quad f_q = \frac{1}{2} \mathrm{erfc}\left(\frac{\ln \frac{r_c}{r_c^*}}{\sqrt{2}\sigma} \right) \tag{9}$$

respectively, where n is a positive exponent and σ is a measure of the width of the distribution. The type of assumed distribution influences significantly the results to be obtained, as will be demonstrated below.

As long as the level of supersaturation increases with time, the right-hand-side of equation (8) also increases, implying that additional sites become activated, and the nucleation fraction continuously rises. After the supersaturation reaches a maximum (local or global), equation (8) predicts a decreasing f_q, which is unphysical. Therefore, in segments of decreasing supersaturation the nucleation fraction is kept constant. When the supersaturation goes through a global maximum, it signals the end of the nucleation period, in which case the fraction of pores ultimately activated, f_{qf}, will be given by equations (8) or (9) at the time of the maximum supersaturation.

The fraction f_{qf} can be directly related to the number of bubbles nucleated per unit pore volume, N_f, a quantity used in Firoozabadi and Kaschiev, (1997) to quantify nucleation. Assuming $n_B = 1$, we have

$$N_f = \frac{f_{qf} N_T}{V_p} \tag{10}$$

where N_T is the total number of pores and V_p is the total pore volume. By noting that $V_p = N_T V_s$, where V_s is a typical volume of a pore, we can further write

$$N_f = \frac{f_{qf}}{V_s} \tag{11}$$

This allows us to relate the nucleation fraction to experimental values of N_f (see below). We note, in advance, that in typical experiments, f_{qf} is very small, of the order of $10^{-6} - 10^{-9}$.

For future use, we also give a brief account of rate-dependent heterogeneous nucleation. Consider the nucleation rate expression

$$\frac{dN}{dt} = K_{het} \exp\left[-\frac{16\pi\gamma^3 f}{3k_B T(KC_\infty - P_l)^2}\right] \tag{12}$$

where K_{het} is a heterogeneous rate constant, f is a dimensionless number expressing the wettability of the medium vis-a-vis nucleation (ranging between 1 and 0 for perfectly homogeneous and perfectly heterogeneous rate-dependent nucleation, respectively), and k_B is Boltzmann's constant. Using the equivalent of (11) we can express (12) in terms of the nucleation fraction f_q,

$$\frac{df_q}{dt} = \frac{K_{het} V_s}{n_B} \exp\left[-\frac{16\pi\gamma^3 f}{3k_B T(KC_\infty - P_l)^2}\right] \tag{13}$$

Compared to (8), equation (13) contains an explicit rate dependence, while the dependence on parameters, such as γ, is different, as expected.

Through the nucleation process, nucleation centers are activated sequentially, giving rise to evolving gas clusters, which grow by mass transfer from the liquid towards the gas. Sequential nucleation results into clusters of different ages (the time passed since a particular

class of gas clusters has been nucleated/activated). Let $\omega(\tau)$ be the number density of clusters nucleated per total number of pores. Then, $\omega(\tau)d\tau$ is the number of new clusters per total number of pores that become activated in the time interval between τ and $\tau + d\tau$. Evidently,

$$\omega(\tau)d\tau = n_B df_q \tag{14}$$

This relation will be used below to simplify the expressions for the growth of the gas phase.

b. Gas phase growth

As noted previously, during the growth of the gas phase we can roughly distinguish two different periods, one in which the growth is within single pores and a second corresponding to gas clusters spanning several pores (Figs. 2a, 2b). The first period extends throughout and following the nucleation stage, the second is the later stage of growth. In either, growth is driven by diffusive mass transfer of the dissolved gas in the liquid. In the first case, mass transfer results mostly in the increase of the volume of the gas. In the second, it also leads to an increase in the pressure of the gas phase, in case the interface is pinned at pore throats (Fig. 2b), until the time when the smallest capillary threshold at the throats is overcome. Then, the gas cluster volume expands accordingly. Assuming that the rate of growth is relatively slow, for viscous effects to be small, the pattern in the latter stage is one of local percolation (Li and Yortsos, 1995b), namely one in which each cluster grows by occupying sequentially the pores with the smallest capillary threshold available to the cluster perimeter. In general, different clusters compete for the available solute in the liquid, the relative mass transfer rates depending on their geometry and relative position. These dynamics were analyzed by Li and Yortsos (1995a, 1995b).

In the absence of competition between adjacent clusters, an isolated cluster j grows at a rate which is proportional to its effective radius, $R_j(t,\tau)$, and the driving force $C_\infty - C_i$, where C_∞ is the far-field concentration and C_i is the equilibrium concentration at the gas-liquid interface. This is true even for ramified fractal clusters, as was verified by Satik and Yortsos (1996) for the case of a percolation cluster. We will proceed, therefore, by assuming that mass transfer is by quasi-steady-state diffusion and that the gas is ideal. Then, we can write the following mass balance for a growing cluster

$$\left(\frac{M_w}{R_g T}\right)\frac{d}{dt}\left(P_l V_g\right) \approx 4\pi\lambda R_j \mathcal{D}(C_\infty - C_i) \tag{15}$$

where M_w is the molecular weight of the gas, R_g is the ideal gas constant, T is temperature, V_g the gas cluster volume and $\mathcal{D}$ the diffusion coefficient. Dimensionless parameter λ is an $O(1)$ geometric constant to account for possible corrections to the mass transfer model depending on the growth period (see below). In equation (15) we have neglected the capillary

pressure, P_c, which in typical applications is small compared to the liquid pressure. From Henry's law, we have

$$C_i = \frac{P_v}{K} = \frac{P_l + P_c}{K} \approx \frac{P_l}{K} \tag{16}$$

where the second equality is again an excellent approximation in typical applications.

The gas volume V_g takes a different expression in the two different periods. For growth within a single pore, $V_g \approx V_c \left(\frac{R_j}{r_c^*}\right)^3$, where V_c is a characteristic cavity volume (defined here as $\frac{4}{3}\pi r_c^{*3}$). For growth of a cluster spanning several pores, we have the different expression, $V_g \approx A^* V_s \left(\frac{R_j}{r_s^*}\right)^{D_f}$, where V_s is the average site volume, r_s^* a characteristic pore body size, D_f is the mass fractal dimension, equal approximately to 2.5 for a 3-D cluster, and A^* is a dimensionless geometric prefactor. To capture both periods with the same equation we will take the general expression

$$\left(\frac{AV_c M_w}{R_g T}\right) \frac{d}{dt}\left[P_l \left(\frac{R_j}{r_c^*}\right)^{D_f}\right] = 4\pi\lambda R_j \mathcal{D}(C_\infty - C_i) \tag{17}$$

with the understanding that $D_f = 3$, $A = 1$, for the nucleation period, and $D_f \approx 2.5$, $A = \frac{A^* V_s}{V_c}\left(\frac{r_c^*}{r_s^*}\right)^{D_f}$ for the second period.

We expect that the nucleation period and the early part of the growth period are adequately represented by equation (17). However, growth during the later stages of the second period, where gas clusters span several pores, cannot in reality be captured by (17). The presence of competing clusters affects the rates of growth in a non-trivial manner. The latter would still be proportional to a mean driving force, $C_\infty - C_i$, where now C_∞ is the volume-averaged concentration in the liquid, and R_j stands for the average size of a cluster. However, the mass transfer coefficient λ may be variable in time and space, while coalescence of clusters will also occur. Accounting for these complexities is a difficult problem, the solution of which requires a pore-network approach (Li and Yortsos 1995a, 1995b). As noted before, in this chapter we are mostly interested in the nucleation and the early stages of growth periods, before the establishment of the critical gas saturation, where gas volume fractions are relatively small. Therefore, we will proceed with these two assumptions, that on average λ is constant and that coalescence occurs only when the sample-spanning cluster is reached. The second assumption was tested using a local percolation model and found to be adequate as long as the nucleation fraction is small (Tsimpanogiannis 2001).

Under these assumptions, therefore, the growth of the gas phase can be described as that of a collection of clusters of size $R(t,\tau)$, the dynamics of each of which is described by equation (17), with R_j replaced by R, namely

$$\left(\frac{AV_cM_w}{R_gT}\right)\frac{\partial}{\partial t}\left[P_l\left(\frac{R}{r_c^*}\right)^{D_f}\right] = 4\pi\lambda R\mathcal{D}(C_\infty - C_i) \tag{18}$$

and subject to the initial condition $R(\tau,\tau) = r_c(\tau)$, where r_c satisfies (4). In the formulation of Firoozabadi and Kashchiev (1997) and more recently of Arora and Kovscec (2001), the equivalent of equation (18) was integrated under a number of simplifying assumptions to obtain an explicit dependence of R on time. Such an approximation will not be used here.

Consider, next, the mass balance for the solute in the liquid phase. We have

$$(1-S_g)V_p\frac{dC_\infty}{dt} = -4\pi\lambda\mathcal{D}(C_\infty - C_i)N_T\int_0^t R(t,\tau)\omega(\tau)d\tau - C_\infty Q(t) \tag{19}$$

where the integration is over all existing clusters and $Q(t)$, the volumetric flow rate of the liquid out of the porous medium, is in general a function of time. Equivalently, we can rewrite (19) as

$$(1-S_g)V_p\frac{dC_\infty}{dt} = -4\pi\lambda\mathcal{D}(C_\infty - C_i)N_T n_B\int_0^{f_q}\hat{R}(t,f)df - C_\infty Q(t) \tag{20}$$

where we introduced the notation $\hat{R}(t,f(\tau)) \equiv R(t,\tau)$, for the radius of a cluster at time t, nucleated when the nucleation fraction is $f(\tau)$. For the case of instantaneous nucleation, e.g. as postulated in Firoozabadi and Kashchiev (1997), $\hat{R}(t,f_q) = R(t)\delta(f_q - f_{qf})$, where f_{qf} is the final nucleation fraction. Then, the above integral reduces to $R(t)f_{qf}$. Unfortunately, f_{qf} is the very quantity we must determine, is not known a priori, and needs to be computed as part of the overall process. This key task is in detail discussed below. Making the assumption of instantaneous nucleation inherently prohibits the evaluation of this key variable.

The volumetric flow rate $Q(t)/V_p$ is related to the pressure decline rate through the mass balance on the liquid, which reads

$$\frac{d}{dt}\left[\rho_l(1-S_g)\right] = -\rho_l\frac{Q(t)}{V_p} \tag{21}$$

where ρ_l is the liquid density. For a slightly compressible liquid,

$$\rho_l = \rho_o\exp[c(P_l - P_o)] \tag{22}$$

where the liquid compressibility, c, takes typical values in the order of $10^{-5} - 10^{-6}\text{psi}^{-1}$. Then,

$$\frac{Q(t)}{V_p} = -(1-S_g)c\frac{dP_l}{dt} + \frac{dS_g}{dt} \tag{23}$$

Finally, the gas saturation is related to the radius of the growing clusters and the nucleation fraction through the relation

$$S_g = Av\int_0^t \left(\frac{R(t,\tau)}{r_c^*}\right)^{D_f} \omega(\tau)d\tau = Avn_B\int_0^{f_q} \left(\frac{\hat{R}(t,f_q)}{r_c^*}\right)^{D_f} df_q \tag{24}$$

where we introduced the volume ratio $v \equiv \frac{V_c}{V_s}$. Subject to the relevant initial conditions, the system of equations (18), (20), (23) and (24) can be integrated. Integration proceeds until the time when the critical gas saturation is reached. As previously mentioned, and in the absence of significant pressure gradients, this is given by the relation

$$S_{gc} = f_{qf}^{1-\frac{D_f}{E}} \tag{25}$$

As far as the critical gas saturation is concerned, it only suffices to model well the events during the nucleation period (as equation (25) shows). Therefore, the approximations made in the description of the later growth period are only likely to affect the rate at which the critical gas saturation is approached but not its value.

c. Dimensionless formulation

To proceed with the solution of the problem, we recast the equations in dimensionless form. Denote dimensionless quantities by subscript D and scale concentrations by $C_b = \frac{P_b}{K}$, pressure by P_b, where subscript b refers to the bubble point, and cluster size by r_c^*. The choice of the characteristic time depends on the process. We will take $t^* = \frac{P_b}{a}$, where a is the pressure decline rate, for the case of constant pressure decline rate, and $t^* = \frac{V_p}{Q}$, for the case of liquid withdrawal at the constant volumetric rate Q.

For the case of constant pressure decline rate, the dimensionless mass balances for the solute in the gas and liquid phases read

$$(1-t_D)\frac{\partial \hat{R}_D^{D_f}}{\partial t_D} = \frac{\Pi_2}{A\Pi_1}(C_{D\infty} - P_{Dl})\hat{R}_D + \hat{R}_D^{D_f} \tag{26}$$

and

$$(1-S_g)\frac{dC_{D\infty}}{dt_D} = -\frac{1}{\Pi_1}(C_{D\infty} - P_{Dl})\int_0^{f_q} \hat{R}_D(t_D,f_q)df_q - \Pi_3(1-S_g)C_{D\infty} - C_{D\infty}\frac{dS_g}{dt_D} \tag{27}$$

where we have used the equlibrium relationship

$$C_{Di} = P_{Dl}(t_D) \tag{28}$$

and implicitly assumed that the process begins ($t_D = 0$) when the pressure is at the bubble point. In the above, we have also defined three dimensionless groups,

$$\Pi_1 = \frac{V_p a}{4\pi\lambda\mathcal{D}P_b N_T r_c^*} = \frac{V_s a}{4\pi\lambda\mathcal{D}P_b n_B r_c^*}, \quad \Pi_2 = \frac{R_g T}{\upsilon n_B M_w K} \quad \text{and} \quad \Pi_3 = cP_b \tag{29}$$

Parameter Π_1 essentially expresses the ratio of the characteristic times for diffusion at the pore scale to that for the decline of pressure. Although a small number in typical applications (see Table 1), it plays a key role in determining the nucleation fraction and the critical gas saturation as shown below. Parameter Π_2 is the product of the geometric constant υn_B with a thermodynamic constant, expressing the ratio of the equilibrium concentrations in the liquid and the gas phases.

The analogous equations for the case of constant liquid withdrawal rate read as

$$P_{Dl}(t_D)\frac{\partial \hat{R}_D^{D_f}}{\partial t_D} + \hat{R}_D^{D_f}\frac{dP_{Dl}}{dt_D} = \frac{\Pi_2}{A\Pi_4}(C_{D\infty} - P_{Dl})\hat{R}_D \tag{30}$$

and

$$(1 - S_g)\frac{dC_{D\infty}}{dt_D} = -\frac{1}{\Pi_4}(C_{D\infty} - P_{Dl})\int_0^{f_q} \hat{R}_D(t, f_q)df_q - C_{D\infty} \tag{31}$$

where

$$\Pi_4 = \frac{Q}{4\pi\lambda\mathcal{D}N_T n_B r_c^*} = \frac{V_s Q}{4\pi\lambda\mathcal{D}V_p n_B r_c^*} \tag{32}$$

Parameter Π_4 expresses the ratio of the characteristic time for diffusion to that for the emptying of the pore volume. Typically, this is also a small number (Table 1). The liquid mass balance becomes

$$\frac{dP_{Dl}}{dt_D} = \frac{1}{\Pi_3(1 - S_g)}\left(\frac{dS_g}{dt_D} - 1\right) \tag{33}$$

As will be shown below, Π_4/Π_3 plays a role equivalent to Π_1.

Finally, in both cases, we have the following relations. The gas saturation is

$$S_g = A\upsilon n_B \int_0^{f_q} \hat{R}(t_D, f_q)^{D_f} df_q \tag{34}$$

In dimensionless notation the cavity size that becomes activated at a given time is

$$r_{Dq} = \frac{\Pi_c}{C_{D\infty}(t_D) - P_{Dl}(t_D)} \tag{35}$$

where we introduced the dimensionless cavity capillary pressure threshold, $\Pi_c = \frac{2\gamma\cos\theta}{r_c^* P_o}$. This is an important parameter in the overall dynamics of the process. In terms of the supersaturation

$$s \equiv C_{D\infty}(t_D) - P_{Dl}(t_D) \tag{36}$$

or, more conveniently, in terms of the rescaled supersaturation

$$s_D \equiv \frac{s}{\Pi_c} \tag{37}$$

expression (35) can be further expressed as $r_{Dq} = s_D^{-1}$. The nucleation fraction is then given by the various expressions

$$f_q = \exp\left(-\frac{\pi}{4s_D^2}\right), \quad f_q = \exp(-\frac{1}{\sigma s_D^n}) \quad \text{or} \quad f_q = \frac{1}{2}\text{erfc}\left(-\frac{\ln s_D}{\sqrt{2}\sigma}\right) \tag{38}$$

depending on the size distribution used, or by

$$\frac{df_q}{dt_D} = h_1 \exp\left[-\frac{h_2}{s^2}\right] \tag{39}$$

in the rate-dependent nucleation case. In the latter we introduced the dimensionless parameters

$$h_1 = \frac{K_{het} t^* V_s}{n_B} \quad \text{and} \quad h_2 = \frac{16\pi\gamma^3 f}{3P_o^2 k_B T} \tag{40}$$

Parameter h_1 is inversely proportional to Π_1 or to Π_4 in the respective cases of constant pressure decline rate or constant liquid withdrawal rate, respectively. If this dependence is extracted, then it reads as

$$h_1 = \frac{\zeta}{\Pi_1} \quad \text{or} \quad h_1 = \frac{\zeta}{\Pi_4} \quad \text{where} \quad \zeta \equiv \frac{K_{het} V_s^2}{4\pi\lambda\mathcal{D} n_B^2 r_c^*} \tag{41}$$

respectively. The initial conditions for the simulations were $C_{D\infty} = 1$, $P_{Dl} = 1$ and $R_D(\tau, \tau) = s_D^{-1}(\tau)$.

d. Scaling

The above system of equations contains two main parameters, Π_1 and Π_4, which contain the effect of the rate of increase of the supersaturation. As shown in Table 1, these can be rather small and a further rescaling of the nucleation fraction and the cluster size is necessary. After some analysis, it is not difficult to show that for the case of the cavity nucleation model, the two parameters can be scaled out of the differential equations if the following scaling is taken (for example for the constant pressure decline rate) $f_q \sim \Pi_1^{\frac{D_f}{D_f - 1}}$ and $f_q R^{D_f} \sim O(1)$. Given that the nucleation fraction varies only during the first period, we must select $D_f = 3$. We anticipate that this rescaling contains the main effect of the pressure decline rate (or the liquid withdrawal rate) on the nucleation fraction. Based on this, we thus define for the respective cases, rescaled nucleation fractions

$$\phi_q = f_q \Pi_1^{-\frac{3}{2}} \quad \text{or} \quad \phi_q = f_q \left(\frac{\Pi_4}{\Pi_3}\right)^{-\frac{3}{2}} \tag{42}$$

and rescaled cluster sizes

$$\rho_D = \Pi_1^{\frac{1}{2}} \hat{R}_D \quad \text{or} \quad \rho_D = \left(\frac{\Pi_4}{\Pi_3}\right)^{\frac{1}{2}} \hat{R}_D \tag{43}$$

In the new notation, the governing equations become as follows:

For the case of constant rate of pressure decline,

$$(1 - t_D)\frac{\partial \rho_D^{D_f}}{\partial t_D} = \frac{\Pi_2}{A}\Pi_1^{-\frac{3-D_f}{2}} s\rho_D + \rho_D^{D_f} \tag{44}$$

and

$$(1 - S_g)\frac{ds}{dt_D} = -s\int_0^{\phi_q} \rho_D(t_D, \phi_q)d\phi_q - (s + 1 - t_D)\left[\Pi_3(1 - S_g) + \frac{dS_g}{dt_D}\right] + 1 - S_g \tag{45}$$

while, for the case of constant rate of liquid withdrawal

$$\Pi_3 P_{Dl}(t_D)\frac{\partial \rho_D^{D_f}}{\partial t_D} + \Pi_3 \rho_D^{D_f}\frac{dP_{Dl}}{dt_D} = \frac{\Pi_2}{A}\left(\frac{\Pi_4}{\Pi_3}\right)^{-\frac{3-D_f}{2}} s\rho_D \tag{46}$$

and

$$\Pi_3(1 - S_g)\frac{ds}{dt_D} = -s\int_0^{\phi_q} \rho_D(t_D, \phi_q)d\phi_q - \Pi_3(P_{Dl} + s) - \frac{dS_g}{dt_D} + 1 \tag{47}$$

The last two equations are also accompanied by equation (33). The gas saturation expression becomes

$$S_g = A\upsilon n_B \Pi_1^{\frac{3-D_f}{2}} \int_0^{\phi_q} \rho(t_D, \phi_q)^{D_f} d\phi_q \quad \text{or} \quad S_g = A\upsilon n_B \left(\frac{\Pi_4}{\Pi_3}\right)^{\frac{3-D_f}{2}} \int_0^{\phi_q} \rho(t_D, \phi_q)^{D_f} d\phi_q \tag{48}$$

in the respective cases. In the above, we take $A = 1$, $D_f = 3$ for the nucleation period and $A = \frac{A^* V_s}{V_c}\left(\frac{r_c^*}{r_s^*}\right)^{D_f}$, $D_f \approx 2.5$ during the later stages of growth. Thus, during the nucleation period, and for the case of the cavity nucleation model, the dependence on parameters Π_1 and Π_4 does not appear explicitly in the equations for growth, but only in the expression for ϕ_q and in the initial condition for ρ_D (which now reads: $\rho_D(\tau, \tau) = s_D^{-1}(\tau)\Pi_1^{\frac{1}{2}}$ or $s_D^{-1}(\tau)\left(\frac{\Pi_4}{\Pi_3}\right)^{\frac{1}{2}}$, in the respective cases). An explicit dependence on Π_1 (or Π_4) will arise during the second period, when the gas clusters eventually reach a fractal structure and $D_f \approx 2.5$. For the case of rate-dependent nucleation, the rescaled nucleation fraction reads as

$$\frac{d\phi_q}{dt_D} = h_1^* \exp\left[-\frac{h_2}{s^2}\right] \tag{49}$$

where $h_1^* = h_1 \Pi_1^{-\frac{3}{2}}$ or $h_1^* = h_1 \left(\frac{\Pi_4}{\Pi_3}\right)^{-\frac{3}{2}}$ in the respective cases.

The solution of the system of rescaled equations will be sought numerically in the following. Before we proceed, we also briefly mention the thermodynamic equilibrium curve for the respective cases.

e. The thermodynamic equilibrium curve

In the absence of rate effects, the equilibrium relationship $C_{D\infty} = P_{Dl}$ applies. To obtain an expression for the evolution of the gas saturation S_g, we use equations (27) and (26), and (31), (30) and (33), in the respective cases of constant pressure decline rate and constant liquid withdrawal rate. Since this pertains to growth following nucleation, we replace the integral term in (30) and (34) with $f_q R_D$ and $f_q R_D^{D_f}$, respectively. Then, by eliminating the mass transfer term proportional to s we obtain

$$(1 - t_D)\left[1 + \frac{1}{\kappa}\right]\frac{dS_g}{dt_D} = (1 - S_g)(1 - \Pi_3(1 - t_D)) + \frac{S_g}{\kappa} \tag{50}$$

for the case of the constant pressure decline rate, and

$$\left[1 - S_g + \frac{S_g}{\kappa}\right]\frac{dP_{Dl}}{dt_D} + \frac{P_{Dl}}{\kappa}\frac{dS_g}{dt_D} = -P_{Dl} \tag{51}$$

and

$$\Pi_3(1 - S_g)\frac{dP_{Dl}}{dt_D} - \frac{dS_g}{dt_D} = -1 \tag{52}$$

for the case of constant rate of liquid withdrawal, where we introduced the thermodynamic parameter $\kappa \equiv \frac{R_g T}{M_w K}$. The solution of the above can be readily obtained if we assume a small Π_3, which is typically the case. We find

$$P_{Dl} = \left(1 - S_g + \frac{S_g}{\kappa}\right)^{\frac{\kappa+1}{\kappa-1}} \approx 1 - \frac{\kappa + 1}{\kappa} S_g \tag{53}$$

for either case, and in addition

$$P_{Dl} = \left[1 - \left(\frac{\kappa - 1}{\kappa}\right) t_D\right]^{\frac{\kappa+1}{\kappa-1}} \tag{54}$$

for the case of constant rate of liquid withdrawal. Equation (54) is in fact equivalent to (53), given the assumption of negligible liquid volume expansion (small Π_3), and where $t_D = S_g$. Since t_D is the dimensionless measure of the liquid volume expelled, either of these

equations express the $P - V$ thermodynamic equilibrium relation and will be compared to the non-equilibrium results.

III. RESULTS

The system of differential equations was solved numerically using a fourth-order Runge-Kutta method (Press et al., 1994). A typical calculation requires the time to be marched forward. A difficulty is that the total number of classes of gas clusters is not known *a priori*, but it is an outcome of the computation during the nucleation process. In theory, this number is infinite, and the problem becomes one of solving an infinite system of differential equations. In practice, the number of equations is constrained by the size of the time step. At each time step we examine whether nucleation of a new class of gas clusters is possible, namely whether the supersaturation is increasing. If so, a new class of gas clusters is added. Then, the simultaneous growth of all different classes of clusters is computed. When the supersaturation reaches a maximum, further nucleation stops. Computations during the nucleation process were also facilitated with an asymptotic analysis, to be described in more detail in a later section.

a. Constant Pressure Decline Rate

In the typical case, parameters which can vary over a significant range are Π_1 and Π_c (and possibly Π_2). An additional important variable is the type of the cavity size distribution used in the calculation of the nucleation fraction. The sensitivity to these parameters was examined in the simulations.

The effect of Π_1 and Π_c on the rescaled nucleation fraction, ϕ_q, the mean rescaled radius, $\rho_{D,m}$, the rescaled supersaturation, s_D, and the gas saturation, S_g, is shown in Figs. 4-7. In these calculations, we used a Rayleigh size distribution, Π_2 and Π_3 were kept constant to the values 5.28×10^6 and 2.2×10^{-2}, respectively, while Π_1 varied over several orders of magnitude (from 10^{-8} to 10^{-2}).

The variation of ϕ_q as a function of the dimensionless time, t_D, and of the parameters Π_1 and Π_c is shown in Fig. 4. It is shown to increase very rapidly in a small time interval, and then to stabilize to a final value, at the conclusion of the nucleation period. Such behavior is characteristic of nucleation processes, and has features similar to the work of El Yousfi et al. (1991, 1997), but it is demonstrated here for the first time for the case of nucleation from pre-existing, trapped gas. The rapid variation of ϕ_q is approximately a stretched exponential of the form

$$\phi_q \sim \exp\left(-\frac{\pi \Pi_c^2}{4 t_D^2}\right), \qquad \phi_q \sim \exp\left(-\frac{\Pi_c^n}{\sigma t_D^n}\right), \qquad \phi_q \sim \mathrm{erfc}\left(\frac{\ln \frac{\Pi_c}{\sigma t_D}}{\sqrt{2}\sigma}\right) \tag{55}$$

for the various cases, as during the early nucleation period we have $s \sim t_D$ (see below). Equation (55) suggests that, e.g. for the Rayleigh distribution case, a plot of $-\ln\phi_q$ vs. t_D^{-2} is linear with slope $\frac{\pi\Pi_c^2}{4}$. Such a behavior is indeed observed in the numerical results. Because of the very sharp rise, the process can be interpreted as instantaneous nucleation (IN), although the details of its evolution to the final values are indeed important. Fig. 4a shows that for constant Π_c, the effect of Π_1 on the rescaled nucleation fraction is not very significant at small Π_1, but that it becomes stronger (roughly a power law) as Π_1 takes larger values. The relatively weak dependence on Π_1 verifies the correctness of the scaling (91) taken above. At the same time, the stronger dependence at larger Π_1 is important, and it is needed in order to explain experimental data, as will be shown below. In terms of the actual nucleation fraction, these findings imply that an increase in Π_1 leads to an increase in the final fraction, f_{qf}, according to a power law scaling, which is roughly $\sim \Pi_1^{\frac{3}{2}}$ at very small Π_1, and $\sim \Pi_1$ at larger Π_1. The effect of Π_c is also significant. As Π_c increases, the final nucleation fraction ϕ_{qf} (hence f_{qf}) decreases (Fig. 4b). The increase of f_{qf} with an increase in Π_1 and a decrease in Π_c is expected. Larger values of Π_1 imply a faster decline rate, a greater departure from equilibrium, the establishment of a greater supersaturation in the system, hence the activation of more nucleation sites. Likewise, smaller Π_c imply that nucleation is facilitated at increasingly smaller supersaturations, as larger size cavities can be activated. An approximate analysis shown below will provide a theoretical explanation of the behavior observed.

Fig. 5 shows the corresponding effects on the mean rescaled size ρ_{Dm}. As anticipated, there are two regions, one corresponding to the nucleation period, and another to growth after nucleation. The two periods can be roughly approximated as power-law regimes (as a function of time) with slopes approximately equal to 1 and 0.63, respectively. The effect of Π_1 is relatively insignificant at small Π_1, confirming the validity of the scaling (91). The effect of Π_c is more significant. Smaller values of Π_c lead to an increase in the nucleation fraction, and a corresponding decrease in the size of the gas clusters at the conclusion of nucleation.

Fig. 6a shows plots of the rescaled supersaturation s_D as a function of time for different Π_1 and Π_c. At the beginning of the process and during nucleation, the supersaturation increases with time almost linearly, suggesting that $C_{D\infty}$ does not vary significantly in that period. As nucleation and growth occurs, the rate of supersaturation increase slows down and, at some point, s_D reaches a maximum value, s_{Dm}. It is at that point where nucleation terminates. Following this, the supersaturation decreases monotonically. The maximum value s_{Dm} is plotted in Fig. 6b as a function of Π_1 and Π_c. We first note that s_{Dm} is in general of the order of 10^{-1}. The dependence on the parameters is weak at small Π_1 and large Π_c, but becomes stronger at larger Π_1 and smaller Π_c. The behavior is consistent

with that of the nucleation fraction discusssed above. From a compilation of experimental results Scherpenisse et al., (1994) suggested that s_{Dm} behaves roughly as a power-law of the pressure decline rate with exponent 1/4. Our analysis indicates that such a power law is not universally valid, although it may apply in a certain range of Π_1. It is interesting that the sensitivity of s_{Dm} to Π_c and Π_1 (and in particular to the latter) is not as large as one might have intuitively anticipated. However, in spite of the weak sensitivity, its effect on the nucleation fraction can be significant, due to the exponential dependence, as can be seen for example in the following expression for the Rayleigh distribution

$$\phi_q = \exp\left(-\frac{\pi}{4s_D^2} - \frac{D_f}{(D_f-1)}\ln\Pi_1\right) \tag{56}$$

Because of the s_D^{-2} dependence and because s_{Dm} is of the order of 10^{-1}, even small changes in s_D can have a very large effect on ϕ_q, thus on the nucleation fraction. This large sensitivity counterbalances the weak sensitivity of s_{Dm} on Π_1 and β and leads overall to a non-trivial effect. Of course, different distributions may lead to different conclusions, as further analyzed below.

The evolution of the gas saturation is shown in Fig. 7. It follows that of f_q, during the nucleation period, and that of ρ_{Dm}, during the period of growth. The latter gives a power-law segment of slope 0.63. The effect of Π_c is indirect, in that smaller values of Π_c promote larger values of S_g due to an increase in both f_{qf} and ρ_D. The difference between the equilibrium and the actual curve depends on the value of Π_1, increasing as the latter increases, but remaining constant following the end of the nucleation period. Fig. 8 shows the effects of Π_1 and Π_c on the critical gas saturation S_{gc}. Recall that the latter pertains to the formation of a sample-spanning cluster, in the absence of viscous or gravity effects. Thus, Fig. 8 actually reflects the variation of f_{qf}. Fig. 8 shows that S_{gc} can be considered a power-law both of Π_1 and of Π_c with exponents that vary between 0.16 and 0.25 with respect to Π_1 and between -0.33 and -0.22, with respect to Π_c, respectively. These trends are consistent with the experimental evidence (Scherpenisse et al., 1994; Bora et al., 1997).

b. Constant Rate of Liquid Withdrawal

Similar results were obtained for the case of constant rate of liquid withdrawal. The effect of Π_4 and Π_c on the rescaled nucleation fraction, ϕ_q, the mean value of the rescaled radius, $\rho_{D,m}$, the rescaled supersaturation, s_D, and the gas saturation, S_g, is shown in Figs. 9-12. In these calculations, we again used the Rayleigh size distribution, Π_2 and Π_3 were kept constant to the values 5.28×10^6 and 2.2×10^{-2}, respectively, while Π_4 varied over several orders of magnitude (from 10^{-10} to 10^{-4}). The effect of the parameters is almost identical to the constant pressure decline rate, subject to the change $\Pi_1 \rightarrow \Pi_4/\Pi_3$ and to

the rescaling of time by Π_3. Thus, we anticipate a scaling of the form: $f_{qf} \sim \Pi_4^{\frac{3}{2}}$ at small Π_4, and $f_{qf} \sim \Pi_4$ at larger Π_4; and of the form: $f_{qf} \sim \Pi_c^{-2}$ at large Π_c, and $f_{qf} \sim \Pi_c^{-1.3}$ at smaller Π_4. The critical gas saturation has the analogous scaling: $S_{gc} \sim \Pi_4^{0.25}$ at small Π_4, and $S_{gc} \sim \Pi_4^{0.16}$ at larger Π_4; and $S_{gc} \sim \Pi_c^{-0.22}$ at large Π_c, and $S_{gc} \sim \Pi_c^{-0.33}$ at smaller Π_4. The discussion and interpretation of these findings is similar to the previous.

What is different in the case of constant rate of liquid withdrawal is the evolution of pressure with time (Fig. 13). Indeed, during the nucleation period, the pressure declines almost linearly with time, $P_{Dl} \approx 1 - \frac{t_D}{\Pi_3}$, following equation (33). This decrease slows down rapidly as the maximum supersaturation is approached, however, in the very near region of which the pressure reaches a local minimum. Following this minimum, the pressure increases, reaches a maximum and subsequently decreases, roughly paralleling the equilibrium curve. The pressure minimum decreases as Π_4 increases (Fig. 13), the dependence being roughly the same as that of s_{Dm}, namely weak at small Π_4 and stronger at larger Π_4 (where the 1/4 power law may be applicable).

The non-equilibrium behavior reflects the competition between mass transfer and solute availability as explained in the following. Roughly, the ideal gas law requires $P_g V_g = n R_g T$. The rate of change dn/dt of the moles in the gas phase is dictated by the mass transfer rate. At the end of the nucleation period, near s_{Dm}, this rate is the highest. Now, if the rate by which the gas volume expands, dV_g/dt (which is almost equal to Q), is not sufficiently large, the increase in volume due to mass transfer cannot be compensated, thus the pressure, P_g, must increase. An increasing pressure leads to a successively decreasing supersaturation (since C_i increases), thus to a continuous decrease of the mass transfer rate. Eventually, this decrease becomes sufficiently large for the volume expansion rate to balance mass transfer. Then, the pressure goes through a maximum and subsequently begins to decline.

In the above, we used the cavity-based nucleation model. Qualitatively similar results were also obtained for the model based on rate-dependent nucleation. A comparison of the predictions of the two models will be discussed in a later section. The numerical solution will be compared against available experimental results. However, before doing so it is beneficial to provide an interpretation of the main numerical findings, using a simpler model to be developed in the next section.

IV. INTERPRETATION USING A SIMPLER MODEL

To interpret the results obtained we consider a simpler model that captures the essential features of the problem. Consider, first, the nucleation period for the case of constant pressure decline rate.

a. Nucleation

To approximately describe the nucleation period, we use the following equations for the gas phase growth and the supersaturation

$$\frac{\partial \rho_D^3}{\partial t_D} \approx \Pi_2 s \rho_D \tag{57}$$

and

$$\frac{ds}{dt_D} \approx 1 - (1+\kappa) s \int_0^{\phi_q(s)} \rho_D d\phi_q \tag{58}$$

respectively. These are subject to the initial conditions

$$s(0) = 0 \quad \text{and} \quad \rho_D(\tau, \tau) = \frac{\Pi_1^{\frac{1}{2}}}{s_D(\tau)} \tag{59}$$

At early times and for small Π_1, the solution of this system is approximately

$$s \approx t_D \quad \text{and} \quad \rho_D \approx \left(\frac{\Pi_1 \Pi_c^2}{s^2(\tau)} + \frac{\Pi_2 (s^2 - s(\tau)^2)}{3} \right)^{\frac{1}{2}} \tag{60}$$

Equation (60) shows that the dimensionless supersaturation is identical to the dimensionless time and that the mean cluster size becomes evantually a power-law of time with exponent 1. Both these are consistent with the numerical results during the nucleation period shown in Figs. 5 and 6.

We will use (58) and (60) to approximate the approach to the maximum supersaturation. The latter is reached when $\frac{ds}{dt_D} = 0$, namely when

$$s \int_0^{\phi_q} \rho_D d\phi_q \approx \frac{1}{1+\kappa} \tag{61}$$

We will approximate the solution of (61) by taking $\rho_D \approx \left(\frac{\Pi_2}{3}\right)^{\frac{1}{2}} s(t_D)$. Then, using (60) and the definition of ϕ_q, leads to an approximate algebraic equation for the rescaled maximum supersaturation, s_{Dm}. For the case of Rayleigh distribution we find,

$$\frac{\pi}{4 s_{Dm}^2} - 2 \ln s_{Dm} \approx \ln(1+\kappa) - \frac{1}{2}\ln 3 - \frac{3}{2}\ln \Delta \tag{62}$$

where we introduced the combination of variables

$$\Delta \equiv \Pi_1 \Pi_c^{-\frac{4}{3}} \Pi_2^{-\frac{1}{3}} \tag{63}$$

Likewise, we get

$$\sigma^{-1}s_{Dm}^{-n} - 2\ln s_{Dm} \approx \ln(1+\kappa) - \frac{1}{2}\ln 3 - \frac{3}{2}\ln\Delta \tag{64}$$

in the case of a stretched exponential, and

$$s_{Dm}^2 \mathrm{erfc}\left[\frac{\ln\frac{1}{s_{Dm}}}{\sqrt{2}\sigma}\right] \approx 2\sqrt{3}(1+\kappa)^{-1}\Delta^{\frac{3}{2}} \tag{65}$$

in the case of a log-normal distribution.

Equations (62)-(65) are significant. First, they suggest that the dependence of the maximum supersaturation on the various parameters of the problem, other than the thermodynamic ones, enters only through parameter Δ. The solution for the Rayleigh distribution is plotted in Fig. 14, as a function of Δ. We note that s_{Dm} varies weakly, in the range $0.1 - 1$, as Δ varies over many orders of magnitude. For very small Δ, the maximum supersaturation is practically constant. However, as Δ takes larger values, s_{Dm} increases weakly and eventually much more strongly, as Δ exceeds the order of one (compare also with Fig. 6). Shown also in the logarithmic coordinates of Fig. 14 is a line with slope 1/4, corresponding to the 1/4 power-law, postulated by Scherpenisse et al., (1994) to describe several experimental data. Although the power law does not capture the overall behavior, it is a reasonable approximation within a certain interval of Δ. Plotted in the same figure are also the results of the numerical solution of the full problem for a number of different parameter values. The agreement between the numerical results and the simple analytical model is remarkable and demonstrates the validity of the simple equation (62). The solution of (64) and (65) for different values of the parameters is plotted in Fig. 15. As the tail of the cavity size distribution becomes longer (which occurs for smaller values of $n > 0$ and/or for larger σ) the dependence of s_{Dm} on Δ becomes stronger. In addition, the region where a power-law scaling with exponent $\approx 1/4$ tentatively fits the results, increases and also covers a range with smaller values of Δ.

We can use (62)-(65) to approximate the final nucleation fraction, ϕ_{qf}, and the time (or pressure) at the end of nucleation. For all cases we have

$$\phi_{qf} \approx s_{Dm}^{-2}(1+\kappa)^{-1}(\Pi_c)^{-2}\left(\frac{\Pi_2}{3}\right)^{-\frac{1}{2}} \tag{66}$$

thus, the final nucleation fraction reads

$$f_{qf} \approx s_{Dm}^{-2}(1+\kappa)^{-1}\Pi_1^{\frac{3}{2}}(\Pi_c)^{-2}\left(\frac{\Pi_2}{3}\right)^{-\frac{1}{2}} \tag{67}$$

This equation is another important result of this chapter. We can use (67) to deduce the following:

(a) In the region where s_{Dm} varies weakly with Δ (namely at small Δ) the final nucleation fraction varies as a power law of Π_1, with slope equal to 3/2. This is consistent with the anticipated increase in the nucleation fraction as the rate of pressure decline increases. The equation also suggests a power-law dependence on the capillary properties of the cavity. One should interpret this carefully, however, since information on the cavity properties is included in all parameters Π_1, Π_2 and Π_c (through r_c^* and v). For example, if we were to consider only the dependence on r_c^*, we would find the power-law scaling $f_{qf} \sim r_c^{*2}$, indicating a smaller nucleation fraction as the cavity size decreases. This is also as expected.

(b) In the region where s_{Dm} may approximated by a power-law dependence on Δ, e.g. as $s_{Dm} \sim \Delta^m$, we have the power-law scaling

$$f_{qf} \sim (1+\kappa)^{-1}\Delta^{\frac{3}{2}-2m} \tag{68}$$

Such a dependence on Δ leads to a decrease in the exponent in the power-law scaling. For example, if we take the region where $m \approx 1/4$ (as suggested by Scherpenisse et al., 1994), we read

$$f_{qf} \sim \Pi_1 \qquad \text{and} \qquad f_{qf} \sim r_c^{*\frac{4}{3}} \tag{69}$$

Such a linear dependence of the rate on Π_1 was postulated in Scherpenisse et al., (1994) and McDougal and Sorbie (1999), to fit available experimental data. These results are also consistent with the full numerical solutions shown in Fig. 4.

Likewise, the time, hence the pressure, P_m, when nucleation ends can be approximated using (60). we find

$$\frac{P_b - P_m}{P_b} \approx \Pi_c s_{Dm} \tag{70}$$

thus, the supersaturation at the end of nucleation is directly related to s_{Dm}. This means, of course, that in this approximation $C_{D\infty} \approx 1$. It follows that in the region where s_{Dm} is insensitive to Δ, the supersaturation only varies linearly with Π_c. A rate dependence, which has been observed experimentally in some cases, enters only insofar as s_{Dm} varies with Δ. Assuming again a power-law variation with $m \approx 1/4$, as above, the maximum pressure supersaturation in that case varies as

$$\frac{P_b - P_m}{P_b} \sim \Pi_1^{\frac{1}{4}} \qquad \text{and} \qquad \frac{P_b - P_m}{P_b} \sim r_c^{-\frac{2}{3}} \tag{71}$$

The 1/4 power-law dependence was found to fit well experimental data (see below). It is interesting that the maximum supersaturation relative to the bulk bubble point is only weakly dependent on the rate of pressure decline, for example varying by only a factor of 2 when the pressure decline rate varies by two orders of magnitude, in the range considered.

A similar analysis applies for the case of constant liquid withdrawal rate. The equivalent equations now read

$$\Pi_3 \frac{d\rho_D^3}{dt_D} \approx \Pi_2 s \rho_D \tag{72}$$

and

$$\Pi_3 \frac{ds}{dt_D} \approx 1 - \left(1 + \frac{\kappa}{\Pi_3}\right) s \int_0^{\phi_q} \rho_D d\phi_q \tag{73}$$

The early-time solution for this problem is identical to the previous (60), where t_D must now be replaced by t_D/Π_3. Again, the linear scaling of the size of the cluster with time is consistent with the full numerical solution.

Proceeding as above, we find that the maximum rescaled supersaturation, s_{Dm}, is now given by a similar equation

$$\kappa s \rho_D \phi_q \approx \Pi_3 \tag{74}$$

where ρ_D satisfies (60). Thus, the solution of (74) is the same as that of (62), except that one must replace Π_1 with $\frac{\Pi_4}{\Pi_3}$, and -ln(1 + κ) with ln(Π_3/κ). For exactly the same reasons, the final nucleation fraction is given by (67), by substituting Π_1 with $\frac{\Pi_4}{\Pi_3}$ and $\frac{1}{1+\kappa}$ with $\frac{\Pi_3}{\kappa}$. The previous analysis for the constant pressure decline rate applies directly to the constant rate of liquid withdrawal, subject to the substitution indicated. A comparison between the solution of the full problem (for the cases of the Rayleigh distribution and a strectched exponential with $n = 0.5$ and $\sigma = 1.0$) and of the approximate equation (74) is shown in Fig. 16. We note an excellent agreement for practically all values tested. The scalings obtained are also consistent with the solution of the full equations.

In systems involving a constant rate of liquid withdrawal, the pressure reaches a minimum, as noted above. This will be denoted by subscript n, and we will proceed to identify it as follows. Integrating equation (33), we obtain

$$\Pi_3 P_{Dl} \approx A\upsilon\phi_q\rho_D^3 - t_D + \Pi_3 \tag{75}$$

where we made the same approximation for the integral, as above. Finding the minimum in pressure requires equating the derivative of the above to zero. Using (60) for ρ_D, it is not difficult to show the following equation satisfied by s_{Dn} at that point

$$\phi_q \left(3s_{Dn}^2 + \frac{\pi}{2}\right) \approx \frac{\Pi_3}{A\upsilon} \left(\frac{3}{\Pi_2}\right)^{\frac{3}{2}} \left(\frac{1}{\Pi_c}\right)^2 \tag{76}$$

More generally, for the general stretched exponential case (for $\sigma = 1$) we have,

$$\phi_q \left(3s_{Dn}^2 + ns_{Dn}^{2-n}\right) \approx \frac{\Pi_3}{Av} \left(\frac{3}{\Pi_2}\right)^{\frac{3}{2}} \left(\frac{1}{\Pi_c}\right)^2 \tag{77}$$

Based on these equations, one can show that the pressure reaches its minimum before the supersaturation reaches its maximum, suggesting that nucleation will continue following the minimum in pressure, albeit for a very brief period of time. We can solve the above equations to determine the pressure value at the local pressure minimum. For the Rayleigh distribution we find

$$\frac{P_b - P_n}{P_b} \approx \Pi_c s_{Dn} \left[\frac{2s_{Dn}^2 + \frac{\pi}{2}}{3s_{Dn}^2 + \frac{\pi}{2}}\right] \tag{78}$$

and for the stretched exponential,

$$\frac{P_b - P_n}{P_b} \approx \Pi_c s_{Dn} \left[\frac{2s_{Dn}^n + n}{3s_{Dn}^n + n}\right] \tag{79}$$

Given that s_{Dn} is generally of order 0.1, equations (78) and (79) are very similar to those for the maximum supersaturation in the constant-pressure decline rate case, equation (70). Furthermore, because of the closeness of s_{Dn} to s_{Dm}, we may use the sensitivity analysis we conducted before to assess the dependence of $\frac{P_b - P_n}{P_b}$ to the various parameters. For example, in the region where s_{Dm} is insensitive to Δ, the supersaturation $\frac{P_b - P_n}{P_b}$ varies linearly with Π_c. When s_{Dm} is more sensitive, with the assumed power-law variation with $m = 1/4$, the supersaturation at the minimum pressure varies roughly as

$$\frac{P_b - P_m}{P_b} \sim \left(\frac{\Pi_4}{\Pi_3}\right)^{\frac{1}{4}} \Pi_c^{\frac{2}{3}} \Pi_2^{-\frac{1}{12}} \tag{80}$$

Such a dependence can be used to guide the matching of the experimental data to be discussed below.

We close this section by applying a similar analysis, now for the different rate-dependent nucleation model. For the latter we recall the rescaled expression

$$\frac{d\phi_q}{dt_D} = h_1^* \exp\left[-\frac{h_2}{s^2}\right] \tag{81}$$

where $h_1^* = h_1 \Pi_1^{-\frac{3}{2}}$ or $h_1^* = h_1 \left(\frac{\Pi_4}{\Pi_3}\right)^{-\frac{3}{2}}$ in the respective cases. We proceed as before to evaluate the time when nucleation terminates, which is the time when the maximum supersaturation is reached. To find the maximum supersaturation, one needs to determine the evolution of ϕ_q. For this we use in (49) the relation $s \approx t_D$, to write

$$\frac{d\phi_q}{ds} \approx h_1^* \exp\left[-\frac{h_2}{s^2}\right] \tag{82}$$

the solution of which is readily found

$$\phi_q = h_1^* \left(s \exp\left[-\frac{h_2}{s^2} \right] - \sqrt{\pi h_2} \mathrm{erfc}\left[\frac{\sqrt{h_2}}{s} \right] \right) \tag{83}$$

Thus, the maximum supersaturation occurs when the right-hand-side of (82) vanishes, which approximately occurs when the following equation is satisfied

$$s_{Dm}^{*3} \exp\left(-\frac{1}{s_{Dm}^{*2}} \right) - s_{Dm}^{*2} \sqrt{\pi} \mathrm{erfc}\left(\frac{1}{s_{Dm}^*} \right) = \Delta_h^{\frac{3}{2}} (1+\kappa)^{-1} \tag{84}$$

where we defined the reduced supersaturation $s_D^* = s/\sqrt{h_2}$ and the new combination of parameters

$$\Delta_h = \Pi_1 h_1^{-\frac{2}{3}} h_2^{-1} \Pi_2^{-\frac{1}{3}} \quad (= \Pi_1^{\frac{5}{3}} \zeta^{-\frac{2}{3}} h_2^{-1} \Pi_2^{-\frac{1}{3}} \quad \text{or} \quad = \frac{\Pi_4^{\frac{5}{3}}}{\Pi_3} \zeta^{-\frac{2}{3}} h_2^{-1} \Pi_2^{-\frac{1}{3}}) \tag{85}$$

in the respective cases of constant pressure decline rate and constant rate of liquid withdrawal. For relatively small s_{Dm}^*, the solution of the above equation also reads

$$\frac{1}{s_{Dm}^{*2}} - 5 \ln s_{Dm}^* \approx \ln(1+\kappa) - \frac{1}{2}\ln 3 - \ln 2 - \frac{3}{2}\ln \Delta_h \tag{86}$$

A plot of the solution of the general equation (84) is shown in Fig. 17. We note features very similar to the cavity nucleation model, namely a region of weak sensitivity and another, at higher Δ_h, of stronger sensitivity. Close examination shows that the rescaled supersaturation for the rate-dependent nucleation model is slightly higher in the region of small Δ_h, but its increase at higher Δ_h is weaker than for the cavity model. Given the stronger dependence of Δ_h on rate, the dependence of the maximum supersaturation could be at first glance be considered stronger. For example, for s_{Dm} to vary as a power-law of the rate with exponent m, it suffices for it to follow a power law with respect to Δ_h with exponent $3m/5$. Interestingly, however, this higher sensitivity is counterbalanced by the lower sensitivity to Δ_h at higher Δ_h compared to the cavity model. For example, if we were to demand $m = 1/4$, then we should consider a range of Δ_h in Fig. 17 where the exponent is of the order of $3/20$. As shown in the Figure, this roughly corresponds to the same range as that of Δ for the cavity model (Figs. 15, 16).

The nucleation fraction at the time of the maximum supersaturation can be estimated as before. We find

$$f_{qf} = s_{Dm}^{*-2} h_2^{-1} \left(\frac{\Pi_2}{3} \right)^{-\frac{1}{2}} (1+\kappa)^{-1} \Pi_1^{\frac{3}{2}} \tag{87}$$

As expected, the nucleation rate increases with a decreasing h_2, namely with smaller values of the interfacial tension γ and the heterogeneous nucleation parameter f. It is interesting

to note that the combination $h_1^{\frac{1}{2}} h_2^{\frac{3}{4}}$ plays here the role of Π_c. For the same reasons, as before, the pressure at the end of nucleation, which is also approximately the minimum pressure, is given by

$$\frac{P_b - P_m}{P_b} \approx \sqrt{h_2} s^*_{Dm} \tag{88}$$

In matching experimental data using this model, we would need to infer two parameters, the rate constant K_{het} and the heterogeneous parameter f. The variation of the supersaturation with the parameters, and particularly with Π_1 is shown in Figure 18.

Working likewise for the constant liquid withdrawal rate, we find that the maximum supersaturation corresponds to an equation identical to (84), provided that one must substitute $1+\kappa$ with κ/Π_3 and κ with Π_3. The minimum pressure varies approximately following (88).

b. Gas cluster growth

To simplify the modeling of the growth regime, where nucleation has terminated we consider only one class of clusters and write the mass balances as follows. For the case of constant pressure decline rate we approximate

$$\frac{dC_{D\infty}}{dt_D} \approx -(C_{D\infty} - 1 + t_D)z - \kappa k_1 C_{D\infty} \frac{dz^{D_f}}{dt_D} \tag{89}$$

and

$$(1 - t_D)\frac{dz^{D_f}}{dt_D} = k_1^{-1}(C_{D\infty} - 1 + t_D)z + z^{D_f} \tag{90}$$

where we introduced the variable

$$z \equiv \phi_{qf} \rho_D \tag{91}$$

and the parameter

$$k_1 = \frac{\phi_{qf}^{1-D_f} \Pi_1^{\frac{1}{4}}}{\Pi_2} \tag{92}$$

Values for the final value of the rescaled nucleation fraction, ϕ_{qf}, are to be obtained from the previous analysis. Likewise, for the case of constant liquid withdrawal rate, we have similar equations, except that now one must use Π_4/Π_3 in place of Π_1,

$$\frac{dC_{D\infty}}{dt_D} \approx -\frac{1}{\Pi_3}(C_{D\infty} - P_{Dl})z - C_{D\infty} \tag{93}$$

and

$$\Pi_3 P_{Dl} \frac{dz^{D_f}}{dt_D} + z^{D_f} \left[\kappa k_2 \frac{dz^{D_f}}{dt_D} - 1 \right] = k_2^{-1} (C_{D\infty} - P_{Dl}) z \tag{94}$$

along with

$$\frac{dP_{Dl}}{dt_D} \approx \frac{1}{\Pi_3} \left(\kappa k_2 \frac{dz^{D_f}}{dt_D} - 1 \right) \tag{95}$$

where we defined

$$k_2 = \frac{\phi_{qf}^{1-D_f} \left(\frac{\Pi_4}{\Pi_3} \right)^{\frac{1}{4}}}{\Pi_2} \tag{96}$$

The comparison of the full numerical results with those corresponding to the approximate model are shown in Fig. 19, for the constant rate of liquid withdrawal. We note a good agreement. In particular, the approximate model captures well the pressure increase, following the mimimum, its subsequent leveling and the gradual decline paralleling the equilibrium curve.

V. COMPARISON WITH EXPERIMENTS

The above model and predictions were checked against various published experimental results. We attempted to match the following quantities and their dependence on parameters, particularly the rate: the final nucleation fraction, the maximum supersaturation s_{Dm}, the critical gas saturation, S_{gc}, the minimum pressure, for the case of constant rate of liquid withdrawal, and finally the evolution of pressure or saturation as a function of time and the various process parameters.

Experimental data for maximum superaturation, for the case of constant pressure decline rate experiments, are reported by Scherpenisse et al., (1994). As pointed out in the previous section, the experimental dependence is reported to be roughly linear. As explained in detail in the previous section, matching these results requires the use of a window in the parameter Δ, in the s_{Dm} vs. Δ relationship, where approximately a 1/4 power-law is observed. The corresponding window is identified in Fig. 19 for the cavity model and in Fig. 17 for the rate-dependent nucleation model. The combination Δ contains a number of geometric variables, which are not known a priori. For example,

$$\Delta \sim V_s (r_c^* v)^{\frac{1}{3}} \tag{97}$$

while, the cavity size distribution is also not known. We used best estimates for V_s and a range of values for the cavity size characteristics, to indicate the range of values of Δ where

the various experimental results may fall for the various size distributions considered. In order for the theory to agree with the experiments, values of $n = 0.223$ and $\sigma = 0.046$ are needed. Likewise, the predictions of the rate-dependent nucleation model were also tested. Here, parameters that must be estimated include the wettability parameter f and the heterogeneous nucleation rate K_{het}, since

$$\Delta_h \sim K_{het}^{-\frac{2}{3}} f^{-1} \tag{98}$$

Interestingly, the nucleus initial size is not included in this dependence. The corresponding window for this model is indicated in Fig. 17, for the experiments of Scherpenisse et al., (1994). It is shown that for the reported dependence to be matched, the following parameter values must be used: $f = 2. \times 10^{-4}$ and $K_{het} = 0.03867$. This is rather extreme for the model considered.

Estimates for the final nucleation fraction for the experiments by Scherpenisse et al., (1994) are shown in Fig. 20. We note that as anticipated, f_{qf} is quite small, of the order of 10^{-10}-10^{-7}. In order to estimate the final nucleation fraction for the experimental data we, first, calculate the number of nucleation sites per unit volume, $N_f \sim R_N^{-3}$, where R_N is half the average distance between nucleations and is given by Scherpenisse et al., (1994). Then, f_{qf} is calculated using equation (11). The power-law scaling with exponent 1, as predicted by the theory, is well supported by the data.

Additional comparisons, including constant liquid withdrawal rate experiments, are in progress.

VI. CONCLUSIONS

In this chapter we developed an effective continuum model to describe the nucleation and subsequent growth of a gas phase from a supersaturated, slightly compressible binary liquid in a porous medium, driven by solute diffusion. The evolution of the gas results either from the reduction of the system pressure at a constant rate, or from the withdrawal of the liquid at a constant rate. The model addresses two stages before the onset of bulk gas flow, nucleation and gas phase growth. We assume negligible gradients due to gravity or viscous forces, thus the critical gas saturation, which signals the onset of bulk gas flow, is only a function of the nucleation fraction.

We showed that the important quantities characterizing the process, such as the fraction of pores that host activated sites, the deviation from thermodynamic equilibrium, the maximum supersaturation in the system and the critical gas saturation depend crucially on the nucleation characteristics of the medium. We used a heterogeneous nucleation models primarily in the form of pre-existing gas, trapped in hydrophobic cavities, but also in terms

of a rate-dependent nucleation, to investigate in detail the nucleation behavior. Using scaling analysis and a simpler analytical model we showed that the relevant quantities during nucleation can be expressed in terms of a simple combination of dimensionless parameters, which include rate effects, for either type of nucleation model.

The theory predicts that the maximum supersaturation in the system is a weakly increasing function of rate, which in the region of typical experimental parameters, can be approximated as a power law with a small exponent. This function depends sensitively on the probability density function of the nucleation cavity sizes. It also predicts that the final nucleation fraction, thus the critical gas saturation, is a power law of the decline (or the withdrawal) rate. The theoretical exponents were shown to fit the experimental data.

References

[1] Andarcia, L., Kamp, A.M., and P. Vaca, "Heavy Oil Solution Gas Drive in the Venezuelan Orinoco Belt: Laboratory Experiments and Field Simulation" paper *SPE 69715*, presented at the SPE International Thermal Operations and Heavy Oil Symposium, Margarita Island, Venezuela, 12-14 March 2001.

[2] Arora, P., and A.R. Kovscek, "Mechanistic Modeling of Solution-Gas Drive in Viscous Oils," paper *SPE 69717*, presented at the SPE International Thermal Operations and Heavy Oil Symposium, Margarita Island, Venezuela, 12-14 March 2001.

[3] Bora, R., Maini, B.B., and A. Chakma, "Flow visualization Studies of Solution Gas Drive Process in Heavy Oil Reservoirs Using a Glass Micromodel," *SPE Reservoir Eval. Eng.*, **3**, 224-229 (2000).

[4] Bora, R., Maini, B.B., and A. Chakma, "Flow visualization Studies of Solution Gas Drive Process in Heavy Oil Reservoirs Using a Glass Micromodel," paper *SPE 37519* presented at the SPE International Thermal Operations and Heavy Oil Symposium, Bakersfield, CA, 10-12 February 1997.

[5] Doughty, C. and K. Pruess, "A Similarity Solution for Two-Phase Fluid and Heat Flow Near High-Level Nuclear Waste Packages Emplaced in Porous Media," *Int. J. Heat Mass Transfer*, **33**, 1205-1222 (1990).

[6] Du, C., and Y.C. Yortsos, "A Numerical Study of the Critical Gas Saturation in a Porous Medium," *Transport in Porous Media*, **35**, 205-225 (1999).

[7] El Yousfi, A., Zarcone, C., Bories, S. and R. Lenormand, "Mècanismes de Formation d'une Phase Gazeuse par détente d'un liquide en Milieu Poreux," *C.R. Acad. Sci. Paris, Série II,* **313**, 1093-1098 (1991).

[8] El Yousfi, A., Zarcone, C., Bories, S. and R. Lenormand, "Physical Mechanisms for Bubble Growth During Solution Gas Drive," paper *SPE 38921* presented at the SPE Annual Technical Conference and Exhibition, San Antonio, TX, 5-8 October 1997.

[9] Feder, J., *Fractals,* Plenum, New York (1988).

[10] Firoozabadi, A., and A. Aronson, "Visualization and Measurement of Gas Evolution anf Flow of Heavy and Light Oil in Porous Media," *SPE Reservoir Eval. Eng.*, **2**, 550-557 (1999).

[11] Firoozabadi, A., and D. Kashchiev, "Pressure and Volume Evolution During Gas Phase Formation in Solution Gas Drive Processes," *SPE Journal*, **1**, 219-227 (1997).

[12] Firoozabadi, A, Ottesen, B, and M. Mikkelsen, "Measurements of Supersaturation and Critical Gas Saturation," *SPE Form. Eva.*, 337-344 (December 1992).

[13] Jones, S.F., Evans, G.M., and K.P. Galvin, "Bubble Nucleation from Gas Cavities - A Review," *Adv. Colloid Interface Sci.*, **80**, 27-50. (1999).

[14] Ho, C.K., and K.S. Udell, "Mass Transfer Limited Drying of Porous Media Containing an Immobile Binary Liquid Mixture," *Int. J. Heat Mass Transfer*, **38**, 339-350 (1995).

[15] Kamp, A.M., Joseph, D.D., and R. Bai, "A New Modeling Approach for Heavy Oil Flow in Porous Media," paper *SPE 69720*, presented at the SPE International Thermal Operations and Heavy Oil Symposium, Margarita Island, Venezuela, 12-14 March 2001.

[16] Kamp, A.M., Heny, C., Andarcia, L., Lago, M. and A. Rodriguez, "Experimental Investigation of Foamy Oil Solution Gas Drive," paper *SPE 69725*, presented at the SPE International Thermal Operations and Heavy Oil Symposium, Margarita Island, Venezuela, 12-14 March 2001.

[17] Kumar, R., Pooladi-Darvish, M., and T. Okazawa, "An Investigation Into Enhanced Recovery Under Solution Gas Drive in Heavy Oil Reservoirs," paper *SPE 59336*, presented at the SPE/DOE Improved Oil Recovery Symposium, Tulsa, OK, 3-5 April 2000.

[18] Laaksonen, A., Talanquer, V., and D.W. Oxtoby, "Nucleation: Measurements, Theory, and Applications," *Annu. Rev. Phys. Chem.*, **46**, 489-524 (1995).

[19] Li, X., and Y.C. Yortsos, "Visualization and Simulation of Bubble Growth in Pore Networks," *AIChE J.*, **41**, 214-222 (1995a).

[20] Li, X., and Y.C. Yortsos, "Theory of Multiple Bubble Growth in Porous Media by Solute Diffusion," *Chem. Eng. Sci.*, **50**, 1247-1271 (1995b).

[21] McDougall, S.R., and K.S. Sorbie, "Estimation of Critical Gas Saturation During Pressure Depletion in Virgin and Waterflooded Reservoirs," *Petroleum Geoscience*, **5**, 229-233 (1999).

[22] Maini, B., "Foamy Oil Flow in Primary Production of Heavy Oil Under Solution Gas Drive," paper *SPE 56541*, presented at the SPE Annual Technical Conference and Exhibition, Houston, TX, 3-6 October 1999.

[23] Maini, B., "Foamy Oil Flow in Heavy Oil Production," *J. Canadian Petroleum Technology*, **35**(6), 21-24 (1996)

[24] Moulu, J.C., and D.L. Longeron, "Solution-Gas Drive: Experiments and Simulation," *Proc.,* Fifth European Symposium on Improved Oil Recovery, Budapest, Hungary, April 1989.

[25] Pooladi-Darvish, M., and A. Firoozabadi, "Solution-gas Drive in Heavy Oil Reservoirs," *J. Canadian Petroleum Technology*, **38**(4), 54-61 (1999).

[26] Prats, M., *Thermal Recovery,* SPE Monograph, Dallas, TX, 1982.

[27] Press, W.H., Teukolsky, W.T., Vettering, S.A., and B.P. Flannery, *Numerical Recipies,* 2nd ed. Cambridge University Press, (1992).

[28] Renard, G., Nauroy, J.-F., Deruyter, Ch., Moulu, J.-C., Sarda, J.-P., and J.-F. Le Romancer, "Production Froide des Huiles Visqueuses," *Oil & Gas Science and Technology - Rev. IFP*, **55**, 35-66 (2000).

[29] Scherpenisse, W., Wit, K., Zweers, A.E., Shoei, G., and A. van Wolfswinkel, "Predicting Gas Saturation Buildup during Depressurisation of a North Sea Oil Reservoir," paper *SPE 28842*, presented at the European Petroleum Conference, London, UK, 25-27 October 1994.

[30] Satik, C., and Y.C. Yortsos, "A Pore Network Study of Bubble Growth in Porous Media Driven by Heat Transfer," *ASME J. of Heat Transfer*, **118**, 155-462 (1996).

[31] Sheng, J.J., Maini, B.B., Hayes, R.E., and W.S. Tortike, "Critical Review of Foamy Oil Flow," *Transport in Porous Media*, **35**, 157-187 (1999a).

[32] Sheng, J.J., Hayes, R.E., Maini, B.B., and W.S. Tortike, "Modeling Foamy Oil Flow in Porous Media," *Transport in Porous Media*, **35**, 227-258 (1999b).

[33] Smith, G.E., "Fluid Flow and Sand Production in Heavy-Oil Reservoirs Under Solution-Gas Drive," *SPE Prod. Eng.*, 169-180 (May 1988).

[34] Tang, G.-Q., and A. Firoozabadi, "Gas and Liquid-Phase Relative Permeabilities for Cold Production from Heavy Oil," paper *56540* presented at the SPE Annual Technical Conference and Exhibition, Houston, TX, 3-6 October 1999.

[35] Thome, J.R., *Enhanced Boiling Heat Transfer,* Hemisphere Publishing Co., New York, (1990).

[36] Tsimpanogiannis, I.N. , PhD Diss., Univ. of Southern California, In preparation. (2001).

[37] Tsimpanogiannis, I.N., and Y.C. Yortsos. In preparation (2001).

[38] Wang, X., and K.K. Mohanty, "Critical Condensate Saturation in Porous Media," *J. Colloid Interface Sci.*, **214**, 416-426 (1999).

[39] Yortsos, Y.C., and M. Parlar, "Phase Change in Binary Systems in Porous Media: Application to Solution Gas Drive," paper *SPE 19697*, presented at the SPE Annual Technical Conference and Exhibition, San Antonio, TX, 8-11 October 1989.

Table 1. Characteristic values for the various parameters.

Parameter	*Pressure decline*	*Liquid Withdrawal*
MW (g/mol)	18.6	16.0
D (cm^2/s)	$2.40x10^{-5}$	$1.35x10^{-5}$
γ $(dynes/cm)$	8.2	13.0
T (R)	566.3	566.3
P_b $(psia)$	870.0	1400.0
K $(psia\ cm^3/g)$	12476	4487.9
c $(psia^{-1})$	$1.0x10^{-5}$	$1.4969x10^{-5}$
r_s (cm)	$9.0x10^{-4}$	$1.0x10^{-2}$
r_c (cm)	$8.0x10^{-6}$	$7.1x10^{-6}$
A^*	1.	1.
n_B	1.	1.
λ	1.	1.
α $(psia/h)$	14.5	-
Q (cm^3/s)	-	$1.67x10^{-5}$
V_p (cm^3)	-	132.24
Π_1	$5.859x10^{-6}$	-
Π_2	$2.327x10^{6}$	$1.476x10^{10}$
Π_3	$8.700x10^{-3}$	$1.600x10^{-2}$
Π_4	-	$4.392x10^{-4}$
Π_c	$3.417x10^{-2}$	$4.959x10^{-2}$

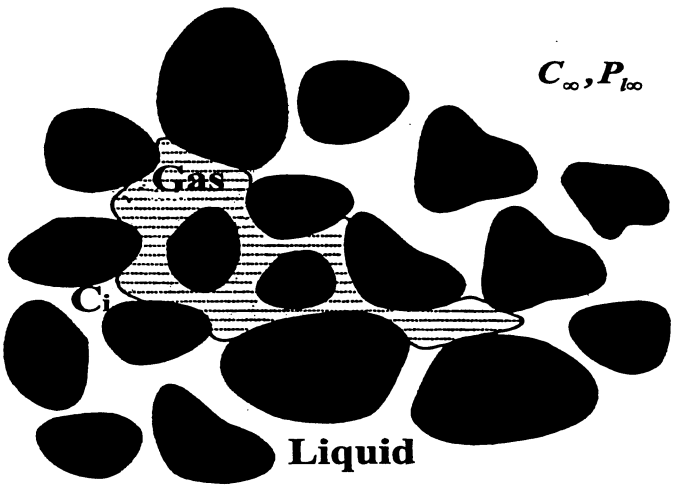

Figure 1: Schematic of a gas cluster growth in a porous medium.

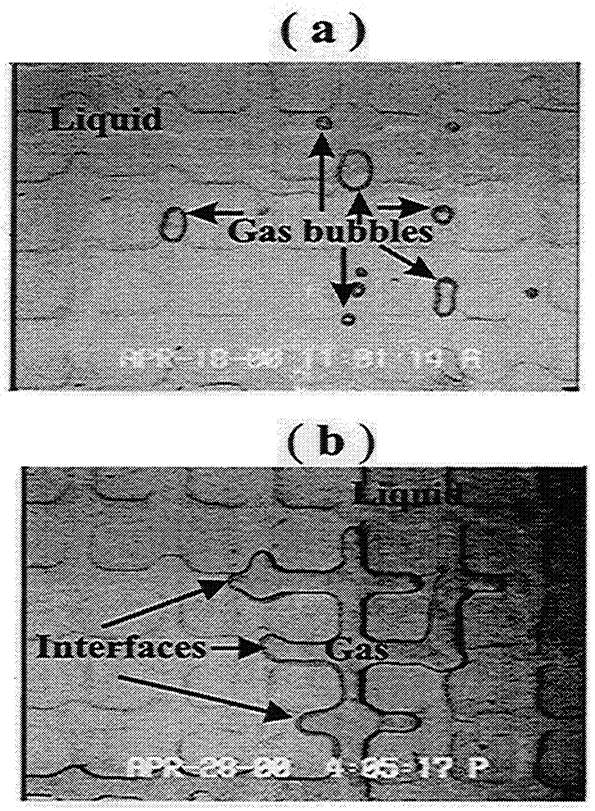

Figure 2: Micromodel snapshots indicating: **(a)** Gas bubbles confined within single pore throats/bodies. **(b)** A gas bubble spanning several pore bodies.

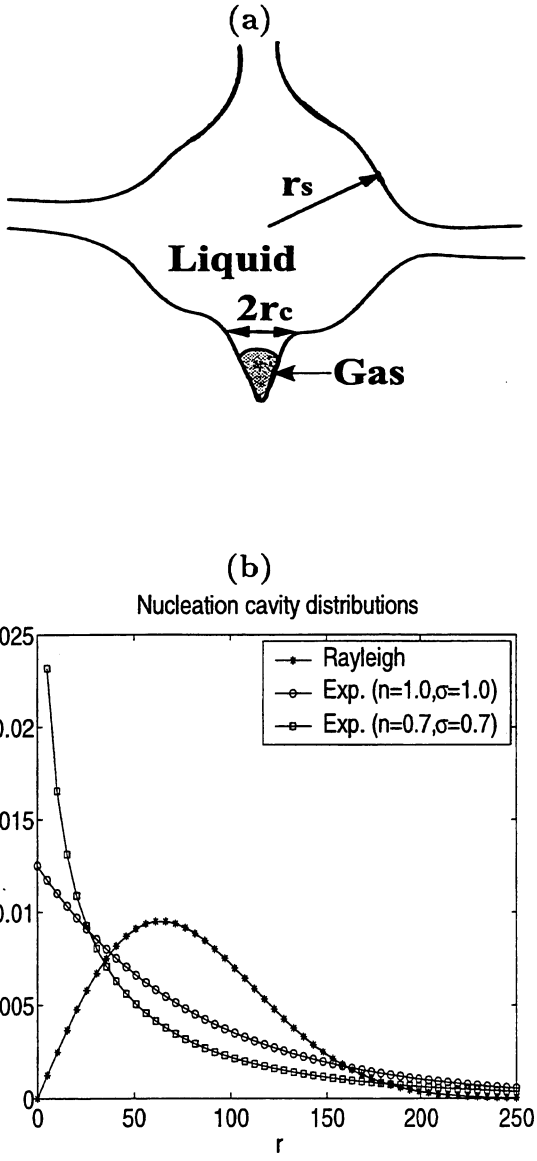

Figure 3: Cavity nucleation properties: (a) Schematic of a nucleation cavity in a host pore body. (b) Rayleigh and stretched exponential distributions for nucleation cavities (dimensionless sizes).

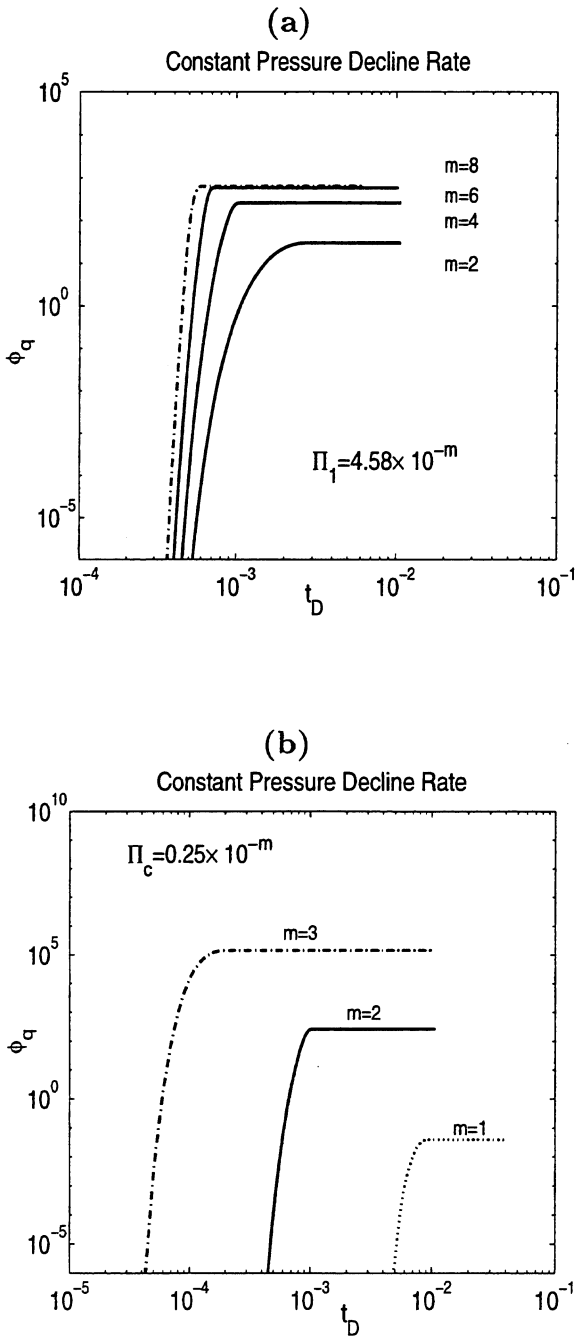

Figure 4: Variation of the rescaled nucleation fraction, ϕ_q, as a function of dimensionless time, t_D, for constant pressure decline rate: **(a)** Effect of $\Pi_1 = 4.58x10^{-m}$, for $\Pi_c = 2.5x10^{-3}$, $\Pi_2 = 5.28x10^6$ and $\Pi_3 = 2.2x10^{-2}$. **(b)** Effect of $\Pi_c = 0.25x10^{-m}$, for $\Pi_1 = 4.58x10^{-4}$ and $\Pi_3 = 2.2x10^{-2}$

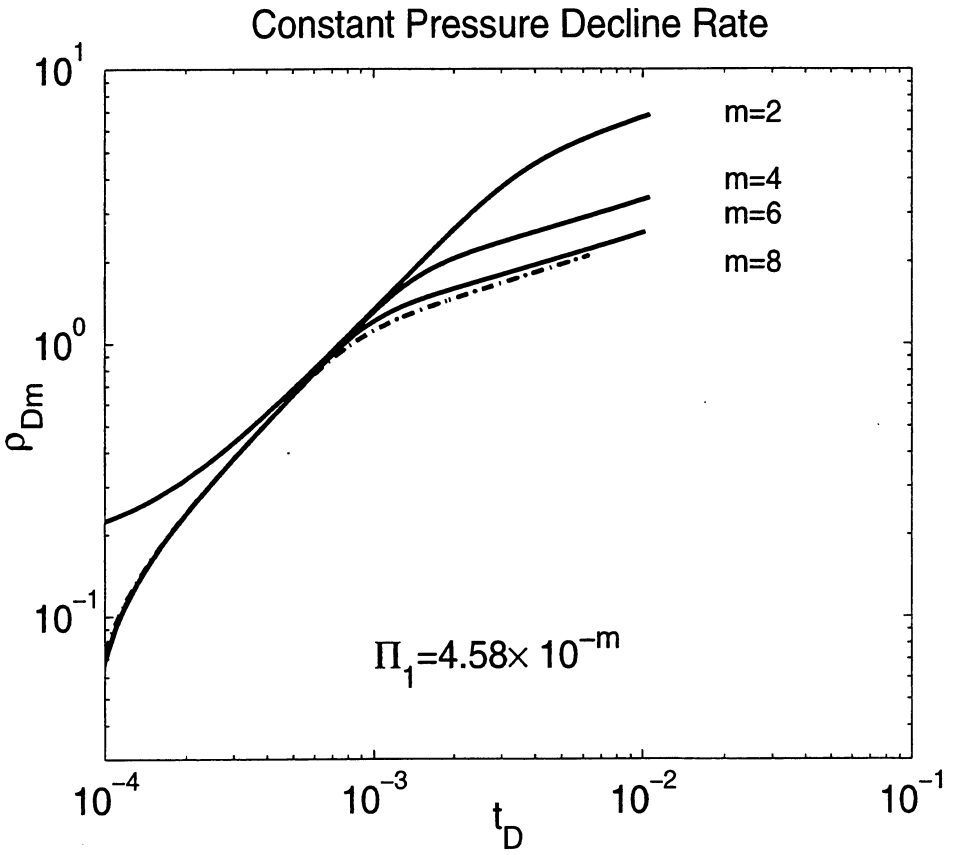

Figure 5: Variation of the mean rescaled dimensionless radius, ρ_{Dm}, as a function of dimensionless time, t_D, for constant pressure decline rate. Effect of $\Pi_1 = 4.58x10^{-m}$, for $\Pi_c = 2.5x10^{-3}$, $\Pi_2 = 5.28x10^6$ and $\Pi_3 = 2.2x10^{-2}$.

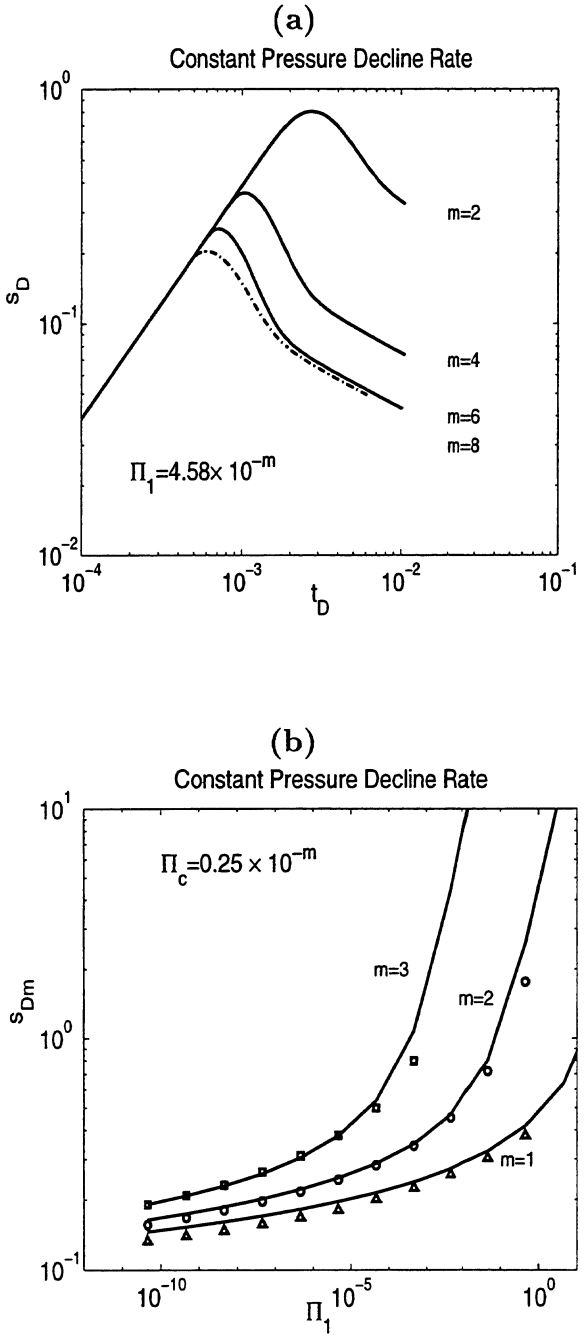

Figure 6: Constant pressure decline rate: **(a)** Variation of the rescaled supersaturation, s_D, as a function of dimensionless time, t_D. Effect of $\Pi_1 = 4.58x10^{-m}$, for $\Pi_c = 2.5x10^{-3}$, $\Pi_2 = 5.28x10^6$ and $\Pi_3 = 2.2x10^{-2}$. **(b)** Effect of the dimensionless parameter Π_1 on the maximum rescaled supersaturation, s_{Dm}, for $\Pi_c = 0.25x10^{-m}$. Points correspond to the full numerical solution, solid lines correspond to the simpler problem.

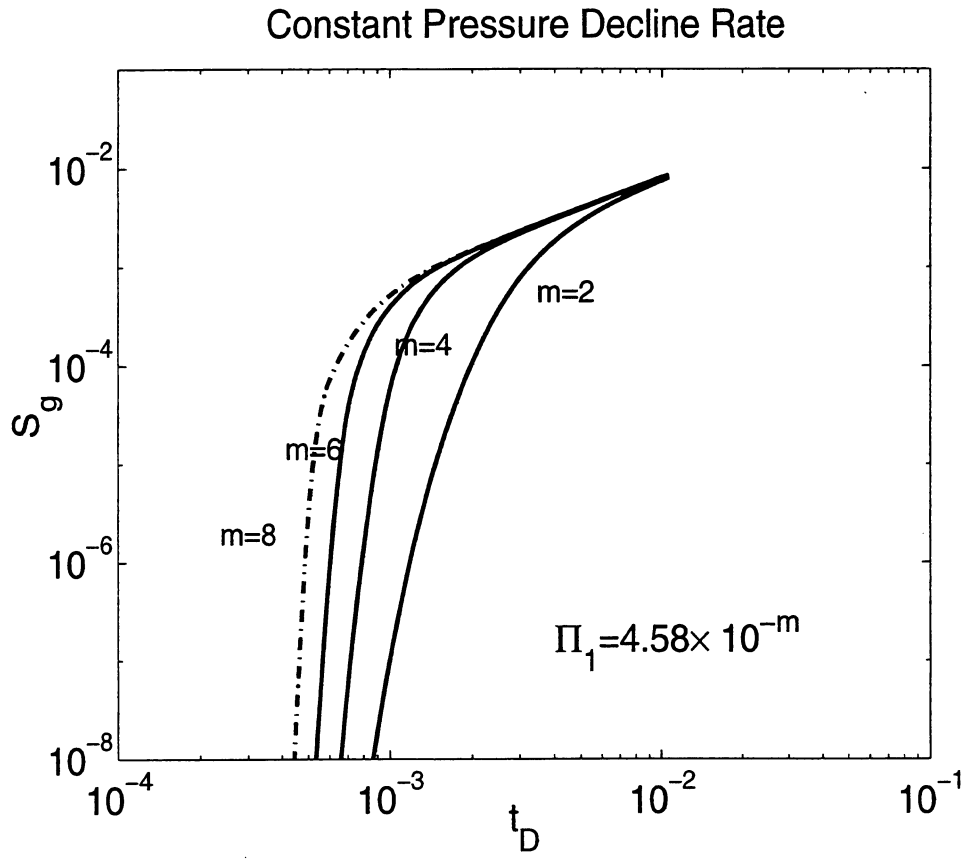

Figure 7: Variation of the gas saturation, S_g, as a function of dimensionless time, t_D, for constant pressure decline rate. Effect of $\Pi_1 = 4.58x10^{-m}$, for $\Pi_c = 2.5x10^{-3}$, $\Pi_2 = 5.28x10^{6}$ and $\Pi_3 = 2.2x10^{-2}$.

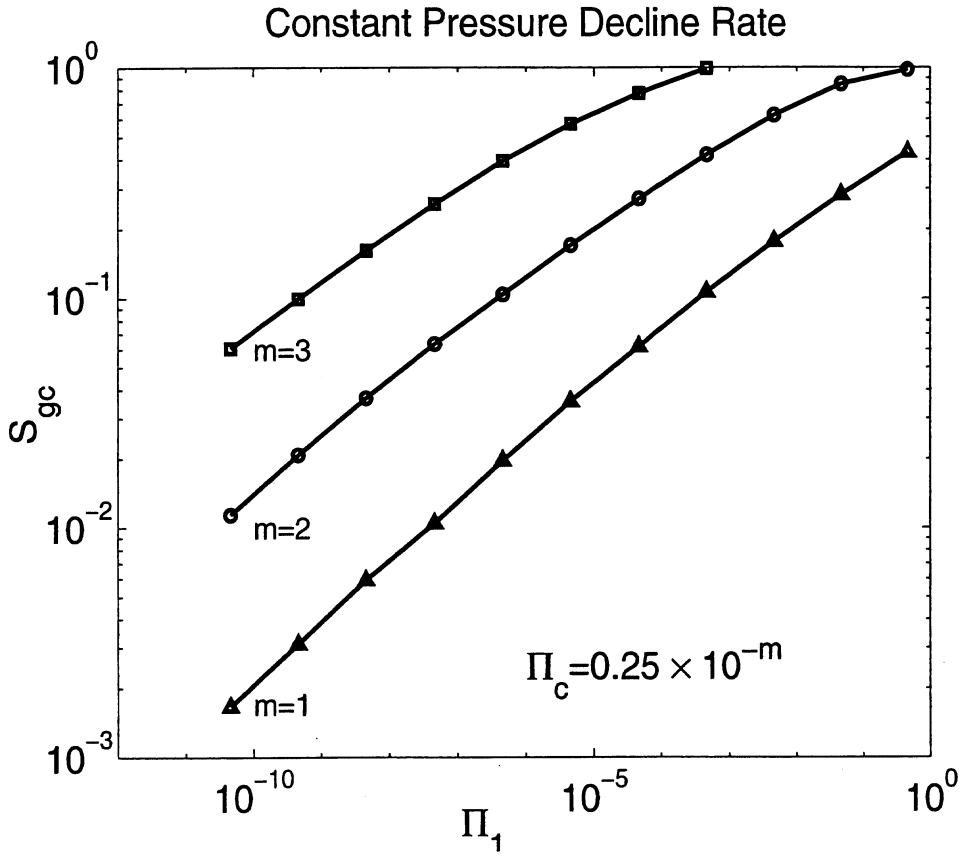

Figure 8: Effect of the dimensionless parameter Π_1 on the critical gas saturation, S_{gc}, for $\Pi_c = 0.25x10^{-m}$ and constant pressure decline rate. Points denote the full numerical solution.

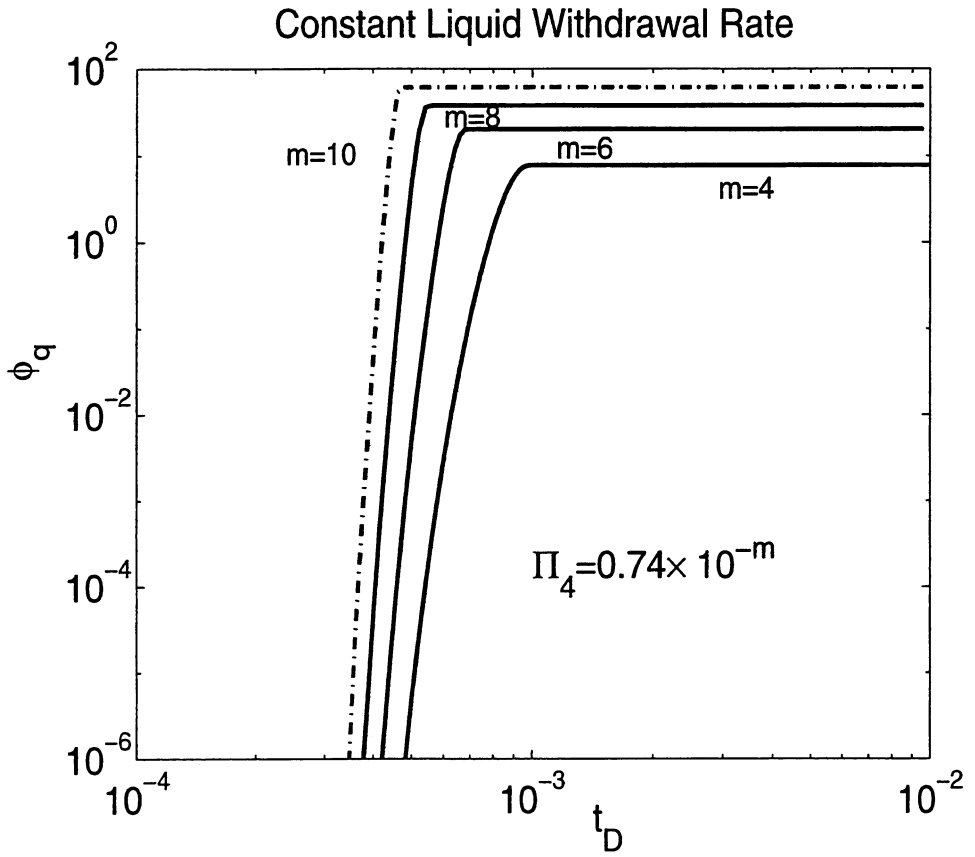

Figure 9: Variation of the rescaled nucleation fraction, ϕ_q, as a function of dimensionless time, t_D, for constant liquid withdrawal rate. Effect of $\Pi_4 = 0.7446x10^{-m}$, for $\Pi_c = 2.5x10^{-3}$, $\Pi_2 = 5.28x10^6$ and $\Pi_3 = 2.2x10^{-2}$.

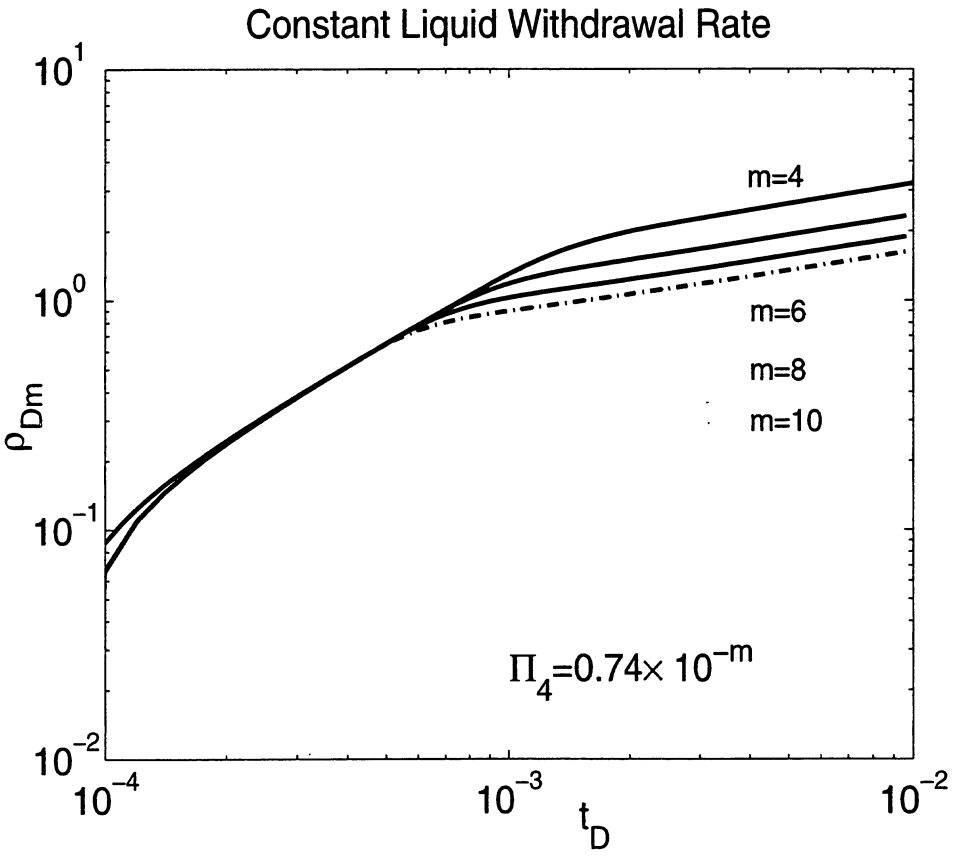

Figure 10: Variation of the mean rescaled dimensionless radius, ρ_{Dm}, as a function of dimensionless time, t_D, for constant liquid withdrawal rate. Effect of $\Pi_4 = 0.7446x10^{-m}$, for $\Pi_c = 2.5x10^{-3}$, $\Pi_2 = 5.28x10^6$ and $\Pi_3 = 2.2x10^{-2}$.

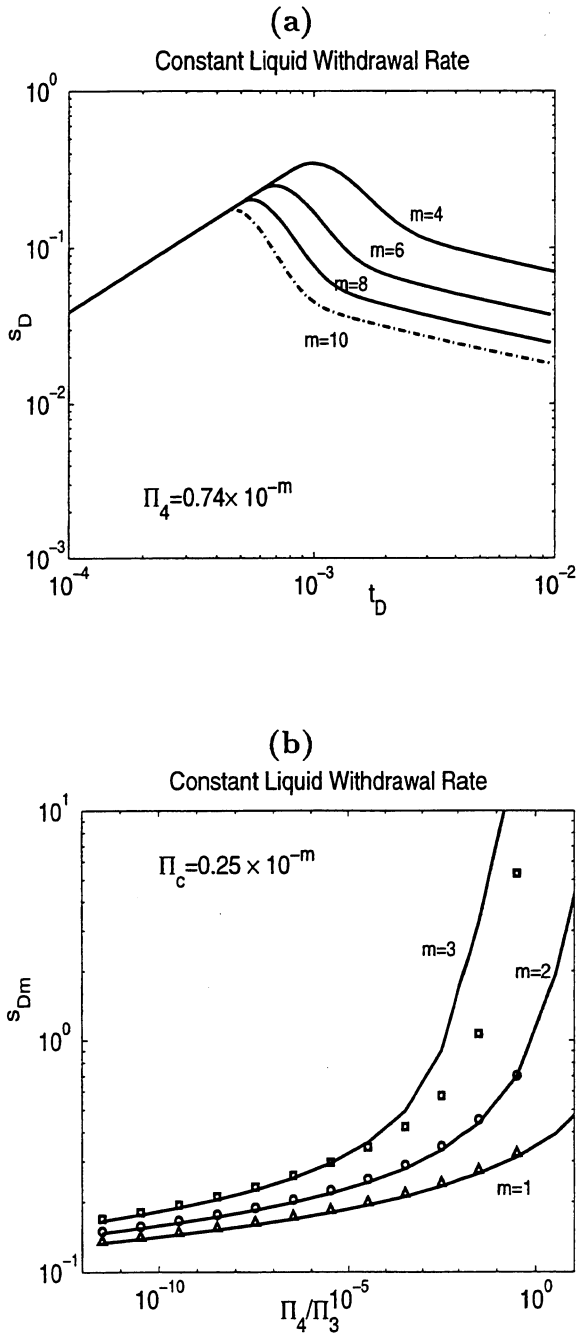

Figure 11: Constant liquid withdrawal rate: **(a)** Variation of the rescaled supersaturation, s_D, as a function of dimensionless time, t_D. Effect of $\Pi_4 = 0.7446x10^{-m}$, for $\Pi_c = 2.5x10^{-3}$, $\Pi_2 = 5.28x10^6$ and $\Pi_3 = 2.2x10^{-2}$. **(b)** Effect of the dimensionless parameter Π_4/Π_3 on the maximum rescaled supersaturation, s_{Dm}, for $\Pi_c = 0.25x10^{-m}$. Points correspond to the full numerical solution, solid lines correspond to the simpler problem.

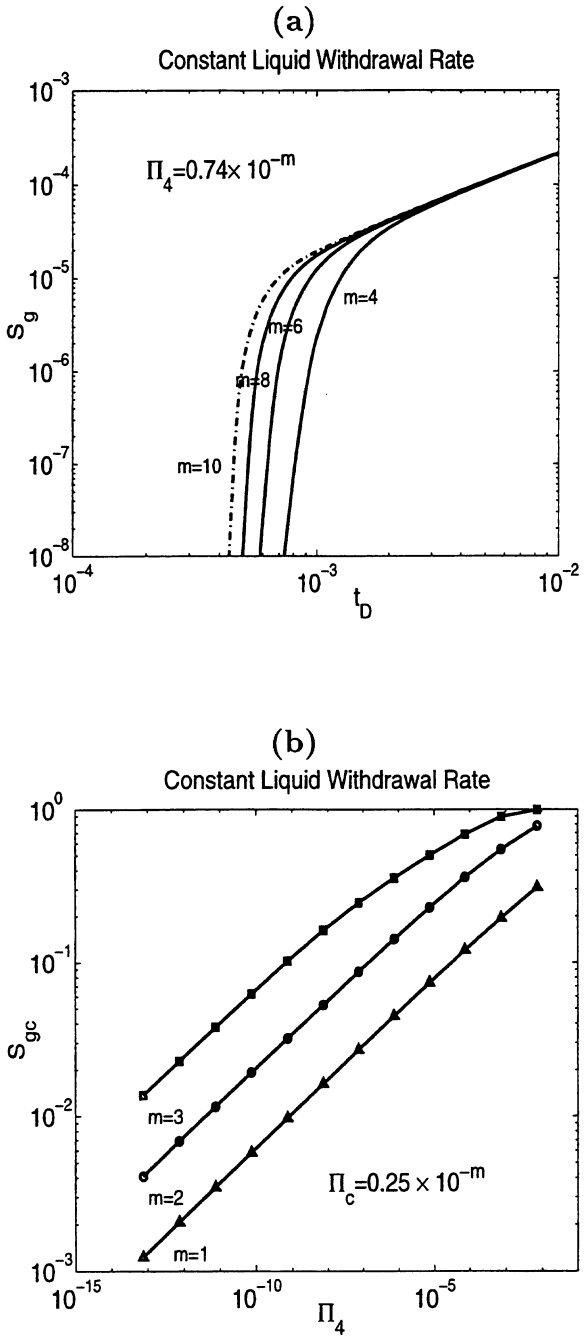

Figure 12: Constant liquid withdrawal rate: (a) Variation of the gas saturation, S_g, as a function of dimensionless time, t_D. Effect of $\Pi_4 = 0.7446x10^{-m}$, for $\Pi_c = 2.5x10^{-3}$, $\Pi_2 = 5.28x10^6$ and $\Pi_3 = 2.2x10^{-2}$. (b) Effect of the dimensionless parameter Π_4 on the critical gas saturation, S_{gc}, for $\Pi_c = 0.25x10^{-m}$. Points denote the full numerical solution.

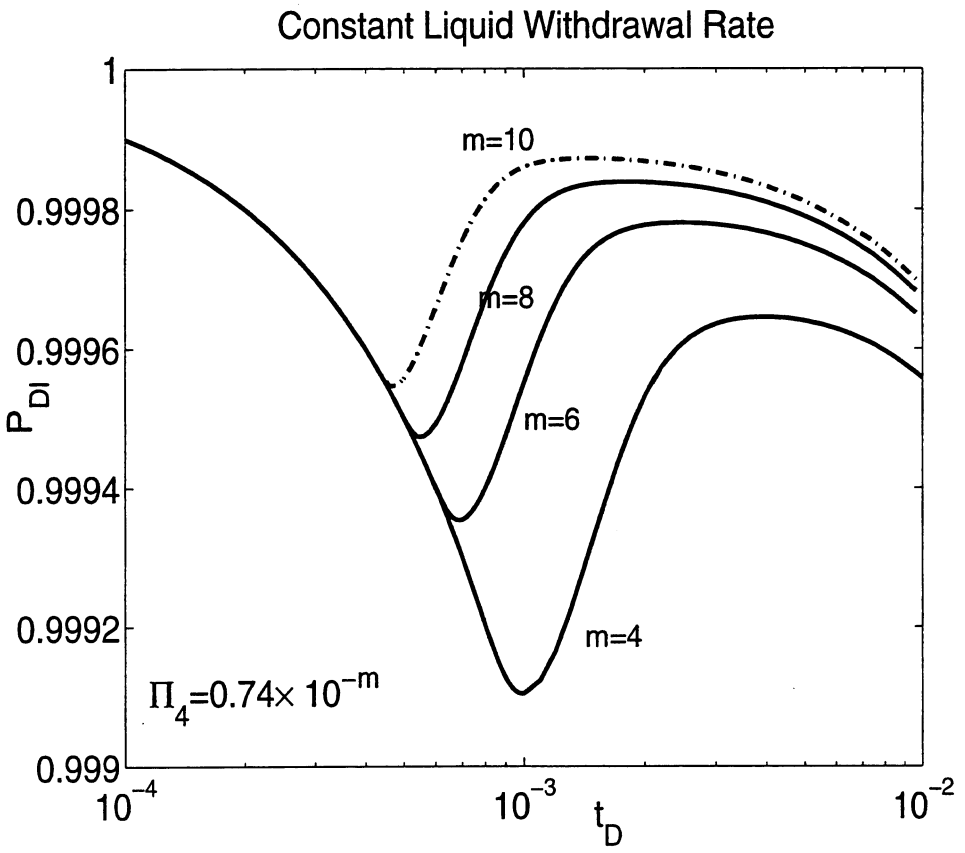

Figure 13: Variation of the dimensionless pressure, P_{Dl}, as a function of dimensionless time, t_D, for constant liquid withdrawal rate. Effect of $\Pi_4 = 0.7446x10^{-m}$, for $\Pi_c = 2.5x10^{-3}$, $\Pi_2 = 5.28x10^6$ and $\Pi_3 = 2.2x10^{-2}$.

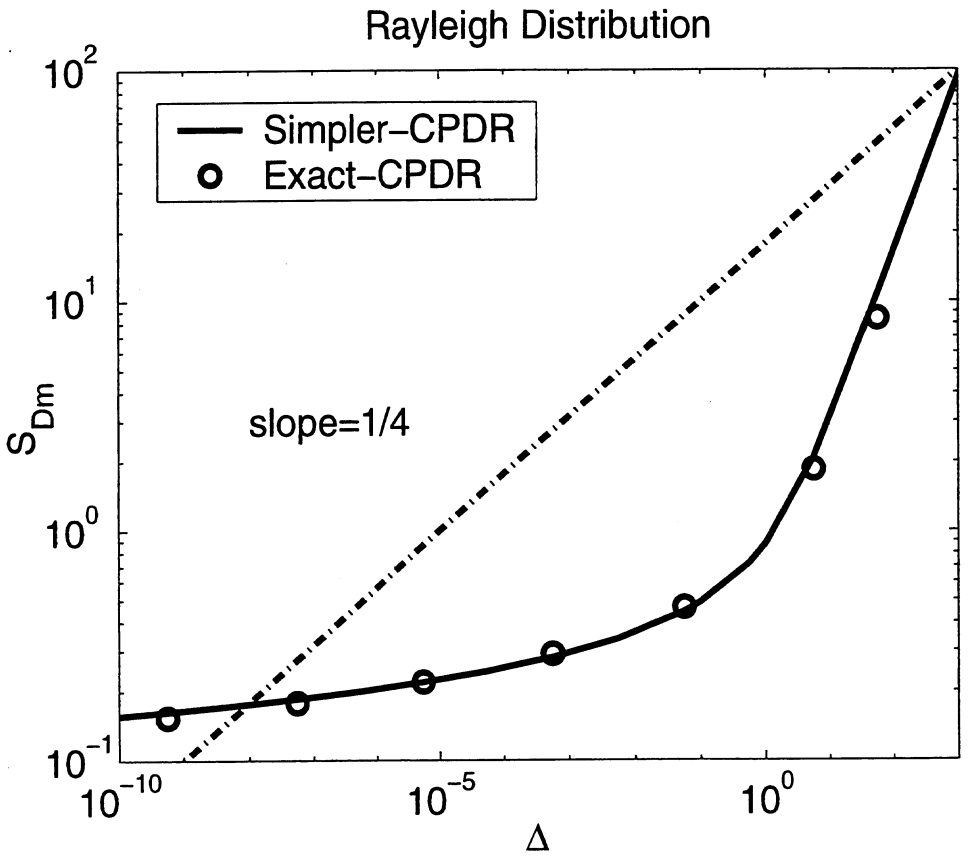

Figure 14: Maximum rescaled supersaturation, s_{Dm}, as a function of Δ for the case of constant pressure decline rate, using Rayleigh cavity size distribution. Solid line corresponds to the simpler model, circles denote the full numerical solution.

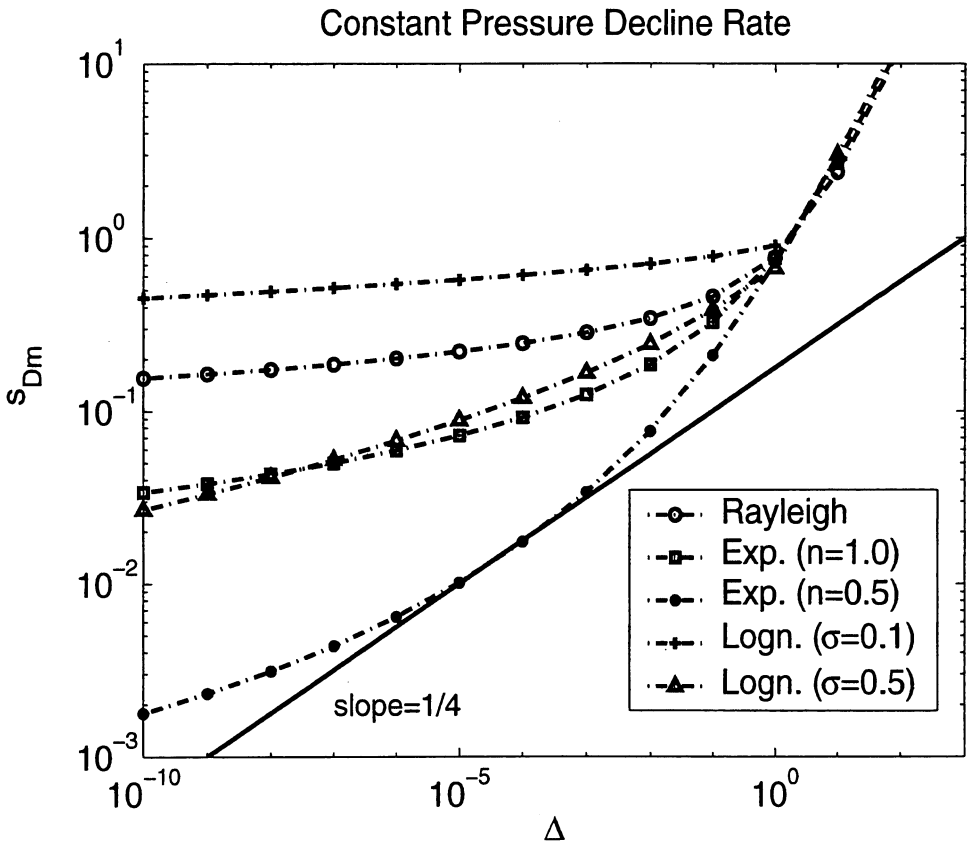

Figure 15: Maximum rescaled supersaturation, s_{Dm}, as a function of Δ for the case of constant pressure decline rate, using various cavity size distributions. The solution corresponds to the simpler model.

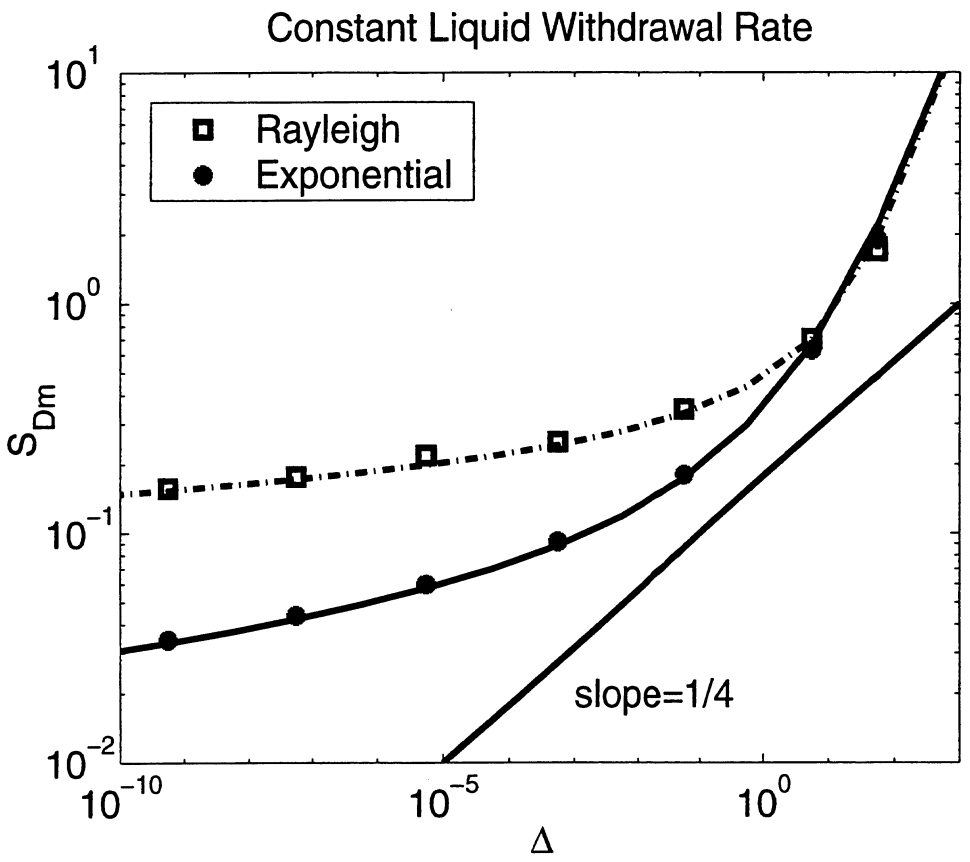

Figure 16: Maximum rescaled supersaturation, s_{Dm}, as a function of Δ for the case of constant liquid withdrawal rate. Comparison between the simpler model (connected lines) and the full numerical solution (denoted by stars for the stretched exponential cavity size distribution with $n = 0.5$ and $\sigma = 1.0$ and by squares for the Rayleigh cavity size distribution).

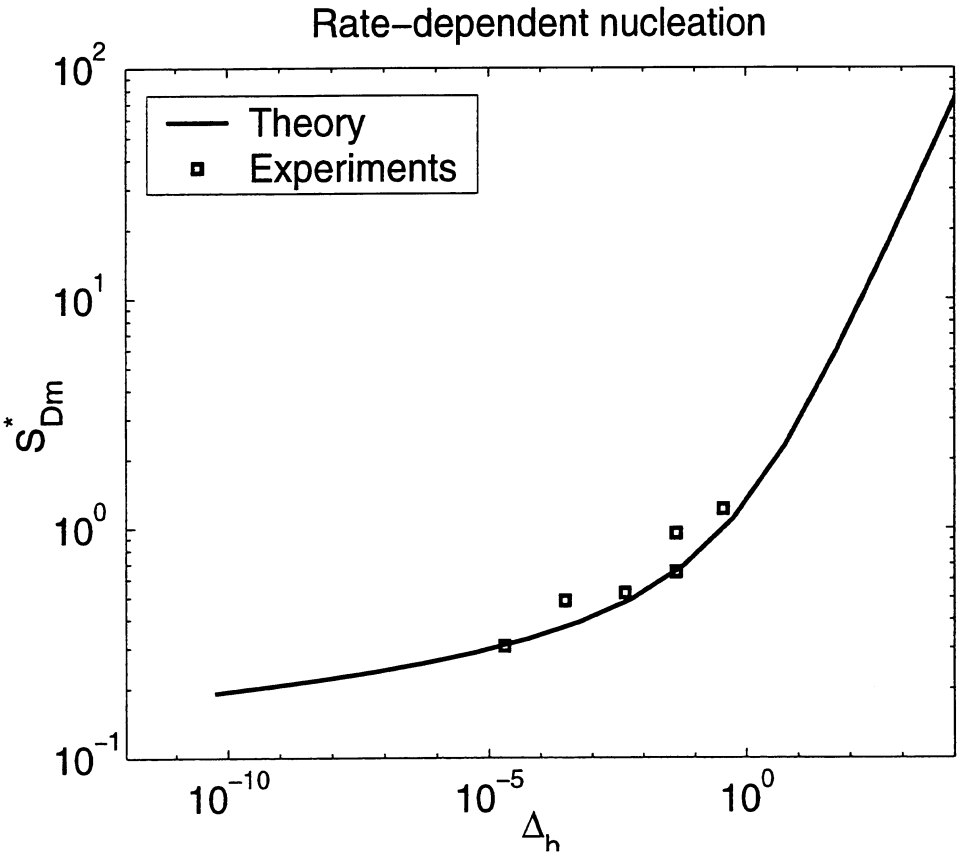

Figure 17: Maximum rescaled supersaturation, s^*_{Dm}, as a function of Δ_h for the case of rate-dependent nucleation. Solid line corresponds to the simpler model. Squares denote, values calculated using experimental data from Scherpenisse et al., (1994).

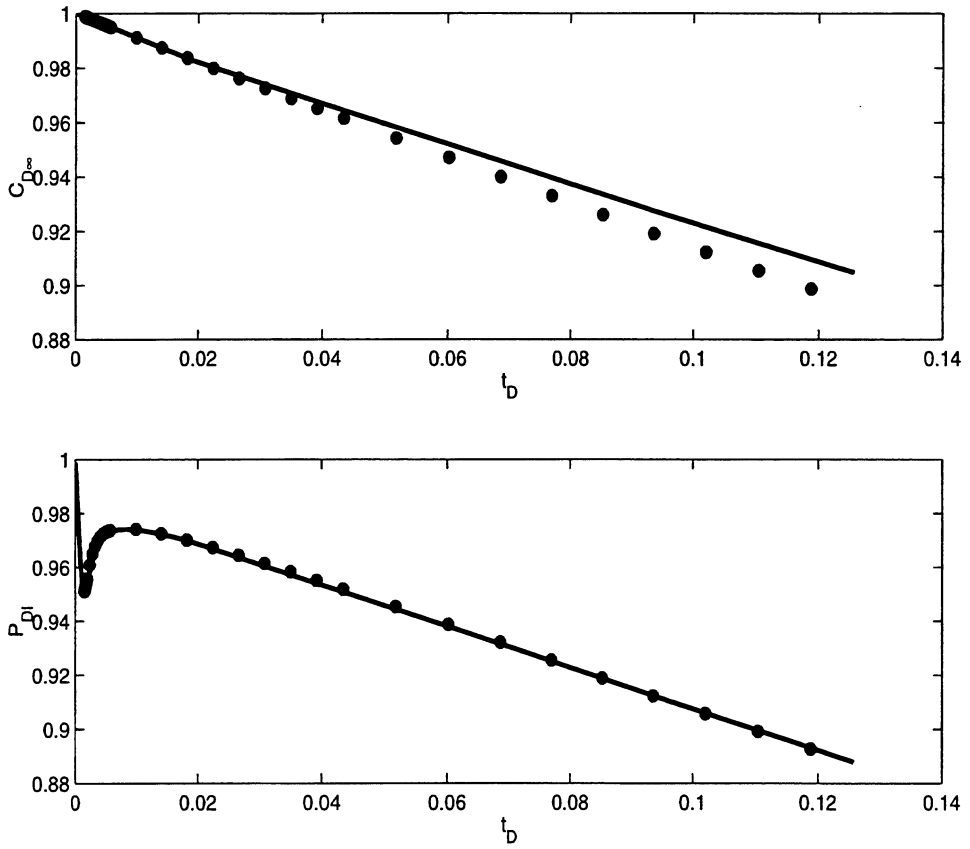

Figure 18: Comparison of the full numerical results (denoted by solid lines) with the approximate model (denoted by stars) for the case of constant liquid withdrawal rate and using a stretched exponential cavity size distribution.

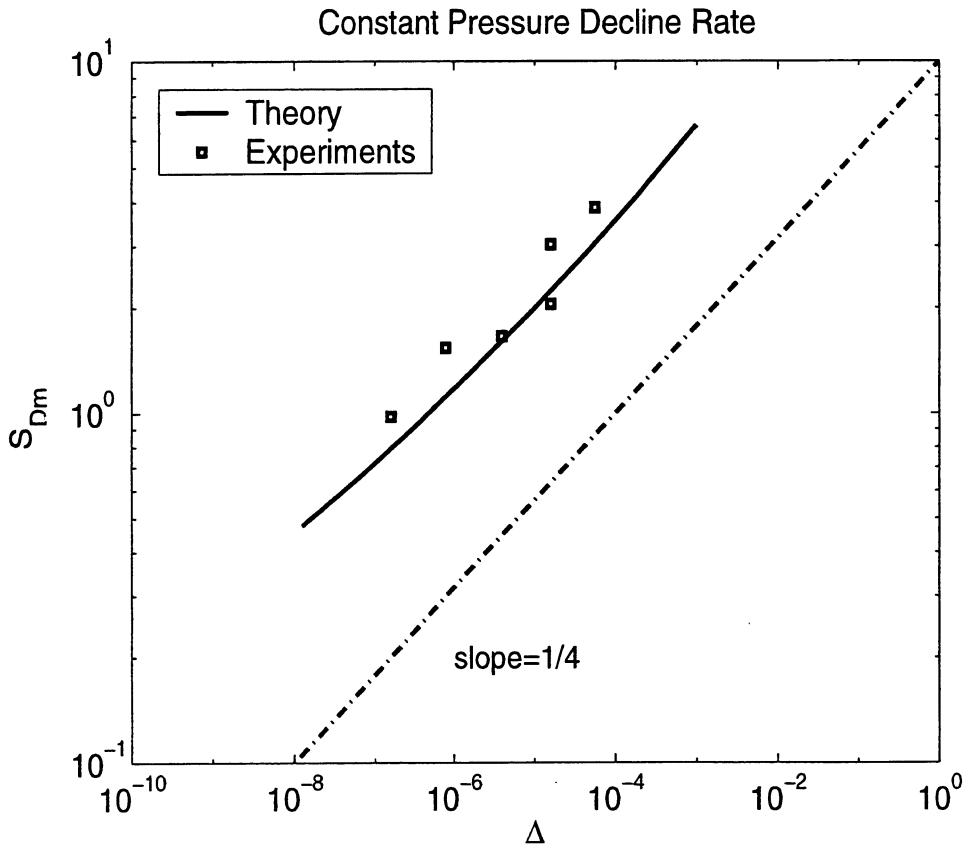

Figure 19: Maximum rescaled supersaturation, s_{Dm}, as a function of Δ for the case of constant pressure decline rate, when a stretched exponential ($n = 0.223$ and $\sigma = 0.046$) cavity size distribution is used. Solid line corresponds to the simpler model, squares denote values calculated using experimental data from Scherpenisse et al., (1994).

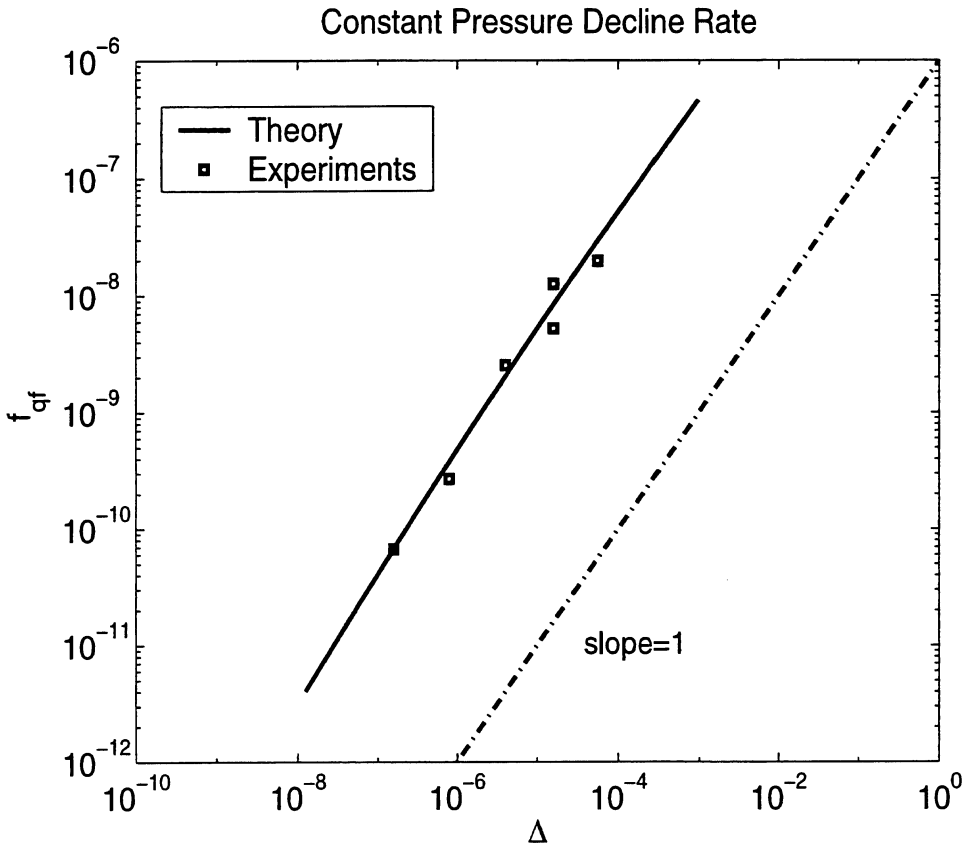

Figure 20: Final nucleation fraction, f_{qf}, as a function of Δ for the case of constant pressure decline rate, when a stretched exponential ($n = 0.223$ and $\sigma = 0.046$) cavity size distribution is used. Solid line corresponds to the simpler model, squares denote values calculated using experimental data from Scherpenisse et al., (1994).

PHASE CHANGE IN POROUS MEDIA

Yanis C. Yortsos and Athanassios K. Stubos

INTRODUCTION

Phase change in porous media is a broad subject. It encompasses the gas, liquid or solid phases occupying the pore space, or the solid matrix of the porous medium itself. The structure of the latter may be rigid or evolving as a result of the phase change, for example, as in the preparation of porous media or sol-gel processing. However, the focus of this review will be on rigid porous media and on the phase change of resident fluids. Phase change in porous media occurs in the confines of the pore space but it is driven by the application of a supersaturation at the external boundaries of the porous medium. Intermolecular forces between the fluids and the pore surface and the transport of mass or heat within the pore structure, therefore, determine phase equilibria and growth kinetics, respectively.

Porous media involve geometries at various scales, from rough pore surfaces to isolated pores to pore networks to the macroscopic continuum. The study of phase change encompasses different issues on these different scales. Nucleation is affected by surface roughness; phase equilibria by the intermolecular interaction between confined fluid and solid surface, in micropores, and by capillary forces in meso- and macropores; growth kinetics are controlled by the transport of supersaturation in the pore space or the solid matrix, and by the competition between growing clusters, if multiple nucleation centers exist, and between dissolving blobs, if the phase becomes disconnected; curvature effects at phase boundaries are related to the individual pore geometries rather than the effective interface, as in the bulk; boundary conditions and macroscale heterogeneity control the large-scale behavior. A schematic of the distribution of host and growing phases in a pore network and of their interactions is shown in Figure 1.

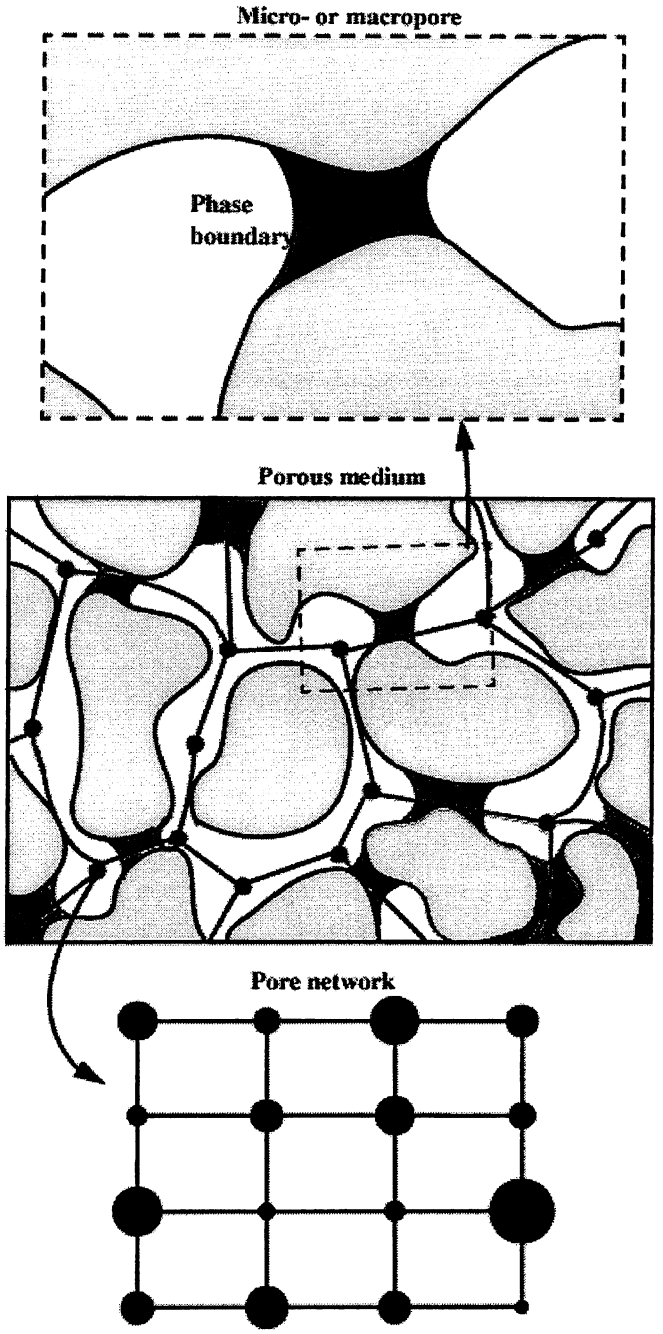

Figure 1: Schematic of phase change in a porous medium at three different scales, including single-pore and pore-network scales. The schematic pertains to a gas-liquid transition, although other phases can obviously be considered. The shaded areas denote the liquid phase, the gas phase is white (and shown to be disconnected).

This review reports on notable advances in these issues published during 1999, and to the best of the authors' knowledge. Thermodynamics and kinetics of phase change are considered. For presentation purposes, the review is organized based on the type of the phase change. Specific applications include: adsorption-desorption (and capillary condensation) of single-component fluids, the melting-freezing transition, the boiling, drying and evaporation of a liquid phase, the evolution of gas from a multicomponent supersaturated liquid, the condensation of a gas phase, and the dissolution of a liquid phase. Advances in each area are further classified in three different classes, wherever appropriate, one dealing with molecular interactions, another with the geometrical-topological effects of the porous micro-structure, and a third dealing with the macroscopic level (see schematic of Figure 1).

1. Adsorption-Desorption

Advances reported in the period reviewed include a review article and several studies to relate sorption properties to the microstructure. A review of adsorption-desorption of a single-component gas in porous media appeared by the first author [1]. The article describes multilayer adsorption, capillary condensation and desorption over the different scales comprising a porous medium, from rough pore surfaces to micropores to pore networks. It particularly focuses on the analysis of sorption isotherms for determining pore-size distributions.

Ma et al. [2] reported experimental results for the fractal dimension of a rough surface using SANS (small-angle neutron scattering) mesaurements during multilayer adsorption. The results do not agree with conventional theories, and the authors cite the lack of the validity of Kelvin's equation as one reason for the discrepancy. Determining the correct scaling relation remains an open issue. The effort to characterize micropore size distributions in the absence of por network effects based on a combination of phase transition simulations (using Monte Carlo or Density Functional Theory (DFT) methods and experimental data continued [3]. Griffiths and Nilson [4] integrated the DFT equations across several pore widths and obtained closed-form expressions for the condensation pressure in terms of the pore size, surface tension and the Lennard-Jones

parameters. The equation reduces to Kelvin's for pores of large sizes. Frink and van Swol [5] also used nonlocal DFT to model compressive stresses in fluids confined in nanopores due to the interaction with the pore walls.

To incroporate pore-network effects in adsorption-desorption processes in porous media, several studies made use of Kelvin's equation. Murray et al. [6] proposed an extension of previously developed nitrogen adsorption methods for pore networks to media involving macropores. The influence of the porespace morphology on the adsorption-desorption hysteresis was revisited by Stepanek et al. [7], who studied the process in reconstructed porous media. The latter have been used recently in a variety of porous media applications and represent an interesting alternative to conventional pore network models. An algorithmic approach was implemented to determine the thermodynamic equilibria of vapor-liquid interfaces in the reconstructed pore space. As in pore-network models, hysteresis arises from a combination of geometrical and pore-blocking effects. Two analytically tractable, but approximate models, a Bethe lattice representation of the porous medium and the Effective Medium Approximation were used by Rajniak et al. [8] to calculate transport properties in adsorption-desorption.

2. Melting-Freezing

A number of studies were published on the effect of the microporous confinement on the freezing and melting of fluids. These parallel previous investigations on the effect of confinement on vapor-liquid equilibria and probe effects of hysteresis and the shift of equilibria.

The transition of Lennard-Jones fluids, confined in a single slit pore, was studied with Monte-Carlo simulation by Dominguez et al. [9]. For sufficiently repulsive walls, the freezing line shifts down in temperature compared to the bulk, the shift being larger as the pore thickness decreases. This result is consistent with a Gibbs-Thomson condition. Similar results were reported by Sliwinska-Bartkowiak et al. [10]. The transition of carbon tetrachloride in Vycor and porous glasses was experimentally studied using Differential Scanning Calorimetry (DSC). Simulations of a Lennard-Jones methane in slit pores revealed the depression of the melting point as the confinement increases. Other experiments showed similar trends. For example, Huber and Knorr [11] studied the

transition of Ar in porous glass using X-Ray Diffraction (XRD) and reported a depression of the melting point. Using DSC, Morineau et al. [12] examined the glass transition, freezing and melting of a series of liquids in the mesoporous silicate material MCM-41 (cylindrical pores of 4 nm diameter). A moderate decrease in the melting of organic liquids was observed. However, the glass transition temperature was found not to be significantly different than in the bulk. XRD was used by Morishige and Kawano [13] to study the freezing and melting of water, confined in MCM-41 cylindrical pores (1.2-2.9 nm) and in Vycor glass. Freezing-melting hysteresis and a size-dependent supercooling was reported. Kaneko et al. [14] examined the freezing transition of carbon tetrachloride inside graphitic micropores (average width 1.1 nm) using DSC but reported an elevation of the freezing temperature.

The effect of the pore network on the melting-freezing transition was not explored in the period reviewed. Two interesting investigations at the continuum level were conducted, however. Cummings et al. [15] provided an analytic framework for solidification or melting in 2-D and in the absence of surface tension, but where the supersaturation is convected by a forced potential flow. As is well known, potential flow also applies to single-phase flow in homogeneous porous media. Thus, the problem in Ref. [15] also pertains to porous media, and in fact to an arbitrary phase change therein under forced flow. The formalism developed allows for the construction of explicit solutions and includes a parabolic tip as a special case. In a separate study, the linear stability of the Rayleigh-Benard instability of a solidifying liquid in a porous medium was carried out [16]. Solidification occurs above a superheated liquid. The flow is described using a Darcy-Brinkman model, which allows enforcing a no-slip condition at the solidifying boundary. As in [15], curvature or surface tension effects were not included, the transition between the two phases being a sharp interface. The improved description of interface phenomena that also accounts for the effects of the microstructure should be pursued in future research.

3. Boiling

Progress was reported in boiling in porous media at the various scales of interest. The nucleate boiling from surface cavities was studied by Zhang and Chao [17], who focused on the detachment of bubbles from nucleation cavities. They report on an unusual Marangoni effect associated with aqueous solutions of long-chain alcohols in which the surface tension is a non-monotonic function of temperature. In such solutions, above a certain temperature, the surface tension increases with temperature, thus generating a non-trivial driving force for bubble detachment. This leads to an increase in the critical heat flux and the delay in the onset of dryout.

Considerable attention was paid during the period reviewed on micro heat pipes, considered for the cooling of micro-electronic devices. In essence, these are capillary grooves of various geometries, in which the confined liquid flows between a condensation and an evaporation region. In a certain sense, they also represent single-pore analogues. Advances were reported by Peterson and Ma [18], Hopkins et al. [19], and Lin and Faghri [20]. Evaporation-condensation and the return flow of a fluid confined in the capillary groove was simulated using conventional models. Thin-film evaporation at the fringe of the evaporating menisci was accounted using disjoining pressures. The effect of the geometric design on the heat transfer efficiency was investigated.

Pore-network effects were analyzed in the study of Figus et al. [21], who described the steady-state distribution of vapor and liquid in a porous capillary pump using a pore-network model. The model accounts for heat transfer in the solid matrix and the pore space, viscous flow, and phase change at the liquid-vapor menisci, each residing in individual pores. As is conventional in such models [22], flow and heat transfer is described using lumped pore- or grain-level conductances, as opposed to the detailed calculations for single-pore geometries. A comparison with a continuum model, based on a constant capillary pressure, is also made. It is shown that the vapor-liquid interface is rough at the pore-network scale, with the roughness increasing with the variance in the pore-size distribution. This capillary dispersion effect is expected. By contrast, gravity stabilizes and limits its extent. Simulations of this type can be useful for applications involving porous media of a small thickness, for example in porous coatings used as

micro-cooling devices, and where continuum models are questionable. The development of vertical vapor channels and their influence in increasing the dryout heat flux was discussed in Stubos and Buchlin [23].

Various studies were also conducted using conventional continuum models involving a liquid-vapor phase change, in which various effects of boundary conditions and process parameters were analyzed. An interesting review of liquid-vapor phase change at the continuum level with emphasis on steam-water flows in porous media was given by Woods [24]. Forced flows, as a result of liquid injection in a hot porous medium, and natural convection flows, associated with vertical heat transfer, were analyzed.

4. Drying-Evaporation

Advances in the evaporation of a single-component liquid from a porous medium focused mostly on effects of microstructure at the pore-network scale. Under slow evaporation conditions, capillarity is dominant at the single-pore scale, and vapor-liquid interfaces conform to the pore-scale geometry. This allows modeling the process using pore networks.

The analogy of drying to drainage, which is the displacement in a porous medium of a wetting by a non-wetting fluid, was exploited in the studies by Tsimpanogiannis et al. [25], Le Bray and Prat [26], and Prat and Bouleux [27], under the assumption of isothermal conditions. Tsimpanogiannis et al. [25] discuss the connection between drying and Invasion Percolation (IP), first postulated by Prat [28]. By accounting for viscous flow they further make an analogy with Invasion Percolation in a Stabilizing Gradient (IPSG). Here, and in contrast to external drainage, the viscous fluid velocity is opposite to the front velocity, thus viscous forces are stabilizing. Using IPSG arguments, they relate by a power law the width of the drying front σ to a diffusion-based capillary number. Le Bray and Prat [26] extend the IP description of drying to a 3-D pore-network in the absence of gravity or viscous effects. Their model demonstrates the existence of dry patches at the evaporating interface and the occurrence of a constant-rate period, both of which have been observed experimentally. They follow as a direct consequence of the IP character of the displacement. Prat and Bouleux [27] describe 2-D pore-network simulations, where the stabilizing effect of gravity is considered. They provide various

numerical and theoretical results for variables at the front, including the evolution of the drying interface and the evaporation of disconnected liquid clusters (a rough sketch is indicated in Figure 1). By applying previous theories on percolation with trapping they are able to obtain a scaling relation in 2-D for the overall extent of the front, defined as the perpendicular distance between the front's most advanced and least advanced points. This scaling has a slightly different exponent than the classical one for the front width.

Coussot et al. [29] provide experimental results for the drying of layered media, which demonstrate the dominance of capillarity under slow drying conditions. Layers of high permeability regions are shown to dry preferentially, regardless of their distance from the external interface. These findings are consistent with a capillary control of the process, as postulated in the above pore-network studies.

Continuum-level studies were also published based on conventional macroscopic models. These contain a number of coefficients, the validity of the expressions for which is currently unclear. Given that the front region, where most of the action occurs, is under IP (hence possibly fractal) conditions, a conventional continuum may in fact be questionable. Pore-network models can provide the missing link. However, detailed upscaling studies have not yet been reported. Furthermore, existing pore-network models do not yet account for (thin or thick) film flow, temperature and Marangoni (thermocapillary) and Marangoni-Gibbs effects. An interesting by-product of such an effort would be the assessment of the validity of concepts, such as that of enhanced diffusion, proposed by Philip and De Vries [30]. According to the latter, transport of vapor at conditions of relatively low moisture content is enhanced by a sequence of condensation-evaporation phenomena across liquid bridges. We note that this effect was not observed in recent experiments of Plumb et al. [31], although this may be due to the difficulty in interpreting experiments in real porous media due to the interplay of a number of phenomena.

Using continuum models Wang and Chen [32] and Ni et al. [33] simulated 1-D drying under conditions of convection and microwave heating, respectively. In contrast to the pore-network models cited, here drying is driven by the imposed heat flux or by internal heat generation, respectively, where the gas is at conditions of thermodynamic equilibrium. Of interest is the case of intensive microwave heating, where the vapor

generated internally displaces the liquid like in external drainage, thus resulting in high drying rates. The important coupling between temperature, phase change and fluid flow is of interest and needs to be examined in more detail. One may add that in contrast to the previous applications, for example [25], here the flow of the liquid is not countercurrent, viscous forces are destabilizing and can lead to the possibility of viscous fingering patterns.

The vaporization of hydrocarbon mixtures in porous media was studied experimentally by Liang and Udell [34], and Ruiz et al. [35], and by a chromatoghraphic modeling approach by Zaidel and Zazovsky [36]. Liang and Udell [34] focus on the effect of the amount of water present on the rates of vaporization in a water-wet medium, which they find to be minimal. Ruiz et al. [35] discuss the effect of vapor adsorption on the solid (sand) particles and the competition for adsorption in the presence of humidity. Zaidel and Zazovsky [36] consider the propagation of evaporation-condensation fronts in the evaporation of multicomponent liquids, by formulating the problem as one in chromatographic transport. This formalism is generic to soil vapor extraction. Under conditions of thermodynamic equilibria, the component volatilities are shown to control the sequence of the propagating fronts.

5. Gas Phase Evolution from Supersaturated Liquids

Gas phase growth from a binary (or multicomponent) supersaturated liquid by pressure lowering (also known as pressure depletion) is common to many applications, for example to solution-gas drive for the recovery of oil from oil reservoirs. Pressure lowering occurs as a result of the overall flow of the supersaturated liquid. Following nucleation, the driving force for gas growth is mass transfer in the liquid phase in a direction towards the growing interface. This is in contrast to drying or evaporation, where the driving force is mass transfer in the gas phase and in a direction opposite to the interface advance.

In the year reviewed, emphasis was given to the critical gas saturation and the mobility of the gas phase. The critical gas saturation, S_{gc}, denotes the value of the gas pore-volume fraction at which the gas phase becomes mobile for the first time. This definition is not unambiguous, however. In the absence of gravity or viscous effects, Li and Yortsos [37]

defined S_{gc} as the condition at which a sample-spanning gas-phase cluster first arises (which in the schematic of Figure 1 corresponds to the case when the growing phase spans the porous medium). Clearly, the latter would be a function of the fraction of pores, f_q, which host active nucleation sites. Using pore-network simulations, Du and Yortsos [38] confirmed a universal power-law scaling between S_{gc} and f_q, first reported in [37], for a variety of nucleation sequences. In the presence of gravity or viscous forces, mobilization of a gas cluster can occur before the onset of a sample-spanning cluster, and results from the imbalance of gravity or viscous forces and capillarity. In such a case, S_{gc} will also depend on the gravity Bond number or the capillary number. Pore-network simulations by McDougal and Sorbie [39], which included buoyancy, led to various correlations for S_{gc} as a function of the gravity Bond number and other parameters. These authors also considered the dependence of interfacial tension (IFT) on pressure. If IFT increases as pressure decreases, as is the case in some applications of interest, it will lead to an increase in S_{gc} in the presence of gravity.

When the liquid has very high viscosity, as in the case of heavy oils, viscous forces dominate, perhaps even at the pore scale. Then, macroscopic bubbles in nucleation sites could detach as a result of viscous shear, and the mobilization of the gas phase may occur well before the onset of a sample-spanning cluster, thus leading to a small S_{gc}. Under such conditions, S_{gc} is expected to be capillary-number dependent, much like in the case of gravity, with S_{gc} decreasing as the capillary number increases. In addition, the size of the mobilized gas clusters may be comparable to the pore size. A number of papers addressed this subject. At issue is the observed anomalously high production of heavy oil following the onset of gas flow, which appears to be in contrast to what is expected in the solution-gas drive of light oils. The term 'foamy oil' was used to describe such a condition.

A review of the foamy oil problem was presented in Sheng et al. [40]. From micromodel experiments they infer the existence of microbbubles (smaller than 2 microns), which contribute to the expansion and production of oil. They suggest that such microbbubles originate from cavities at the pore walls, from which they grow in macroscopic size, detach, entrain and subsequently break-up due to the strong viscous forces in the liquid phase and the porous medium variable geometry. The resulting gas-in-oil dispersion may

be possibly stabilized by asphaltenes deposited at the gas-liquid interface. Wong et al. [41] suggested that this foamy oil flow occurs between the bubble point and the onset of critical gas saturation, which they reported in the range 8-13%. From experiments outside of a porous medium, Sheng et al. [42] find that such dispersion is metastable, the fraction of microbubbles decreasing exponentially in time. By contrast, Pooladi-Darvish and Firoozabadi [43] discount the concept of a gas-in-liquid dispersion (and of the foamy oil terminology). Instead, they attribute the enhanced liquid production in heavy oils to the reduced gas mobility, following S_{gc}, as a result of the intermittent and fluctuating bubble flow. In their hypothesis, low gas mobility is due to bubble break-up and the accompanying increased resistance to mobilization and flow. Analogous results are reported in Firoozabadi and Aronson [44]. In both studies, S_{gc} is of the order of 3-5%, which is lower than in [40]. At the present time, the issue of foamy oil flow has not been conclusively settled. In particular, besides some empirical modeling attempts [45], a comprehensive model of the process to quantitatively account for the observed behavior is still to be developed.

6. Gas Condensation

The reverse problem, namely the condensation of a gas phase in a porous medium was addressed in only one study published in 1999, to our knowledge. Wang and Mohanty [46] used a pore-network model to simulate the condensation of a multicomponent gas under pressure decline, in a process of retrograde condensation. The model assumes that condensation occurs under negligible supersaturation at the throats of the porespace (as roughly shown in Figure 1). The pore geometry is crucial in determining condensate volume and connectivity. Much like in capillary condensation, thermodynamic equilibrium dictates the radius of curvature of the liquid-gas interface. Small throats fill first and connected condensate blobs are identified. The critical condensate saturation, S_{cc}, is reached when a connected blob becomes large enough for gravity forces to overcome capillarity and mobilize the fluid. Due to the large connectivity of the throats, the critical condensate saturation is found to be small. In this approach, gravity is the dominant factor for determining S_{cc}. However, the scaling of the latter with respect to the gravity Bond number is not given.

7. Liquid Dissolution

The final area to be addressed in this review is the dissolution of a stationary liquid phase in a porous medium due to the flow of another liquid phase (solvent). Applications range from the dissolution of organic contaminants (Non Aqueous Liquid Phases, NAPL) in subsurface soils to drug release from porous membranes (e.g. Tarvainen et al. [47]). Often, the dissolving liquid phase is entrapped in the form of disconnected blobs or ganglia (again roughly shown in the generic schematic of Figure 1). The forced dissolution process is inherently unstable, as flow of the solvent is amplified where the number of ganglia (hence the flow resistance) decreases.

In the context of this review, of most importance is the mass transfer between the disconnected ganglia and the injected liquid. Various experiments and simulations were reported during the period reviewed. Experiments on the dissolution of octane blobs in packed beds were conducted by Johns and Gladden [48]. Using Magnetic Resonance Imaging (MRI) these authors mapped the interfacial area and the flow velocities during solubilization, and used the information obtained to determine an effective mass transfer coefficient. Mayer et al. [49] and Johnson et al. [50] reported on the experimental determination of mass transfer coefficients in surfactant-enhanced solubilization of TCE and PCE, respectively. Bradford et al. [51] discussed the influence of fractional wettability on the increased dissolution of trapped organic liquids. In less water-wet media, organic liquids are likely to spread also in the form of films rather than as disconnected blobs only, thus creating a larger surface area and, accordingly, a higher rate of solubilization. Jia et al. [52] investigated mass transfer from disconnected blobs to a flowing liquid by carrying out experiments in etched glass micromodels and corresponding pore-network simulations. These authors reported that the dissolution rates are sensitive to the local mass transfer coefficients, and particularly to their dependence on local velocity.

Upscaling of dissolution was modelled by Quintard and Whitaker [53] with the use of classical volume-averaging methods, which take into account in detail the effect of the microstructure. In particular, an evolution equation for the volume fraction of the dissolving phase was derived, the determination of which requires the solution of certain,

rather complex, closure problems. The approach is based on the assumption of scale separation at the microscale, however, which may be violated in processes at relatively high rates of dissolution.

CONCLUSIONS

In this review we discussed various aspects of phase change in porous media. We focused on the issues of the confinement in micropores, which affects phase equilibria and phase transitions, and of the porous medium microstructure, which affect the kinetics of phase change. Significant progress has been reported in various areas, including condensation-evaporation and freezing-melting. Additional work is required, however, to couple phenomena at the various scales and to improve the macroscopic description.

REFERENCES

1. Yortsos YC: **Probing pore structures by sorption isotherms and mercury porosimetry**. In *Experimental Methods in the Physical Sciences*, vol. 33. Edited by Wang P-Z. New York: Academic Press; 1999:69-117.

2. Ma J, Qi H, Wong PZ: **Experimental study of multiplayer adsorption on fractal surfaces in porous media.** *Phys Rev E* 1999, 59:2049-2059.

3. Davies GM, Seaton NA, Vassiliadis VS: **Calculations of pore size distributions of activated carbons from adsorption isotherms**. *Langmuir* 1999, 15:8235-8245.

4. Nilson RH, Griffiths SK: **Condensation pressures in small pores: An analytical model based on density functional theory**. *J Chem Phys* 1999, 111, 4281-4290.

5. Frink LJD, van Swol F: **Stress isotherms of porous thin materials: Theoretical predictions from nonlocal density functional theory**. *Langmuir* 1999, 15:3296-3301.

6. Murray KL, Seaton NA, Day MA: **An adsorption-based method for the characterization of pore networks containing both mesopores and macropores.** *Langmuir* 1999, 15:6728-6737.

7. Stepanek F, Marek M, Adler PM: **Modeling capillary condensation hysteresis cycles in reconstructed porous media.** *AICHE J* 1999, 45:1901-1912.

8. Rajniak P, Soos M, Yang RT: **Unified network model for adsorption-desorption in systems with hysteresis.** *AICHE J* 1999, 45:737-750.

9. Dominguez H, Allen MP, Evans R: **Monte Carlo studies of the freezing and condensations transitions of confined fluids.** *Mol Phys* 1999, 96:209-229.

10. Sliwinska-Bartowiak M, Gras J, Sikorski R, Radhakrishnan R, Gleb L, Gubbins KE: **Phase transition in pores: Experimental and simulation studies of melting and freezing.** *Langmuir* 1999, 15:6060-6069.

11. Huber P, Knorr K: **Adsorption-desorption isotherms and x-ray diffraction of Ar condensed into a porous glass matrix.** *Phys Rev B* 1999, 60:12657-12665.

12. Morineau D, Dosseh G, Alba-Simionesco C: **Glass transition, freezing and melting of liquids confined in the mesoporous silicate MCM-41.** *Phil Mag B* 1999, 79:1847-1855.

13. Morishige K, Kawano K: **Freezing and melting of water in a single cylindrical pore: The pore-size dependence of freezing and melting behavior.** *J Chem Phys* 1999, 110:4867-4872.

14. Kaneko K, Watanabe A, Iiyama T, Radhakrishnan R, Gubbins KE: **A remarkable elevation of freezing temperature of CCl4 in graphitic micropores.** *J Phys Chem B* 1999, 103:7061-7063.

15. Cummings LM, Hohlov YE, Howison SD, Kornev K: **Two-dimensional solidification and melting in potential flows.** *J. Fluid Mech* 1999, 378:1-18.

16. Mackie C, Desai P, Meyers C: **Rayleigh-Benard stability of a solidifying porous medium.** *Int J Heat Mass Tran* 1999, 42:3337-3350.

17. Zhang N, Chao DF: **Models for enhanced boiling heat transfer by unusual Marangoni effects under microgravity conditions.** *Int Comm Heat Mass Transfer* 1999, 26:1081-1090.

18. Peterson GP, Ma HB: **Temperature response of heat transport in a micro heat pipe.** *J Heat Trans-Trans ASME*, 1999, 121:438-445.

19. Hopkins R, Faghri A, Khrustalev D: **Flat miniature heat pipes with micro capillary grooves.** *J Heat Trans-Trans ASME*, 1999, 121:102-109.

20. Lin L, Faghri A: **Heat transfer in micro region of a rotating miniature heat pipe.** *Int J Heat Mass Tran* 1999, 42:1363-1369.

21. Figus C, Le Bray Y, Bories S, Prat M: **Heat and mass transfer with phase change in a porous structure partially heated: continuum model and pore network simulations.** *Int J Heat Mass Tran* 1999, 42:2557-2569.

22. Satik, C, Yortsos YC: **A pore-network study of bubble growth in porous media driven by heat transfer.** *J Heat Trans- Trans ASME* 1996, 118:455-462.

23. Stubos AK, Buchlin JM: **Enhanced cooling via boiling in porous layers: The effect of vapor channels.** *J Heat Trans-Trans ASME* 1999, 121:205-210.

24. Woods AW: **Liquid and vapor flow in superheated rock.** *Ann Re Fluid Mech* 1999, 31:171-199.

25. Tsimpanogiannis IN, Yortsos YC, Poulou S, Kanellopoulos N, Stubos AK: **Scaling theory of drying in porous media.** *Phys Rev E* 1999, 59:4353-4365.

26. Le Bray Y, Prat M: **Three-dimensional pore-network simulation of drying in capillary porous media.** *Int J Heat Mass Tran* 1999, 42:4207-4224.

27. Prat M, Bouleux F: **Drying of capillary porous media with a stabilized front in two dimensions.** *Phys Rev E* 1999, 60:5647-5656.

28. Prat, M: **Percolation model of drying under isothermal conditions in porous media.** *Int J Multiphase Flow* 1993, 19, 691-704.

29. Coussot P, Gauthier C, Nadji D, Borgotti JC, Vie P, Bertrand F: **Capillary motions during the drying of a granular paste.** *CR Acad Sci IIB* 1999, 327:1101-1106.

30. Philip JR, De Vries DA: **Moisture movement in porous materials under temperature gradients.** *Trans Amer Geophys Union* 1957, 38:222-232.

31. Plumb OA, Gu LM, Webb SW: **Drying of porous materials at low moisture content.** *Dry Technol* 1999, 17:1999-2011.

32. Wang ZH, Chen GH: **Heat and mass transfer during low intensity convection drying.** *Chem Eng Sci* 1999, 54:3899-3908.

33. Ni H, Datta AK, Torrance KE: **Moisture transport in intensive microwave heating of biomaterials: a multiphase porous media model.** *Int J Heat Mass Trans* 1999, 42, 1501-1512.

34. Liang HC, Udell KS: **Experimental and theoretical investigation of vaporization of liquid hydrocarbon mixtures in water-wetted porous media.** *Water Resour Res* 1999, 35:635-649.

35. Ruiz J, Bilbao R, Murillo MB: **Convective transport and removal of vapors of two volatile compounds in sand columns under different air humidity conditions.** *Environ Sci Technol* 1999, 33:3774-3780.

36. Zaidel J, Zazovsky A: **Theoretical study of multicomponent soil vapor extraction: propagation of evaporation-condensation fronts.** *J Contam Hydrol* 1999, 37:225-268.

37. Li X, Yortsos YC: **Theory of multiple bubble growth in porous media by solute diffusion.** *Chem Eng Sci* 1995, 50:1247-1271.

38. Du C, Yortsos YC: **A numerical study of the critical gas saturation in a porous medium.** *Transport Porous Med* 1999, 35:205-225.

39. McDougall SR, Sorbie KS: **Estimation of critical gas saturation during pressure depletion in virgin and waterflooded reservoirs.** *Petroleum Geoscience* 1999, 5:299-233.

40. Sheng JJ, Maini BB, Hayes RE, Tortike WS: **Critical review of foamy oil flow.** *Transport Porous Med* 1999, 35:157-187.

41. Wong, RCK, Guo F, Weaver JS, Barr WE: **Heavy oil flow under solution-gas drive: Pressure depletion tests.** *J Can Pet Tech* 1999, 38:31-37.

42. Sheng JJ, Maini BB, Hayes RE, Tortike WS: **A non-equilibrium model to calculate foamy oil properties.** *J Can Pet Tech* 1999, 38:38-45.

43. Pooladi-Darvish M, Firoozabadi A: **Solution-gas drive in heavy oil reservoirs.** *J Can Pet Tech* 1999, 38:54-60.

44. Firoozabadi A, Aronson A: **Visualization and measurement of gas evolution and flow of heavy and light oil in porous media.** *SPE Reservoir Eval & Eng* 1999, 2:550-557.

45. Sheng JJ, Maini BB, Hayes RE, Tortike WS: **Modeling foamy oil flow in porous media.** *Transport Porous Med* 1999, 35:227-258.

46. Wang X, Mohanty KK: **Critical condensate saturation in porous media.** *J Colloid Interf Sci* 1999, 214:416-426.

47. Tarvainen T, Svarfvar B, Akerman S: **Drug release from a porous ion-exchange membrane in vitro**. *Biomaterials* 1999, 20:2177-2183.

48. Johns ML, Gladden LF: **Magnetic resonance imaging study of the dissolution kinetics of octanol in porous media**. *J Colloid Interf Sci* 1999, 210: 261-270.

49. Mayer AS, Zhong LR, Pope GA: **Measurement of mass-transfer rates for surfactant-enhanced solubilization of nonaqueous phase liquids**. *Environ Sci Technol* 1999, 33:2965-2972.

50. Johnson JC, Sun SB, Jaffe PR: **Surfactant enhanced perchloroethylene dissolution in porous media: The effect on mass transfer coefficients**. *Environ Sci Technol* 1999, 33:1286-1292.

51. Bradford SA, Vendlisnki RA, Abriola LM: **The entrapment and long-term dissolution of tetrachloroethylene in fractional wettabillity porous media**. *Water Resour Res* 1999, 35:2955-2964.

52. Jia C, Shing K, Yortsos YC: **Visualization and simulation of non aqueous phase liquids dissolution in pre networks**. *J Contam Hydrol* 1999, 37:225-268.

53. Quintard M, Whitaker S: **Dissolution of an immobile phase during flow in porous media**. *Ind Eng Chem Res* 1999, 38:833-844.

II. VAPOR-LIQUID FLOWS

The simultaneous flow of vapor and liquid phases is common to steam injection. Counter-current flows are encountered in Steam-Assisted-Gravity-Drainage (SAGD), and in steam injection in horizontal wells. They also appear in the context of heat pipes in a variety of processes (from geothermal to high-level numclear waste disposal). Concurrent flows are found in typical displacements, in solution gas-drives near wells, and various other contexts. The interaction between heat transfer, heat flux, buoyancy and fluid flow affects the occupancy of phases and the flow characteristics, such as relative permeabilities. In this section we report on two studies, one dealing with transient gas-liquid flows with an evaporating component, although at time scales where evaporation is not significant, and another on the dynamics of two-phase flows in heterogeneous media where capillarity induces a trapped phase. The first study shows how the flow rates of the produced fluids in laboratory displacements can be used to assess the exponent of the relative permeability of the flowing liquid. We propose a novel diagnostic technique to infer these properties, which allows for the mechanism of fluid flow to be uncovered. The second study is a new approach, based on what we term Darcian Dynamics, to describe the dynamics of the flow of a disconnected phase, in the form of ganglia, in the flow field of a displacing continuous phase. This effort parallels the analogous effort in Stokes flows, called Stokesian Dynamics. It is a computationally fast approach for the evaluation of quantities such as the critical capillary number for mobilization, the subsequent movement of the mobilized phase, and its possible stranding and/or coalescence. These two studies do not address phase-change or heat transfer issues, which are currently under consideration.

TIME SCALING OF THE RATES OF PRODUCED FLUIDS IN LABORATORY DISPLACEMENTS

Catherine Laroche[1], Min Chen and Yanis C. Yortsos

Department of Chemical Engineering,

University of Southern California, Los Angeles, CA 90089-1211

and

Jairam Kamath

Chevron Petroleum Technology Company, San Ramon, CA 94583-0719

INTRODUCTION

Relative permeabilities are important functions for the modeling and prediction of the recovery of fluids from porous media. They express integrated information on the pore structure topology and geometry and on the pore occupancy by the corresponding fluids. Of particular interest is their dependence near the end-point saturations (corresponding to residual or trapped fluids), where a power-law behavior is expected. Sensitivity studies using numerical simulation have shown that this behavior has the most important effect on recovery rates. Reflecting the same fact, most of the empirical models used (e.g. Corey, see Bear[2]) contain a power law in the residual saturation region. From theoretical considerations, this power-law dependence reflects two different mechanisms, the trapping of a disconnected non-wetting phase, where film flow is absent, in the case of imbibition, and the continuous drainage of a wetting phase, through film flow, in the case of drainage. In the latter case, the residual saturation is theoretically zero.

The trapping of a non-wetting phase by capillarity can be described by percolation theory and its extensions, such as invasion percolation[3] and gradient percolation[4]. Percolation theory predicts that the approach of various functions to the trapped saturation satisfies a power law with universal exponents, independent of the local pore structure. For example, Wilkinson[5] showed that the relative permeability of the displaced phase, k_{rd}, near the trapping threshold in a random medium obeys the scaling

$$k_{rd} \sim (S - S_r)^b \qquad (1)$$

[1]Now at the Institut Français du Pétrole, Reservoir Engineering Department, Rueil-Malmaison, France.

where S is the displaced phase saturation and subscript r denotes trapped. The important parameter in (1) is exponent b, which depends only on the dimensionality of the pore network through the relation

$$b = \frac{\mu}{1+\beta} \tag{2}$$

Here μ is the conductivity exponent and β the percolation exponent, both of which are universal. For example, in 3-D we have $\mu \approx 2$, $\beta = 0.45$, hence $b \approx 1.38$.

This analysis applies under the assumption that the displaced phase is non-wetting, thus it becomes trapped by capillary forces. However, if the displaced phase is wetting, it can escape through film flow. Now drainage of the wetting phase continues, albeit at low rates. Film flow occurs either in the form of thick films and corner (or pocket) flows or through continuous thin films. In such cases, the residual saturation will ultimately vanish, while the exponent of the relative permeability curve is different from that for drainage. Theoretical results for the dependence of the relative permeability of the wetting phase under conditions of film flow were obtained by de Gennes[6], Novy et al.[7] and Toledo et al.[8] In the thick-film flow regime, de Gennes' theory predicts an exponent of the form

$$b = \frac{5-D}{3-D} \tag{3}$$

where D is the fractal dimension of the pore surface. For values of D in the order of 2-2.5, one obtains estimates for b in the range 3-5. The theory was based on the assumption of parallel pores. If the flow is controlled by thin films, the power-law exponent is additionally related to the power m of the dependence of the disjoining pressure Π on the film thickness h (namely $\Pi(h) \sim h^{-m}$), through the relation

$$b = \frac{3}{m(3-D)} \tag{4}$$

(see Toledo et al.[8]). For values of D in the order of 2.3-2.6 and $m = \frac{1}{2}$, one obtains estimates for b in the range 8.4 to 16.8. These values are significantly higher and different than for drainage.

The experimental determination of the relative permeability functions, including their behavior near the trapped saturation, is usually done using steady- or unsteady-state

displacements. The well-known JBN technique[9] provides information on the relative permeabilities in the saturation region after breakthrough of the injected fluid. It is based on an analysis of fluid rate production data and of the pressure drop across the sample, using the classical Buckley-Leverett equation[10]. In general, however, the method is most accurate away from trapped saturations, where relative permeabilities are not too small. An alternative for determining the exponent of the power law dependence near residual saturations is to consider the behavior at late times. In a recent study[1], we showed that for displacements in porous media and various injection patterns, the variation of the ratio of the produced flow rates as a function of time can be used to identify certain geometrical and petrophysical characteristics of the medium. In particular, for a 1-D displacement this ratio can be used to estimate the relative permeability exponents. Motivated by this finding, the objective of this chapter is to evaluate the potential of such a method as a diagnostic tool for displacements in laboratory cores. For this purpose we will assess the conditions for which the approach of Ref. [1] is applicable, provide a suitable extension and subsequently apply to experimental data in gas-liquid displacements.

Deriving an expression for the time dependence of the ratio of the produced fluids is straightforward in the absence of capillary effects. Capillarity will affect saturation profiles, and possibly flow rates, in places where permeability varies with position. A most extreme, but routine, example of capillary heterogeneity is at the ends of the core sample, where the permeability contrast is theoretically infinite and gives rise to well known end effects. Effects of capillary heterogeneity were analyzed in detail under steady-state flow conditions[11]. In unsteady-state displacements, most of our understanding comes from numerical investigations[12]. Analytical results do exist for a number of problems involving counter-current imbibition[13, 14]. In the later, however, the process is controlled by capilly dispersion, rather than by viscous forces, as is the case in the Buckley-Leverett problem. To access the effect of capillarity we will consider the influence of end effects, other effects of capillary heterogeneity, and late-time regimes, where capillarity may be important, even at high rates of displacement. For this purpose, boundary-layer analyses and late-time asymptotics will be provided. These will be verified using analytical solutions of the full problem based on a simple model that follows Burgers' equation[15]. The latter is one among a few nonlinear equations of the

second order, which are exactly solvable[16]. The results will then be applied to obtain relative permeability exponents from a set of gas-liquid displacements.

The chapter is organized as follows: We first derive the basic theory for the dependence of the ratio of the produced fluids as a function of time in homogeneous media and under viscous control. Then, the end-effect at the production end is analyzed using a boundary layer description, when capillarity is small. Under the same conditions, we derive the dependence for late-time regimes, where capillarity may be significant. A discussion of more general effects of heterogeneity is also provided. Subsequently, we verify the asymptotic results analytically, by constructing solutions of a model problem based on Burgers' equation. Experiments are then reported involving the displacement of various liquids (brine, methanol and toluene) with methane at high rates. The exponents obtained are interpreted using pore scale models, which allow inferring possible flow mechanisms near the residual saturation.

THEORY

The equation describing 1-D immiscible 2-phase flow in porous media, where capillary forces are accounted for, is well known. For homogeneous media, it reads in dimensionless form

$$u_t + (F(u))_x - \varepsilon(D(u)u_x)_x = 0 \tag{5}$$

where u is the reduced saturation of the displacing phase (namely, $u = \frac{s-s_r}{s_m-s_r}$, where s_m is the maximum saturation), $F(u)$ is its fractional flow function and $D(u)$ is a dimensionless capillary diffusivity. In the general case, the fractional flow function has the form

$$F(u) = \frac{1 - N_{gx}k_{r1}(u)}{(1 + \frac{\kappa(u)}{M})} \tag{6}$$

where $\kappa(u)$ is the ratio of the relative permeabilities of displaced to displacing phases, $M = \frac{\mu_2}{\mu_1}$ is the ratio of the corresponding viscosities, and $N_{gx} = \frac{(\rho_1-\rho_2)kg_x}{q\mu_1}$ is the gravity number, where g_x is the acceleration of gravity component in the direction of displacement,subscripts 1 and 2 denote initial and injected phases, respectively, and ρ denotes density. However, most of our interest is on the approach near the trapped

saturation of the displaced phase. There, gravity effects are secondary and can be neglected. Near that region we can assume, in view of the theoretical of expectations cited above, that the ratio of the relative permeabilities obeys a power law

$$\kappa(u) \approx c(1-u)^b \tag{7}$$

where $b>1$ and c is a constant prefactor. We must also note that at intermediate saturations, an exponential dependence (the so-called X-plot) was found to successfully describe relative permeability field data[17].

Parameter ε is the inverse of a modified capillary number,

$$\varepsilon = \frac{\sqrt{k\phi}\gamma}{\mu_1 q_T L} \tag{8}$$

where k denotes permeability, ϕ is porosity, γ is interfacial tension, μ is viscosity, q_T is the injection rate and L is the system length. Small or large ε denote, respectively, the limits of viscous or capillary control. The dimensionless capillary dispersivity is

$$D(u) = (const)\frac{k_{r1}(u)}{(1+\frac{\kappa(u)}{M})}\left|\frac{dJ}{du}\right| \tag{9}$$

where the constant prefactor accounts for the fact that u is a normalized saturation, J is the J-function representing capillary pressure and the absolute value is taken to allow for a common description for both drainage and imbibition. The dependence of $D(u)$ near the residual saturation has been discussed by various authors. In the corner (pocket) flow regime, de Gennes[6] predicted hypodiffusion, namely the vanishing of the capillary dispersivity,

$$D(u) \sim (1-u)^{\frac{1}{3-D}} \tag{10}$$

When thin films dominate, the behavior is more complicated. de Gennes' theory predicts hyperdispersion, where

$$D(u) \sim (1-u)^{-1} \tag{11}$$

but Novy et al.[7] provide arguments for both hypodiffusion and hyperdispersion, depending on the values of the fractal dimension of the pore surface and the exponent of the disjoining pressure.

The problem is completed with the initial condition

$$u = 0 \text{ at } t = 0 \tag{12}$$

and the following boundary conditions. At the inlet, assuming injection at a constant rate, we have

$$F(u) - \varepsilon D(u) u_x = 1 \text{ at } x = 0 \tag{13}$$

At the outlet, the end effect dictates

$$u = 0 \text{ at } x = 1 \tag{14}$$

for the case of drainage, and

$$u = 0 \text{ when } F(u) - \varepsilon D(u) u_x = 0, \text{ otherwise } u = 1, \text{ at } x = 1 \tag{15}$$

for the case of imbibition. Because of its nonlinearity, the above problem must generally be solved numerically. However, analytical solutions are possible in some limiting cases, where the functions $F(u)$ and $D(u)$ take a specific form[15, 16]. One such model will be used below to verify the asymptotic predictions. In the next section we consider, first, the solution in the limit when viscous forces are dominant.

Viscous Control, ε<<1.

In the case of viscous control, ε<<1, capillarity is negligible, and equation (5) becomes the well-known Buckley-Leverett equation. Its solution will be referred to as the outer solution and denoted by superscript (0). This solution is singular in the following places: around the shock front, if one develops, around the inlet $x = 0$ at early times of order $O(\varepsilon)$, around the outlet $x = 1$ near and after breakthrough, and possibly at late times of order $O(\varepsilon^{-1})$. Corrections to the Buckley-Leverett solutions in these limits will be discussed in later sections.

1.The outer solution

In the small ε limit, we obtain

$$u_t^{(0)} + F(u^{(0)})_x = 0 \tag{16}$$

the solution of which is obtained by the method of characteristics,

$$F'(u^{(0)}) = \frac{x}{t} \tag{17}$$

This solution is also valid for variable injection rates, where t expresses the fraction of pore volumes injected. Of interest to this chapter is the reduced saturation at the outlet $u^{(0)}(1) = u_L^{(0)}$. From (17), this is readily shown to satisfy

$$\frac{\kappa'(u_L^{(0)})}{\left(1+\frac{\kappa(u_L^{(0)})}{M}\right)^2}=-\frac{M}{t} \tag{18}$$

Then, the fractional flow of the displaced phase at the outlet, $F_{1,L}^{(0)}$, can be calculated

$$F_{1,L}^{(0)}=1-F(u_L^{(0)})=1-\frac{1}{1+\frac{\kappa(u_L^{(0)})}{M}} \tag{19}$$

The variation of the produced flow rate ratio with time has been used originally by Welge[18], in laboratory displacements, by Omoregie and Ershaghi[17] (X-plot method) for field analysis, and by Yortsos et al.[1], as a diagnostic tool in waterfloods.

Consider, now, relatively large times (to be more precisely defined below), where $u_L^{(0)}$ is sufficiently large for equation (7) to apply. Substitution of the latter in (18) gives after some manipulations the result

$$\left(\frac{F_{1,L}^{(0)}}{1-F_{1,L}^{(0)}}\right)^{\frac{1}{b}}\approx bc^{\frac{1}{b}}M^{-\frac{1}{b}}t \tag{20}$$

This can be further re-arranged to read

$$\log\left(\frac{F_{1,L}^{(0)}}{1-F_{1,L}^{(0)}}\right)=b\log(tF_{1,L}^{(0)}(1-F_{1,L}^{(0)}))+const \tag{21}$$

Thus, under conditions of viscous control and at sufficiently large times, a log-log plot of $\frac{F_{1,L}^{(0)}}{1-F_{1,L}^{(0)}}$ vs $tF_{1,L}^{(0)}(1-F_{1,L}^{(0)})$ is a straight line with slope b. By definition ($b>1$), the latter slope must be larger than 1. Equation (21) is a more general and, as it will turn out, a better diagnostic tool for relative permeability exponents, than what was presented in Ref. [1] (see also discussion below). In the latter we considered the further limit of small $F_{1,L}^{(0)}$, to obtain the power law dependence

$$F_{1,L}^{(0)}\approx\frac{\kappa(u_L^{(0)})}{M}\approx\frac{c}{M}\left(\frac{M}{cbt}\right)^{\frac{b}{b-1}} \tag{22}$$

from which one can infer exponent b. For reasons that will become clear below, in this chapter we consider the more general expression (21). An important reason is that the use of such a plot allows to differentiate sharply the power-law regime from that of the X-

plot. Indeed, if X-plot conditions were applicable, in which case the relation $\kappa(u) \sim \exp(-du)$ is assumed to apply, the expression equivalent to (21) reads

$$1 = (const) t F_{1,L}^{(0)} (1 - F_{1,L}^{(0)}) \tag{23}$$

suggesting that in the appropriate plot, the combination $tF_{1,L}^{(0)}(1 - F_{1,L}^{(0)})$ is a constant. In simulations and experiments to be described below, this property will be used to differentiate between the X-plot and the other regimes.

To verify the above results, we computed the solution of problem (18) and plotted the results in the logarithmic plot suggested by (21). Results for b=2 and b=5 and for four different values of M are shown in Figures 1a and 1b, respectively. In these examples, we have taken the relative permeability dependence, $\kappa(u) = (1 - u^b)/u^2$. The arrows in the curves of Figure 1 point in the direction of increasing time. As expected, for sufficiently small $F_{1,L}^{(0)}$, at sufficiently large times, the plots show the existence of a straight segment with slope b equal to what is theoretically expected, regardless of the value of M. The latter only affects the results by shifting downwards the region of applicability of the power-law regime as M increases. The straight line segment is preceded by an earlier-time regime in which X-plot conditions apply, and in which a constant ordinate is expected (region near the vertical slope). At least for the simulations of Figure 1, it is apparent that this region does not last for an extended period in the logarithmic coordinates. The examples in Figure 1 confirm the validity of the above analysis and its scaling predictions in the absence of capillarity. The results will be contrasted to the experiments, to be analyzed later in this chapter.

Equation (21) was derived assuming t sufficiently larger than 1 and the absence of capillary effects. As pointed out above, however, even under the condition $\varepsilon << 1$, the solution (17) becomes singular at various places: at the inlet, at the shock front of the propagating Buckley-Leverett front (if any) and at the outlet, where boundary layers must be inserted (see Figure 2). These layers have a thickness of order ε, in space or time, or around the shock. In addition, capillarity cannot be neglected at large times of the order of $\frac{1}{\varepsilon}$. How these affect the above scaling of the effluent flow ratio will be analyzed below.

2. Outlet-end effect

Let t_f denote the time of breakthrough of the injected fluid. In the neighborhood of the outlet and for $t<t_f$, the solution of the full problem is identically equal to $u=0$ (if $D(0)=0$) or it is exponentially small (if $D(0)\neq 0$), and the viscous solution satisfies both the differential equation and the boundary condition, for either drainage or imbibition. After breakthrough, however, the outer solution at the outlet, $u_L^{(0)}$, does not satisfy boundary conditions (14) or (15), in the respective cases. A boundary layer in terms of the stretched coordinate $\xi=\frac{1-x}{\varepsilon}$ must be inserted. Rescaling equation (5) in this coordinate gives to leading-order the equation

$$-(F(u))_\xi=(D(u)u_\xi)_\xi \tag{24}$$

the integration of which is

$$\int_0^u \frac{D(u)du}{F(u)-A(t)}=-\xi \tag{25}$$

for the case of drainage, and

$$\int_1^u \frac{D(u)du}{F(u)-A(t)}=-\xi \tag{26}$$

for the case of imbibition. Parameter $A(t)$ is independent of ξ and is determined by matching the outer limit ($\xi\to\infty$) of (25) and (26) with the outer solution $u_1^{(0)}$. Then, we find, to leading-order

$$A(t)=F(u_{1,L}^{(0)}) \tag{27}$$

Inserted back in (25) and (26), this expression gives closed-form expressions for the behavior of the saturation near the outlet.

For illustration, we consider the case $F(u)=1-(1-u)^2$ (shown in the schematic of Figure 3), which implies $u_L^{(0)}=1-\frac{1}{2t}$ and $F(u_{1,L}^{(0)})=1-\frac{1}{4t^2}$, for $t>t_f=\frac{1}{2}$. We also take for simplicity, $D(u)=1$. Direct substitution gives the following expression near the outlet,

$$u = 1 - \frac{1}{2t}\left[\frac{1+\left(\frac{2t-1}{2t+1}\right)\exp\left(-\frac{1-x}{\varepsilon t}\right)}{1-\left(\frac{2t-1}{2t+1}\right)\exp\left(-\frac{1-x}{\varepsilon t}\right)}\right] \text{ for } t>\frac{1}{2} \tag{28}$$

for the case of drainage, and

$$u = 1 - \frac{1}{2t}\left[\frac{1-\exp\left(-\frac{1-x}{\varepsilon t}\right)}{1+\exp\left(-\frac{1-x}{\varepsilon t}\right)}\right] \text{ for } t>\frac{1}{2} \tag{29}$$

for the case of imbibition.

The variation of u as a function of time and position for the above two cases is shown in Figures 4a and 4b. The well-known end effect is apparent in both drainage and imbibition. However, and even though the saturation profile undergoes a significant change near the outlet, the fluid rates remain continuous across the thin boundary layer. Hence, in this limit, expressions (21) and/or (22), which are based on $u_L^{(0)}$, still give at leading-order the correct expressions for the flow ratio at the outlet. This will be demonstrated by a specific example in a later section. Therefore, we conclude that even though they affect the saturation profile, end-effects do not change to leading order the time scaling of the outlet fractional flow rates.

3. Capillary heterogeneity

This also applied to the more general heterogeneous media. There, the permeability variation will induce a corresponding capillary heterogeneity. The effect will be manifested primarily as an additional term to the fractional flow, the strength of which is proportional to ε and the gradient of the dimensionless permeability, k_D, as shown in the following equation

$$u_t + (F(u))_x + \varepsilon\left(D(u)\frac{\frac{d\sqrt{k_D}}{dx}}{\frac{J'}{J}}\right)_x - \varepsilon(D(u)\sqrt{k_D}u_x)x = 0 \tag{30}$$

which is the corresponding version of (5) for heterogeneous media[11-13]. Steady- and unsteady-state saturation profiles in the presence of capillary heterogeneity have been discussed before [11-14]. From (30) it is apparent that the effect of heterogeneity is strongest when the permeability is discontinuous, in which case it acts as an equivalent end-effect. As in the end effect in homogeneous media, however, there exists a sufficiently small ε (sufficiently high rate) such that the heterogeneity effect is negligible on the flow rate

ratio, although not necessarily on the saturation. Therefore, in the theoretical limit $\varepsilon<<1$, we expect that equation (21) would still be valid for describing the ratio of the flow rates at the outlet. The more heterogeneous the medium, the smallest the value of ε required for the power-law scaling behavior previously derived to apply. For example, Figure 5 reprinted from Ref. [11] shows that even for $\varepsilon=0.1$, heterogeneity affects non-trivially the saturation profile. In general, its effect would be to lower the average value of the saturation profile. (In an unpublished numerical study we have also found that at small values of ε, the effective relative permeabilities, hence the effective fractional flow rates, are the same with the point relative permeabilities evaluated at the average saturation.) Therefore, the main effect of heterogeneity would be to delay the onset of the power-law behavior (7) over the sample. Precise estimates on the value of ε for which this delay is negligible require knowledge of the detailed permeability field and flow parameters, however.

We conclude that if ε is sufficiently small, capillary heterogeneity or end effects, although affecting saturation profiles, would not substantially affect the flow rate ratio, which should approach the scaling given by (21) and/or (22), sometime after breakthrough. Capillarity is expected to affect the eventual approach to a steady- state, at a later time, however. This is addressed next.

4. Late-time behavior

In the large-time limit, equations (25) and (26) show that u approaches a steady state u. In the case of imbibition, it is the flat profile u =1. In the case of drainage, the steady state is a function of ξ, obtained from the solution of

$$\varepsilon\int_0^u \frac{D(u)du}{1-F(u)}=1-x \tag{31}$$

Our interest in this section is on the rate of approach to this asymptotic state. Consider, first, the case of constant capillary dispersivity.

a. Case of constant dispersivity, $D_\infty = D(1)\neq 0$.

In the viscous control region outside the boundary layer at the outlet end, $u\to 1$ as $\varepsilon\to 0$. Defining $v=1-u$, and taking into account that in this limit equation (7) is valid, we find that v satisfies the equation

$$v_t + \frac{cb}{M} v^{b-1} v_x \approx \varepsilon D_\infty v_{xx} \tag{32}$$

where we assumed $D_\infty = D(1) \neq 0$. This is to be solved subject to the boundary conditions

$$-\frac{1}{M} v^b + \varepsilon D_\infty v_x = 0 \text{ at } x = 0 \text{ and } v_x = 0 \text{ at } x = 1 \tag{33}$$

Because of the assumed constant capillary diffusivity and the fact that $b > 1$, equation (32) admits a solution which decays exponentially in time,

$$v = \exp(-\lambda t) g(x,t) \tag{34}$$

The positive constant λ is determined by substituting in (32) and taking the large-time limit, $\lambda t >> 1$. Then, the viscous term contributes only a higher-order correction, and g satisfies the eigenvalue problem

$$\varepsilon D_\infty g_{xx} + \lambda g = 0 \tag{35}$$

with

$$g_x = 0 \text{ at } x = 0 \text{ and at } x = 1 \tag{36}$$

The solution of this problem is straightforward. We find $g \sim \cos\sqrt{\frac{\lambda}{\varepsilon D_\infty}} x$, where the eigenvalue is obtained by applying the boundary condition at $x = 1$, hence

$$\lambda = \varepsilon D_\infty \pi^2 \tag{37}$$

Thus, the solution in the outer region outside the boundary layer, approaches at late times, $t >> \frac{1}{\varepsilon}$, the expression

$$u = 1 - \exp(-\pi^2 \varepsilon D_\infty t) g(x,t) + \cdots \tag{38}$$

indicating an exponential decay in time. Regarding the flow rate ratio, we note that the dominant component in the flux of the displaced phase, $1 - F(u) - \varepsilon D_\infty v_x \approx \frac{c v^b}{M} - \varepsilon D_\infty v_x$, is the capillary term $\varepsilon D_\infty v_x$, as the nonlinear term contributes only a higher-order correction. Using (38) we then find in this limit the scaling behavior

$$F_{1,L} \sim \exp(-\pi^2 \varepsilon D_\infty t) \tag{39}$$

Equation (39) shows that at large times, where capillarity dominates, the log-log plot of $\frac{F_{1,L}}{1-F_{1,L}}$ vs $tF_{1,L}(1-F_{1,L})$ is a straight line, but now with slope equal to unity, subject to

some logarithmic corrections. To examine the behavior when the capillary dispersivity vanishes, we consider the following case.

b. Hypodiffusive case, $D\sim(1-u)^{b+n-1}$.

Consider the asymptotic behavior in the large-time limit for the hypo-diffusive case, where $D(1)=0$. For this, we need to assume the behavior $\left|\frac{df}{du}\right|\sim(1-u)^{n-1}$, where $1-b<n<1$. For example, according to de Gennes' theory[6] for corner flow, $n=1+\frac{1}{3-D}-b$. Now, the equivalent to (32) equation is

$$v_t+\frac{cb}{M}v^{b-1}v_x\approx\varepsilon_D(v^{(b+n-1)}v_x)_x \tag{40}$$

where we have incorporated various constants in the modified capillary dispersivity, ε_D. By further defining $\omega=v^{b+n}$, this equation reads

$$\omega_t+\frac{cb}{M}\omega^{\zeta}\omega_x\approx\varepsilon_D\omega^{\gamma}\omega_{xx} \tag{41}$$

where $\zeta=\frac{b-1}{b+n}$ and $\gamma=\frac{b+n-1}{b+n}$. At large times, we take a solution of (41) in the asymptotic form

$$\omega\sim t^{-\nu} \tag{42}$$

where the exponent ν is to be determined. Substituting in (41) shows that balancing the dominant terms is possible if the transient term is balanced by the capillary term, namely if

$$\nu=\frac{1}{\gamma}=\frac{b+n}{b+n-1} \tag{43}$$

This implies that in the capillary limit, the viscous term makes a negligible contribution to leading order. The contribution to the flux comes only from capillary effects, hence

$$F_{1,L}\sim t^{-\frac{b+n}{b+n-1}} \tag{44}$$

It follows that in this case, the log-log plot of $\frac{F_{1,L}}{1-F_{1,L}}$ vs $tF_{1,L}(1-F_{1,L})$ is a straight line with a slope $b+n$, greater than 1. For example, using de Gennes' theory, we find a slope equal to $1+\frac{1}{3-D}$, which for $D=1$, which is the non-fractal limit in his theory, gives the

value 1.5. The scaling predicted by (44) was verified with numerical simulations of the full problem, which will not be reported here for the sake of brevity.

In theory, therefore, the capillary control segment, with slope 1 or $1+\frac{1}{3-D}$ follows the straight-line segment corresponding to viscous control, which has the slope $b>1$. For the two segments to be clearly distinguished requires sufficiently small ε, so that the late-time regime where capillarity is important, $\varepsilon t>>1$, does not overlap with the viscous control regime after breakthrough, where t is sufficiently large, but not too large, for equation (7) to apply. An analytical example illustrating these regimes will be provided below.

Exact Solution for a Model Case

In the above we showed that the flow rate ratio has a different behavior depending on whether the problem is viscous- or capillary- controlled. To verify these limits, we will use an exact result for a model case in a homogeneous medium, including end effects, based on Burgers' equation. This involves the quadratic fractional flow function

$$F(u)=1-(1-u)^2 \tag{45}$$

which corresponds to a power-law near the trapping treshold ($u\sim 1$) with exponent $b=2$. Function $F(u)$ was plotted in Figure 3. Based on (45), the corresponding Buckley-Leverett problem ($\varepsilon=0$) admits the spreading wave (no shock) solution, $u^{(0)}=1-\frac{x}{2t}$. For a constant dispersivity, $D=1$, the general displacement is described by the non-linear equation

$$u_t+2(1-u)u_x=\varepsilon u_{xx} \tag{46}$$

which through the further substitution $v=1-u$, can be transformed to Burgers' equation[13]

$$v_t+2vv_x=\varepsilon v_{xx} \tag{47}$$

This is to be solved subject to the initial condition $v=1$ at $t=1$, and the boundary conditions: $v^2-\varepsilon v_x=0$ at $x=0$, and

$$v=1 \text{ at } x=1 \tag{48}$$

for the case of drainage, or

$$1-v^2+\varepsilon v_x=0 \text{ if } v\neq 0, \text{ and } 1-v^2+\varepsilon v_x\neq 0 \text{ if } v=0, \text{ at } x=1 \tag{49}$$

for the case of imbibition. Now, it is well-known that using the Cole-Hopf transformation,

$$v = -\varepsilon \frac{\phi_x}{\phi} \tag{50}$$

Burgers' equation is mapped to the linear heat equation

$$\phi_\tau = \phi_{xx} \tag{51}$$

where we introduced the rescaled time $\tau = \varepsilon t$. Then, the initial and boundary conditions become $\phi = \exp(-\frac{x}{\varepsilon})$ at $\tau = 0$, $\phi = 1$ at $x = 0$, and

$$\frac{\phi_x}{\phi} = -\frac{1}{\varepsilon} \text{ at } x = 1 \tag{52}$$

for the case of drainage, or

$$\phi = \exp\left[\frac{\tau}{\varepsilon^2} - \frac{1}{\varepsilon}\right] \text{ if } \phi_x \neq 0, \text{ and } \phi_x = 0 \text{ otherwise, at } x = 1 \tag{53}$$

for the case of imbibition. In this notation, the fractional flow of the displaced phase at the outlet is

$$F_{1,L} = \varepsilon^2 \frac{\phi_\tau}{\phi}\bigg|_{x=1} \tag{54}$$

for either drainage or imbibition.

Consider, now the solution of this problem in the case of drainage. The corresponding solution for imbibition is described in the Appendix. By subtracting the steady-state solution, $\bar{\phi} = 1 - \frac{x}{1+\varepsilon}$, from ϕ and defining the variable $\omega = \phi - \bar{\phi}$, we obtain an initial-boundary value problem which can be solved using classical methods[19]. After several manipulations we find the result

$$\omega = \sum_{n=1}^{\infty} Z_n(x) \exp(-\beta_n^2 \tau) \int_0^1 Z_n(\xi) G(\xi) d\xi \tag{55}$$

where Z_n $(n = 1,2,3,\cdots)$ is the eigenfunction

$$Z_n(x) = \frac{\sqrt{2(\varepsilon^2 \beta_n^2 + 1)} \sin \beta_n x}{\sqrt{\varepsilon^2 \beta_n^2 + 1 + \varepsilon}} \tag{56}$$

β_n $(n = 1,2,3,\cdots)$ is the eigenvalue, obtained as the n^{th} root of the algebraic equation

$$\tan\beta_n = -\beta_n\varepsilon \tag{57}$$

and $G(x) = \exp(-\frac{x}{\varepsilon}) + \frac{x}{1+\varepsilon} - 1$. The solution for ϕ reads

$$\phi(x,\tau) = 1 - \frac{x}{1+\varepsilon} - 2\sum_{n=1}^{\infty} \frac{\sin(\beta_n x)\exp(-\beta_n^2\tau)}{\beta_n(\varepsilon^2\beta_n^2 + 1 + \varepsilon)} \tag{58}$$

from which the saturation $u = 1 + \varepsilon\frac{\phi_x}{\phi}$ and other quantities can be explicitly expressed. In particular, we find the following expression for the fractional flow at the outlet,

$$F_{1,L}(\tau) = -\frac{\varepsilon^2(1+\varepsilon)\sum_{n=1}^{\infty}\frac{\beta_n^2\cos\beta_n\exp(-\beta_n^2\tau)}{\varepsilon^2\beta_n^2+1+\varepsilon}}{\left[\frac{1}{2} + (1+\varepsilon)\sum_{n=1}^{\infty}\frac{\cos\beta_n\exp(-\beta_n^2\tau)}{\varepsilon^2\beta_n^2+1+\varepsilon}\right]} \tag{59}$$

The analytical saturation profiles are plotted in Figure 6 for two different values of the dimensionless time τ (small τ in Figure 6a and large τ in Figure 6b) and for various values of ε. At small ε (Figure 6a), the profile is close to the outer viscous solution (Buckley-Leverett) profile, $u^{(0)} = 1 - \frac{x}{2t}$, as expected (curves with ε=0.001 and 0.01 in Figure 6a, where we should also note that for constant τ, different values of ε correspond to different times). In both cases, inlet and outlet effects are apparent, the inlet effect delaying the approach of the inlet saturation to its maximum value of 1. At larger times (Figure 6b), the corresponding profiles are almost flat, except near the boundary layer at the outlet. As ε increases, the saturation profiles are being controlled by capillarity and lose the linear relationship predicted by the viscous solution.

The variation of $\frac{F_{1,L}}{1-F_{1,L}}$ with $tF_{1,L}(1-F_{1,L})$ for different values of ε is shown in Figure 7. At small values of ε the plot has the main features of the viscous solution (compare with Figure 1), provided that time is not too large. At early times, before breakthrough, the curve has a negative slope. For sufficiently small times after breakthrough the X-plot regime sets in, and the curve approaches a vertical slope. The regime of the power-law approach to the trapped saturation is the straight-line segment that follows with slope $b = 2$. This is as expected from the outer viscous solution, where $b = 2$. This regime is quite apparent for sufficiently small ε (ε<0.1 in Figure 7), although its extent decreases with increasing ε. Also shown in Figure 7 is the viscous solution (denoted in the figure

as the B-L curve), which for the particular fractional flow taken for Burgers' equation satisfies the implicit equation

$$Y = -\log(4t^2 - 1);\ X = \log\frac{1}{4t}(1 - \frac{1}{4t^2}) \tag{60}$$

in the logarithmic coordinates X, Y of Figure 7. As expected the analytical solution approaches this limiting curve, as ε becomes smaller.

At larger times, the curve changes slope, reflecting the onset of the exponential decay regime. According to the asymptotic theory, in this region the plot should be a straight line with a slope equal to unity. We first remark that this is also the limit of the exact solution (59). Indeed, in the limit of large times, the leading-order in (59) is the first term in the series, namely

$$F_{1,L} \approx -2\varepsilon^2\beta_1^2 \cos\beta_1 \exp(-\beta_1^2\tau) \tag{61}$$

where β_1 is the first root of the algebraic equation. In the small ε limit, we further have $\beta_1 \approx \pi$, thus

$$F_{1,L} \approx 2\pi^2\varepsilon^2 \exp(-\pi^2\tau) \tag{62}$$

The exponential decay is as predicted theoretically and coincides with (39), where $D_\infty = 1$. Figure 7 shows that this capillary regime with unit slope is indeed approached at sufficiently large times.

As ε increases, the curves in Figure 7 retain the linear character of the viscous solution, but in progressively smaller intervals. In fact, above $\varepsilon \approx 0.1$, the capillary regime overlaps the viscous regime, and it is difficult to discern the existence of the latter. For $\varepsilon > 10$, all curves practically coincide to a single, capillary-controlled curve. This curve can be obtained by considering equation (59) in the limit $\varepsilon >> 1$. Then,

$$F_{1,L} \approx 2\frac{\sin\beta_1}{\beta_1}\exp(-\beta_1^2\tau) \tag{63}$$

where β_1 is the first root of the algebraic equation and, in the large ε limit, $\beta_1 \approx \frac{\pi}{2}$. Thus,

$$F_{1,L} \approx \frac{4}{\pi}\exp(-\frac{\pi^2}{4}\tau) \tag{64}$$

In the X, Y plot of Figure 7, this curve has the implicit dependence

$$Y = -\log\left[\frac{\pi}{4}\exp(\frac{\pi^2}{4}\varepsilon t) - 1\right];\ X = \log\left[\frac{te^Y}{(1+e^Y)^2}\right] \tag{65}$$

Similar results were obtained for the case of imbibition, as described separately in the Appendix.

In summary, the above theory suggests that for sufficiently small values of the capillary parameter ε, corresponding to sufficiently high rates, a plot of the effluent flow rate ratio in the form $\frac{F_{1,L}}{1-F_{1,L}}$ vs. $tF_{1,L}(1-F_{1,L})$ will give a straight-line segment with a slope greater than one. This is equal to the exponent of the power-law approach of the relative permeability of the displaced phase to its trapped saturation. This segment is followed by a subsequent one with slope equal to one (or with a slope greater than one, in the hypodiffusive case), where capillarity dominates. The above behavior is valid regardless of whether the displacement is drainage or imbibition (see Appendix).

EXPERIMENTS AND DISCUSSION

The theoretical predictions were subsequently used to analyze laboratory experiments. The experiments consisted of a series of room-temperature methane floods of a core sample containing various liquids (brine, brine/methanol mixture and toluene). Humid methane was injected from the top, while maintaining a constant pressure drop of 10 psi. The core sample consisted of a preserved, composite (3 plugs) sandstone with porosity 0.16, permeability 14 md, length 16 cm and pore volume of 30 cc. Since the injection rate was variable, the value of ε was estimated at the later times of the displacement, where gas is the main flowing phase. For γ=50 mN/m, and a viscosity ratio $M \approx 100$, equation (8) shows that $\varepsilon \approx 0.02$ for these experiments.

The measured data consisted of the gas flow rate, the volume of gas injected, the flow rate of the liquid expelled, and the change in the weight of the core at the end of each flood. Figure 8 shows log-log plots of $\frac{F_{1,L}}{1-F_{1,L}}$ vs. $tF_{1,L}(1-F_{1,L})$ for different experiments, where methane displaces respectively, methanol (MeOH), toluene, brine (KCl), a 1:1 mixture of brine and methanol, and a 3:1 mixture of brine and methanol. All these plots should be compared to the small ε curves in the corresponding figure for the Burgers' model, Figure 7. We note similar features in all the experimental results. The curves consist of segment with a negative slope, at early times, followed by a segment with an

almost vertical slope, which then becomes a straight line with a slope greater than one, and eventually approaches at large times a segment with slope close to unity. Guided by the previous theory, we identify these regimes as corresponding to a regime before breakthrough, the X-plot regime, the regime of the power-law dependence near the trapped saturation and the capillary regime, respectively.

The segment with the power-law behavior can be identified well in most of the experiments but not as well in the displacement of brine (Figure 8c). The methanol, toluene and KCL-MeOH data (Figures 8a, 8b, 8d and 8e) show well-defined power-law regions in the viscous control regime. However, the region of applicability of the power-law decreases in this sequence, due to the increase of ε, since the interfacial tension increases in the sequence, and the increasing overlap with the capillary regime (compare also with Figure 7). The experiment involving the displacement of brine (Figure 8c) has the least well-defined power-law region, which is also consistent with the high interfacial tension (72 dyn/cm) for this system. From the theory, we can extract the appropriate value of b. We estimate b=3.15, 3.28, 3.54, 4.5 and 4.8 for Figures 8a, 8b, 8c, 8d and 8e, respectively.

The capillary regime has a slope close to unity, with an exponent varying in the range 1.18-1.20 for MeOH and toluene and in the range 1.02-1.05 for the brine solution. It is suggesting either a constant dispersivity (for the latter case) or a weakly-hypodiffusive case (for the former). The first case predicts a slope equal to one, but subject to logarithmic corrections, which are not negligible in this time regime. The second predicts a slope greater than one (and equal to 1.5 in the case of a Euclidean (not fractal) surface), according to de Gennes' theory.

Comparison with the percolation results of Wilkinson[4], equations (1) and (2), which predict an exponent of the order of 1.38 for 3-D, clearly shows that trapping in the absence of film flow is not the operating mechanism in these experiments. Instead, it is apparent that drainage continues, albeit at slow rates, through the action of film flow. The values of the exponents obtained are consistent with the theory of de Gennes[6] for pocket flow over a weakly fractal pore-surface (for example, where D=2.2 for b=3.5 and D=2.42 for b=4.5). We note that our results cannot be compared with Novy et al.[7] or Toledo et al.[8], whose pore-network simulations do not agree with de Gennes, as their

saturations take much smaller values (in the range 10^{-3}-10^{-1}) compared to those in our experiments (of the order of 10^{-1} and higher). In either of the latter theories, the phase distribution at the pore-network scale is controlled by capillary forces. It is possible, although this was not confirmed, that the trapped saturation in our experiments reflects macroscopic trapping due to permeability heterogeneity (similar to that shown in Figure 5) or viscous fingering at various scales. In such cases, the exponents obtained would reflect drainage through film flow along the displacement patterns in a fashion different than the one predicted by de Gennes. As far as we know, an analysis of this problem does not exist at present.

In summary, we are led to the conclusion that the displacement in the experiments reported is a drainage process, where following the trapping of the displaced phase, drainage continues, albeit at slow rates, through corner and pocket flow. The exponent of the relative permeability obtained, of the order of 3-4, is consistent with de Gennes' theory, with flow occurring over a weakly fractal pore surface. At the same time, we cannot exclude the possibility of trapping due to heterogeneity or viscous fingering, the slow drainage around which may contribute to analogous exponents. What appears to be certain is that thin film flow did not contribute to the observed behavior in this regime. This is consistent with two facts: that the exponents are much smaller than what would be expected if thin films dominated (order of 6 and higher), and that they appear to be weakly dependent on the chemistry of the displaced fluid, which rules out disjoining pressure effects.

Finally, we must add that in a preliminary report[20] of this analysis, we were led to a different conclusion and reported considerably larger exponents, which supported flow dominated by thin films. That analysis was based on analyzing plots of $\log F_{1,L}$ vs. $\log t$, which according to this chapter and Ref. [1], should asymptotically approach a straight line with slope equal to $-b/(b-1)$ (for example, compare with (22)). The slopes obtained were close to one, which is possible only if b is large indeed. It was realized in retrospect, however, that in fact we were matching data, which did not pertain to the power-law regime of the curve, but rather to the X-plot regime. In a $\log F_{1,L}$-$\log t$ plot, this regime is also a straight line with slope 1, but more importantly, it cannot be clearly

distinguished from the power-law segment. Using the new plot $\frac{F_{1,L}}{1-F_{1,L}}$ vs. $tF_{1,L}(1-F_{1,L})$, on the other hand, allows for a much sharper distinction, as the X-plot regime theoretically corresponds to a vertical slope, which can be clearly separated from the power-law segment, which has a finite slope. To demonstrate the usefulness of this new plot, as a diagnostic tool, we have plotted all the curves for the various experiments in one Figure (Figure 9). The curves have very similar characteristics with the theoretically expected (e.g. compare with Figure 7) in the limit of small capillarity, and allow for the identification of the viscous control regime.

CONCLUSIONS

In this chapter, we proposed the use of an asymptotic method, based on the time scaling of the ratio of produced fluids, to infer the relative permeability exponent of the displaced phase near its residual saturation, for immiscible displacements in laboratory cores. We showed that at sufficiently large injection rates, the existence of a power law can be detected, and its exponent inferred, by plotting in an appropriate plot the ratio of the flow rates of the two fluids at the effluent for some time after breakthrough. In this time interval, the plot is a straight line with a slope equal to the exponent in the relative permeability power law. Capillary end effects do not affect the results to leading order at high rates. However, at sufficiently large times, capillarity becomes important. In such a plot, it is manifested by a straight line with a slope equal to one, if the capillary dispersivity is constant, or greater than one, if the process is hypodiffusive. The theoretical findings were verified by comparison with an exact solution. Application of the results to laboratory displacements of various liquids by methane resulted in exponents for the relative permeability of the wetting phase which were consistent with pore-scale models of corner (or pocket) film flow.

REFERNCES

1. Yortsos, Y.C., Choi, Y., Yang, Z. and Shah, P.C., SPEJ 4, 413 (1999).
2. Bear, J., Dynamics of Fluids in Porous Media, Elsevier, New York (1972).
3. Wilkinson, D. and Willemsen, J.F., J. Phys. A (1983) 16, 3365.
4. Hulin, J.P., Clment, E., Baudet, C., Gouyet, J.F. and Rosso, M., Phys. Rev. Lett. (1988) 61, 333.
5. Wilkinson, D., Phys. Rev. A 34, 1380 (1986).
6. de Gennes, P.G., In Physics of Disordered Media (Edited by D. Adler, E. Fritzsche and S.R. Ovshinsky), pp. 227-241, Plenum Press, New York (1985).
7. Novy, R.A., Toledo, P.G., Davis, H.T. and Scriven, L.E., Chem. Eng. Sci. 44, 1785 (1989).
8. Toledo, P.G., Novy, R.A., Davis, H.T. and Scriven, L.E., Soil Sci. Soc. Am. J. 54, 673 (1990).
9. Johnson, E.F., Bossler, D.P., and Naumann, V.O., Trans. AIME 216, 370 (1959).
10. Buckley, S.E. and Leverett, M.C., Trans. AIME 146, 107 (1942).
11. Yortsos, Y.C. and Chang, J., TiPM 5, 399 (1990).
12. Chang, J. and Yortsos, Y.C., SPERE 285 (1992).
13. van Duijn, C.J., Molenaar, J., and de Neef, M.J., TiPM 21, 71 (1995).
14. de Neef, M.J., Doctoral Dissertation, Delft University (2000).
15. Witham, G., Linear and Non-linear Waves, Wiley (1974).
16. Fokas, A.S., and Yortsos, Y.C., SIAM J. Appl. Math. 42, 318 (1982).
17. Ershagi, I. and Omoregie, O., J. Pet. Tech., 203 (1978).
18. Welge, H., Trans. AIME 195, 91 (1952).
19. Carslaw, H.S. and Jaeger J.C., Conduction of Heat in Solids, Oxford: Clarendon Press (1990).
20. Laroche, C., Yortsos, Y.C. and Kamath, J., Proc. ECMOR VII, Baveno, Italy (Sept. 5-8, 2000).

APPENDIX

In this Appendix we provide the derivation of the exact solution in the case of imbibition. As noted in the main text, for this we will seek a solution of the heat equation (51) subject to the boundary condition (53). The first part of the boundary condition, namely before the breakthrough of the displacing phase, applies first. Hence, for $\tau < \tau_f$, where the breakthrough time τ_f is determined from the condition $\phi_x = 0$, we take

$$\phi = \exp\left[\frac{\tau}{\varepsilon^2} - \frac{1}{\varepsilon}\right] \text{ at } x = 1 \tag{1}$$

The solution of this problem is obtained by standard methods. We find

$$\phi = 1 - x + \sum_{t}^{\infty} b_n \sin n\pi \exp(-n^2\pi^2\tau) + \sum_{1}^{\infty} c_n \sin n\pi \exp(\frac{\tau}{\varepsilon^2}) \tag{2}$$

where the unknown coefficients are

$$b_n = -\frac{2}{n\pi(1+\varepsilon^2 n^2\pi^2)} \tag{3}$$

and

$$c_n = (-1)^{n+1} \frac{2\pi\varepsilon^2 n}{1+\varepsilon^2 n^2\pi^2} \exp(-\frac{1}{\varepsilon}) \tag{4}$$

The breakthrough time is the solution of the equation

$$\frac{1}{\pi} = \sum_{1}^{\infty} (-1)^n n b_n \exp(-n^2\pi^2\tau_f) + \sum_{1}^{\infty} (-1)^n n c_n \exp(\frac{\tau_f}{\varepsilon^2}) \tag{5}$$

Equivalently, one may use a different expansion for the solution of this problem, by considering a Laplace transform. Then, it is not difficult to show that τ_f solves the following equation

$$2 = \sum_{n=-\infty}^{\infty} \left[\exp\left(\frac{2}{\varepsilon}(n+1)\right) \left(erfc\left(\frac{\sqrt{\tau_f}}{\varepsilon} + \frac{(n+\frac{1}{2})}{\sqrt{\tau_f}} \right) - s_n \right) + \exp\left(-\frac{2n}{\varepsilon}\right) \left(erfc\left(\frac{\sqrt{\tau_f}}{\varepsilon} - \frac{(n+\frac{1}{2})}{\sqrt{\tau_f}} \right) + s_n \right) \right] \tag{6}$$

where $s_n = sign(n+1/2)$. This equation is better suited both for numerical evaluation and for analytical manipulations. For example, one can show after some manipulations, that the solution of (6) in the limit $\varepsilon << 1$ is $\tau_f = \frac{\varepsilon}{2}$, as expected from the viscous solution

case, where $t_f = 1/2$. For completeness, we show in Figure A1 the solution of (6) for different values of ε. As expected, the breakthrough time is given by the Buckley-Leverett solution, $t_f = 1/2$ at small ε and approaches $t_f = 1$ as the problem is controlled by capillarity.

For times $\tau > \tau_f$, we need to solve again the heat equation, but now using the boundary condition $\phi_x = 0$ at $x = 1$. Based on the initial condition $\phi = \phi(x, \tau_f)$, obtained from the above, we obtain the result

$$\phi = 1 - 2\sum_{1}^{\infty} \sin(\lambda_n x) \exp(-\lambda_n^2 (\tau - \tau_f)) \left[\frac{\sin \lambda_n}{\lambda_n^2} - \frac{1}{2} \sum_{0}^{\infty} f_m(\tau_f) \left(\frac{\sin(\lambda_n - m\pi)}{\lambda_n - m\pi} - \frac{\sin(\lambda_n + m\pi)}{\lambda_n + m\pi} \right) \right] \tag{7}$$

where $\lambda_n = (2n+1)\frac{\pi}{2}$ and

$$f_m(\tau_f) = b_m \exp(-m^2 \pi^2 \tau_f) + c_m \exp(\frac{\tau_f}{\varepsilon^2}) \tag{8}$$

Although in an explicit form, the solution of the problem requires the numerical evaluation of τ_f. The results for the fractional flow at the outlet, $F_{1,L}$, are plotted in the log-log plot of $\frac{F_{1,L}}{1-F_{1,L}}$ vs. $tF_{1,L}(1-F_{1,L})$ in Figure A2 for various values of ε. The curves obtained have similar characteristics with the drainage case discussed in the main text.

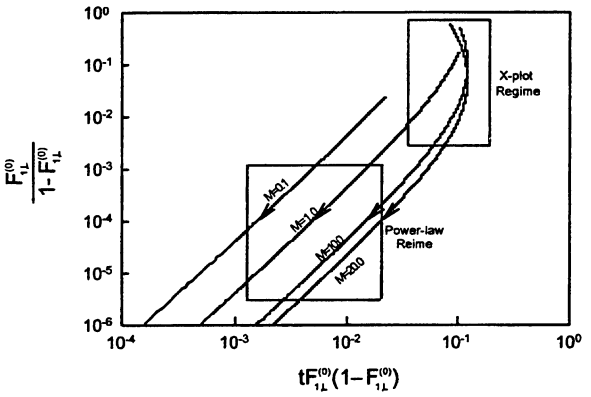

Figure 1(a)

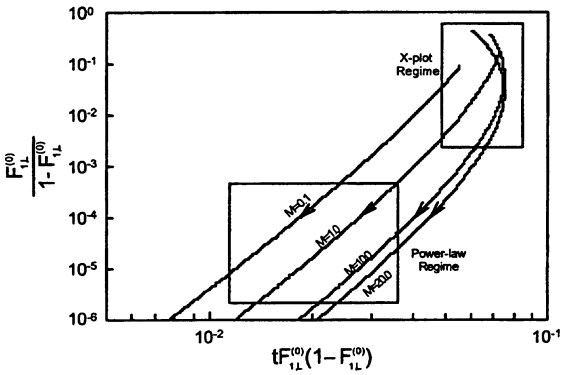

Figure 1(b)

Figure 1. Log-log plot of $\frac{F_{1,L}^{(0)}}{1-F_{1,L}^{(0)}}$ vs. $tF_{1,L}^{(0)}(1-F_{1,L}^{(0)})$ for the outlet fractional flow of the liquid under viscous control, for different values of b and M. (a) $b=2$, (b) $b=5$. Arrows indicate the direction of increasing time. The straight-line segment at large times has slope equal to b. The X-plot regime corresponds to the region around the vertical slope.

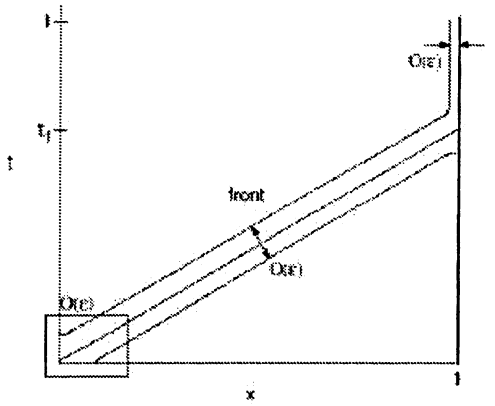

Figure 2. Location of boundary layers in the limit of small ε.

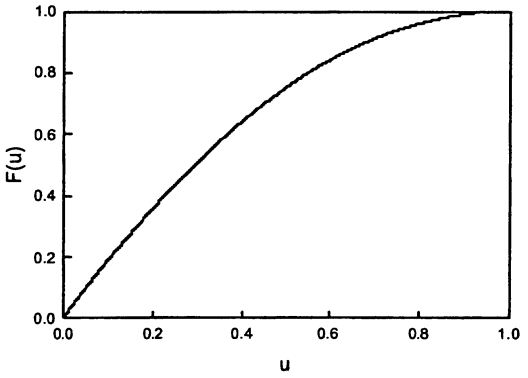

Figure 3. The model fractional flow function $F(u) = 1-(1-u)^2$.

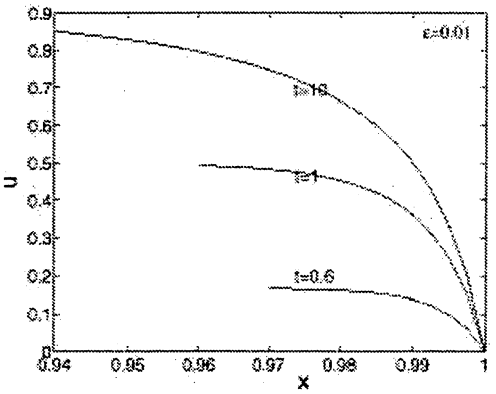

Figure 4a

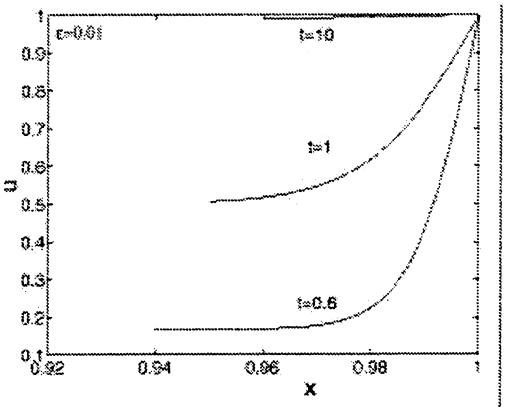

Figure 4b

Figure 4. The saturation profile in boundary layer coordinates, near the outlet end for the fractional flow of Figure 3: (a) drainage, (b) imbibition.

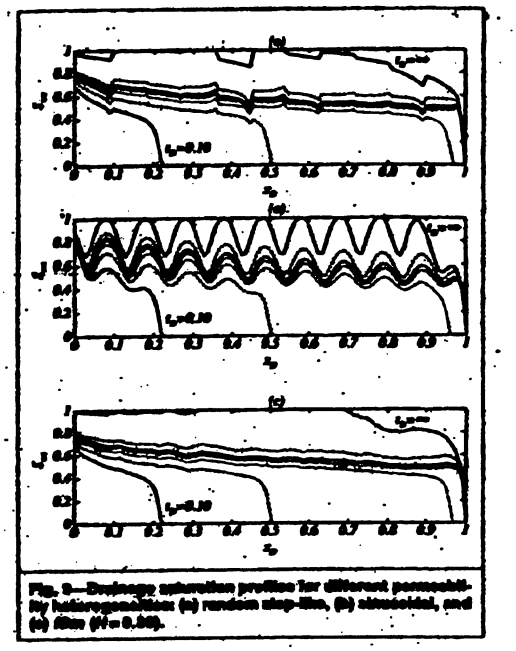

Figure 5a

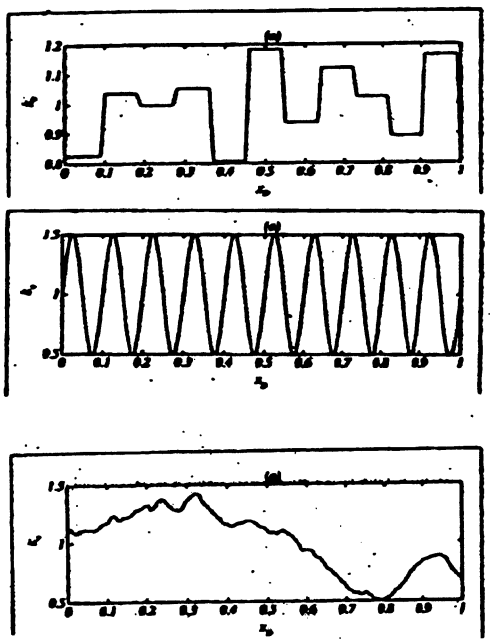

Figure 5b

Figure 5. Drainage saturation profiles in a heterogeneous medium for $\varepsilon = 0.1$, $M = 10$ and for different values of time (0.1, 0.25, 0.50, 0.75, 1.0, 2.0 and 8): (a) Saturation profiles, (b) the imposed permeability variation. (From Ref. [12]).

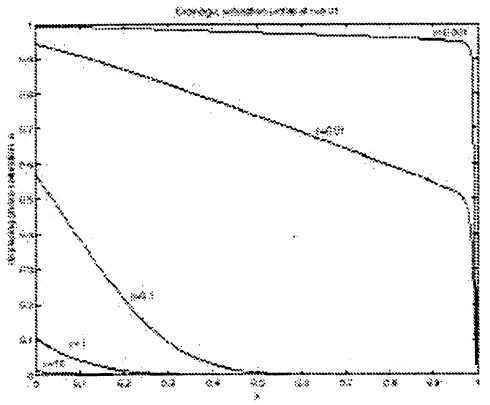

Figure 6a

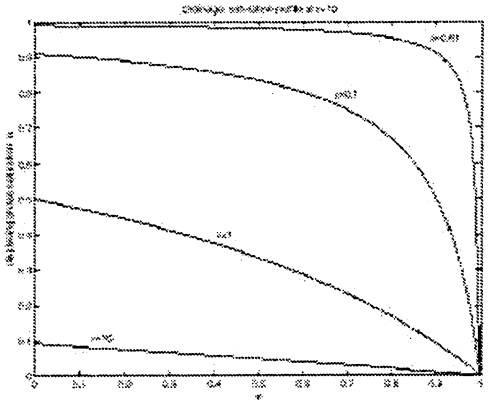

Figure 6b

Figure 6 Saturation profiles for drainage obtained from the exact solution based on Burgers' equation, for different values of ε and two different values of τ (a) τ=0.01, (b) τ=10.

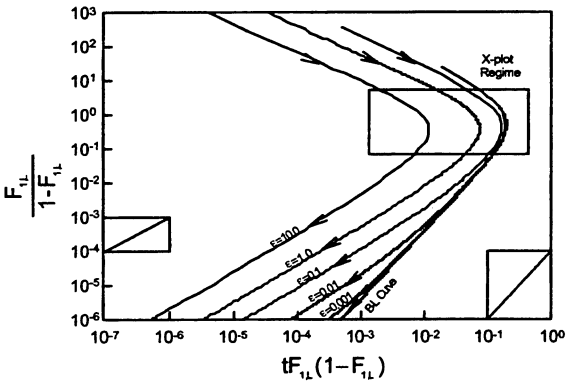

Figure 7. Log-log plot of $\frac{F_{1,L}}{1-F_{1,L}}$ vs $tF_{1,L}(1-F_{1,L})$ for the outlet fractional flow of the liquid as obtained from the exact solution of the Burgers' equation for drainage, for different values of ε. Plotted also is the solution corresponding to the viscous solution. For ε<0.1, a straight line segment with slope 2, corresponding to the viscous solution can be identified. The late-time segment with slope 1 corresponds to capillary control. The two different slopes are separately indicated in the figure.

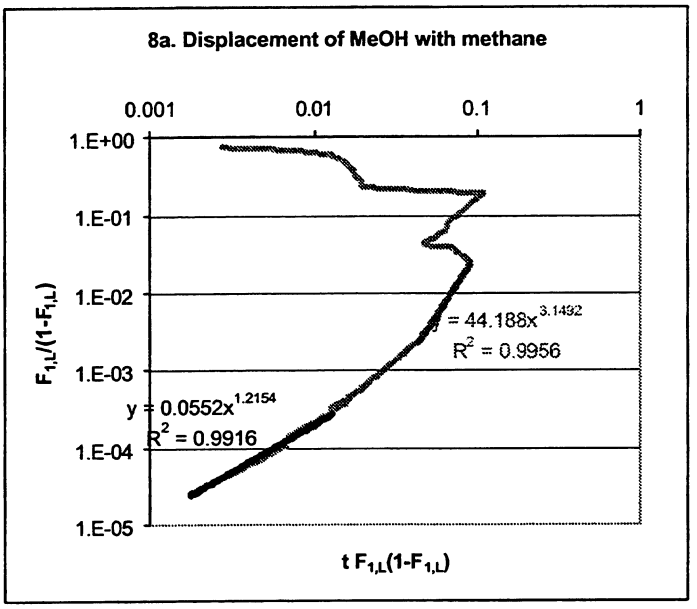

Figure 8a

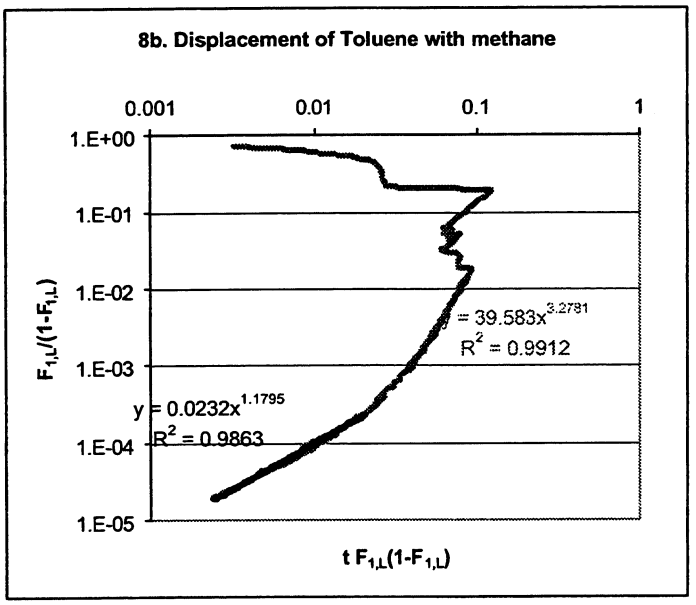

Figure 8b

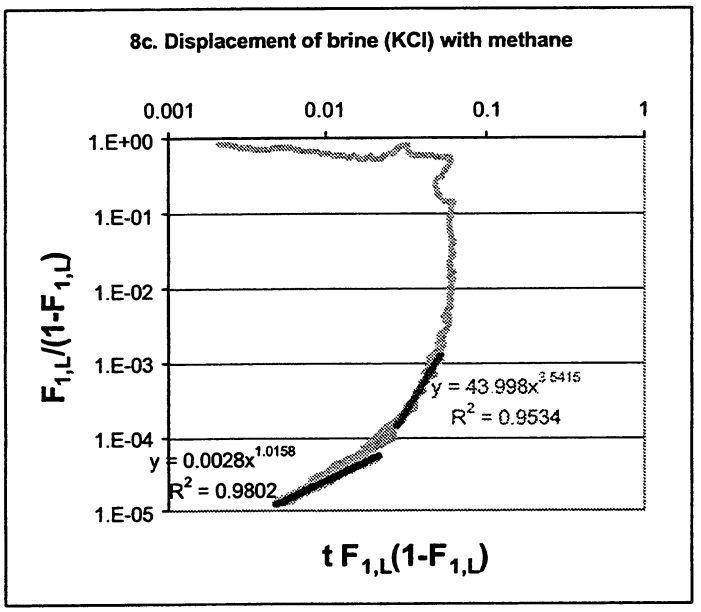

Figure 8c

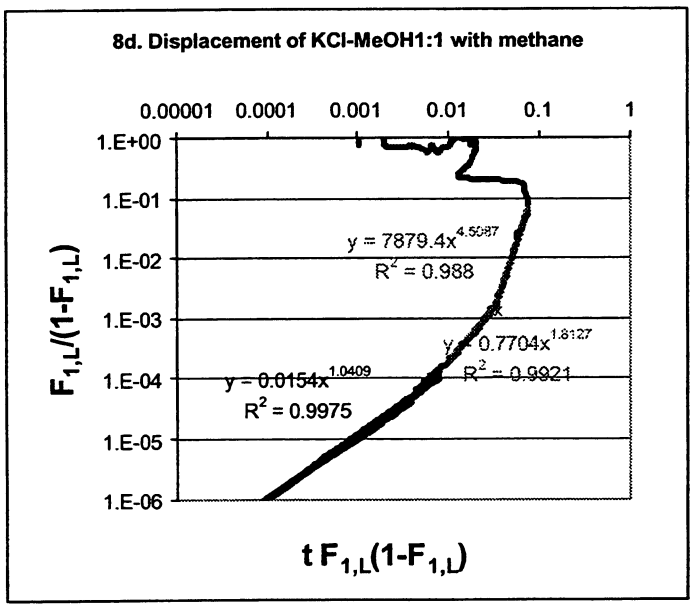

Figure 8d

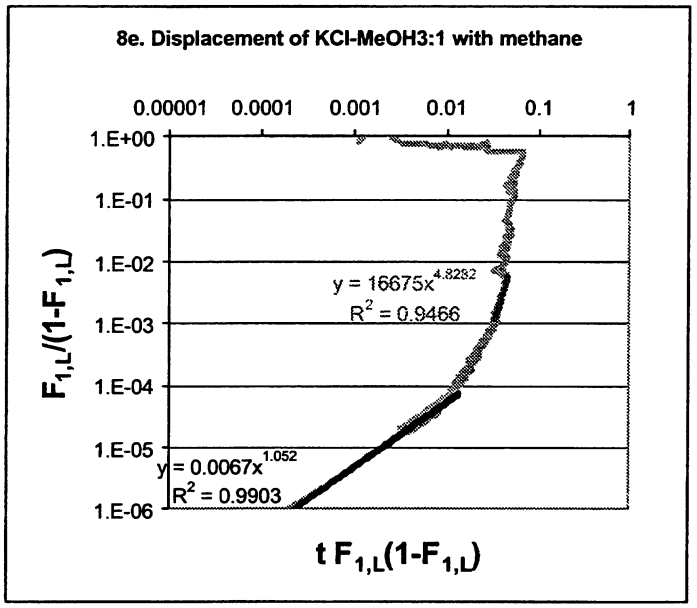

Figure 8e

Figure 8 Log-log plot of $\frac{F_{1,L}}{1-F_{1,L}}$ vs $tF_{1,L}(1-F_{1,L})$ for the outlet fractional flow in the following experiments: (a) methanol (MeOH) displaced by methane, (b) toluene displaced by methane, (c) brine (KCl) displaced by methane, (d) an 1:1 mixture of brine and methanol displaced by methane, and (e) a 3:1 mixture of brine and methanol displaced by methane. The slopes of the viscous control and capillary control straightline segments are 3.15 and 1.21, 3.28 and 1.18, 3.54 and 1.02, 4.5 and 1.04, and 4.8 and 1.05, respectively.

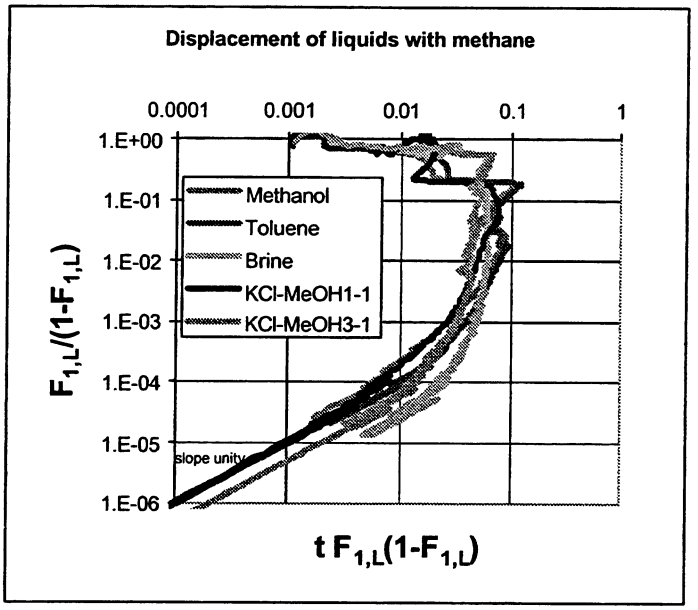

Figure 9. Log-log plot of $\frac{F_{1,L}}{1-F_{1,L}}$ vs $tF_{1,L}(1-F_{1,L})$ for the outlet fractional flow of all the curves in Figures 8-12. Comparison with Figure 7 at small ε shows that the experimental curves are consistent with the theoretical expectations

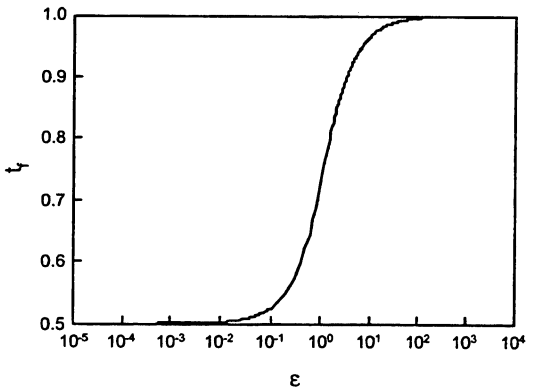

Figure A1. The breakthrough time t_f as a function of the parameter ε for imbibition, obtained from the exact solution corresponding to Burgers' equation. At small ε, the breakthrough time approaches the viscous limit $\frac{1}{2}$, while at large ε it approaches the capillary limit 1.

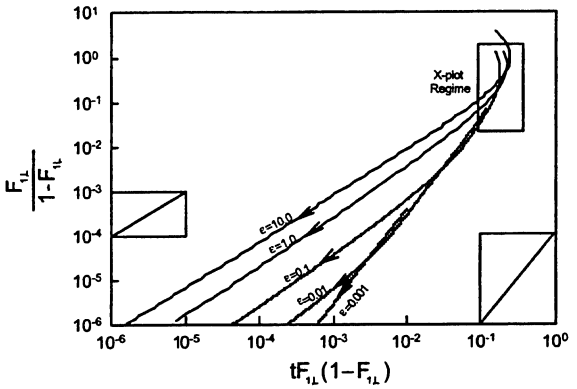

Figure A2. The counterpart of Figure 7 for the case of imbibition. At small ε, the two curves are qualitatively similar

DARCIAN DYNAMICS

Pouya Amili and Yanis C. Yortsos

I. Introduction

Two-phase flow in porous media has been the subject of many studies for decades due to its importance in many applications such as oil recovery, geothermal reservoirs, nuclear waste repositories and so on. In many applications, two-phase flow is also accompanied by phase-change, thus effects of heat transfer are important as well, for example, in thermally enhanced oil recovery. Of interest to this part of the report are co-current and counter-current vapor-liquid flows in porous media. While this topic is important in many applications, it has not received a fundamental attention. A difficulty arises from the fact that due to capillary forces, there is the possibility that one phase becomes disconnected or stranded. Conversely, a stranded phase, consisting of blobs or ganglia, can be mobilized, if the flow rate of the other phase is sufficiently large. The existence of such blobs disturbs in turn, the flow, which consequently affects trapping and mobilization conditions.

Modeling of the trapping, mobilization and or coalescence of disconnected ganglia in porous media has been investigated using two models: percolation and pore-network simulation. The advantage of percolation models is that they are fast, however they only apply to very small flow rates, where the process can be considered as quasi-static. A full-scale pore-network simulation does not have this disadvantage, and applies to general dynamic flow conditions [5], [6], [7]. However, it is computationally intensive and requires a great deal of detail of the microstructure. In this work, we provide an alternative approach, which utilizes the fact that at the small scale, fluid flow is in fact described by Poiseuille's equation (which can lead to a macroscale description based on Darcy's law). The linear character of this equation allows us to apply a Boundary Integral Method in which all the relevant flow information is mapped on the boundaries of the two phases. Moreover, because the underlying equation is the Laplace equation, we can use the many important advances made in potential theory.

An analogous situation exists in the bulk fluid flow of a suspension of small particles, droplets or bubbles, where the flow is controlled by viscous forces. One method to understand the flow properties of such systems is Stokesian Dynamics introduced by Brady and Bossis [1]. Stokesian Dynamics is a molecular-dynamics-like method to numerically simulate the suspension behaviour at small Reynolds number. It is based on the linearity of the problem at small Reynolds numbers, where Stokes equations apply, and relies on a boundary integral method to compute the hydrodynamic forces between particles as transmitted through the flowing fluid. In the flow of fluids in the bulk, these forces are driven by viscous shear, which compete with thermal and interparticle forces. In fluid flow through porous media, however, the main forces that compete with capillarity are pressure forces, which can be expressed via Darcy's law. In this report, we propose an analogue to Stokesian dynamics, based on Darcy's law, which we call Darcian Dynamics. While our ultimate interest is vapor-liquid flows, we have found that the simpler problem of isothermal flows is not really well understood, in this context, thus this preliminary effort addresses first, the problem in the absence of phase change. The latter will be considered in the next phase of this project.

The objective of this work, therefore, is to use a Boundary Integral Method, based on potential theory, to formulate a methodology for Darcy flows, which is analogous to that for Stokesian Dynamics. The foundation of this method is described in this work. The method will enable us to investigate the interaction between a flowing and a dispersed phase in a porous medium, which is held trapped or has its motion hindered, by capillary forces. The method provides a fast way to model the system behavior and its dependence on the various geometric parameters, such as ganglia configuration and location, the flow rate, the capillary number, and other variables. By using the new approach, the pressure distribution on the interface of the various ganglia can be directly obtained. This is a function of various parameters, such as the size and shape of each ganglion as well as the position and the distance between ganglia. Using this information, the overall pressure force on each ganglion can be calculated to study the possibility of mobilization or movement of ganglia. This movement is related to the population, distribution, as well as the size and configuration of

the ganglia. In addition, forces such as gravity will play a role in ganglia mobilization. We note that following the mobilization of a ganglion above a critical flow rate, all or some of the ganglia can be moved, although after some steps, some of them may become stranded. Flowing ganglia may break up and form two or more daughter ganglia, which in turn may be stranded. Another possibility is coalescence between two ganglia resulting in the formation of a larger ganglion.

II. Theory

The governing equations for the flow of a fluid in a homogeneous porous medium are obtained from momentum and mass conservation as follows

$$\overline{U} = -\frac{k}{\mu}(\nabla P - \rho \mathbf{g}) \tag{1}$$

and

$$\nabla \cdot \overline{U} = 0 \tag{2}$$

where $\overline{U}, \mu, k$ and P are the flow rate, dynamic viscosity of the flowing fluid, permeability of the porous medium and pressure, respectively. By substituting (1) in (2) and taking k and μ constant, Laplace's equation for pressure is obtained

$$\nabla^2 P = 0 \tag{3}$$

whose solution provides the pressure profile in the system. Consider, now, a two-dimensional system with flow of the fluid in the direction of the x-axis with far-field velocity $\overline{U}_t = \overline{U}_o$. The system contains trapped blobs or ganglia of another phase and is considered to be infinitely extended in the direction of flow. The existence of the ganglia perturbs the flow, consequently the total pressure and flow rate can be described as

$$\begin{aligned} P_t &= P_d + P_o \\ \overline{U}_t &= \overline{U}_d + \overline{U}_o \end{aligned} \tag{4}$$

where subscripts t, d and o represent total, perturbed and original values, respectively.

The boundary conditions of the system are defined at the far field and at the interfaces between the two phases. At the far-field, the perturbed flow rate vanishes, namely

$$\overline{U}_t = \overline{U}_{ox}$$

At the surface of the ganglia, the normal flow velocity is zero, therefore we can write

$$(\overline{U}_t)_n = 0$$

where $\hat{n}$ is the outward unit normal vector at the surface of the ganglia. This can be further written as

$$\begin{aligned} \overline{U}_t \cdot \hat{n} &= \overline{U}_d \cdot \hat{n} + \overline{U}_o \cdot \hat{n} = 0 \\ -\frac{k}{\mu}\frac{\partial P_d}{\partial n} &+ \overline{U}_o \cdot \hat{n} = 0 \\ \frac{k}{\mu}\frac{\partial P_d}{\partial n} &= \overline{U}_{ox}\cos\theta \end{aligned} \tag{5}$$

where θ is the angle between the normal vector, $\hat{n}$, and the direction of flow.

In order to make equations dimensionless, the following reference quantities are introduced

$$\overline{U}_D = \frac{\overline{U}}{\overline{U}_o}; \quad P_D = \frac{P}{P^*}; \quad L_D = \frac{L}{l} \tag{6}$$

Here we have defined $P^* = \frac{\mu l \overline{U}_o}{k}$, where μ, $\overline{U}_o$, k and$l$ are dynamic viscosity, flow rate, permeability and the characteristic pore length, respectively. In this notation, Laplace's equation and the boundary conditions can be rewritten as

$$\nabla_D^2 (P_d)_D = 0 \tag{7}$$

$$\frac{\partial (P_d)_D}{\partial n} = \cos\theta \qquad \text{on the interface} \tag{8}$$

and

$$(\overline{U}_t)_D = 1 \qquad x \to \infty \tag{9}$$

From this point on, subscript D will be omitted for simplicity, however all parameters are assumed dimensionless. Solving Darcy's equation for the original state, results in $P_o = -x$, therefore the total pressure is given by

$$P_t = P_d - x \tag{10}$$

where P_d is the solution to Eqn.(7).

There is a wealth of material regarding the solution of (7) with different boundary conditions. These methods can be classified in two different general categories, differential methods and integral methods. In differential methods, the differential form of Laplace's equation is used for the solution (for example, using Finite Differences (FD)). In the integral equations approach, the Green's function technique is employed, where the pressure (potential) is expressed in terms of the integral of the Green's function. As Eqn.(8) suggests, the boundary condition is expressed in terms of the normal derivatives of pressure. Using the integral equation approach to solve (7) with boundary condition of (8) results in a Fredholm integral equation of the second kind. These equations are similar to potential problem in electrostatic. For example, this problem is similar to the charge distribution on a surface (simple layer and double layer). We use techniques from potential theory to solve the problem, as shown below.

Method of Solution: 1. Infinite system

Since the potential theory of electrostatic is well understood, we will use the terminology of electrostatic to describe the solution procedure. The free-space potential due to a point source in two dimensions $\varphi(\overline{\rho})$, is defined

$$\varphi(\overline{\rho}) = \frac{1}{2\pi} \ln |\overline{\rho} - \overline{\rho}'| \tag{11}$$

where $\overline{\rho}'$ is the location of the source and $\overline{\rho}$ is the observation point. If we consider the distributed sources with density q_l on C, by superposition the potential of the entire charge distribution at point $\overline{\rho}$ will be

$$\varphi(\overline{\rho}) = \int_C q_l(\overline{\rho}')\frac{1}{2\pi}\ln|\overline{\rho}-\overline{\rho}'|\,dl_{\overline{\rho}'} \tag{12}$$

Here, contour C represents the location (cross-section) of a two-dimensional charge distribution and can be a closed or open contour. Define, next, $Q_l(\overline{\rho}') = q_l(\overline{\rho}')$, then we have

$$\varphi(\overline{\rho}) = \int_C \frac{Q_l(\overline{\rho}')}{2\pi}\ln|\overline{\rho}-\overline{\rho}'|\,dl_{\overline{\rho}'} \tag{13}$$

Now, if $\overline{\rho}$ is not on C we can calculate $\partial\varphi/\partial n$ by differentiating (13). We obtain

$$\frac{\partial\varphi}{\partial n_{\overline{\rho}}}(\overline{\rho}) = \int_C Q_l(\overline{\rho}')\frac{\partial}{\partial n_{\overline{\rho}}}[\frac{1}{2\pi}\ln|\overline{\rho}-\overline{\rho}'|]dl_{\overline{\rho}'} = \int_C Q_l(\overline{\rho}')\frac{\cos(\overline{\rho}-\overline{\rho}',\hat{n})}{2\pi|\overline{\rho}-\overline{\rho}'|}dl_{\overline{\rho}'} \quad \forall\,\overline{\rho}\notin C \tag{14}$$

The boundary condition is specified on the contour C, thus we need to evaluate the above in the limit $\overline{\rho}\to C$. To avoid the possible singularity we divide the contour C into two complementary parts C_s and C_0, and let C_s approach zero. In the limit when $\overline{\rho}$ approaches C, e.g. at point C_s (see Fig.(1)), then equation (14) becomes

$$\lim_{\overline{\rho}\to C^+}\frac{\partial\varphi}{\partial n_{\overline{\rho}}}(\overline{\rho}) = \int_{C_0} Q_l(\overline{\rho}')\frac{\cos(\overline{\rho}-\overline{\rho}',\hat{n})}{2\pi|\overline{\rho}-\overline{\rho}'|}dl_{\overline{\rho}'} + \int_{C_s} Q_l(\overline{\rho}')\frac{\cos(\overline{\rho}-\overline{\rho}',\hat{n})}{2\pi|\overline{\rho}-\overline{\rho}'|}dl_{\overline{\rho}'} \tag{15}$$

The second integral contains a possible singularity as $\overline{\rho}\to\overline{\rho}'$. At the limit C_s approaches zero and can be considered as a straight line. For a smooth C_s, we set up the following geometry by assuming the origin at the center of C_s, see Fig.(1). As $\overline{\rho}\to\overline{\rho}'$, $h\to 0$. Therefore, the second integral in (15) can be rewritten as

$$\lim_{w\to\infty}\left[\lim_{h\to 0}\int_{-w}^{w}\frac{\cos(h-x,\overline{n})}{2\pi|h-x|}Q_l(0)\,dx\right] \tag{16}$$

where

$$\cos(h-x,\overline{n}) = \frac{h}{\sqrt{h^2+x^2}} \quad \text{and} \quad |h-x| = \sqrt{h^2+x^2}$$

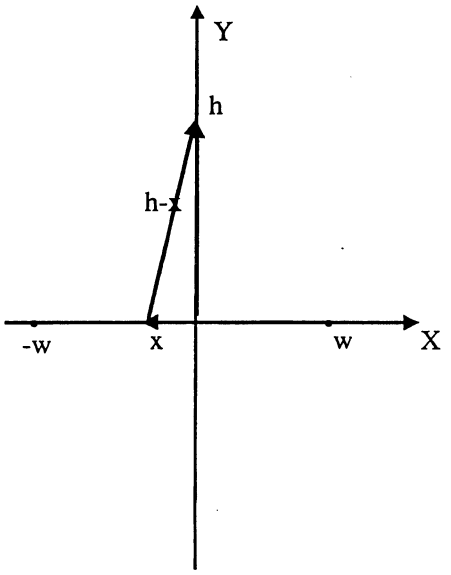

Figure 1: The local geometry as point $\overline{\rho}$ (denoted as point h), approaches contour C at point C_s along the normal to the contour.

Eqn.(16) is evaluated as

$$\lim_{w\to\infty}\left[\lim_{h\to 0}\int_{-w}^{w}\frac{\frac{h}{\sqrt{h^2+x^2}}}{2\pi\sqrt{h^2+x^2}}\,Q_l(0)\,dx\right] = \lim_{w\to 0}\left[\lim_{h\to 0}\frac{hQ_l(0)}{2\pi}\int_{-w}^{w}\frac{dx}{h^2+x^2}\right] =$$

$$\frac{Q_l(0)}{2\pi}\left(\frac{\pi}{2}+\frac{\pi}{2}\right) = \frac{1}{2}Q_l(0) \tag{17}$$

Using the result obtained in Eqn.(17) in (15),we arrive at

$$\lim_{\overline{\rho}\to C+}\frac{\partial\varphi}{\partial n_{\overline{\rho}}}(\overline{\rho}) = +\frac{1}{2}\,Q_l(C) + \int_{C_0} Q_l(\overline{\rho}')\,\frac{\cos(\overline{\rho}-\overline{\rho}',\hat{n})}{2\pi\mid\overline{\rho}-\overline{\rho}'\mid}\,dl_{\overline{\rho}'} \tag{18}$$

Equation (18) is a Fredholm integral equation of the secondkind which can be solved numerically by applying a methods of Moments as explained below.

The Method of Monents

The basic idea of this method is to reduce a functional equation to a matrix equation, and then solve the matrix equation by known techniques [2]. When the equation is reduced to a suitable matrix form, the solution can be found by matrix inversion. The problem can be cast in the form $L(f) = g$, where we must identify the operator L, its domain (the functions f on which it operates), and its range (the functions g resulting from the operation). Furthermore, we usually need the scalar inner product $< f, g >$. If the solution to $L(f) = g$ exists and is unique for all g, then the inverse operator L^{-1} exists such that

$$f = L^{-1}(g) \tag{19}$$

If g is known, then (19) represents the solution to the original problem. Let f, the unknown, be expanded in a series of functions $f_1, f_2, f_3, \ldots$ in the domain of L, as

$$f = \sum_n \alpha_n f_n \tag{20}$$

where the α_n are constants. We shall call f_n *expansion functions* or *basis functions.* For exact solutions, (20) is usually an infinite summation and f_n form a complete set of basis functions.

For approximate solutions, (20) is a finite summation. Substituting (20) in $L(f) = g$, and using the linearity of L, we have

$$\sum_n \alpha_n L(f_n) = g \tag{21}$$

It is assumed that a suitable inner product $< u, k >$ can be defined as

$$< u, k >= \int u(x)k(x)dx \tag{22}$$

Now let us define a set of *weighting functions,* or *testing functions*, $w_1, w_2, w_3, \ldots$ in the range of L, and take the inner product of (21) with each w_m. The result is

$$\sum_n \alpha_n < w_m, Lf_n >=< w_m, g > \qquad m = 1, 2, 3, \ldots \tag{23}$$

This set of equations can be written in matrix form

$$[l_{mn}][\alpha_n] = [g_m] \tag{24}$$

where

$$[l_{mn}] = \begin{bmatrix} < w_1, Lf_1 > & < w_1, Lf_2 > & \ldots \\ < w_2, Lf_1 > & < w_2, Lf_2 > & \ldots \\ \ldots & \ldots & \ldots \end{bmatrix} \tag{25}$$

$$[\alpha_n] = \begin{bmatrix} \alpha_1 \\ \alpha_2 \\ \ldots \end{bmatrix} \quad [g_m] = \begin{bmatrix} < w_1, g > \\ < w_2, g > \\ \ldots \end{bmatrix} \tag{26}$$

If the matrix $[l]$ is nonsingular, its inverse $[l^{-1}]$ exists. The α_n are then given by

$$[\alpha_n] = [l^{-1}_{nm}][g_m] \tag{27}$$

and the solution for f is given by (20).

The choice of the functions f_n and w_n decides if this solution is exact or approximate. The f_n should be linearly independent in order to approximate f reasonably well by superposition of (20). The w_n should also be linearly independent in the product $< w_n, g >$. We

choose *point-matching* and *subsectional bases* methods to decide what kind of functions we must use for our weighting and basis functions respectively. A simple way to obtain approximate solutions is to require that equation (21) be satisfied at discrete points in the region of interest. This procedure is called a point-matching method. It is equivalent to using Dirac delta functions as weighting functions. Another approximation is the method of subsections involving the use of basis functions f_n each of which exists only over subsections of the domain of f. Using pulse function as basis function can satisfy this purpose. Then each α_n of expansion (20) affects the approximation of f only over a subsection of the region of interest.

Numerical Solution of the Two-Dimensional Problem

The governing equation and the boundary conditions in our case read as follows. We recall that Laplace's equation for the perturbed pressure is

$$\nabla^2 P_d(\overline{\rho}) \;=\; 0 \tag{28}$$

At the interface between the two phases, the boundary condition is

$$\frac{\partial P_d(\overline{\rho})}{\partial n} = \cos\theta \qquad \overline{\rho} \in C \tag{29}$$

Using the previous result, we have

$$\lim_{\overline{\rho}\to C^+} \frac{\partial P_d}{\partial n_{\overline{\rho}}}(\overline{\rho}) \;=\; \frac{1}{2}\, Q_l(\overline{\rho}) \;+\; \int_{C_0} Q_l(\overline{\rho}\,')\, \frac{\cos(\overline{\rho}-\overline{\rho}\,', \hat{n_{\overline{\rho}}})}{2\pi|\,\overline{\rho}-\overline{\rho}\,'\,|}\, dl_{\overline{\rho}\,'} \quad \overline{\rho} \in C \tag{30}$$

therefore, we obtain

$$\frac{1}{2}\, Q_l(\overline{\rho}) \;+\; \int_{C_0} Q_l(\overline{\rho}\,')\, \frac{\cos(\overline{\rho}-\overline{\rho}\,', \hat{n_{\overline{\rho}}})}{2\pi|\,\overline{\rho}-\overline{\rho}\,'\,|}\, dl_{\overline{\rho}\,'} \;=\; \cos\theta \tag{31}$$

Boundary condition Eqn(31) must be satisfied for all points on C. Result (28) is of course valid at a general point outside C, where

$$P_d(\overline{\rho}) = \int_c Q_l(\overline{\rho}\,')\frac{1}{2\pi} \ln|\overline{\rho}-\overline{\rho}\,'|\, dl_{\overline{\rho}\,'} \tag{32}$$

The following will describe an application of the Moment Method with subsectional bases and point-matching to numerically solve the integral equation (31).

An arbitrary two-dimensional contour of reasonable smoothness (here the ganglion) can be approximated by N straight segments, given sufficiently large N. We then assume that the unknown function Q_l is constant on each straight segment. The Moment Method enables us to numerically find the unknowns of the problem (Q_l on each segment). Once the distribution of Q_l is obtained, (32) can be used to find the pressure at an arbitrary point outside C. Our problem can be formulated in the following form

$$Lf = g \tag{33}$$

where f (the unknown) is approximatedas

$$f = \sum_{j=1}^{N} \alpha_j f_j \tag{34}$$

therefore (33) becomes

$$L \sum_{j=1}^{N} \alpha_j f_j = g \tag{35}$$

Because of linearity,

$$\sum_{j=1}^{N} \alpha_j \, Lf_j = g \tag{36}$$

In our problem, the operator L is

$$\frac{1}{2}[f(\overline{\rho})] + \int_C [f(\overline{\rho}')] \frac{\cos(\overline{\rho} - \overline{\rho}', \hat{n}_{\overline{\rho}})}{2\pi|\overline{\rho} - \overline{\rho}'|} \, dl_{\overline{\rho}'} \quad \forall \overline{\rho}' \in C \tag{37}$$

The inner product defined for two functions u and k is

$$< u, k >= \int u(x)k(x) \, dx \tag{38}$$

This definition satisfies the linear properties required for an inner product. Using this definition, we find the inner product of a weighting or testing function w_i, with both sides of Eqn. (36). This results in

$$< \sum_{j=1}^{N} \alpha_j \, Lf_j \, , \; w_i > = < g, w_i > \qquad \text{for } i = 1, 2, \ldots, N \tag{39}$$

or

$$\sum_{j=1}^{N} \alpha_j \; < Lf_j \, , \; w_i > = < g, w_i > \qquad \text{for } i = 1, 2, \ldots, N \tag{40}$$

Applying Eqn. (40) at N points is required for the boundary condition to be satisfied on all N segments. We thus arrive at a system of N equations with N unknowns. At this point we need to choose approximate functions f and w. For simplicity and computational efficiency these functions are assumed to be *pulse* and *delta* functions respectively

$$f_j = \begin{cases} 1 & \text{on } j^{\text{th}} \text{ segment} \\ 0 & \text{elsewhere} \end{cases} \tag{41}$$

$$w_i = \begin{cases} \delta(\overline{\rho_i^c}) & \text{on the center of } i^{\text{th}} \text{ segment} \\ 0 & \text{elsewhere} \end{cases} \tag{42}$$

where, i and j represent field and source points, respectively. The inner product of Lf_j and w_i is

$$< Lf_j \, , \; w_i > = \int_C (Lf_j \cdot w_i) \, dl \; = \; \int_C (Lf_j \cdot \delta(\overline{\rho_i})) \, dl \; = \; Lf_j \Big|_{\overline{\rho_i}} \tag{43}$$

which can be written as

$$< Lf_j \, , \; w_i > = \frac{1}{2} f_j(\overline{\rho_i}) \; + \; \int_C f_j(\overline{\rho}_j') \, \frac{\cos(\overline{\rho_i} - \overline{\rho_j}', \hat{n}_i)}{2\pi | \, \overline{\rho_i} - \overline{\rho_j}' \, |} \, dl_{\overline{\rho_j}'} \tag{44}$$

In the case that the source and the observation points are the same ($i = j$), then we have

$$f_j(\overline{\rho}') \; = \; 1 \;\; \text{and}, \;\; \cos(\overline{\rho_i} - \overline{\rho_j}', \hat{n}_i) \; = \; \cos(\pi/2) \; = \; 0$$

which gives

$$< Lf_j \, , \; w_i > = \; \frac{1}{2}$$

If $\overline{\rho_i}$ and $\overline{\rho}'$ do not coincide ($i \neq j$) then

$$f_j(\overline{\rho_i}) \;=\; 0 \;\text{ and }\; f_j(\overline{\rho_j}') \;=\; 1$$

therefore, we have

$$< Lf_j \,,\; w_i > = \int_{j^{th}\,\text{segment}} \frac{\cos(\overline{\rho_i} - \overline{\rho_j}', \hat{n_i})}{2\pi|\overline{\rho_i} - \overline{\rho_j}'|}\, dl_{\overline{\rho_j}'} \tag{45}$$

In general, the left hand side of equation (40) is

$$< Lf_j \,,\; w_i > = \begin{cases} \frac{1}{2} & \text{for } i = j \\ \int_{j^{th}} \frac{\cos(\overline{\rho_i} - \overline{\rho_j}', \hat{n_i})}{2\pi|\overline{\rho_i} - \overline{\rho_j}'|}\, dl_{\overline{\rho_j}'} & \text{for } i \neq j \end{cases}$$

and the right hand side of equation (40) can bewritten as

$$< g, w_i > = \int_C g \cdot \delta(\overline{\rho_i}^{\,c})\, dl \;=\; g(\overline{\rho_i}^{\,c}) \;=\; \cos(\theta_i) \tag{46}$$

Note that $\overline{\rho_i}^{\,c}$ is the center point of the i^{th} segment and θ_i is the angle between normal vector $\widehat{n_i}$, and x coordinate (the direction of flow). Equation (40) in matrix form reads as

$$\begin{bmatrix} < Lf_1, w_1 > & < Lf_2, w_1 > & \dots & < Lf_N, w_1 > \\ < Lf_1, w_2 > & < Lf_2, w_2 > & \dots & < Lf_N, w_2 > \\ \dots & \dots & \dots & \dots \\ < Lf_1, w_N > & < Lf_2, w_N > & \dots & < Lf_N, w_N > \end{bmatrix} \begin{bmatrix} \alpha_1 \\ \alpha_2 \\ \dots \\ \alpha_N \end{bmatrix} = \begin{bmatrix} < g, w_1 > \\ < g, w_2 > \\ \dots \\ < g, w_N > \end{bmatrix} \tag{47}$$

After finding Q_{l_j}, the pressure can be found for each segment by evaluating (32). The pressure at each segment i is of course influenced by the total effects of all j segments. When the observation point, $\overline{\rho}$, is on C and we have $\overline{\rho} = \overline{\rho}'$, the singularity in the integral is integrable. For example, consider the segment i as a flat segment, see Fig. (2).

Then,

$$P_d(\overline{\rho_i}) = \lim_{h \to 0} \int_{-l_i/2}^{l_i/2} \frac{Q_{li}}{2\pi} \ln\, |h - x|\, dx \;=\; \frac{Q_{li}}{2\pi} \int_{-l_i/2}^{l_i/2} \ln\, |x|\, dx \tag{48}$$

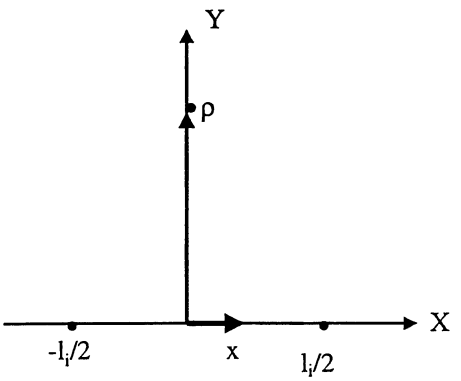

Figure 2: Illustration of segment i, with origin of coordinates at its center.

and

$$P_d(\overline{\rho_i}) = (\frac{Q_{li}}{2\pi}) \lim_{\varepsilon \to 0} \Big[\int_{-l_i/2}^{-\varepsilon} \ln |x|\, dx + \int_{\varepsilon}^{l_i/2} \ln |x|\, dx \Big] = (\frac{Q_{li}}{2\pi}) \left[l_i \left(\ln(l_i/2) - 1 \right) \right] \quad (49)$$

Therefore, the total perturbed pressure at segment i is

$$P_d(\overline{\rho_i}) = \frac{Q_{l_i}\, l_i}{2\pi} \left[\ln(l_i/2) - 1 \right] + \sum_{j=1\ j \neq i}^{N} \left(\int_{j^{th} segment} \frac{Q_{l_j}}{2\pi} \ln |\overline{\rho_i} - \overline{\rho_j}'|\, dl_j \right) \quad (50)$$

The matrix equation (47) is solved numerically by using the back-substitution technique. By substituting the solution in equation (50) the pressure in each segment can be calculated.

Accuracy of the numerical results

In order to examine the accuracy of the numerical solution, we compare it with an analytical solution. In two-dimensional systems, the pressure distribution on the surface of a circle or an ellipse can be found analytically, when they are located as a stationary solid object in an irrotational flow field, or they move with a uniform velocity in a stagnant fluid. Consider circle of radius a moving with velocity $\overline{U}$ perpendicular to its length, in an infinite mass of liquid which is at rest at infinity. By taking the x, y axes in the plane, with x in the direction of the velocity $\overline{U}$, Lamb [3] has found that the resulting pressure, ϕ, is

$$\phi = \frac{\overline{U} a^2}{r} \cos\theta \quad (51)$$

If we add a velocity $-\overline{U}$, the problem is equivalent to a fluid flowing with the far-field velocity $\overline{U}$ past a stationary circle. Adding to ϕ the terms $\overline{U} r \cos\theta$ we get

$$\phi = \overline{U}(r + \frac{a^2}{r}) \cos\theta \quad (52)$$

We are interested in finding the pressure distribution at the surface of the circle ($r = a$), which is

$$\phi = \overline{U} a \cos\theta \quad (53)$$

Note that pressure is not dimensionless in this equation.

A comparison between the numerical and the analytical solutions is shown in Fig.(3) for the circle discretized as shown in Fig.(4). The center of the circle is at the origin of the Cartesian coordinates and its radius is equal to one. For the numerical solution, the circle was divided into 50 equal segments.

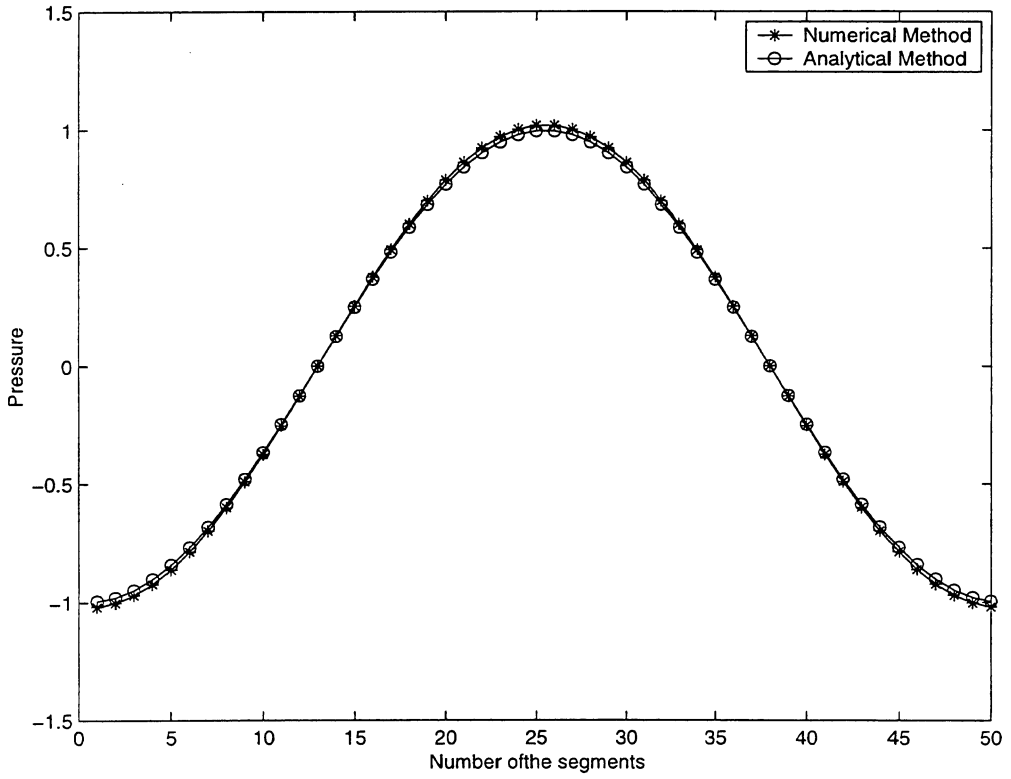

Figure 3: Comparison of the analytical solution of equation (53) and the numerical solution ($P = P_{Disturbed}$). The far-field velocity is 1.

We see an excellent agreement between the two results.

Another case for which a comparison is possible is with flow past an ellipse. Lamb has given the solution in terms of an Elliptical coordinate system. Elliptical coordinates ξ, η, are related to Cartesian coordinates by

$$x + iy = c\cosh(\xi + i\eta), \tag{54}$$

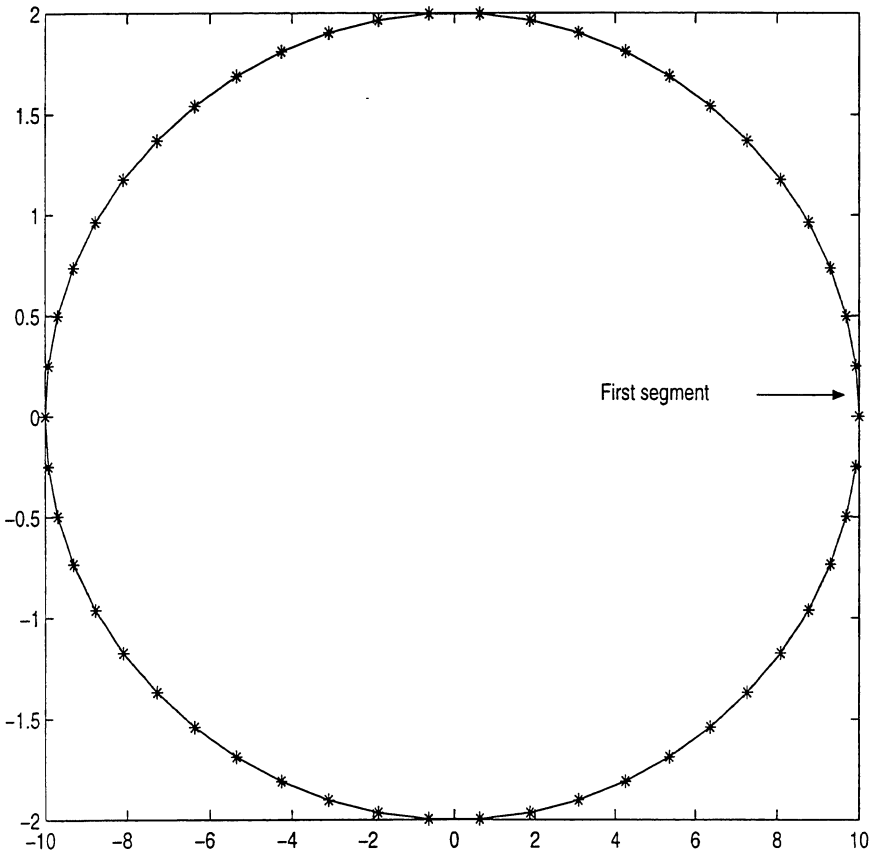

Figure 4: Numerical discretization of the unit circle. The segment numbering increases in the counter-clockwise direction.

$$\left.\begin{array}{r} \text{or } x = c\cosh\xi\cos\eta \\ y = c\sinh\xi\sin\eta \end{array}\right\} \tag{55}$$

where ξ ranges from 0 to ∞, and η from 0 to2π. The relation for the complex potential (streamfunction Ψ and pressure ϕ) is

$$\phi + i\Psi = Ce^{-(\xi+i\eta)} \tag{56}$$

where C is a real constant, equal to

$$C = \frac{Ubc}{a-b} = Ub(\frac{a+b}{a-b})^{\frac{1}{2}} \tag{57}$$

where a and b are the semi-axes of the ellipse. Thus,

$$\Psi = -Ce^{-\xi}\sin\eta \tag{58}$$

and

$$\phi = Ce^{-\xi}\cos\eta \tag{59}$$

In $x-y$ coordinates, we have

$$u = \frac{A+\sqrt{A^2-4B}}{2}$$

where

$$u = \cosh^2\xi, \quad A = x^2+y^2+1, \quad \text{and} \quad B = x^2$$

then:

$$\xi = Arc(\cosh(\sqrt{u})) \quad \text{and} \quad \cos\eta = \frac{x}{\sqrt{u}}$$

therefore

$$\phi = C\exp(-Arc(\cosh(\sqrt{u})))\,\frac{x}{\sqrt{u}} \tag{60}$$

We consider the example of an ellipse with $a = \sqrt{5}$ and $b = 1$ (Fig. (5)). The resulting numerical and analytical solutions are compared in Fig. (6).

We observe excellent comparison for this case as well.

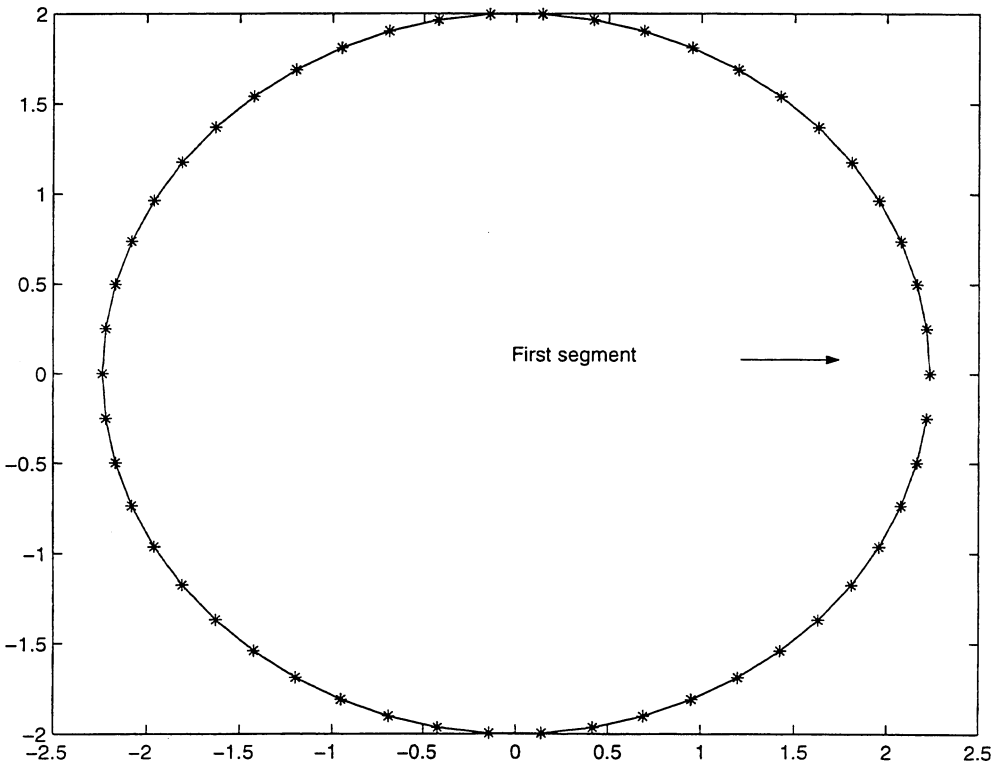

Figure 5: The numerical discretization of an ellipse with center at the origin with $a = \sqrt{5}$ and $b = 1$. The first segment is indicated. Segment numbering increases in the counterclockwise direction.

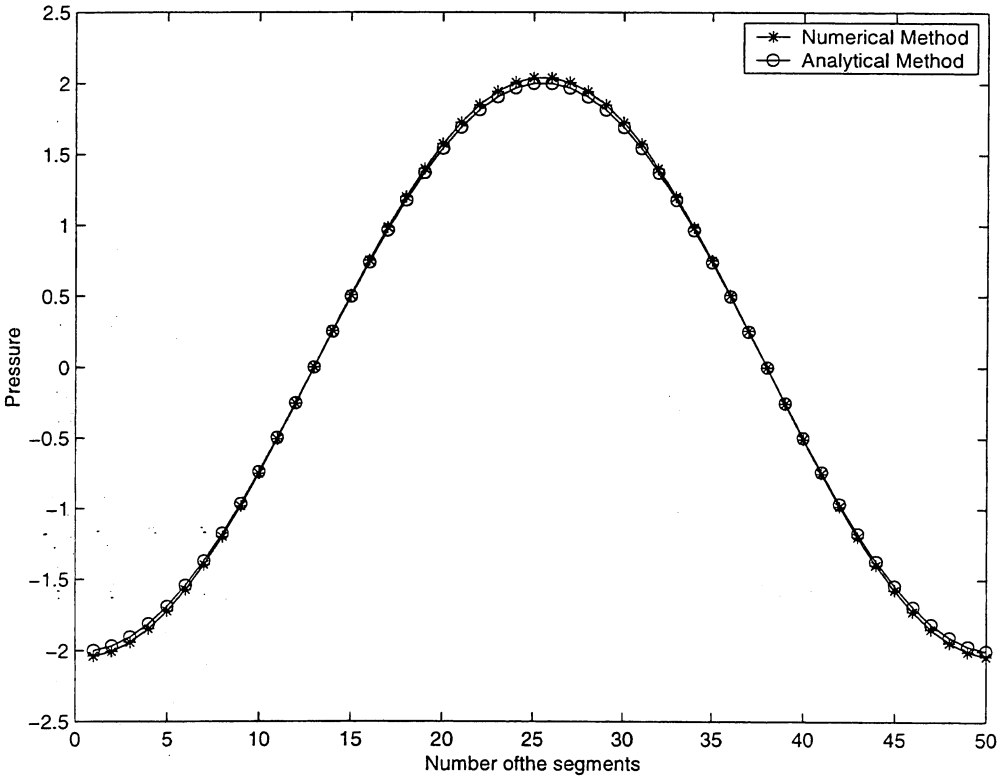

Figure 6: Comparison of analytical and numerical solutions for the ellipse of Fig. (5).

Method of Solution: 2. Finite system

In the previous part the solution described was for an infinite system, where we used the Green's function of the free space. In a real situation, the flow typically occurs in a finite domain (e.g. between two impermeable plates). Then, the above solution needs to be modified. For this reason, we consider a system constrained by two parallel boundaries with a no-flux boundary condition prescribed. One needs to find the Green's function for this new problem. We use the method of images [4]. This method is useful for symmetric domains. Here, the problem in a finite system with one source transforms into an infinite system with an infinite number of image sources and sinks. By superposing the potentials produced by each source/sink, we can find a potential that satisfies the specified no-flux boundary conditions.

Consider a porous medium with thickness d along the y-axis. The source point is located at (x_0, y_0). and we need to find the potential or the pressure at an arbitrary point (x, y). The complex potential, w, for an infinite array is

$$w = \Phi + i\Psi = \sum_{-\infty}^{\infty} \frac{1}{2\pi} \ln[(x - x_0) + i(y - (nd + (-1)^n y_0))] =$$
$$\sum_{n=0,\pm2,\pm4,\ldots}^{\infty} \frac{1}{2\pi} \ln[(x - x_0) + i(y - y_0 - nd)] + \sum_{n=\pm1,\pm3,\pm5,\ldots}^{\infty} \frac{1}{2\pi} \ln[(x - x_0) + i(y + y_0 - nd)] \tag{61}$$

For an infinite array of equidistant sinks, with distance d apart along the x-axis, Bear [4] shows that the complex potential is

$$w = m \sum_{-\infty}^{\infty} \ln[z - nd] = -m \ln \sin \frac{\pi z}{d} \tag{62}$$

where $z = x + iy$. Applying the above solution, one can then find the solution for the pressure Green's function

$$\Phi(x, y; x_0, y_0) = \frac{1}{4\pi} \ln \frac{1}{2}[\cosh \frac{\pi}{d}(x - x_0) - \cos \frac{\pi}{d}(y - y_0)] +$$
$$\frac{1}{4\pi} \ln \frac{1}{2}[\cosh \frac{\pi}{d}(x - x_0) - \cos \frac{\pi}{d}(y + y_0 - d)] \tag{63}$$

Eqn.(63) gives the potential at the observation point (x, y) caused by a source point at (x_0, y_0). Denote the observation point as $\overline{\rho}$ and the source point as $\overline{\rho}'$ and consider a distributed charge with density q on C, where C is the contour of all source points. By working as before, using superposition, the potential at the observation point is

$$\Phi(\overline{\rho}) = \int_C \frac{q(\overline{\rho}')}{4\pi}\{\ln\frac{1}{2}[\cosh\frac{\pi}{d}(x-x_0)-\cos\frac{\pi}{d}(y-y_0)]+\ln\frac{1}{2}[\cosh\frac{\pi}{d}(x-x_0)-\cos\frac{\pi}{d}(y+y_0-d)]\}dl_{\overline{\rho}'} \tag{64}$$

As in the infinite system case, the boundary condition at the interface is $\frac{\partial\Phi}{\partial\hat{n}} = \cos\theta$. In the present problem, this can be obtained by differentiating Eqn. (64). Note that $\hat{n}$ is the outward unit normal vector on the contour C. We find

$$\frac{\partial\Phi}{\partial\hat{n}}(\overline{\rho}) = \frac{1}{4d}\int_C q(\overline{\rho}')\{(\frac{\sinh\frac{\pi}{d}(x-x_0)}{\cosh\frac{\pi}{d}(x-x_0)-\cos\frac{\pi}{d}(y-y_0)} + \frac{\sinh\frac{\pi}{d}(x-x_0)}{\cosh\frac{\pi}{d}(x-x_0)-\cos\frac{\pi}{d}(y+y_0-d)})\hat{a}_x$$
$$+(\frac{\sin\frac{\pi}{d}(y-y_0)}{\cosh\frac{\pi}{d}(x-x_0)-\cos\frac{\pi}{d}(y-y_0)} + \frac{\sin\frac{\pi}{d}(y+y_0-d)}{\cosh\frac{\pi}{d}(x-x_0)-\cos\frac{\pi}{d}(y+y_0-d)})\hat{a}_y\}\cdot\hat{n}_{\overline{\rho}}dl_{\overline{\rho}'}$$
$$\forall\overline{\rho}\notin C \tag{65}$$

Eqn.(65) is valid for all observation points not on the C contour. Since our boundary condition is given on C, we need to evaluate this relation when $\overline{\rho}\to C$. Again, we divide the contour C into two complementary parts, C_s and C_o, and let C_s approach zero. In the limit when $\overline{\rho}$ approaches C, let point $\overline{\rho}$ be on C_s, then Eqn.(65) becomes

$$\frac{\partial\Phi}{\partial\hat{n}}(\overline{\rho}) = \frac{1}{4d}\int_{C_o}\cdots + \frac{1}{4d}\int_{C_s}\cdots \tag{66}$$

The first integral is well behaved as $\overline{\rho}\neq\overline{\rho}'$. The second must be evaluated as $\overline{\rho}\to\overline{\rho}'$. Working as previously we find that in the limit, the contribution is the same, namely

$$\frac{q(\overline{\rho}_c)}{2}$$

where $\overline{\rho}_c$ represents the center of the observation segment. Therefore we have

$$\lim_{\overline{\rho}\to C+}\frac{\partial\Phi}{\partial\hat{n}}(\overline{\rho}) = \frac{q(\overline{\rho}_c)}{2} + \frac{1}{4d}\int_C q(\overline{\rho}')\{(\frac{\sinh\frac{\pi}{d}(x-x_0)}{\cosh\frac{\pi}{d}(x-x_0)-\cos\frac{\pi}{d}(y-y_0)}+$$
$$\frac{\sinh\frac{\pi}{d}(x-x_0)}{\cosh\frac{\pi}{d}(x-x_0)-\cos\frac{\pi}{d}(y+y_0-d)})\hat{a}_x + (\frac{\sin\frac{\pi}{d}(y-y_0)}{\cosh\frac{\pi}{d}(x-x_0)-\cos\frac{\pi}{d}(y-y_0)}+$$
$$\frac{\sin\frac{\pi}{d}(y+y_0-d)}{\cosh\frac{\pi}{d}(x-x_0)-\cos\frac{\pi}{d}(y+y_0-d)})\hat{a}_y\}\cdot\hat{n}_{\overline{\rho}}dl_{\overline{\rho}'} \tag{67}$$

From this point on, we can employ the Moment Method for solving the integral equation, as before, except that now L is given by Eqn.(67). The procedure is exactly like that for the infinite system. The only difference is in the calculation of the potential, which is computed from Eqn.(64). We note that when $\overline{\rho} = \overline{\rho}'$, the first part of (64) has an integrable singularity. To evaluate this contribution at $\overline{\rho_i^c}$ (the center of segment i), we write for segment i

$$\int_{-li/2}^{li/2} \frac{q(\overline{\rho}_i)}{4\pi} \ln \frac{1}{2}[\cosh \frac{\pi}{2}(x_i - x_j) - \cos \frac{\pi}{2}(y_i - y_j)] dl_{\overline{\rho}_j'} \tag{68}$$

Integral (68) can be rewritten in two parts as

$$\lim_{\varepsilon \to 0}\{\int_{-li/2}^{-\varepsilon} \ldots + \int_{\varepsilon}^{li/2} \ldots\} = \frac{q(\overline{\rho}_i)}{2\pi}[(\frac{li}{2}) \ln \frac{\pi^2}{4d^2} + li(\ln|\frac{li}{2}| - 1)] \tag{69}$$

Therefore the potential can be computed as follows

$$\begin{aligned}
&\Phi(\overline{\rho}_i) = \frac{q(\overline{\rho}_i)}{2\pi}[(\frac{li}{2}) \ln \frac{\pi^2}{4d^2} + li(\ln|\frac{li}{2}| - 1)] + \\
&\int_{i^{th}segment} \frac{q(\overline{\rho}_i)}{4\pi} \ln \frac{1}{2}[\cosh \frac{\pi}{d}(x_i - x_j) - \cos \frac{\pi}{d}(y_i + y_j - d)] dl_{\overline{\rho}_i'} + \\
&\sum_{j=1, i \neq j}^{N} \int_{j^{th}segment} \frac{q(\overline{\rho}_j)}{4\pi} \{\ln \frac{1}{2}[\cosh \frac{\pi}{d}(x_i - x_j) - \cos \frac{\pi}{d}(y_i - y_j)] + \\
&\ln \frac{1}{2}[\cosh \frac{\pi}{d}(x_i - x_j) - \cos \frac{\pi}{d}(y_i + y_j - d)]\} dl_{\overline{\rho}_j'}
\end{aligned} \tag{70}$$

III.Results

The boundary integral method enables us to study the effects of the presence of disconnected ganglia in a porous medium. The presence of the ganglia perturbs the fluid flow. This perturbation is a function of the shape and size of the ganglia and their configuration. Consider, first, a square shape ganglion, located in the middle of a porous domain limited by two boundaries at the top and the bottom, see Fig. (7). The pressure profile on the surface of the ganglion was calculated both for an infinite system as well as for a finite system when the two boundaries are located at $y = -2$ and $y = 2$ ($d = 4$). The resulting pressure profiles are shown in Fig.(8). The pressure drop for the finite system is clearly higher than for the infinite system, as expected. This difference decreases as the width of the system increases.

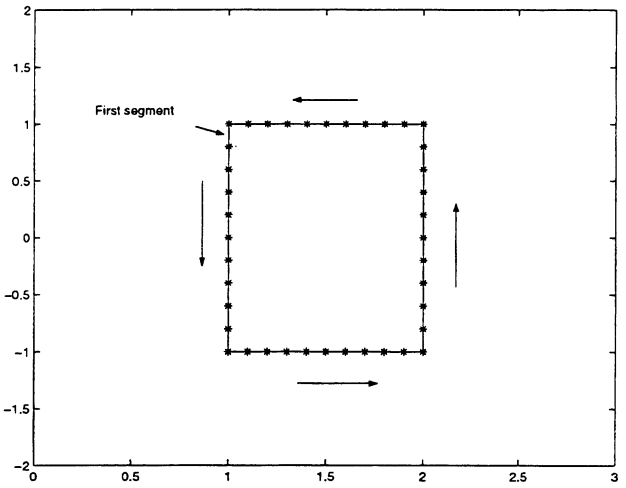

Figure 7: A square-shaped ganglion in the middle of a finite domain with thickness $d = 4$.

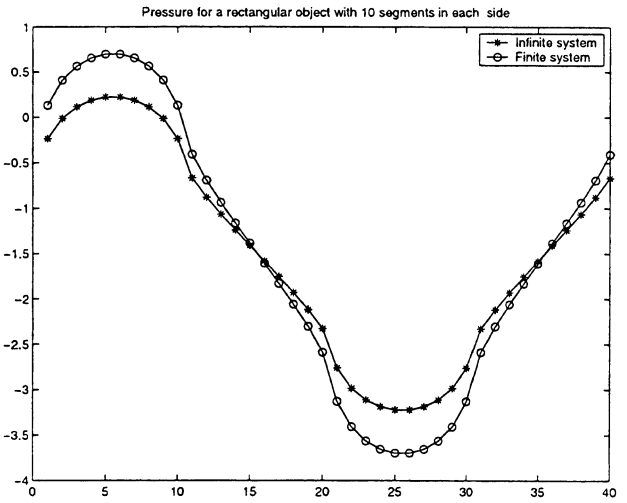

Figure 8: Comparison between the pressures at the interface of the square ganglion for the two cases of a finite and an infinite system ($d = 4$).

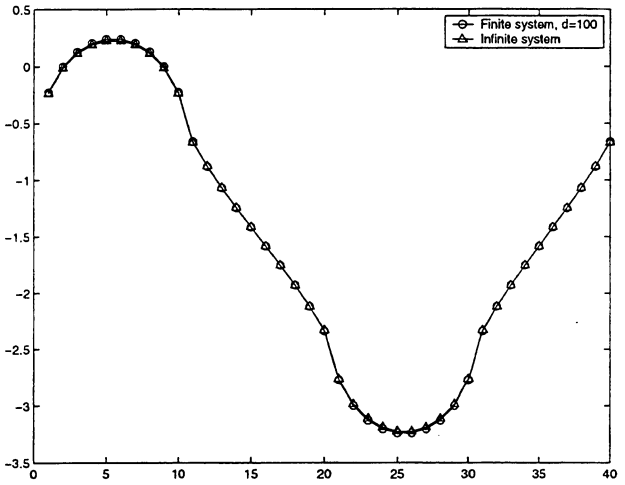

Figure 9: Comparison between the pressures at the interface of the square ganglion for the two cases of a finite and an infinite system ($d = 100$).

Fig(9) shows the corresponding results when the distance between two boundaries is $d = 100$. Clearly the pressure profiles for two systems are almost the same.

To see the effect of the presence of more than one ganglia, consider the geometry described in Fig.(10). The corresponding pressure profiles are calculated for each situation as shown in Fig.(11). As the number density of ganglia increases, the pressure drop across the initial ganglion is also increasing. This crowding effect will affect the mobilization and movement of the respective ganglia. Similar effects apply to the other ganglia in the system.

The effect is less when the pressure is computed using the solution for an infinite system (Fig. (12)). Although the overall behaviour is the same, the differences between the four cases are not as pronounced as for the finite system (please note the difference in scales as well).

As mentioned previously, a stranded ganglion can become mobilized, if the applied pressure difference is sufficient to overcome the capillary forces. Using the above approach, the mobilization and subsequent movement of each ganglion can determined as a function of various factors, including the capillary number, the size and the distribution of ganglia and so on. For each ganglion, a critical capillary number can be identified, above which the gan-

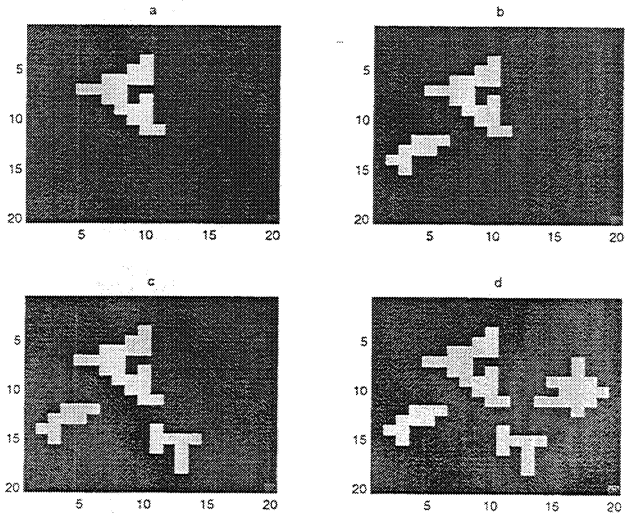

Figure 10: Four different configurations involving an increasing number of disordered ganglia.

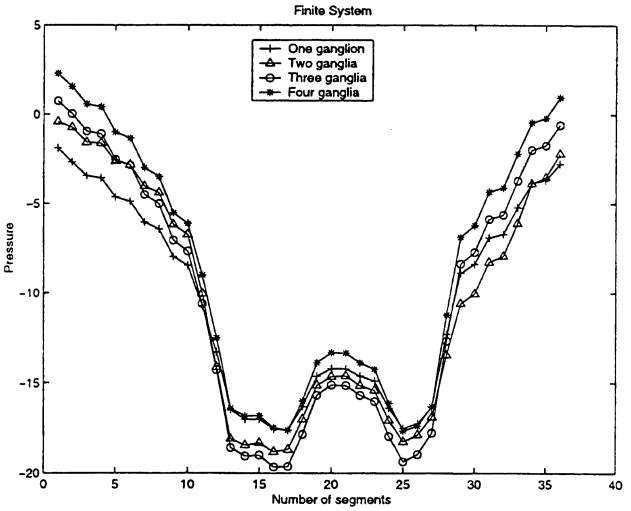

Figure 11: The pressure profile on the ganglion shown at the top left of Fig. (10) as a function of the addition of other ganglia. Computation for a finite system.

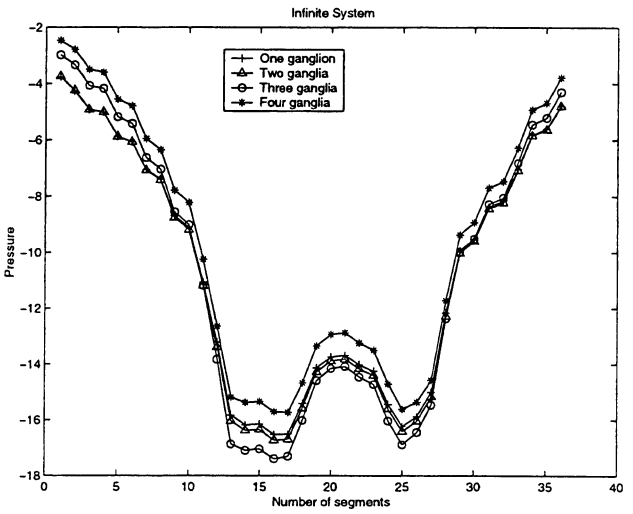

Figure 12: The pressure profile on the ganglion shown at the top left of Fig. (10) as a function of the addition of other ganglia. Computation for an infinite system.

glion can be mobilized. The critical capillary number decreases as the population of ganglia increases. The moving ganglion may be stranded again, or split in two or more daughter ganglia, some of which may then be stranded. It is also possible for a moving ganglion to coalesce with other ganglia. How this occurs will be reported in a subsequent report.

IV. Conclusions

In this report, we introduced Darcian Dynamics, a method to simulate the effect and the interaction between trapped phases inside a moving phase in a porous medium. This method enables us to understand the interactions between two phases inside a porous medium when one phase is disconnected. It is therefore, useful for the modeling of co-current and counter-current flows, where such effects can be present. Work on the mobilization of ganglia, and extensions to vapor-liquid flows will be reported in the future.

References

[1] J.F. Brady and G. Bossis, "Stokesian Dynamics", Ann. Rev. Fluid Mech. **20**, 111-157 (1988).

[2] R.F. Harrington, *Field Computation by Moment Method*, Robert E. Krieger Publishing, Malabar, Florida (1968).

[3] Sir H. Lamb, *Hydrodynamics*, Dover, New York (1945).

[4] J. Bear, *Dynamics of fluids in porous media*, American Elsevier, New York (1972).

[5] M.M. Dias and A.C. Payatakes, "Network models for two-phase flowin porous media. Part 1. Immiscible microdisplacement of non-wetting fluids.", J. Fluid Mech. **164**, 305-336 (1986).

[6] M.M. Dias and A.C. Payatakes, "Network models for two-phase flow in porous media. Part 2. Motion of oil ganglia.", J. Fluid Mech.**164**, 337-358 (1986).

[7] G.N. Constantinides and A.C. Payatakes, "Network simulation of steady-state two-phase flowin consolidated porous media.", AIChE Journal. **42**, 369-382 (1996).

[8] C. Pozrikidis, *Boundary integral and singularity methods for linearized viscous flow*, Cambridge (1992).

[9] I. Stakgold, *Green's functions and boundary value problems* John Wiley & Sons (1979).

III. DYNAMICS OF IN-SITU COMBUSTION AT VARIOUS SCALES

A well-established method for the recovery of heavy oils is in-situ combustion. Despite its long history, however, many aspects of the process are not well understood. Two particular aspects are analyzed in this project: The description of the process at the pore-network scale, and its upscaling at the large scale for field applications. A detailed pore-network simulator is described in the first study. It is the first of its kind, as far as we know. The simulator accounts for all relevant phenomena at the microscale, including mass transfer by convection and diffusion, viscous flow, heat transfer in the porespace and the solid matrix and chemical reactions. It predicts small-scale patterns, including particularly the structure of the combustion zone and associated instabilities. The simulator can be used to understand the combustion process from first principles and to delineate ignition, extinction and sustained propagation phenomena. In the second study, we continue our previous work and apply an asymptotic approach to describe the movement of combustion fronts in porous media as gas-dynamic discontinuities. This approach is essential for the upscaling of the process at the field scale and for the assessment of the effect of macrcoscale heterogeneity on issues such as sustained front propagation, extinction, efficiency, etc. The novel aspect of the present effort is the incorporation of the effect of heat losses in non-adiabatic combustion processes.

A PORE-NETWORK MODEL OF IN-SITU COMBUSTION IN POROUS MEDIA

Chuan Lu and Yanis C. Yortsos
Department of Chemical Engineering
University of Southern California
Los Angeles, CA 90089-1211

May 2001

INTRODUCTION

In-situ combustion (ISC) is a well-known process for the recovery of heavy oil from oil reservoirs. Extensive reviews of the method and its field applications have been provided in the literature (Prats, 1982). Even though one of the oldest techniques for heavy oil recovery, however, ISC is also one of the most complex. In addition to the common mechanisms it shares with conventional recovery methods, such as waterflooding and steamflooding, ISC involves the additional complexity of the oxidation reactions. These serve to, first, form the fuel in a regime of Low Temperature Oxidation (LTO) and, subsequently, provide the main combustion reaction under conditions of High Temperature Oxidation (HTO). The main goal of ISC is the sustained propagation of combustion fronts, to supply the necessary heat for viscosity reduction and the self-sustaining of the overall process. As a result, issues of front stability, sustained front propagation and possible extinction are of fundamental importance.

A large number of studies have been published in the literature on ISC, addressing a wide range of issues, from the detailed kinetics of the reaction processes to mathematical models to field applications. Of specific interest to this study is the modeling of the combustion process. Typically, this is done using conventional continuum models, in which reaction rates, concentrations and temperatures are volume-averaged continuum variables. The solution of such models is then sought in the various applications of interest, including laboratory and field scales. This approach has validity as long as the following conditions hold: that the variables of interest, such as concentrations, temperature and reaction rates, do not involve large gradients in space at the underlying microscale, for volume-averaged quantities to be meaningful; and that the effective parameters used in the continuum models reflect fairly accurately the actual processes. Because of the strong non-linearities involved

in reaction kinetics, particularly of the Arrhenius dependence of the true reaction rate on temperature,

$$r \propto C \exp(-\frac{E}{RT})$$

the volume average of the rate will not have the same dependence, namely

$$< r > \neq < C > \exp(-\frac{E}{R < T >})$$

if the local concentration or temperature vary significantly over the averaging volume.

Large gradients at the microscale may occur for a number of reasons. The development of sharp propagating fronts is one of them. In displacement processes, fronts arise naturally, due to the different characteristic velocities of the initial and the injected states (a classical example of which is the shock front in a Buckley-Leverett type displacement). The thickness of such fronts is controlled by dissipation, like diffusion, capillarity and conduction. For the case of ISC, however, sharp fronts also result from the fast kinetics of the combustion reactions in the HTO region and the depletion of some of the various chemicals that participate in the reaction. The resulting reaction zones are thin, and give rise to large gradients within the microstructure. The possible development of spatial instabilities is another important cause of large gradients.

The second concern is, in general, the effect on the overall process of small-scale heterogeneities of fluid flow, mass and heat transfer, and chemical reactivity. Local heterogeneities arise due to the randomness of the microstructure, and may result in a distribution of the local variables that can affect the volume-averaged rates as noted above. In addition, of importance to sustained propagation and extinction is the spatial distribution of the fuel in the pores of the microstructure. If the fuel is sparsely distributed, the sustained spreading of combustion across the pore network requires certain conditions on the rates of reaction, heat and mass transfer. Otherwise, the process will become extinct. For problems in which sustained propagation or extinction are critical issues, having an accurate assessment of the phenomena at the microscale becomes then an important objective. This is possible

with the development of a pore-network model of ISC, which forms the objective of this study.

As is well known, there are several distinct regions during an ISC process (Prats, 1982, Boberg, 1988). From the injection well, they are the swept region, the combustion/cracking zone, the vaporization and LTO zone, the steam zone, the hot water bank, the oil bank and the initial zone (see schematic of Figure 1). For simplicity and by necessity, in this chapter we will focus on the HTO regime and ignore the other downstream regimes. Thus, the problem to be modeled is the combustion of a solid fuel, deposited in the porespace, by the injection of a gas-phase oxidant. In a sense, the problem under consideration is similar to what is known as Filtration Combustion (FC) (Aldushin, 1993). The latter finds a variety of applications and has been analyzed in considerable detail in recent years, using continuum models. Some of these results will be reviewed below.

Pore-network models have been successfully used to model a variety of problems in porous media in the absence of reaction, from immiscible displacements to boiling (Lenormand et al., 1988, Blunt et al., 1991, Li and Yortsos, 1995, Satik and Yortsos, 1996). This has allowed for an accurate representation of effective parameters and for a better incorporation of small-scale mechanisms in continuum models. In processes involving reactions, applications of pore networks have been mainly in the areas of heterogeneous reactions on catalysts, catalysts deactivation, acidization, dissolution of trapped pollutants, etc. [8-11]. Discrete models for FC, and more specifically for ISC processes, have not appeared in the literature to our knowledge (see also below). This report attempts to fill this gap. The approach to be implemented is analogous to an earlier effort to model thermal processes at the pore-network scale, for example in heat-transfer driven bubble growth. The important difference is that here the exothermic combustion reaction at the pore surface must also be included.

Before proceeding, we need to mention that similarities exist between ISC and the process of self-propagating high temperature synthesis (SHS) for the development of new materials (Hwang et al., 1997, 1998). The difference is that in the latter process, the reaction rate

depends only on temperature and not on gas-phase concentrations. Experimental investigations have provided much information concerning SHS processes. An understanding of the microscopic processes is crucial to predicting the microstructure and properties of the final product. A numerical model akin to a pore-network model was developed by Hwang et al. (1998), based on which they were able to simulate effects of heterogeneity on the conversion patterns, as a function of various parameters.

The model to be developed here is considerably more complex than that of Hwang et al. (1998). In addition to heat transfer, it accounts for the convection and diffusion of the injected oxidant, its chemical reaction with the fuel and the possible enhancement of permeability as a result of the HTO. Effects of heterogeneity in permeability, fuel distribution, and other variables are also included. The report is organized as follows: First, we describe the aspects of the pore-network model. Before we provide numerical simulation results, we also review some findings from continuum analyses of FC, in order to verify the validity of the model in special cases. Then, we provide numerical simulation results to examine the sensitivity of the system to various parameters. Finally, we discuss their implication regarding continuum models.

PORE-NETWORK MODEL AND NUMERICAL METHOD

In this section, we describe the pore-network model and the numerical method used for its solution. Findings from the continuum model of FC are also discussed.

Model Description

The pore-network model consists of a dual network of pores and throats, which is embedded in a network of solid sites, representing the solid matrix (Figure 2). The pores (sites) are the places where reaction occurs and contain solid fuel of constant composition. They are interconnected via throats (bonds), which control transport of mass, momentum and heat, and which have distributed sizes. The network of solid sites is needed to account for heat transfer in the solid (e.g. see Satik and Yortsos, 1996). The coupling of solid and pore-space occurs through the heat transfer between pores and solid sites as shown in Figure 2.

In the 2-D simulations to be reported below, both networks are square lattices, of an adjustable length and width. The features on mass and heat transport include the following:

1. In 2-D, each solid site communicates with 4 solid sites (shown in Figure 2a by the thin solid line between solid sites) and 1 pore site (the dash line between solid and pore sites), through heat conduction. A heat transfer coefficient is used to model the pore-solid exchange.
2. Injection of a mixture of oxidant and inert gas occurs at one end, where pressure, temperature and composition are specified. The outlet end is at a constant pressure to maintain the injection rate. Flow in the pore throats is governed by Poiseuille's law. The oxidant in the gas phase is delivered by gas-phase diffusion and convection.
3. The following heterogeneous reaction is assumed,

$$\text{Solid Fuel} + \mu \text{ Gas Oxidant} \rightarrow \mu_1 \text{ Solid product} + \mu_2 \text{ Gas Product} \qquad (1)$$

where μ, μ_1, and μ_2 are the stoichiometric coefficients. Implicit in the above is the assumption that the reaction is heterogeneous and does not involve the propagation of flame in the pore network. The reaction rate is expressed by the one-step kinetic model

$$R = k_r A_r P X_O H(V_f) \exp(-\frac{E_a}{RT}) \qquad (2)$$

where H is the step function, V_f is the volume of fuel, P is the total pressure, k_r is the kinetic constant, A_r is the interface area in an individual pore site, X_o the mass fraction of the oxidant and E_a the activation energy. More complex kinetics, including multi-step, parallel or serial schemes, could also be adopted.

4. Within a pore site, thermodynamic equilibrium is assumed, such that concentrations, pressure and temperature are uniform. This also implies that fuel and gas are at thermal equilibrium. However, heat transfer does take place between adjacent pore sites, between pore and solid sites and between adjacent solid sites. Though this configuration and our code allow for different thermodynamic and transport

parameters, they are taken constant to avoid extra complexity. Variables assigned to sites and bonds are listed in Table 1.

Governing Equations

The governing equations for FC have been developed for some time now. Due to the multi-phase nature of the process, they must be able to account separately for the properties of the different phases and to also describe their interaction mechanisms. Ohlemiller (1986) provided a formalism that includes single particle/bulk condensed phase equations, to describe the behavior of the solid phase temperature and mass balance, and bulk gas equations, to determine the temperature, concentration, pressure and velocity profiles in the gas phase. Currently, most models of the FC processes adapt the bulk equations for both gas and condensed phases along with considerable other simplifications [15, 16].

Using appropriate mass and energy balances, we can write conservation equations for each site in the pore network, as follows:

Pore Site I, Adjacent to Pore-Site j:

Gas Phase Component k Mass Balance

$$\frac{\Delta(\frac{P_i V_i}{RT_i} y_{i,k} M_k)}{\Delta t} = -\sum_j u_{ij} r_{ij}^2 \frac{P_i y_{i,k}}{RT_i} M_k - \frac{D_e}{lR} \sum_j r_{ij}^2 (\frac{P_i + P_j}{2})(\frac{2}{T_i + T_j})(y_{i,k} - y_{j,k}) + \mu_k (k_r A_i^r \frac{P_i y_{i,O_2}}{RT_i} \exp(-\frac{E_a}{RT_i})) H(V_{i,f}) \quad (3)$$

Solid Fuel Conservation

$$\rho_f \frac{\Delta V_{i,f}}{\Delta t} = k_r A_i^r \frac{P_i y_{i,O_2}}{RT_i} \exp(-\frac{E_a}{RT_i}) H(V_{i,f}) \quad (4)$$

Energy Balance

$$\frac{\Delta E_i}{\Delta t} = -\sum_j u_{ij} r_{ij}^2 \frac{E_{g,i}}{V_i} - \frac{K_{gs}}{l} \sum_j r_{ij}^2 (T_i - T_j) - h_s \sum_S A_{is}^h (T_i - T_s) - h_{L,P} A_{i,l}^h (T_i - T_0) \quad (5)$$

where, we defined the energy content of a site by

$$E_i = E_{f,i} + E_{g,i}$$

$$E_{f,i} = m_{f,i}(C_{p,f}T_i + \Delta_c H_f);\ E_{g,i} = \sum_k \frac{P_i V_i}{RT_i} M_k y_{i,k}(C_{pg,k}T_i + \Delta_c H_f) \tag{6}$$

Momentum Balance

$$u_{ij} = \frac{r_{ij}^4}{8\mu l}(P_i - P_j) \tag{7}$$

Solid Site Energy Balance

$$\rho V C_{ps} \frac{\Delta T}{\Delta t} = -\frac{k_s^h}{l}\sum_{s'} A_{ss'}^h (T_s - T_{s'}) + h_s \sum_j A_{js}^h (T_j - T_s) - h_{L,S} A_{s,l}^h (T_s - T_0) \tag{8}$$

The sum in the energy balances express the heat exchange between pore and solid sites, while $h_{L,S}$ denotes heat loss to the surroundings. In addition, ideal gas behavior was assumed. Finally, the bond radius was correlated to the depth of conversion.

To make the equations dimensionless we introduce the characteristic values listed in Table 2. The corresponding dimensionless groups obtained are shown in Table 3.Together with other parameters, such as the initial temperature, the volume ratio of solid site to the pore site, the average initial fuel amount in pore sites and the oxidant concentration at injection, the dimensionless parameters constitute the main set of variables affecting the process.

Remarks

The above model allows for simulating both forward and reverse combustion. These are differentiated by controlling the ignition point, which is the first row in the inlet for the case of forward combustion, and the row before the last in the outlet, for the reverse case (Figure 3). Our emphasis in this work is on forward combustion, although some brief comments on reverse combustion will also be made, where appropriate.

- Although the relation between flow rate and pressure difference depends on the Reynolds number, we will only assume laminar, Poiseuille flow. At the continuum level, this is equivalent to Darcy's law, an assumption which is very often made in the literature.

- Though radiation may play an important role because of the high temperature at the fronts, most analytical solutions and numerical simulations omit its effect. It was neglected in our model as well.

- As mentioned above, the kinetics of ISC are rather complicated. They can be accompanied by pyrolysis, evaporation and condensation, multi-step reactions and also by some gas-phase reactions [3, 17, 18, 19]. However, in contrast to the well-developed flame kinetics, a detailed reaction mechanism for heterogeneous systems is still not widely used. Instead, one-step kinetics, as assumed above, is commonly accepted for the combustion of solid fuels.

- Finally, in our model, the heat released by the reactions is expressed in an implicit form. This differs from most previous works. The advantage of this formalism lies in the fact that one can ignore the detailed kinetics and the associated physical processes. The shortcomings are that it cannot describe processes at very high flow rates, which can break the thermal equilibrium between the gas phase and the fuel sites.

Numerical Method

The dimensionless equations were solved by standard implicit schemes. Because of the stiffness of the problem, time steps were confined to less than 1s. However, because the spatial scale needs to be large enough, it takes quite a long time to obtain reasonably accurate results. In previous works in homogeneous problems and stability investigations, adaptive pseudo-spectral algorithms have been applied (Bayliss and Matkowsky, 1987). Since the pore-network model has many features in common with a discretization scheme, we can assign transport properties, either by making the scheme 2^{nd} order accurate or of an upwind character. In our calculations, it was found that numerical dispersion affects the results only when the injection rate is sufficiently high (Pe >O(1)). For such cases, special methods were adopted. An implicit predictor-corrector method was employed for the temporal evolution. This method is 2^{nd} order accurate in most cases.

In order to speed up the computations, further simplifications were necessary. To this effect, we introduced the following assumptions:

1. Constant pressure

   Since the gas viscosity is small, the pressure perturbation can be ignored in all governing equations, except in Poiseuille's law (Equation (7)). This assumption is based on the condition that the flow rate is significantly smaller than the speed of sound, and is widely used in the simulations of laminar flames in open space. The computational advantages are that the momentum equation becomes decoupled, while the continuity equation is linearized.

2. Quasi-steady state in the gas phase

   Because of the difference between the densities of gas and solid, the corresponding time scales are greatly different. Using dimensional analysis, Ohlemiller (1985) and Aldushin and Matkowsky (1998) pointed out that the transient gas terms can be neglected; then, the bulk gas as well as the gas within the condensed phase can be treated as quasi-steady.

Numerical simulation results showed that use of these assumptions dramatically decrease the computation time, without significant loss in accuracy in the pressure, temperature and concentration profiles.

In the general case, the equations are nonlinear and were solved by a Newton-Raphson method. A high-performance linear equations solver is needed. We have tried a traditional SOR method, a preprocessed conjugated gradient (PJCG) method and LSOR methods, which are effective for heterogeneous systems (where properties are different in different directions). The results show that at the beginning stage, the PJCG method converges faster. Then, the LSOR or the SOR methods have better performance. All of these three methods were used as appropriate. We must add that once a step diverges or the solid fuel depletes, the time step should be cut and integration must be repeated. This approach is similar to the PICO technique [22]. Instead of setting a constraint on the number of iteration times, however, we reduce the time step if convergence cannot be reached after 5 iterations in order to maintain accuracy. Although modified several times, and its performance sped up by more than 20 times, the computational scheme is still time consuming. For 2-D cases, its accuracy and speed are acceptable. More effort on the optimization of the code is still needed, however, before it can be employed in 3-D simulations.

RESULTS AND DISCUSSION

In this section we present results from the numerical simulations. First, we test the validity of the model in some simple cases.

1-D Simulations

To test the validity of the pore-network model we first conducted 1-D simulations of forward combustion and compared the results with the analysis of Aldushin et al. (1999). These author showed that the dimensionless parameter $\delta = \frac{c_g \mu \rho_{f0}}{C_s a_0}$ determines the condition for the existence of three different structures, a reaction-leading pattern ($\delta>1$), where the reaction front leads the thermal front, a reaction-trailing pattern ($\delta<1$), where the reaction front trails the thermal front, and a wave with maximum energy accumulation ($\delta=1$), in which the two fronts coincide and the temperature at the front increases with time, according to the equation $T_b - T_0 = Q_A a_0 \sqrt{\frac{G_0 l}{\pi \lambda c_g}}$. Our numerical results plotted in the left panel of Figure 4 are in good agreement with the theoretical predictions. In the first two cases, it is apparent that a traveling wave solution is rapidly reached, which propagates at a constant velocity. This velocity and the extent of the separation between fronts depend on a number of parameters, such as injection rate, heat conductivity, capacity, etc. Our model allows also to investigate the sensitivity of the results to heat losses. The right panel of Figure 4 shows the temperature profiles corresponding to the three cases, but with heat losses included. Although parameter δ appears to still remain the determining factor in the classification of patterns, the heat loss affects both the propagation velocity and the temperature patterns.

2-D Simulations: 1. Base case

We subsequently report on 2-D results using the base-case parameters listed in Table 4. We note that the porous medium has relatively large particles (the distance between pore sites is of the order of 0.5 mm), the fuel is uniformly partitioned in the pore sites, heat losses occur

from the pore network to the surroundings at a rate which is 5% of the heat transfer rate between the gas and the solid, while the Peclet number for mass transfer is 0.05, for the relatively low injection rate used in the base case. The main local heterogeneity in the base state was on the pore throats, the size of which was randomly distributed. In addition, for the particular stoichiometry used, no net production or loss of moles in the gas phase can occur, namely the volumetric flux of the gas phase remains constant. The base case does not include a change of the pore throat size due to the fuel depletion. These have implications on the front stability, as will be discussed below.

For the values of the base state ($\delta<1$), the pattern is reaction-leading. Typically, the basic structure consists of a leading reaction zone, where most of the combustion reaction occurs, the oxidant and the fuel are depleted fast, and the temperature rises sharply. This combustion front rapidly reaches a steady-state and propagates at constant velocity. Figure 5 shows typical simulation results for the fuel conversion depth, the temperature, the pressure (with respect to the pressure at the outlet end, and multiplied by a factor for illustration purposes) and the oxidant concentration. The extent of the reaction zone is estimated to be of the order of 1.5 mm, which in this case is equivalent to 3 pore lengths. This is consistent with estimates obtained from continuum calculations (Akkutlu and Yortsos, 2000). The profiles have some roughness, departing from strictly piston-like displacement, and temperature and concentrations (particularly the former) exhibit fluctuations. Averaging these fluctuations for use in continuum models would be an important consideration, as noted in the Introduction. However, there is no indication of fingering or instability in this base case. The pressure profiles indicate that the pressure varies significantly near the combustion region, as a result of its high temperature. In addition, there is almost complete consumption of the injected oxidant at the front, thus there is no oxidant leakage across the front.

2-D Simulations: 2. Sensitivity Study

Using the base-case parameters, we next proceeded to a sensitivity study in order to assess the following effects: The possibility of extinction, instead of sustained propagation, the development of instabilities at the pore-network scale, the effect of spatially correlated pore-space and the effect of the distribution of the fuel in the pore network.

a. Extinction

The sustained front propagation was influenced mainly by the following factors: ignition, the oxidant concentration, the amount of heat losses and the fuel density. In all simulations, ignition was found necessary for the onset of the combustion reaction. For this, the temperature of the inlet row was raised to a sufficiently high value, while that of the adjacent row was also slightly raised (thus mimicking an initially sharp exponential profile) (see also Figure 3). Ignition was also found necessary for reverse combustion. In its absence or when the ignition temperature was low, the front quickly became extinct.

Extinction was also promoted by increased heat losses and decreased concentrations of the injected oxidant. For otherwise constant values of the base-case parameters, we found that extinction occurred if heat losses were increased to about 50% or higher of the rate of heat transfer between the porespace and the solid sites. For a more accurate determination of the threshold additional simulations are needed, however the onset of extinction as the rate of heat losses increases is consistent with continuum model predictions (Akkutlu and Yortsos, 2001). These also suggest that for otherwise constant values, extinction can be circumvented by an increase in the injection rate. The effect of the injection rate is currently being studied. In addition, it was found that sustained front propagation is not possible if the mole fraction of the oxidant at the inlet is reduced to 28%. Again, this value is only indicative of a lower boundrather than a true threshold. It does indicate, however, that injection of a sufficiently rich mixture is required to sustain combustion. A detailed analysis is still in progress.

Before proceeding we show simulation results for the dependence of the front velocity on the injection rate for the base-case but in the absence of heat losses. As shown in Figure 6, the front velocity varies linearly with the injection rate and it is about two orders of magnitude smaller. The dependence in this region can be explained by simple mass balance arguments, given that both oxidant and fuel are completely consumed at the front. We note that in these simulations there is front propagation, even at very small injection rates, reflecting the fact that in this region combustion is promoted by diffusion only. However, it is unlikely that

such a front will propagate further in an extended porous medium. We must also note that if the injection rate increases beyond the range shown in Figure 6, the front slows down.

b. Instabilities

From continuum analyses it is known that forward combustion fronts become stabilized by heat conduction, diffusion, and the net reduction in the number of gas moles due to the combustion reaction. They become destabilized by the net increase in the number of gas moles (expansion) and by an increase in the permeability of the burned region. As mentioned, in this work we only considered the case in which the next expansion is zero, an assumption which greatly facilitates computations. As a result, in the base case the fronts are stable (Figure 5), reflecting the stabilizing influence of conduction and diffusion. To investigate the onset of viscous fingering instability we considered cases in which the pore throat radii of the burned region increase by a constant multiplier. We considered two cases in which the multiplier was 2 and 4, respectively. Given the use of Poiseuille's law, this translates into an effective increase of the permeability of the burned region by $2^4 = 16$, and $4^4 = 256$, respectively. Figure 7 shows the corresponding results for the second case. The effect of this rather substantial permeability contrast (which is analogous to a displacement with a mobility ratio of 256) is evident. The conversion depth acquires features of a viscous fingering pattern, the extent of reaction is non-uniform and the fluctuations of temperature and concentrations are substantial, despite the small size of the pore network. A distinct feature is that the corrugation of the front now gives rise to incomplete conversion in certain regions and a corresponding leakage of oxidant. This phenomenon was also observed when the pore structure was correlated (see below). Similar, but not as strong, effects were found in the case of the milder permeability contrast of 16.

The simulations in Figure 7 indicate that pore-network scale instabilities are possible provided that the permeability enhancement is sufficiently strong. While the level of such enhancement may be unrealistic, such instabilities will also develop when there is gas expansion at the front as a result of the combustion reaction. Our simulations cannot answer at present the question whether or not these instabilities at the pore-network scale will

ultimately lead to process extinction. For their suppression requires a decrease of the injection rate, to promote the stabilizing effects of conduction and diffusion. A study of this effect is currently in progress. Such a decrease must not be too strong, however, since it may lead to extinction as a result of heat losses, as discussed above.

In passing, we must note that strong instabilities do develop in the case of reverse combustion. Now, diffusion is destabilizing, and at sufficiently small injection rates the developed pattern is unstable. For the sake of completeness we show in Figure 8 the results from a typical simulation of reverse combustion. Patterns reminiscent of viscous fingering, including shielding, trapping and tip splitting are obtained. These patterns are accentuated as the injection rate decreases. An elaborate account of this problem will be presented elsewhere.

c. Correlated porespace

Sensitivity studies were subsequently conducted to investigate the effect of the pore-size distribution and its spatial correlation. First, we examined variations in the pore-size distribution.

Figure 9 shows results for the base case, but with the (uniform) pore-size distribution stretched so that the ratio of the end points increased from 3 (which is the base case) to 10. The simulations show that front roughness, reaction zone thickness and temperature and concentration fluctuations all increase. It is interesting to note, however, that there is no leakage of oxidant across the front. The effects shown in Figure 9 reflect the increased contrast in flow rates, hence in the convected flux of the gas oxidant, among the various pores. Subsequently, the effect of spatial correlations was investigated, by taking a pore-size distribution obeying fBm statistics (Du et al., 1996). These statistics reflect long-range correlations and, for the specific problem considered here, correspond to a correlation length equal to the network size. Corresponding results are shown in Figure 10 for a Hurst exponent H=0.7, which represents smooth fields with channel-like features. One effect of the correlated porespace is to increase the roughness of the front, as well as the fluctuations in

temperature and concentrations. This is expected, due to the features of the correlated noise. What is important, in the correlated case, however, is that the gas oxidant is not completely consumed at the front. Rather, many regions develop at the front where the oxidant leaks through, partly unreacted (Figure 10). The incomplete combustion is a rather striking effect of the spatial correlation and was observed also in other simulations. The fact that the underlying pore structure influences the pattern to be developed is shown in Figure 11, for the case of a "microfissure" in the porespace. In these simulations, one row in the pore-network has a uniform pore-size distribution the end points of which were four times larger than in the rest. The results of Figure 11 correspond to an injection rate 10 times larger than in the base case. With this rate, the process becomes convection-controlled and the patterns reflect clearly the underlying features of the pore-space. The process is similar to the displacement of one fluid by another in a fractured medium. Whether or not this pattern will persist for a long time, however, cannot be answered by the pore-scale simulations, and must be addressed by different means. We must note that by decreasing the injection rate, the "imprint" of the microstructure on the combustion pattern waned, as expected.

d. Distribution of fuel

The final effect studied in the sensitivity analyses was the distribution of fuel in the porespace. The issue that arises is the following. Assume that the fuel is randomly distributed in the sites of the pore-network, namely that there is a probability p that a site contains fuel. The question is whether there exists a critical value (a percolation threshold) p_c, above which sustained propagation is possible, but below which extinction occurs. It is clear that this value will depend on a number of parameters, an important one being the thermal conductivity of the solid. The role of the latter is not trivial: If conductivity is small, then the sustained propagation of combustion requires that fuel sites, which here act as a heat source, are sufficiently close, hence that p_c is large. In that region, we expect that as the thermal conductivity increases, then p_c will decrease. However, as the thermal conductivity is sufficiently large it is possible that the heat generated spreads out more than needed resulting in the extinction of the process, unless p_c increases. Results from simulations are shown in the graph of Figure 12. Consistent with the above, the curve of p_c vs. thermal conductivity is

non-monotonic. At low values of the thermal conductivity the percolation threshold is a decreasing function, then reaches a relatively flat plateau, and subsequently increases with further increase in thermal conductivity. It is interesting to note that in this process values larger than the typical percolation threshold of 0.59 for site percolation in a square lattice can be obtained. The results of such simulations suggest that the volume-averaged fraction of fuel per unit volume must exceed a critical value for the sustained propagation of a combustion front. This critical value reflects not only intrinsic thermodynamic and kinetic properties, but also the spatial arrangement of the fuel in the porespace.

CONCLUDING REMARKS

In this report we developed a pore-network model to simulate the High Temperature Oxidation region of in-situ combustion in porous media. The pore-network model is based on dual pore networks (pores and solid sites) and has the objective to incorporate the effect of microstructure on combustion processes in porous media. The model accounts for flow and transport of the gas phase in the porespace, where convection predominates, and for heat transfer by conduction in the solid phase. Gas phase flow in the pores and throats is assumed to be governed by viscous forces. Heterogeneous combustion with one-step finite kinetics was assumed. The validity of the model was tested against existing 1-D solutions. A variety of 2-D simulations were conducted to investigate the effects of parameters. In particular, we focused on the patterns of the extent of conversion, temperature, pressure and oxidant concentration.

In the absence of gas phase expansion at the front, the combustion fronts are found to be generally stable and of a finite degree of roughness. The latter increases with a more broad pore-size distribution and with spatially correlated pores. In the base case, both fuel and oxidant are fully consumed within a thin reaction zone, the thickness of which does not exceed a few pore lengths. When spatial correlations occur, however, the oxidant leaks through the front, along the correlated pathways. The development of sustained front propagation was studied as a function of various parameters, which included heat losses,

instabilities, and the distribution of fuel. Particular attention was paid to the latter, where it was found that the geometric distribution of the fuel in the pore sites is also a parameter that affects the extinction boundaries. The problem can be posed as an extended percolation like process from which percolation-like thresholds can be computed.

The implications of the study to the validity and the application of continuum models are many-fold. Even in the absence of 2-D effects, the pore-network study shows that the HTO zone is very thin and of the order of a few pore lengths, a fact that makes the application of continuum models questionable, given that the latter presume the absence of gradients over the volume of averaging (which is of the order of hundreds of pores). When 2-D and 3-D effects are included, fronts additionally show roughness, instabilities or non-uniform properties. Existing continuum models, based on a direct extrapolation of intrinsic kinetics to the continuum scale, do not account for many of these effects. Salvaging the continuum description can be obtained by incorporating the findings at the pore-network scale. One such method would be to derive effective kinetic parameters, such as rate constants and activation energies, by matching the steady-state predictions from continuum and pore-network models. Such a study is currently underway. The results for the effect of the spatial fuel distribution on the sustained propagation of combustion fronts should also be incorporated in continuum models, as the latter are intrinsically incapable for such an account.

REFERENCES

1. Prats, M., *Thermal Recovery*, SPE Monograph Series SPE of AIME (1982).
2. Boberg, T.C., *Thermal Methods of Oil Recovery,* An Exxon Monograph Series (1988).
3. Aldushin, A.P., *New results in the theory of filtration combustion*, COMBUSTION AND FLAME 94: 308-320 (1993).
4. Lenormand, R., Touboule, C. and Zarcone, C., *Numerical Models and Experiments on Immiscible Displacements in Porous Media,* J. FLUID MECH. 189: 165 (1988).
5. Blunt, M., and King, P., *Relative Permeabilities from Two- and Three-Dimensional Pore-Scale Network Modeling,* Transp. Porous Media 6, 407-433 (1991).
6. Li, X., and Yortsos, Y.C., *Visualization and Simulation of Bubble Growth in Pore Networks*, AIChEJ 41, 214 (1995).
7. Satik, C., and Yortsos, Y.C., *A Pore-Network Study of Bubble Growth in Porous Media Driven by Heat* Transfer, J. HEAT TRANSFER 118, 455-462 (1996).
8. Andrade, J.S., Street, D.A., Stanley, H.E., *Diffusion and Reaction in Percolating Pore Networks*, PHYS. REV. E 55, 772-777 (1997).
9. Rieckmann, C., and Keil, F.J., *Multicomponent diffusion and reaction in three-dimensional networks: general kinetics*, IND. ENGNG. CHEM. RES. 36, 3275 (1997).
10. El-Nafaty, U.A., and Mann, R., *Support-pore architecture optimization in FCC catalyst particles using designed pore networks*, CHEM. ENG. SCI. 54, 3475-3484 (1999).
11. Jia, C., Shing, K. and Yortsos, Y.C., *Visualization and Simulation of Non-Aqueous Phase Liquids Solubilization in Pore Networks*, J. CONTAM. HYDR., 35, 363 (1999).
12. Hwang, S., Mukasyan, A.S., Rogachev, A.V., and Varma, A., *Combustion wave microstructure in gas solid reaction systems: experiments and theory*, COMBUST. SCI. AND TECH. 123, 165 (1997).
13. Hwang, S., Mukasyan, A.S., and Varma, A., *Mechanisms of combustion wave propagation in heterogeneous reaction systems*, COMBUST. AND FLAME 115, 354-363 (1998).
14. Ohlemiller, T.J., *Modeling of smoldering combustion propagation,* PROG. ENERGY COMBST. SCI. 11, 277-310 (1985).

15. Henneke, M.R., and Ellzey, J.L., *Modeling of filtration combustion in a packed bed*, COMBUSTION AND FLAME 117, 832 (1999).
16. Goldfarb, I., Gol'dshtein, V., Kuzmenko, G., and Sazhin, S., *Thermal radiation effect on thermal explosion in gas containing fuel droplets* , COMBUSTION THEORY AND MODELLING 3, 769-787 (1999).
17. Summerfield, M., Ohlemiller, T.J., Sandusky, H.W., *A thermophysical mathematical model of steady-draw smoking and predictions of overall cigatte behavior*, COMBUSTION AND FLAME 33, 263-279 (1978).
18. Kisler, J.P., and Shallcross, D.C., *An improved model for the oxidation processes of light crude oil*, Trans IchemE 75A, 392-400 (1997).
19. Leach, S.V., Rein, S., Ellzey, J.L., Ezekoye, O.A., and Torero, J.L, *Kinetics and fuel property effects on forward smoldering*, COMBUSTION AND FLAME 120, 346-358 (2000).
20. Bayliss, A., and Matkowsky, B.J., *Fronts, relaxation oscillations, and period doubling in solid fuel combustion,* J. COMPUTATIONAL PHSICS 71, 147-168 (1987).
21. Aldushin, A.P., and Matkowsky, B.J., *Instabilities, fingering and the Saffman-Taylor problem in filtration combustion,* COMBUST. SCI. TECHN. 133, 293-341 (1998).
22. Issa, R.I., Gosman, A.D., and Ahmadi-Befrui, B., *Solution of the implicitly discretised reacting flow equations by operator splitting*, J.COMPUT. PHYS. 93, 388-410 (1991).
23. Aldushin, A.P., Rumanov, I.E., and Matkowsky, B.J., *Maximal energy accumulation in a superadiabatic filtration comnustion wave*, COMBUSTION AND FLAME 118, 17-90 (1999).
24. Akkutlu, I.Y., and Yortsos, Y.C., *The Dynamics of Combustion Fronts in Porous Media,* paper SPE 63225, presented at the 2000 SPE Fall Meeting, Dallas, Tx (Oct. 2000).
25. Akkutlu, I.Y., and Yortsos, Y.C., in preparation (2001).
26. Du, C., Satik, G., and Yortsos, Y.C., *Percolation in a Fractional Brownian Motion* Lattice, AICHEJ 42, 2392-2395 (1996).

Table 1. Variables Assigned to Sites and Bonds

Pore Site Properties	Solid Site Properties	Bond Properties
Void volume	Volume	Length*
Interface area for reaction	Heat transfer area between solid sites	Radius
Heat capacity of gas and fuel	Heat capacity of solid material	Pressure
Heat transfer area with solid site	Heat transfer area with pore site	Temperature
Pressure	Temperature	Gas phase velocity
Temperature		
Fuel amount		
Initial fuel amount		
Component concentration		

* Except for this term, all other variables can be spatially distributed.

Table 2. Characteristic Parameters

Variable	Characteristic Quantity	Approximate Value
Temperature (T^*)	$\Delta_r H/C_{p,f}$	5000~16000 K
Density	ρ_f	0.5~1.5*10^3 Kg/m3
Pressure	P_0	1.01325*10^5 Pa
Length	L(Bond Site Length)	5*10^{-4} m
Time	L^2/D_e	5*10^{-3} s
$K_0=K_r\exp(-Ea/RT^*)$		10~1.6*10^5
Activation energy	E_a	1,2~1.6*10^6 J/mol
Diffusion coefficient	D_e	5*10^{-5} m^2/s

Table 3. Dimensionless Groups

Dimensionless group	Definition	Approximate Value
Th (Thiele modules)	$(K_0 L D_e^{-1} M_k^*)^{1/2}$	1*10^4~1*10^9
Pe	$u_0 \, l De^{-1}$	1*10^{-3}~10
Le	$K_f \rho_f^{-1} Cp_f^{-1} De^{-1}$	0.001~.0.1
Nu	$h_s \, l \, k_s^{-1}$	0~10
$Nu_{S,L}$	$h_{L,S} \, l \, k_s^{-1}$	0~1
$Nu_{P,L}$	$h_{Lp} \, l \, k_s^{-1}$	0~1
RLSQ	$r^2 \, l^{-2}$	0.01~1
KKGS	$K_{g,f} \, k_s^{-1}$	.001

Table 4. Parameters of the base case (in SI units)

Pore Site Properties	Average Value	Solid Site Properties	Average Value	Bond Site Properties	Average Value
Void volume	L^3	Volume	1.5*L^3	Length	L=5*10^{-4} m
Interface area for reaction	r^2	Heat transfer area between solid sites	r^2	Radius	R =L/2
Heat capacity of fuel	840 J kg^{-1} K^{-1}	Heat capacity of solid material	840 J kg^{-1} K^{-1}	Gas phase diffusivity	5*10^{-5} m^{2}s^{-1}
Heat transfer area with solid site	r^2	Heat transfer area with pore site	r^2	Gas viscosity	40*10^{-6} p
Initial fuel amount	0.5*L^3				
Heat conductivity	0.04 w/(m K)	Heat conductivity	0.04 w/(m K)		
Nu number for heat transfer to solid site	1.0	Nu number for heat loss from pore site	0.05	Nu number for heat loss from solid site	0.05
Reaction rate coefficient			3*10^5 Kg mol^{-1} m s^{-1}		
Activity energy			1.2*10^5 J/mol		
Heat of reaction			15000 KJ/Kg		

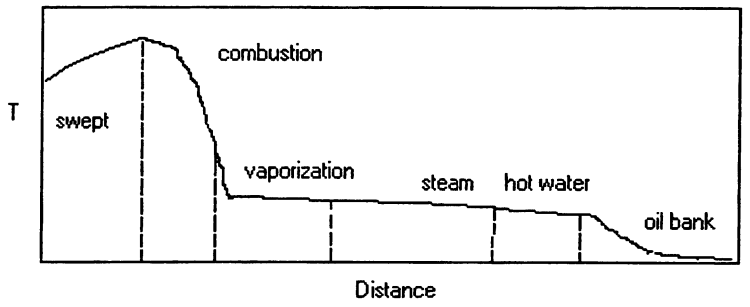

Figure 1. Schematic of Regimes in In-Situ Combustion.

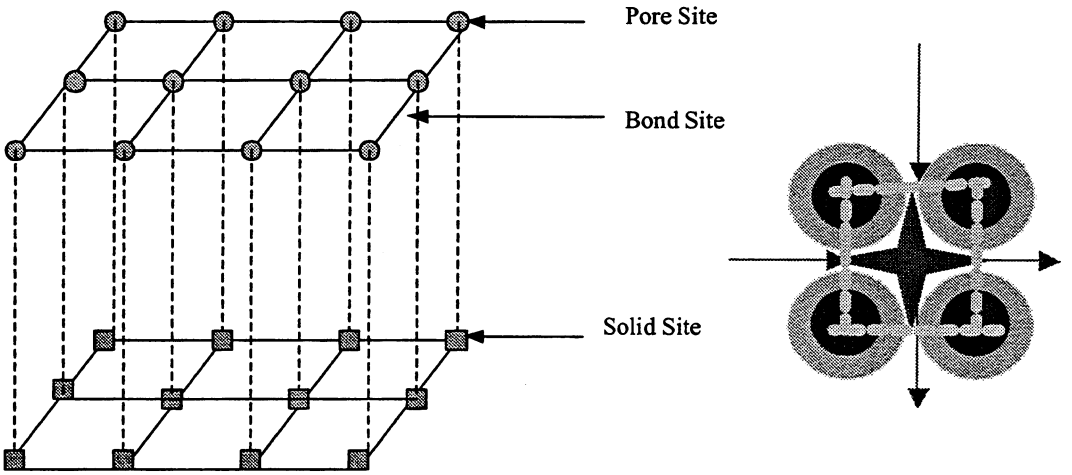

A. The pore-network model

B. Structure of a single pore site containing fuel

Figure 2. Structure of the pore network.

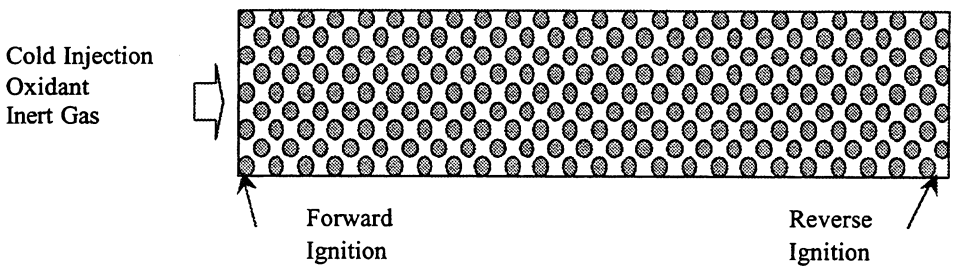

Figure 3. Sketch of the forward and reverse combustion ignition method.

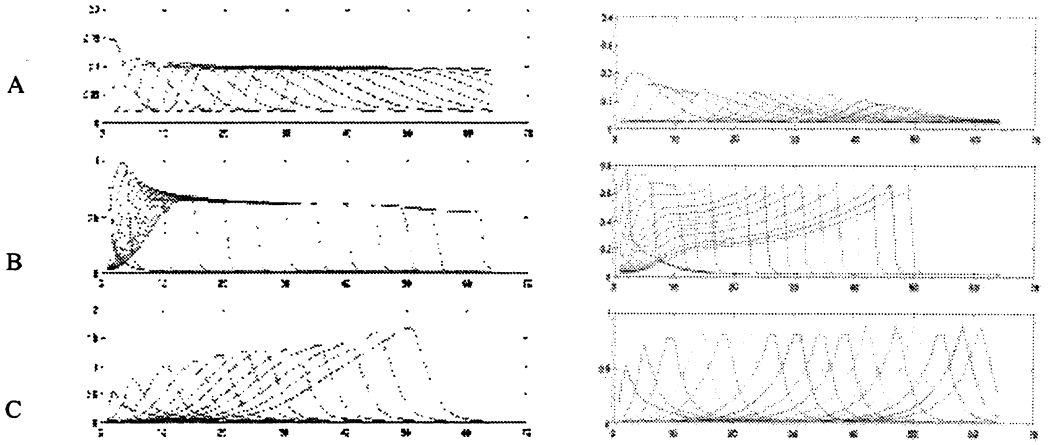

A: Reaction trailing ($\delta>1$), B: Reaction leading ($\delta<1$), C: Maximum Accumulation ($\delta=1$)
Figure 4. 1-D simulation results for three different values of δ. The simulations on the right include heat losses.

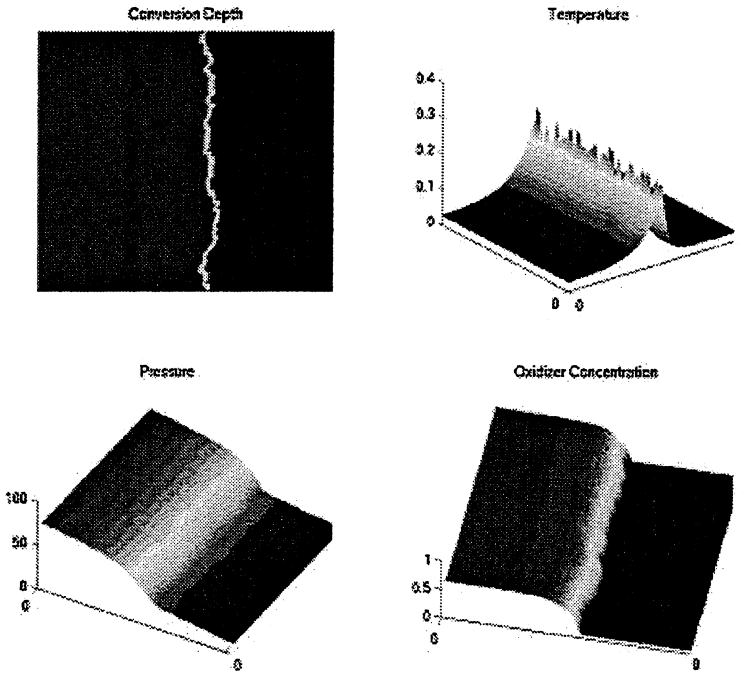

Figure 5. Patterns of forward combustion for the base case.

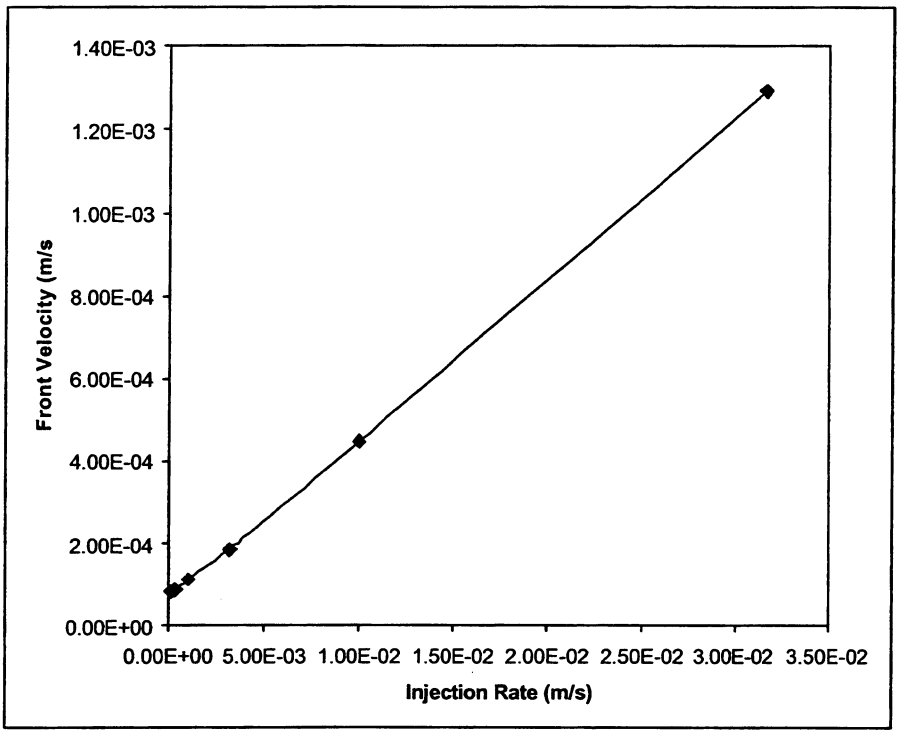

Figure 6. The steady-state front velocity as a function of the injection rate for the base-state.

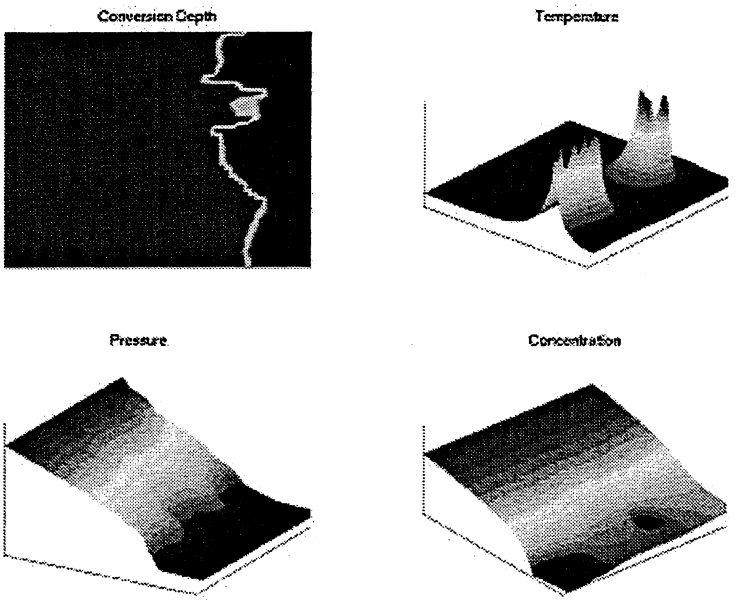

Figure 7. Patterns of forward combustion for the case of enhanced permeability in the burned region

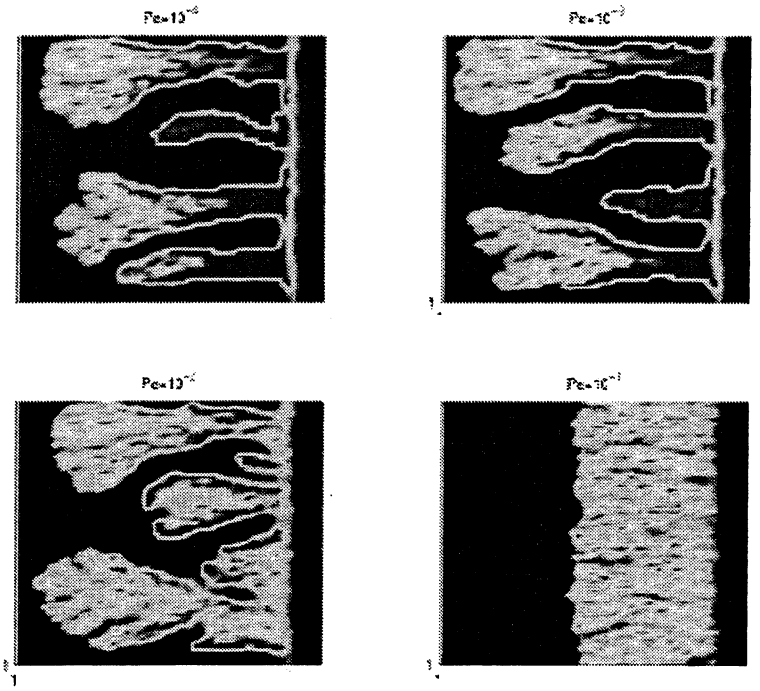

Figure 8. Conversion depth patterns for different values of the Peclet number in reverse combustion: A) $Pe=10^{-4}$; B) $Pe=10^{-3}$; C) $Pe=10^{-2}$; D) $Pe=10^{-1}$

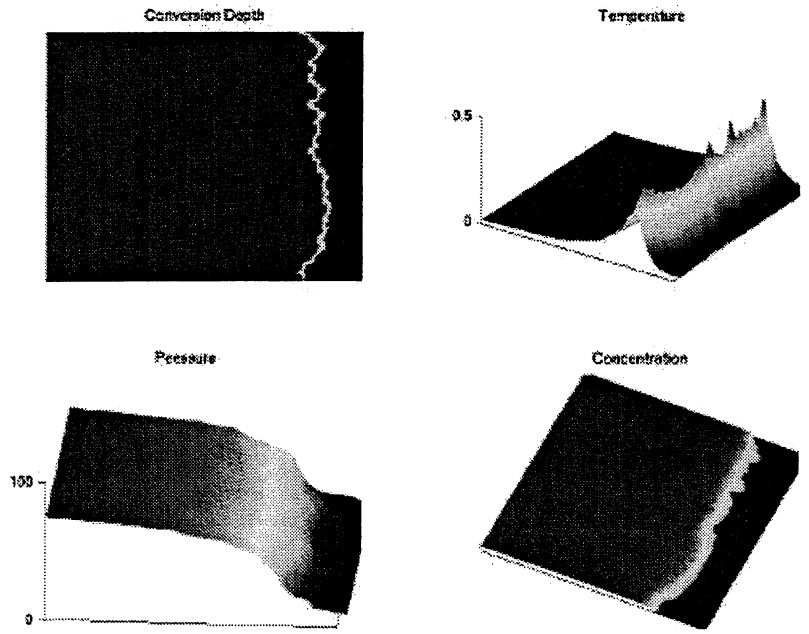

Figure 9. Patterns of forward combustion for the case of a broad pore-size distribution.

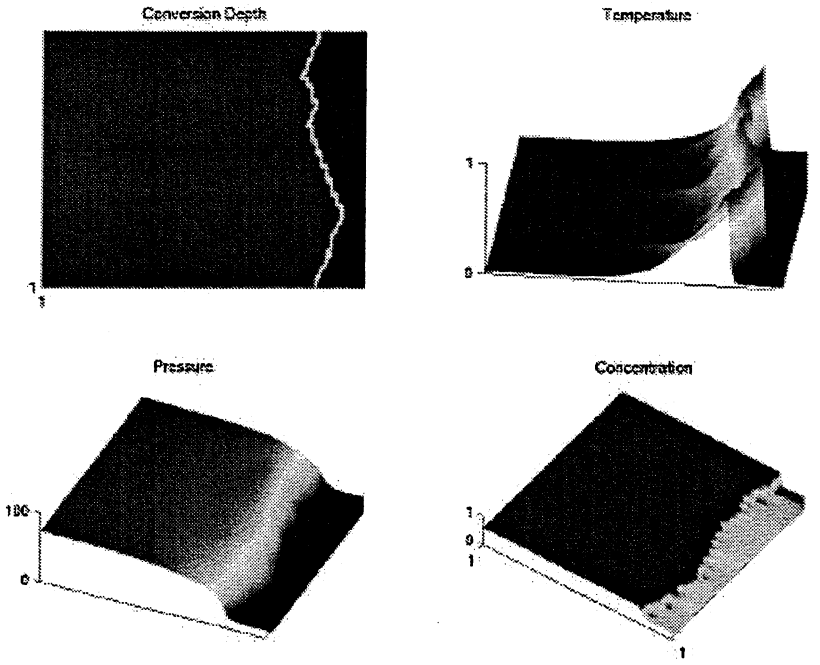

Figure 10. Patterns of forward combustion for the case of fBm pore-size distribution (H=0.7).

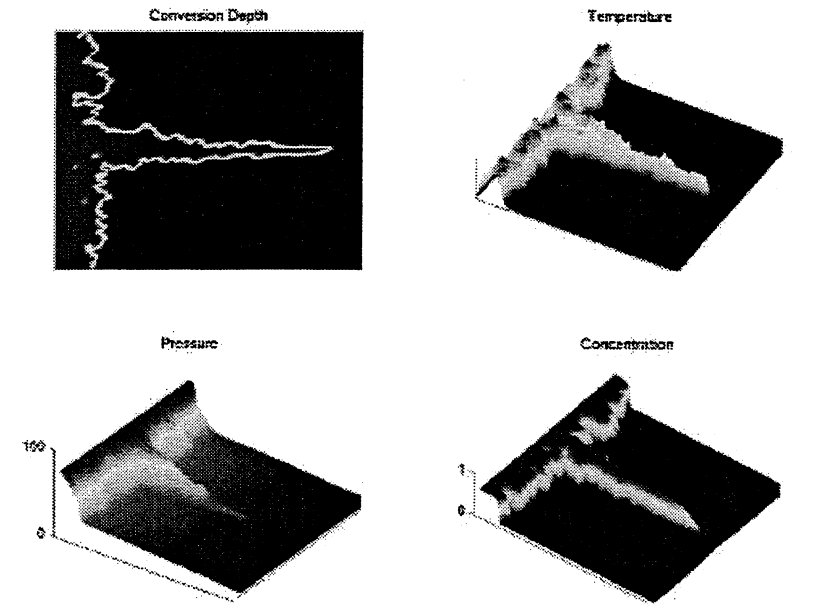

Figure 11. Patterns of forward combustion for the case of a "microfissure" in the middle of the lattice

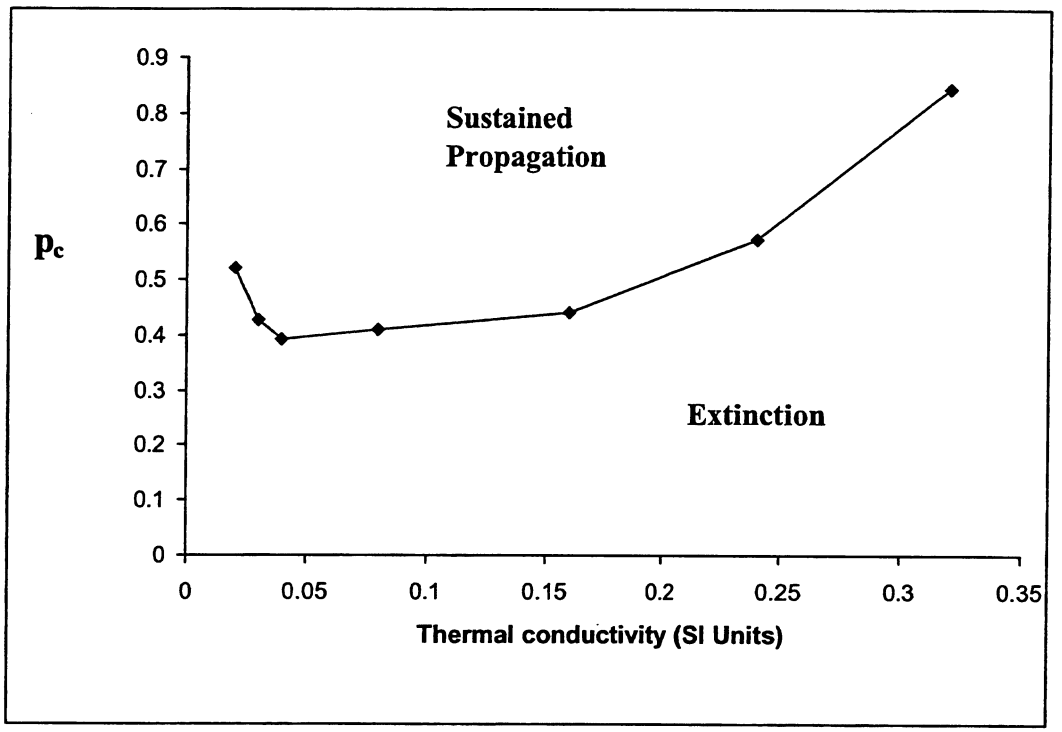

Figure 12. The percolation threshold for the onset of sustained front propagation as a function of the thermal conductivity.

DYNAMICS OF COMBUSTION FRONTS IN POROUS MEDIA: THE NON-ADIABATIC CASE

I. Yucel Akkutlu and Yanis C. Yortsos

1. Introduction

The propagation of combustion fronts in porous media is a subject of interest to a variety of applications, ranging from the *in situ* combustion for the recovery of oil [1], to filtration combustion [6], e.g., smoldering combustion [8]. While these problems may differ in application and context, they share a common characteristic, namely that the main combustion reaction involves the burning of a stationary solid fuel, which in the latter application is part of the initial state of the system, while in the former it is created by preceding processes, such as vaporization and low temperature oxidation. *In situ* combustion for oil recovery has been studied quite extensively since the mid 1950s. The two texts by Prats [1] and Boberg [2] summarize the relevant literature on the subject until the late 1980s. A large number of experimental, analytical and numerical studies have been reported on a variety of *in situ* combustion topics.

Of interest to this chapter is a particular but important issue of *in situ* combustion, the dynamics of the combustion front. These are influenced by a number of factors, including the fluid flow of injected and produced gases, the heat transfer in the porous medium and the surroundings, the rate of reaction(s), the heterogeneity of the medium and possibly the evolution of the pore morphology due to the combustion reaction. Understanding these dynamics is important to a number of issues, including front stability, the sustained propagation of combustion, the effects of heterogeneity, and the scale-up of the process. A specific feature of in-situ combustion is the thin reaction zone, within which combustion occurs, the extent of which is quite small, and certainly much smaller than the typical grid in field simulation. As a result, it is almost necessary to treat the reaction zone as a surface of discontinuity. The existence of frontal discontinuities makes the upscaling of the process (namely its averaging

over larger scales, such as the reservoir grid simulation scale) qualitatively different than ordinary displacements in porous media, e.g. the injection of water to displace oil [3].

Combustion fronts as frontal discontinuities have been studied extensively in the literature of combustion and flames. Among the great deal of articles published we refer to the earlier work of Matalon and Matkowsky [4], the monograph of Pelcé [5] and the more recent work of Schult and co-workers [8]. Ref. [4] discusses the propagation of flames in the combustion of premixed gases, in the absence of a porous medium, and treats the flame front as a surface of discontinuity, separating two regions of different temperature and chemical composition. To capture phenomena occuring within the thin flame region, the methods of singular perturbation and matched asymptotic expansions are used. Pelcé [5] presents an interesting compilation of studies on combustion and flame propagation in a variety of geometries. In his work, common aspects are shown to exist between the seemingly different problems of viscous displacements in a Hele-Shaw cell (which gives rise to viscous fingering in porous media), dendritic solidification and flame propagation. This connection, and particularly with the viscous fingering problem, is of particular interest to in-situ combustion due to the common aspects of the porous medium heterogeneity and other factors. More recently, Aldushin and Matkowsky [6] have used this analogy to argue about the problem of the selection of the width of the Saffman-Taylor finger.

Relatively few modeling studies exist in the literature of *in situ* combustion. Baily and Larkin [12] modeled the heat flow including convection and conduction in linear and radial geometries in the presence of a combustion zone of finite thickness. Gottfried [13] modeled *in situ* combustion by focusing on heat transfer and treating the combustion front as a discontinuity involving a point heat source, represented as a Dirac δ-function. Beckers and Harmsen [14] detailed the propagation of various regimes in *in situ* combustion and its variants, e.g. wet combustion. Burger and Sahuquet [15] analyzed the chemical aspects of the reaction processes. Ağca and Yortsos [16] proposed a simplified description, which takes into account the heat losses to the surroundings to discuss issues of sustained propagation and extinction. The stability of combustion fronts was analyzed by Armento and Miller [17] using a simplified front analysis.

In a series of recent papers, Schult et al. [8, 9] studied the combustion of a solid fuel embedded in a homogeneous porous medium. This problem, known as filtration combustion, appears in applications such as smoldering. It differs from *in situ* combustion, (1) in the fact that the solid fuel is *a priori* available, rather than being in-situ generated, as is the case with *in situ* combustion, (2) in the lack of liquid flow ahead of the combustion front and the various physicochemical changes accompanying it, and (3) in the context of the process, which in in-situ combustion involves subsurface porous media and factors such as non-adiabatic propagation and large-scale heterogeneities. At the same time, the two problems have many common features, for example the propagation of a high-temperature reaction zone in which a gas-solid reaction process takes place. Schult et al. [8, 9] provided an asymptotic analysis of the problem in 1-D following an approach essentially similar to the flame analysis of Ref. [4]. An analogous approach was attempted earlier by Britten and Krantz [10, 11] who examined the structure of the reaction zone in reverse combustion in the context of coal gasification.

In this chapter, we will analyze the problem of *in situ* combustion, by working along similar lines.

The chapter is organized as follows: First, hydrocarbon combustion reactions in porous media are summarized. Then we briefly describe 1-D *in situ* combustion process, its spatially distributed regions based on combustion tube experiments and some field scale observations. Then, we present the framework of the analysis and proceed with a detailed asymptotic treatment of the reaction front. The jump conditions derived are subsequently used to analyze the properties of combustion fronts. Finally, we comment on the effects of porous medium heterogeneity and the closely related issue of scale-up. Our model is a continuum model, in which effective values are used for the kinetic and transport parameters.

2. Preliminaries

In-situ combustion in porous media has a high hydrocarbon displacement efficiency [23]. The major mechanisms for this recovery are viscosity reduction of the flowing fluids, volumetric expansion (and related density decrease) of rock and fluids, in-situ distillation, combustion

supported gas drive, *in situ* steam and distillate drives and water drive. These mechanisms are closely related with thermal effects due to combustion. The changes in physical properties affect the fluid dynamics in a complex manner and give rise to various different regions. In the direction from upstream to downstream, these can be identified roughly as ([1]): (1) the burned zone, (2) the combustion zone, (3) the vaporization zone, (4) the condensation zone, (5) the hot water bank, (6) the oil bank and the (7) initial zone.

The burned zone contains injected air and possibly a residue of unburned fuel depending on the combustion efficiency. Due to the cold air influx and lateral heat losses, the temperature profile in this region increases monotonically downstream, until the combustion zone. In this zone, solid fuel and injected oxygen react exothermically and combustion gases, such as carbon oxides and superheated steam, are generated. In the vaporization zone, fluid hydrocarbons are thermally cracked, distilled by the flowing gas stream and decarboxylated.

The combustion reactions with hydrocarbon mixtures are complex; a great number of reaction products are generated over a large temperature range by hydrocarbon oxidation. Burger *et al.* [15] derived and classified seven reaction processes taking into account the formation of carbon-oxygen bonds. Of these, two dominate at temperatures higher than 300°C (572°F) and lead to destruction of the hydrocarbon chain. The rest occur at relatively low temperatures ($150 < T < 300°C$) and represent oxidations to carboxylic acid, aldehyde, ketone, alcohol and hydroperoxide. Experimental results [20, 21] indicate that a substantial proportion of oxygen consumption occurs at low temperatures. For theoretical investigation purposes, it is not uncommon to reduce these groups of reactions into two lumped-parameter, single-step reactions: high temperature oxidation (HTO), and low temperature oxidation (LTO). HTO occurs where the combustion front is located, whereas LTO precedes the combustion front.

Fuel combustion in the HTO region is often generalized as an oxidation reaction with a large activation energy. The combustion stoichiometry is typically represented by the simple exothermic reaction [18]:

$$CH_x + \left(1 - \frac{m}{2} + \frac{x}{4}\right) O_2 \longrightarrow (1-m)CO_2 + mCO + \frac{x}{2}H_2O, \tag{1}$$

where x is the atomic H/C of the fuel and m is the fraction of carbon oxidized to CO. Fuel formation occurs in the LTO region. Unreacted or bypassed oxygen from the HTO region, reacts with the hydrocarbons ahead of the combustion front. In this range, LTO reactions tend to increase the density, apparent viscosity and boiling range of the liquid phase oil. Mamora and Brigham [19] carried out kinetic tube experiments to investigate the implications of LTO. Their experiments also confirmed the existence of the two reaction regions. Fuel formation is not solely due to LTO reaction, however. It should be considered as a combination of several parallel processes: thermal cracking, vaporization, distillation as well as LTO. Thermal cracking does not require the presence of oxygen; at elevated temperatures crude oil fractions such as maltenes are converted to asphaltenes and then to coke and gaseous products [22]. It is apparent that fuel formation and combustion are interdependent, as they both affect each other. Excessive fuel deposition may retard the rate of advance of the combustion front, whereas insufficient fuel deposition may not provide enough heat supply to self-sustain it.

In this chapter, we will only consider aspects of steady-state propagation of the combustion front, assuming that fuel has been formed as a result of the preceding LTO reaction process. The available fuel reacts with oxygen following a rate-limiting HTO reaction inside the combustion front. By doing so we do not mean to imply that the preceding regions are not important, but rather that the steady-state dynamics can be analyzed separately assuming given values of fuel concentration and other properties downstream.

3. Formulation

We consider the combustion of a solid fuel in a inert porous medium, of known initial composition and concentration. In *in situ* combustion, this fuel is produced as a result of processes preceding the combustion front. Given that these processes and combustion are coupled, the concentration and composition of the fuel are, in principle, not known *a priori* and must be determined as part of the solution of the problem. In the following, however, we will assume that the initial density of the fuel per unit total volume is known and given by ρ_f^o.

At any time, the system consists of two phases, a solid phase including the solid matrix and the fuel, and a gas mixture of injected oxygen, inert gas and reaction products. The matrix is non-reactive, stationary and its thermodynamic properties do not change during the process. The solid fuel reacts with injected oxygen according to the following one-step heterogeneous reaction model

[Fuel] + $\tilde{\gamma}$ [Oxygen] $\longrightarrow$ $\tilde{\gamma}_{gp}$ [Gaseous Product],

where $\tilde{\gamma}_i$ are the stoichiometric coefficients. Pseudo-components for the fuel and the reaction gases are used. In formulating the conservation equations we will assume the following: locally, pore space and solid matrix are in thermal equilibrium, hence a one-temperature model is used for the energy balance; heat transfer by radiation, energy source terms due to pressure increase, and work from surface and body forces are negligible; very rapid mass exchange of the oxygen between the fuel surface, where reaction takes place, and the gas in the pore space occurs (i.e. the rates of local mass transfer, adsorption of oxygen and desorption of combustion products are fast relative to reaction rate), therefore a single oxygen concentration field is used; the ideal gas law is the equation of state for the gas phase; thermodynamic and transport properties, such as conductivity, diffusivity, heat capacity of the solid, heat of reaction, etc. remain constant. We also define a conversion depth for the solid fuel $\eta(\tilde{x},\tilde{y},\tilde{t}\,) = 1 - \rho_f(\tilde{x},\tilde{y},\tilde{t})/\rho_f^o$, such that $\eta = 0$ corresponds to the initial state and $\eta = 1$ to the case of complete fuel consumption.

Conservation equations are written for the following quantities: the total energy, the oxygen mass, the total gas mass and the fuel mass, in terms of the temperature $\tilde{T}(\tilde{x},\tilde{y},\tilde{t}\,)$, the oxygen mass fraction $\tilde{Y}(\tilde{x},\tilde{y},\tilde{t}\,)$, the average gas density $\rho_g(\tilde{T},\tilde{p})$ and the fuel conversion depth. We also use Darcy's law for the flow of the gas phase, in terms of the pressure $\tilde{p}(\tilde{x},\tilde{y},\tilde{t}\,)$. The dimensional form of these equations (superscript tilde) is shown below

total energy

$$(1-\phi)c_s\rho_s\frac{\partial\tilde{T}}{\partial\tilde{t}} + c_g\rho_g\tilde{\boldsymbol{v}}\cdot\tilde{\nabla}\tilde{T} = \tilde{\nabla}\cdot(\lambda\tilde{\nabla}\tilde{T}) + \tilde{Q}\rho_f^o W - \dot{Q}_h, \tag{2}$$

oxygen mass

$$\phi\frac{\partial(\tilde{Y}\rho_g)}{\partial\tilde{t}} + \tilde{\nabla}\cdot(\tilde{Y}\rho_g\tilde{\boldsymbol{v}}) = \tilde{\nabla}\cdot(D_M\rho_g\tilde{\nabla}\tilde{Y}) - \tilde{\mu}\rho_f^o W, \tag{3}$$

total gas mass

$$\phi\frac{\partial\rho_g}{\partial\tilde{t}} + \tilde{\nabla}\cdot(\rho_g\tilde{\boldsymbol{v}}) = \tilde{\mu}_g\rho_f^o W, \tag{4}$$

depth of conversion

$$\frac{\partial\eta}{\partial\tilde{t}} = W, \tag{5}$$

where, $\dot{Q}_h$ is a heat loss term and we introduced the rate of reaction W. Using the law of mass action we will take

$$W = k(\tilde{T})\tilde{a}_s^m(\frac{\tilde{Y}\tilde{p}}{R\tilde{T}})^n\psi(\eta), \tag{6}$$

where

$$k(\tilde{T}) = k_o e^{-E/R\tilde{T}}, \tag{7}$$

E is the activation energy, k_o the pre-exponential factor, and n the exponent in the dependence on oxygen concentration in terms of moles per unit gas volume. The dependence on η is through the dimensionless function ψ, the evaluation of which requires a more elaborate pore-level study [24]. Clearly, $\psi(1) = 0$. The rate is implicitly dependent on porosity through the surface area $\tilde{a}_s$, which is defined as surface area available for reaction per total volume. An average value of the latter could be determined [25]. Exponent m should be determined experimentally. Note that the reaction rate in this form is different from previous studies of combustion in porous media, where the following dependence was taken

$$W_1 = k_1(\tilde{T})(\tilde{Y}\tilde{p})^n\psi(\eta), \tag{8}$$

$$k_1(\tilde{T}) = k_{o1} e^{-E/R\tilde{T}}. \tag{9}$$

we will demonstrate that the difference in both reaction rate models is crucial on the front dynamics, particularly on the front temperature and extinction limits.

In the above, c_i is the average specific heat capacity of species i (gas or solid) at constant pressure, ρ_i is the volumetric density of species i, and we assumed that the solid heat capacity is much larger than that of the gas. The average thermal conductivity, λ, is an effective value including the effects of gas and solid phases on conduction. $\dot{Q}$ represents the heat release of the fuel combustion reaction and is also assumed to be independent of temperature variations. D_M is an effective diffusion coefficient for oxygen in the gas phase flowing through the porous medium, while $\tilde{\mu}$ and $\tilde{\mu}_{gp}$ are mass-weighted stoichiometric coefficients for oxygen and gaseous products, respectively, defined as $\tilde{\gamma}_i M_i / M_f$. The net gas mass production due to reaction is determined by the sign of $\tilde{\mu}_g = \tilde{\mu}_{gp} - \tilde{\mu}$ so that $\tilde{\mu}_g > 0$ or $\tilde{\mu}_g < 0$ corresponds to total gas mass production or consumption, respectively. Finally, we have Darcy's law

$$\tilde{\nabla}\tilde{p} = -\frac{\eta_g}{K(\eta)}\tilde{\boldsymbol{v}} + \rho_g \tilde{\boldsymbol{g}} \tag{10}$$

where $K(\eta)$ is the absolute permeability, η_g is the gas viscosity, $\tilde{\boldsymbol{g}}$ is the vector of gravitational acceleration, and the equation of state, assuming ideal gases

$$\tilde{p} M_g = \rho_g R \tilde{T}. \tag{11}$$

The expression for heat losses can take the simple form

$$\dot{Q}_h = \frac{\tilde{h}}{H}(\tilde{T} - \tilde{T}_o) \tag{12}$$

reflecting convective heat transfer, or the more elaborate expression

$$\dot{Q}_h = \frac{2\sqrt{(\lambda_h c_h \rho_h)}}{H\sqrt{\pi}} \int_0^{\tilde{t}} \frac{\partial \tilde{T}}{\partial \tau} \frac{d\tau}{\sqrt{(\tilde{t} - \tau)}} \tag{13}$$

reflecting heat conduction to a semi-infinite overburden and underburden (Yortsos and Gavalas [27]). The latter is a more realistic condition for processes in the subsurface. Here subscript h refers to the surroundings and H is the thickness of the porous layer subjected to combustion.

4. Scaling and Non-dimensionalization

As shown in Figures 1 and 2, the problem includes three spatial scales, each associated with different dominant processes: the scale of the reactive-diffusive reaction zone, l_R, the scale of the convective-diffusive combustion zone, l_T, and the convective scale l_S. In the combustion zone, convection and conduction are of the same magnitude, namely the Péclet number, $Pe = v_* l_T (1-\phi) c_s \rho_s / \lambda$ is of order 1, where the reference velocity v_* is to be determined. This defines l_T. If the front temperature of a planar combustion layer is $\tilde{T}_f$, also to be determined from the solution of the problem, then we have

$$\begin{aligned} l_R &\equiv \frac{l_T}{Z} \quad \text{where} \quad Z = \frac{E\tilde{T}_o}{R\tilde{T}_f^2}, \\ l_T &\equiv \frac{\lambda}{(1-\phi)c_s\rho_s v_*}, \\ l_S &\equiv \tilde{L}. \end{aligned} \tag{14}$$

The characteristic parameters to be chosen depend on what is the focus of the analysis. If it is the reaction zone, the characteristic time is based on the reaction kinetics

$$t_R \equiv Z^\alpha \left(\frac{k_o (\tilde{Y}_o \tilde{p}_i)^n e^{-E/R\tilde{T}_f}}{l_R^m R\tilde{T}_o} \right)^{-1}, \tag{15}$$

and the characteristic length is the combustion zone length l_T. If the focus is on the combustion zone, then we rescale both the characteristic time and length by δ^{-1}, where $\delta = l_T/l_S \ll 1$. Then, $t_* = \delta^{-1} t_R$ and $x_* = \delta^{-1} l_T$. In either case, we have the reference velocity $v_* \equiv \frac{x_*}{t_*} = \frac{l_T}{t_R}$. This further implies the relation

$$v_* = \sqrt{\frac{\lambda}{(1-\phi)c_s\rho_s t_R}}, \tag{16}$$

which physically hints at the fact that a rigorous burning process takes place, i.e., the Damköhler number is of order 1. In particular, for $\alpha = 1$, $m = 1$ and $n = 1$, we further obtain

$$v_* = \frac{k_o \tilde{Y}_o \tilde{p}_i \exp(-E/R\tilde{T}_f)}{R\tilde{T}_o} \tag{17}$$

This relation will be used below in numerical examples.

Scaling temperature with $\tilde{T}_o$ and density with the initial gas density ρ_{gi} and using the combustion zone formulation, we obtain the conservation equations in the dimensionless form

$$\frac{\partial \theta}{\partial \hat{t}} + a\rho \boldsymbol{v} \cdot \hat{\nabla}\theta = \delta \hat{\Delta}\theta + \delta q \Phi - \dot{Q}_{hD} \tag{18}$$

$$\phi \frac{\partial (Y\rho)}{\partial \hat{t}} + \hat{\nabla} \cdot (Y\rho \boldsymbol{v}) = \frac{\delta}{Le}(\hat{\nabla} \cdot \rho \hat{\nabla} Y) - \delta \mu \Phi \tag{19}$$

$$\phi \frac{\partial \rho}{\partial \hat{t}} + \hat{\nabla} \cdot (\rho \boldsymbol{v}) = \delta \mu_g \Phi \tag{20}$$

and

$$\frac{\partial \eta}{\partial \hat{t}} = \delta \Phi \tag{21}$$

where

$$\Phi = \delta^{-2} Z^{\alpha} a_s^m \left(\frac{Y(1 + \Pi p)}{\theta} \right)^n \psi(\eta) \exp\left(Z\theta_f^2 \left(\frac{1}{\theta_f} - \frac{1}{\theta} \right) \right). \tag{22}$$

In addition, we have

$$\hat{\nabla} p = -\kappa \boldsymbol{v} + \rho \boldsymbol{g} \tag{23}$$

and

$$\rho\theta = 1 + \Pi p. \tag{24}$$

In the above, we introduced the following variables and parameters

$$\begin{aligned}
\theta &= \frac{\tilde{T}}{\tilde{T}_o}, \quad \theta_f = \frac{\tilde{T}_f}{\tilde{T}_o}, \quad Y = \frac{\tilde{Y}}{\tilde{Y}_o}, \quad p = \frac{\tilde{p} - \tilde{p}_i}{\tilde{p}_{inj} - \tilde{p}_i}, \quad \Pi = \frac{\tilde{p}_{inj} - \tilde{p}_i}{\tilde{p}_i}, \\
\mu &= \frac{\tilde{\mu}\rho_f^o}{\rho_{gi}\tilde{Y}_o}, \quad \mu_{pg} = \frac{\tilde{\mu}_{pg}\rho_f^o}{\rho_{gi}\tilde{Y}_o}, \quad \mu_g = \frac{\tilde{\mu}_g\rho_f^o}{\rho_{gi}}, \quad a = \frac{c_g\rho_{gi}}{(1-\phi)c_s\rho_s}, \quad a_s = \tilde{a}_s l_R \\
q &= \frac{Q\rho_f^o}{(1-\phi)c_s\rho_s\tilde{T}_o}, \quad \kappa = \frac{\eta_g x_* v_*}{K(\tilde{p}_{inj} - \tilde{p}_i)}, \quad \Phi = \delta^{-1}Wt_*, \quad Z = \frac{E\tilde{T}_o}{R\tilde{T}_f^2}, \\
\boldsymbol{g} &= \frac{\tilde{\boldsymbol{g}}\rho_{gi}x_*}{(\tilde{p}_{inj} - \tilde{p}_i)}, \quad \dot{Q}_{hD} = \frac{\dot{Q}_h t_*}{(1-\phi)c_s\rho_s T_o}, \quad Le = \frac{\lambda}{D_M(1-\phi)c_s\rho_s},
\end{aligned} \tag{25}$$

where $\tilde{p}_i$ and $\tilde{p}_{inj}$ are the initial and the injection gas pressure in the system. Note that the spatial coordinates are nondimensionalized based on the system length, l_S, which in the limit $\delta \ll 1$ allows to approximate the combustion zone as a thin layer. To focus on the combustion zone, we simply change the scaling, which is equivalent to taking $\delta = 1$ in the above equations.

The boundary conditions depend on the extent of combustion. If the fuel is fully consumed, we take for $\hat{t} \geq 0$:

$$Y = 1, \qquad \theta = \theta_f \qquad \eta = 1 \qquad ; \qquad \hat{x} \to -\infty \tag{26}$$

$$Y = Y_b, \qquad \theta = 1, \qquad \eta = 0 \qquad ; \qquad \hat{x} \to \infty \tag{27}$$

where θ_f and Y_b are to be determined. This is the fuel-deficient case and a reaction-leading structure emerges, where the temperature profile and the high temperature region trails the combustion front. Otherwise, we have

$$Y = 1, \qquad \theta = 1 \qquad \eta = \eta_b \qquad ; \qquad \hat{x} \to -\infty \tag{28}$$

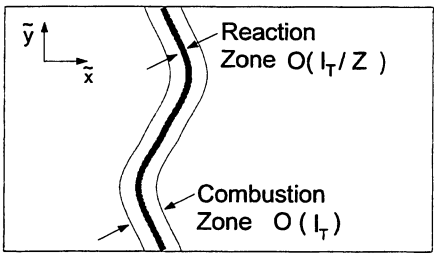

Figure 1: Illustration of Reaction and Combustion Zones

$$Y = 0, \qquad \theta = \theta_f, \qquad \eta = 0 \qquad ; \qquad \hat{x} \to \infty \tag{29}$$

where θ_f and η_b are to be determined. This is the oxygen-deficient case with the high temperature region located ahead of the front, thus yielding a reaction-trailing structure. Only the reaction-leading case will be considered below.

Typically, Z is large. Because of this condition and the fact that the reaction rate is strongly temperature dependent, all combustion reactions are confined to a thin reaction-dominated zone at the combustion front. It is within this zone, where reactions occur at a high rate, temperature, pressure and concentrations being approximately constant. The reaction zone is embedded within the heat transfer layer, as shown in Figure 1, where thermal and molecular diffusion are equally important with convection.

The reaction zone and the heat transfer layer combine to form the combustion zone, Figure 1. Outside this zone, the problem is controlled by convective transport of energy and mass, and also by heat losses to the surroundings. It is outside the combustion zone, where fluid dynamics and permeability heterogeneity are dominant. Now, in most practical applications, the reaction zone has a sufficiently small width, so that it can be viewed as a front. Appropriate jump conditions can then be derived across it. In addition, it is likely that the heat transfer layer width is small compared to the fluid dynamical scale of the problem, l_S. If that is the case, we can define the small parameter $\delta = l_T/l_S$, and consider the combustion zone as a discontinuous front as shown in Figure 2. For such a description, additional jump conditions, now across the combustion front, must be derived.

Before we proceed further, we recall some basic notions related to front propagation. We will restrict our discussion to two-dimensional problems, although an extension to three-dimensions is straightforward. Consider a front propagating in the positive $\tilde{x}$ direction and described by

$$F(\tilde{x}, \tilde{y}, t) \equiv \tilde{x} - f(\tilde{y}, \tilde{t}) = 0 \tag{30}$$

as shown in Figure 2. In our context, this equation separates a burned region ($F < 0$) from an unburned region ($F > 0$), where fresh solid fuel resides in the pore structure. Define the velocity of the surface by $\boldsymbol{\nu}$. Then, the normal velocity with respect to a fixed frame of reference, ν_n, is

$$\nu_n \equiv \boldsymbol{\nu} \cdot \boldsymbol{n} = \frac{-F_{\tilde{t}}}{|\tilde{\nabla} F|} = \frac{f_{\tilde{t}}}{(1 + f_{\tilde{y}}^2)^{1/2}} \tag{31}$$

where $f_{\tilde{t}} = \partial f / \partial \tilde{t}$ and $f_{\tilde{y}} = \partial f / \partial \tilde{y}$, and $\boldsymbol{n}$ is the unit vector normal to the front pointing in the direction of the unburned region

$$\boldsymbol{n} = \frac{\tilde{\nabla} F}{|\tilde{\nabla} F|}. \tag{32}$$

In the flame propagation literature, a useful quantity is the net normal velocity with respect to the moving front,

$$S_f \equiv \tilde{\boldsymbol{v}}_{0^-} \cdot \boldsymbol{n} - \nu_n = \frac{\tilde{v}_{\tilde{x}} - \tilde{v}_{\tilde{y}} f_{\tilde{y}} - f_{\tilde{t}}}{(1 + f_{\tilde{y}}^2)^{1/2}} \tag{33}$$

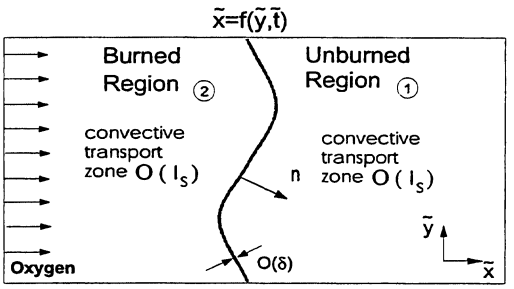

Figure 2: Combustion Front as a Discontinuity

where $\tilde{\boldsymbol{v}}_{0-}$ is the average gas mixture velocity evaluated at $F = 0^-$. In the case of porous media, the above must be modified, due to the presence of the porous medium, to read

$$S_{fp} \equiv \tilde{\boldsymbol{v}}_{0-} \cdot \boldsymbol{n} - \phi \nu_n = \frac{\tilde{v}_{\tilde{x}} - \tilde{v}_{\tilde{y}} f_{\tilde{y}} - \phi f_{\tilde{t}}}{(1 + f_{\tilde{y}}^2)^{1/2}} \tag{34}$$

where ϕ is porosity.

In the following, we will consider in sequence, first a reaction front, and then a combustion front. Using asymptotic expansions, the structure in both fronts will be analyzed and appropriate jump conditions across the fronts will be derived.

5. Moving Coordinates

The final step in the formulation of the problem is to convert to moving coordinates, moving with the combustion front, which in the fuel-deficient case can be defined as the position at which $\eta = 1/2$. If we denote $x = \hat{x} - f(\hat{y}, \hat{t})$, $y = \hat{y}$ and $t = \hat{t}$, then the non-dimensional equations take the form:

$$\frac{\partial \theta}{\partial t} + (a\rho s - f_t)\frac{\partial \theta}{\partial x} + a\rho v_y \frac{\partial \theta}{\partial y} = \delta \Delta\theta + \delta q \Phi - \dot{Q}_{hD} \tag{35}$$

$$\phi \frac{\partial (Y\rho)}{\partial t} + \frac{\partial (Y\rho(s - \phi f_t))}{\partial x} + \frac{\partial (Y\rho v_y)}{\partial y} = \left(\frac{\delta \rho}{Le}\right) \Delta Y - \delta \mu \Phi \tag{36}$$

$$\phi \frac{\partial \rho}{\partial t} + \frac{\partial (\rho(s - \phi f_t))}{\partial x} + \frac{\partial (\rho v_y)}{\partial y} = \delta \mu_g \Phi \tag{37}$$

$$\frac{\partial \eta}{\partial t} - f_t \frac{\partial \eta}{\partial x} = \delta \Phi \tag{38}$$

$$\kappa v_x = -\frac{\partial p}{\partial x} + \rho g_x \tag{39}$$

$$\kappa v_y = -\left(\frac{\partial p}{\partial y} + f_y \frac{\partial p}{\partial x}\right) + \rho g_y \tag{40}$$

$$\rho\theta = 1 + \Pi p \tag{41}$$

Here,

$$s \equiv v_x - v_y \frac{\partial f}{\partial y}, \tag{42}$$

is the longitudinal velocity of the gas mixture in the moving frame and we defined the Laplace operator in moving coordinates

$$\Delta \equiv (1 + f_y^2)\frac{\partial^2}{\partial x^2} + \frac{\partial^2}{\partial y^2} - \frac{\partial^2 f}{\partial y^2}\frac{\partial}{\partial x} - 2\frac{\partial f}{\partial y}\frac{\partial^2}{\partial x \partial y}, \tag{43}$$

For simplicity, the density term in the diffusion of oxygen was approximated as constant. However, this approximation is not made in the subsequent analysis. Having obtained the desired formulation, we proceed next with the analysis of the structure of the reaction zone and then with that of the combustion zone.

6. Asymptotic Analysis

Under the condition $Z \gg 1$, the reaction zone thickness, l_T/Z, is much smaller than l_T. To analyze the structure of the zone, we stretch the longitudinal moving coordinate, $X = Zx$, and expand the dependent variables in an asymptotic series in terms of Z^{-1}. Following [9] it can be shown that, to leading order, temperature, concentration, pressure and density are independent of X. Thus, we take

$$\begin{aligned}
\theta &\sim \theta^o(y,t) + Z^{-1}\theta^1(X,y,t) + \ldots, \\
Y &\sim Y^o(y,t) + Z^{-1}Y^1(X,y,t) + \ldots, \\
p &\sim p^o(y,t) + Z^{-1}p^1(X,y,t) + \ldots,
\end{aligned}$$

$$
\begin{aligned}
\rho &\sim \rho^o(y,t) + Z^{-1}\rho^1(X,y,t) + \ldots, \\
\eta &\sim \eta^o(X,y,t) + \ldots, \\
s &\sim s^o(X,y,t) + \ldots, \\
v_y &\sim v_y^o(y,t) + \ldots, \\
f &\sim f^o(y,t) + \ldots.
\end{aligned} \tag{44}
$$

The respective leading-order terms are obtained after substitution in the governing equations. Combining the energy equation with the fuel balance shows that the leading-order terms are $O(Z^{-1})$, in which case only conduction in the X direction and reaction participate, namely

$$
\delta\left(1 + f_y^{o^2}\right)\frac{\partial^2\theta^1}{\partial X^2} = q f_t^o \frac{\partial \eta^o}{\partial X} \tag{45}
$$

(note that the heat loss term vanishes to leading order ***need to show why***). For the oxygen mass balance, a similar analysis shows that the leading-order terms are convection, diffusion and reaction, hence

$$
Le\rho^o Y^o(y,t)\frac{\partial s^o}{\partial X} - \delta\rho^o\left(1 + f_y^{o^2}\right)\frac{\partial^2 Y^1}{\partial X^2} = \mu Le f_t^o \frac{\partial \eta^o}{\partial X}, \tag{46}
$$

where we have taken into account that ρ^o is constant, while the total gas mass balance reads

$$
\rho^o \frac{\partial s^o}{\partial X} = -\mu_g f_t^o \frac{\partial \eta^o}{\partial X}. \tag{47}
$$

The equation for the fuel mass is expressed to leading-order as

$$
\delta f_t^o \frac{\partial \eta^o}{\partial X} = -Z^{\alpha-1} a_s^m \left\{\frac{\left(Y^o(y,t) + Z^{-1}Y^1(X,y,t)\right)\left(1 + \Pi p^o(y,t)\right)}{\theta^o(y,t) + Z^{-1}\theta^1(X,y,t)}\right\}^n \psi(\eta^o)e^{\theta^1} \tag{48}
$$

where we used a power series expansion for the exponential term. Finally, to leading-order, pressure is constant within the reaction zone.

Integrating equations (45- 47) across the reaction zone determines the jumps in heat, oxygen mass and gas mass fluxes across the front in terms of the jump in depth of fuel conversion,

$$\delta\left(1+f_y^{o^2}\right)\left.\frac{\partial\theta^1}{\partial X}\right|_{-\infty}^{\infty}=qf_t^o\eta^o\,\Big|_{-\infty}^{\infty} \tag{49}$$

$$\delta\rho^o\left(1+f_y^{o^2}\right)\left.\frac{\partial Y^1}{\partial X}\right|_{-\infty}^{\infty}=-\left(\mu+Y^o(y,t)\mu_g\right)Lef_t^o\,\eta^o|_{-\infty}^{\infty} \tag{50}$$

$$\rho^o s^o\,\Big|_{-\infty}^{\infty}=-\mu_g f_t^o\,\eta^o|_{-\infty}^{\infty}\,. \tag{51}$$

The depth of conversion equation (48) can also be integrated across the reaction zone. For this, we first integrate equation (45) using the boundary conditions $\partial\theta^1/\partial X=0$, $\eta^o=1$ as $X\to-\infty$, to give

$$\delta\left(1+f_y^{o^2}\right)\frac{\partial\theta^1}{\partial X}=-qf_t^o(1-\eta^o) \tag{52}$$

Then, multiplying equation (52) by (48) and taking $\alpha=1$ yields

$$q\left(f_t^o\right)^2\left(\frac{1-\eta^o}{\psi(\eta^o)}\right)\frac{\partial\eta^o}{\partial X}=-\left(1+f_y^{o^2}\right)a_s^m\left\{\frac{Y^o(y,t)(1+\Pi p^o(y,t))}{\theta^o(y,t)}\right\}^n e^{\theta^1}\frac{\partial\theta^1}{\partial X} \tag{53}$$

This equation can be now integrated across the reaction zone, to give the following result for the square of the normal front velocity

$$\frac{\left(f_t^o\right)^2}{1+f_y^{o^2}}=\frac{a_s^m\left\{Y^o(y,t)(1+\Pi p^o(y,t))\right\}^n}{q\theta^o(y,t)^n\int_0^1\frac{(1-\eta^o)}{\psi(\eta^o)}d\eta^o}. \tag{54}$$

This expression is primarily related to the unknown mass fraction of oxygen at the completion of the reaction and the pressure at the front.

Conditions (49-51) also express the jump of the corresponding quanities across the reaction zone. Thus, if we define the jump in a quantity π of the combustion zone across the reaction

front as $[\pi]_-^+ = \pi(x = 0^+) - \pi(x = 0^-)$, we obtain for the deficient-fuel case (where $\eta^o|_{-\infty}^{\infty} = 0 - 1 = -1$)

$$[Y]_-^+ = [\theta]_-^+ = [p]_-^+ = 0, \qquad [\eta]_-^+ = -1, \tag{55}$$

and

$$\begin{aligned} \delta\left(1 + f_y^{o^2}\right)\left[\frac{\partial\theta}{\partial x}\right]_-^+ &= -qf_t \\ \delta\rho\left(1 + f_y^{o^2}\right)\left[\frac{\partial Y}{\partial x}\right]_-^+ &= (\mu + Y^o(y,t)\mu_g)\, Lef_t \\ [\rho(s - \phi f_t)]_-^+ &= \mu_g f_t, \end{aligned} \tag{56}$$

In the above we have assumed full consumption of the fuel at *any* point of the front.

7. The Combustion Zone

Consider, next, the combustion zone structure. Outside the reaction zone, chemical reaction rates are insignificant. To analyze this problem, we must consider the conservation equations to either side of the reaction front, across which the jump conditions derived previously apply. For this, we need to consider an expansion valid inside the combustion zone, in which conduction and diffusion, but not chemical reaction, are taken into account.

In the context of the overall problem (Figure 2), the combustion zone has a dimensionless extent of order δ, hence we must introduce the stretched coordinate $\xi = x/\delta$ and seek expansions of the following form

$$\begin{aligned} \theta &\sim \theta_o + \delta\theta_1 + \ldots, \\ Y &\sim Y_o + \delta Y_1 + \ldots, \\ p &\sim p_o + \delta p_1 + \ldots, \\ \rho &\sim \rho_o + \delta\rho_1 + \ldots, \end{aligned} \tag{57}$$

$$\begin{aligned}
\eta &\sim \eta_o + \delta\eta_1 + \ldots, \\
s &\sim s_o + \delta s_1 + \ldots, \\
v_y &\sim v_{yo} + \delta v_{y1} + \ldots, \\
f &\sim f_o + \delta f_1 + \ldots,
\end{aligned}$$

These expansions are then introduced in the equations in moving coordinates. Because it is in this zone that heat losses are important, they must be considered in the analysis. First, we consider the problem in the absence of heat losses.

8. Adiabatic Case

Under the condition $\frac{\dot{Q}_h t_R}{(1-\phi)c_s\rho_s T_o} \ll 1$, the heat loss term does not contribute to leading order, thus the energy balance reads

$$A_o \frac{\partial \theta_o}{\partial \xi} - \left(1 + f_{oy}^2\right) \frac{\partial^2 \theta_o}{\partial \xi^2} = 0 \tag{58}$$

where

$$A_o = a\rho_o s_o - f_{o_t} \tag{59}$$

and

$$s_o = v_{xo} - v_{yo}\frac{\partial f_o}{\partial y} \tag{60}$$

Oxygen, total gas and fuel mass balances become, respectively,

$$\rho_o B_o \frac{\partial Y_o}{\partial \xi} - \frac{1}{Le}\left(1 + f_{oy}^2\right)\frac{\partial}{\partial \xi}\left(\rho_o \frac{\partial Y_o}{\partial \xi}\right) = 0 \tag{61}$$

$$\frac{\partial}{\partial \xi}\left(\rho_o B_o\right) = 0 \tag{62}$$

$$\frac{\partial \eta_o}{\partial \xi} = 0 \tag{63}$$

where

$$B_o = s_o - \phi f_{o_t}. \tag{64}$$

Darcy's law gives

$$\frac{\partial p_o}{\partial \xi} = 0 \tag{65}$$

and the ideal gas law reads

$$\rho_o \theta_o = \text{const.} \tag{66}$$

A_o is an indication of how effectively the stored reaction heat is transferred downstream by the flowing gas. For a reaction-leading structure, the local heat transfer between the solid and the gas must be weak relative to that in the combustion zone, therefore we expect $A_o < 0$. Also, for a propagating front along the positive x direction, we must have $s_o > \phi f_{o_t}$, hence $B_o > 0$. Experimental data obtained in combustion tube experiments (e.g. see Martin et al. [28], or Mamora and Brigham [19]), confirm these assumptions. We can then proceed to integrate the above equations using the following boundary conditions.

$$Y = 1, \qquad \theta = \theta_f \qquad \eta = 1 \qquad ; \qquad \xi \to -\infty \tag{67}$$

$$Y = Y_b, \qquad \theta = 1, \qquad \eta = 0 \qquad ; \qquad \xi \to \infty \tag{68}$$

Because $A_o < 0$, the only possible solution for θ_o in $\xi < 0$ is a constant independent of ξ (otherwise, θ_o will become unbounded as $\xi \to -\infty$). To find the solution for $\xi > 0$, we integrate (58) and make use of the jump condition at the reaction front

$$\left(1 + f_{oy}^2\right) \left[\frac{\partial \theta_o}{\partial \xi}\right]_-^+ = -q f_{o_t} \tag{69}$$

to obtain the result

$$\theta_o = \begin{cases} \theta_f(y,t) & : \ \xi < 0 \\ 1 - \left(\dfrac{q f_{o_t}}{A_o^+}\right) \exp\left(\dfrac{A_o^+}{1+f_{oy}^2}\xi\right) & : \ 0 < \xi \end{cases}$$

showing that the temperature decays exponentially fast downstream of the combustion front.

Similarly, equation (61) shows that because $B_o > 0$, the solution for Y in $\xi > 0$ must be a constant independent of ξ. Equation (62) also shows that $\rho_o B_o$ is a constant. Then, by integrating (61) in $\xi < 0$, where ρ_o is constant, and making use of the jump condition across the reaction front,

$$\rho_o \left(1 + f_{oy}^2\right) \left[\frac{\partial Y_o}{\partial \xi}\right]_-^+ = (\mu + Y_b(y,t)\mu_g)\, Le f_{o_t} \tag{70}$$

we obtain the final result

$$Y_o = \begin{cases} 1 - \left(\dfrac{(\mu + Y_b\mu_g) f_{o_t}}{\rho_o B_o^-}\right) \exp\left(\dfrac{Le B_o^-}{1+f_{oy}^2}\xi\right) & : \ \xi < 0 \\ Y_b(y,t) & : \ 0 < \xi \end{cases}$$

This equation gives the profile of the mass fraction upstream of the reaction front. Finally, equation (63) gives

$$\eta_o = \begin{cases} 1 & : \ \xi < 0 \\ 0 & : \ 0 < \xi \end{cases}$$

assuming, again, complete fuel combustion. Figure 3 show schematic profiles of temperature, mass fraction and conversion across the combustion zone.

Note that A_o in the temperature equation involves the mass flux $\rho_o s_o$ downstream of the reaction front (although its contribution to A_o may be very small due to $a \ll 1$), while B_o in

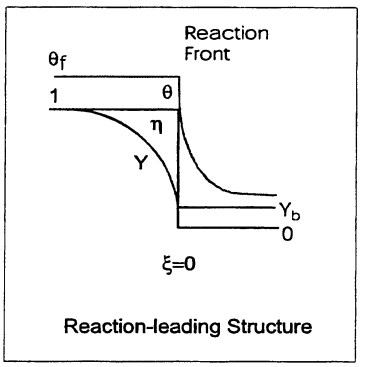

Figure 3: Schematic Profiles of Temperature, Oxygen Mass Fraction and Fuel Conversion in the Combustion Zone with a Reaction-leading Structure.

the mass fraction expression involves the mass flux upstream of the reaction front. The two fluxes are related to each other through the jump condition

$$\left(\rho_o(s_o - \phi f_{o_t})\right) = \mu_g f_{o_t} \tag{71}$$

derived in (56). The above equations represent the leading order "inner" expansion to the large scale problem, for which the combustion front appears as a discontinuity. In the section to follow we will consider the "outer" problem, on either side of the front (see Figure 2) by keeping only the convective transport term in the equations. To match the outer expansions we use the jump conditions derived from the inner problem, namely the problem in the combustion zone. These were derived previously to leading-order, and are summarized below.

$$\begin{aligned}
[\theta_o] &= 1 - \theta_f(y,t) \\
[Y_o] &= Y_b(y,t) - 1 \\
\left[\rho_o(s_o - \phi f_{o_t})\right] &= \mu_g f_{o_t} \\
[\eta_o] &= -1 \\
[p_o] &= 0 \\
\left[\frac{\partial \theta_o}{\partial \xi}\right] = \left[\frac{\partial Y_o}{\partial \xi}\right] = \left[\frac{\partial p_o}{\partial \xi}\right] &= 0
\end{aligned} \tag{72}$$

These equations must be considered along with equation (54) for the normal front velocity, where $Y^o(y,t) = Y_b$.

9. Non-adiabatic Case

In this section we consider the temperature profile in the combustion zone for the non-adiabatic case, due to heat losses to the surroundings. Two different cases are considered, one corresponding to convective-type heat losses and another to conductive-type heat losses.

9.1. Convective Heat Losses

Cosider, first, heat losses of the convective type, $\dot{Q}_h = \frac{\tilde{h}}{H}(\tilde{T} - \tilde{T}_o)$, where $\tilde{h}$ is the convective heat transfer coefficient to the surroundings and H is the reservoir thickness. Then, the energy equation reads

$$A_o \frac{\partial \theta_o}{\partial \xi} - \left(1 + f_{oy}^2\right) \frac{\partial^2 \theta_o}{\partial \xi^2} = -h(\theta_o - 1) \tag{73}$$

where h is a dimensionless heat transfer coefficient

$$h = \frac{\tilde{h} t_R}{(1-\phi) c_s \rho_s H} = \frac{\tilde{h} \alpha_s^2}{v_*^2 \lambda H} \tag{74}$$

and $\alpha_s \equiv \frac{\lambda}{(1-\phi)\rho_s c_s}$ is the thermal diffusivity of the medium. The solution of the above is readily found

$$\theta_o = \begin{cases} 1 + (\theta_f(y,t) - 1)\exp\left\{\frac{1}{2}\left(c_1^- + \sqrt{(c_1^-)^2 + 4c_2}\right)\xi\right\} & : \quad \xi < 0 \\ 1 + (\theta_f(y,t) - 1)\exp\left\{\frac{1}{2}\left(c_1^+ - \sqrt{(c_1^+)^2 + 4c_2}\right)\xi\right\} & : \quad 0 < \xi \end{cases}$$

where $c_1^{\pm} = A_o^{\pm}/(1 + f_{oy}^2)$ and $c_2 = h/(1 + f_{oy}^2)$. Note that $\theta_o \to 1$ as $\xi \to \pm\infty$. This solution can then be used to describe the temperature profile inside the combustion zone.

9.2 Conductive Heat Losses

When heat losses occur by conduction to the surrounding formations, in a direction perpendicular to the main flow direction, the heat transfer coefficient is time-dependent. Developing

an expression for this term was considered by Yortsos and Gavalas [27] in terms of an integral of the local temperature history. To formulate the problem in this case, consider, first, the energy balance in an 1-D problem in which heat is transferred by conduction and convection in the x- direction and by conduction in the direction perpendicular to x. In the moving coordinate system $\tilde{\xi} = \tilde{x} - V\tilde{t}$, $\tilde{\varrho} = \tilde{x} - V\tau$, the dimensional energy balance reads

$$(1-\phi)c_s\rho_s\frac{\partial\tilde{T}}{\partial\tilde{t}} + (c_g\rho_g\tilde{v} - (1-\phi)c_s\rho_s V)\frac{\partial\tilde{T}}{\partial\tilde{\xi}} = \lambda\frac{\partial^2\tilde{T}}{\partial\tilde{\xi}^2} - \frac{2\sqrt{(\lambda_h c_h\rho_h)}}{H\sqrt{\pi}}\int_0^{\tilde{t}}\frac{\partial\tilde{T}}{\partial\tau}(\tilde{\varrho},\tau)\frac{d\tau}{\sqrt{(\tilde{t}-\tau)}}. \quad (75)$$

The integral term in the Right-Hand-Side reflects heat losses by lateral heat conduction in an unbounded medium, as expected for an in-situ combustion problem in the subsurface. We consider the steady-state case, $\tilde{t} \to \infty$, for which equation (75) becomes

$$(c_g\rho_g\tilde{v} - (1-\phi)c_s\rho_s V)\frac{\partial\tilde{T}}{\partial\tilde{\xi}} = \lambda\frac{\partial^2\tilde{T}}{\partial\tilde{\xi}^2} + \frac{2\sqrt{(\lambda_h c_h\rho_h V)}}{H\sqrt{\pi}}\int_0^{\infty}\frac{\partial\tilde{T}}{\partial\tilde{\xi}}(\tilde{\sigma}+\tilde{\xi})\frac{d\tilde{\sigma}}{\sqrt{\tilde{\sigma}}}, \quad (76)$$

where $\tilde{\sigma} = \tilde{\varrho} - \tilde{\xi}$. We may use the previous dimensionless notation to express the equation in terms of ξ. For convenience, however, we introduce a slightly different notation and use the variable

$$\xi' = \frac{\xi}{x_*} \quad (77)$$

where

$$x_* = (1-\phi)\rho_s c_s\delta\left(\frac{Hv_*}{2\sqrt{(\lambda_h c_h\rho_h f_t)}}\right)^{2/3} \quad (78)$$

In this notation, we obtain

$$\frac{1}{\bar{\mu}}\frac{\partial\theta}{\partial\xi'} = \frac{\partial^2\theta}{\partial\xi'^2} + \frac{1}{\sqrt{\pi}}\int_0^{\infty}\frac{\partial\theta}{\partial\xi'}(\sigma+\xi'\frac{d\sigma}{\sqrt{\sigma}} \quad (79)$$

where the coefficient $\bar{\mu}$ is defined as

$$\bar{\mu} = \frac{\alpha_s}{(a\rho s - f_t)}\left(\frac{2\sqrt{\lambda_h c_h\rho_h f_t}}{v_* H\lambda}\right)^{\frac{2}{3}} \approx \frac{1}{(a\rho s - f_t)}\left(\frac{2\alpha_s\sqrt{f_t}}{v_* H}\right)^{\frac{2}{3}} \quad (80)$$

where in the approximation we assumed $\alpha_s \approx \alpha_h$. Note that $\bar{\mu}$ is different ahead and behind the front. Defining $\varphi = \partial\theta/\partial\xi'$, equation (79) simplifies to

$$\frac{1}{\bar{\mu}}\varphi(\xi') = \varphi'(\xi') + \frac{1}{\sqrt{\pi}}\int_0^\infty \varphi(\sigma+\xi')\frac{d\sigma}{\sqrt{\sigma}}. \tag{81}$$

Equation (81) is valid on both sides of the combustion front. Its solution, however, depends on the values of ξ'.

1 - Ahead of the Front, $\xi' > 0$

In this region, Equation (81) becomes

$$\frac{1}{\bar{\mu}_+}\varphi_+(\xi') = \varphi'_+(\xi') + \frac{1}{\sqrt{\pi}}\int_0^\infty \varphi_+(\sigma+\xi')\frac{d\sigma}{\sqrt{\sigma}} \tag{82}$$

and is to be solved with the boundary conditions

$$\begin{aligned} \xi' &= 0, \qquad \theta = \theta_f \\ \xi' &\to \infty, \qquad \theta \to 1 \end{aligned} \tag{83}$$

The solution is an exponential

$$\varphi = c_3 \exp(-z_1\xi'), \qquad \xi' > 0 \tag{84}$$

where $z_1 > -1/\bar{\mu}_+$ is the real positive root of the equation

$$\frac{\bar{\mu}_+^2}{z_1} - (1+\bar{\mu}_+ z_1)^2 = 0. \tag{85}$$

Returning to the original notation and integrating we find

$$\theta = 1 + (\theta_f - 1)\exp(-z_1\xi') \tag{86}$$

where θ_f is to be determined.

2 - Behind the Front, $\xi' < 0$

Behind the front the energy balance reads

$$\frac{1}{\bar{\mu}_-}\varphi_-(\xi') = \varphi'_-(\xi') + \frac{1}{\sqrt{\pi}}\int_0^\infty \varphi(\sigma+\xi')\frac{d\sigma}{\sqrt{\sigma}}. \tag{87}$$

to be solved using the boundary conditions

$$\begin{aligned} \xi' &= 0, \qquad \theta = \theta_f \\ \xi' &\to -\infty, \qquad \theta \to 1. \end{aligned} \tag{88}$$

Note that this integro-differential equation also includes information ahead of the front. When the temperature ahead is smooth and there is no discontinuity at the front, we have

$$\frac{1}{\bar{\mu}_-}\varphi_-(\xi') = \varphi'_-(\xi') + \frac{1}{\sqrt{\pi}}\left(\int_0^{-\xi'} \frac{\varphi_-(\sigma+\xi')d\sigma}{\sqrt{\sigma}} + \int_{-\xi'}^\infty \frac{\varphi_+(\sigma+\xi')d\sigma}{\sqrt{\sigma}}\right) \tag{89}$$

which, after integration of the second term in parantheses using (86), becomes

$$\frac{1}{\bar{\mu}_-}\varphi_-(\xi') = \varphi'_-(\xi') + (1-\theta_f)\sqrt{z_1}\,\exp(-z_1\xi')\,\mathrm{erfc}(\sqrt{(-z_1\xi')}) + \frac{1}{\sqrt{\pi}}\int_0^{-\xi'} \frac{\varphi_-(\sigma+\xi')d\sigma}{\sqrt{\sigma}}. \tag{90}$$

Defining $\zeta = -\xi'$, $\varphi_-(\xi') \equiv h(\zeta)$, this further reads

$$\frac{1}{\bar{\mu}_-}h(\zeta) = -h'(\zeta) + (1-\theta_f)\sqrt{z_1}\,\exp(z_1\zeta)\,\mathrm{erfc}(\sqrt{(z_1\zeta)}) + \frac{1}{\sqrt{\pi}}\int_0^\zeta \frac{h(\varrho)d\varrho}{\sqrt{(\zeta-\varrho)}} \tag{91}$$

For simplicity, we will solve this equation by neglecting the conduction term along the flow direction (first term on the RHS). By taking the Laplace transform of Equation (91) we then have

$$H(s) = \left(\frac{(1-\theta_f)\bar{\mu}_-\sqrt{z_1}}{(\sqrt{s}+\sqrt{z_1})(\sqrt{s}-\mu_-)}\right) \tag{92}$$

the inversion of which gives

$$h(\zeta) = \frac{(1-\theta_f)\bar{\mu}_-\sqrt{z_1}}{\bar{\mu}_- + \sqrt{z_1}} \left(\sqrt{z_1}\exp(z_1\zeta)\,\mathrm{erfc}(\sqrt{(z_1\zeta)}) + \bar{\mu}_-\exp(\bar{\mu}_-^2\zeta)\,\mathrm{erfc}(-\bar{\mu}_-\sqrt{\zeta})\right), \tag{93}$$

Thus, after one more integration we find for the temperature behind the front

$$\theta \approx \theta_f - \frac{(1-\theta_f)\bar{\mu}_-\sqrt{z_1}}{\bar{\mu}_- + \sqrt{z_1}} \times \left(\frac{1}{\sqrt{z_1}}[1-\exp(-z_1\xi')\,\mathrm{erfc}(\sqrt{(-z_1\xi')})] - \frac{1}{\bar{\mu}_-}[1-\exp(-\bar{\mu}_-^2\xi')\,\mathrm{erfc}(-\bar{\mu}_-\sqrt{(-\xi')})]\right). \tag{94}$$

To calculate the unknown front temperature, we must find the flux at the front. We have

$$h(0) \equiv \varphi_-(0) = (1-\theta_f)\bar{\mu}_-\sqrt{z_1} \tag{95}$$

which can be used in the energy jump condition (56)

$$h(0) = (1-\theta_f)z_1 + q' f_t^{\frac{2}{3}}, \tag{96}$$

where

$$q' = q\left(\frac{Hv_*}{2\alpha_s}\sqrt{\frac{\lambda(1-\phi)c_s\rho_s}{\lambda_h c_h \rho_h}}\right)^{\frac{2}{3}} \approx q\left(\frac{Hv_*}{2\alpha_s}\right)^{\frac{2}{3}} \tag{97}$$

Thus, we find

$$\theta_f = 1 + \frac{q' f_t^{\frac{2}{3}}}{(z_1 - \bar{\mu}_-\sqrt{z_1})}. \tag{98}$$

Having obtained θ_f, the temperature profiles ahead of and behind the combustion front can be calculated. Before we proceed, we need to mention that in case the temperature ahead of the front is flat and a discontinuity arises at the front, namely if

$$\theta = \mathcal{H}(-\xi')[\theta(\xi') - \infty] + \infty \tag{99}$$

then, the energy balance (87) becomes

$$\frac{1}{\bar{\mu}_-}\varphi_-(\xi') = \varphi'_-(\xi') + \frac{1}{\sqrt{\pi}}\int_0^{-\xi'} \frac{\varphi_-(\sigma+\xi')d\sigma}{\sqrt{\sigma}} - \frac{1}{\sqrt{\pi}}\frac{(\theta_f - 1)}{\sqrt{(-\xi')}} \tag{100}$$

In a subsequent report, we will illustrate the application of the previous results by considering the particular example of a planar front.

10. Concluding Remarks

In this report, we proposed a method for modeling the propagation of combustion fronts in porous media, by treating the reaction region as a place of discontinuities in the appropriate variables, which include, for example, fluxes of heat and mass. The reaction and combustion fronts have a spatially narrow width within which heat release rates, temperatures and species concentrations vary significantly. The narrow width calls for an approach in which these fronts are treated as surfaces of discontinuity.

Using a rigorous perturbation approach, similar to that used in the propagation of flames [4] and smoldering combustion [8], we derived appropriate jump conditions that relate the change in these variables across the front to leading order. The conditions account for the kinetics of the reaction between the oxygen and the fuel, the changes in the morphology of the pore space and the heat and mass transfer in the reaction zone. Then, the modeling of the problem reduces to the modeling of the dynamics of a combustion front, on the regions of either side of which convective transport of momentum (fluids), heat and mass, but not chemical reactions, must be considered. Properties of the two regions are coupled using the derived jump conditions. This methodology allows to explicitly incorporate permeability heterogeneity effects in the process description, without the undue complexity of the coupled chemical reactions.

We derived explicit expressions, which allow to obtain the steady state burning temperature, front velocity and amount of oxygen left unreacted, in terms of the process variables, such as injection rate and pressure. Nonadiabatic combustion fronts are also investigated with two different approaches considering the heat losses to the surrounding with (1) a convective linear term represented by $h\Delta T$ term, and (2) by a conductive integral term.

References

[1] Prats, M.: "Thermal Recovery," *SPE Monograph Series* SPE of AIME (1982).

[2] Boberg, T.C.: "Thermal Methods of Oil Recovery," *An Exxon Monograph Series* (1988).

[3] Willhite, G.P.: "Waterflooding," *SPE Textbook Series* **3** (1986).

[4] Matalon, M. and Matkowsky, B.J.: "Flames as Gasdynamic Discontinuities," *J. Fluid Mech.* (1982) **124** 239-259.

[5] Pelcé, P.: "Dynamics of Curved Fronts," *Academic Press* (1988).

[6] Aldushin, A.P. and Matkowsky, B.J.: "Instabilities, Fingering and the Saffman-Taylor Problem in Filtration Combustion," *Combust. Sci. and Tech.* (1998) **133.**

[7] Li, X. and Yortsos, Y.C.: "Bubble Growth and Stability in an Effective Porous Medium," *Phys. Fluids* (1994) **6** No.5 1663-77.

[8] Schult, D.A., Matkowsky, B.J., Volpert, V.A., and Fernandez-Pello, A.C.: "Forced Forward Smolder Combustion," *Combust. and Flame* (1996) **104** 1-26.

[9] Schult, D.A., Bayliss, A. and Matkowsky, B.J.: "Traveling Waves in Natural Counterflow Filtration Combustion and Their Stability," *SIAM J. Appl. Math.* (1998) **58** No.3 806-852.

[10] Britten, J.A. and Krantz, W.B.: "Linear Stability of Planar Reverse Combustion in Porous Media," *Combust. and Flame.* (1985) **60** 125-240.

[11] Britten, J.A. and Krantz, W.B.: "Asymptotic Structure of Planar Nonadiabatic Reverse Combustion Fronts in Porous Media," *Combust. and Flame.* (1986) **65** 151-161.

[12] Baily, H.R. and Larkin B.K.: "Conduction-Convection in Underground Combustion," *Trans.* AIME (1960) **219** 320-331.

[13] Gottfried, B.S.: "A Mathematical Model of Thermal Oil Recovery in Linear Systems," *SPEJ* (1965) 196-210.

[14] Beckers, H.L. and Harmsen, G.J.: "The Effect of Water Injection on Sustained Combustion in a Porous Medium," *SPEJ* (1970) 231-49.

[15] Burger, J.G. and Sahuquet, B.C.: "Chemical Aspects of *In Situ* Combustion — Heat of Combustion and Kinetics," *SPEJ* (1972) 54-66.

[16] Ağca, C. and Yortsos, Y.C.: "Steady-State Analysis of *In Situ* Combustion," Paper SPE 13624, presented at California Regional Meeting of SPE, Bakersfield, 447-362 (March 27-29 1985).

[17] Armento, M.E. and Miller, C.A.: "Stability of Moving Combustion Fronts in Porous Media," *SPEJ* (1977) 423-430.

[18] Benham A.L. and Poettmann, F.H.: "The Thermal Recovery Process — An Analysis of Laboratory Combustion Data," *Trans.* AIME (1958) **213** 28-35.

[19] Mamora, D.D. and Brigham, W.E.: "Implications of Low Temperature oxidation in Kinetic and Combustion Tube Experiments," UNITAR 6th. Symposium on Heavy Oil and Tar Sands (1995).

[20] Adegbesan, K.O., Donnelly, J.K., Moore R.G. and Bennion, D.W.: "Low-Temperature-Oxidation Kinetic Parameters for *In Situ* Combustion: Numerical Simulation," *SPERE* (1987)

[21] Sibbald, L.R., Moore, R.G. and Bennion, D.W.: "*In Situ* Combustion Process Study with a Combined Experimental/Analytical Approach," *SPERE* (1991)

[22] Belgrave, J.D., Moore, R.G., Ursenbach, M.G. and Bennion, D.W.: "A comprehensive Approach to *In Situ* Combustion Modeling," *Proceedings* (1990) presented at the SPE/DOE 7th. Symposium on Enhanced Oil Recovery in Tulsa, Oklahama.

[23] Moore, R.G., Mehta, S.A., Ursenbach, M.G., Laureshen, C.J.: "Strategies for Successful Air Injection-Based IOR Processes," UNITAR 7th. Symposium on Heavy Oil and Tar Sands (1998).

[24] Lu, C. and Yortsos, Y.C.: "A Pore-Network Model of *In-Situ* Combustion in Porous Media," SPE 69705, Presented at the Society of Petroleum Engineers International Thermal Operations and Heavy Oil Symposium held in Margarita, Venezuela, 12-14 March 2001.

[25] McCabe, W.L., Smith, J.C., Harriott, P.: "Unit Operations of Chemical Engineering," McGraw-Hill 5th. ed. (1993) 929-935.

[26] Zik, O. and Moses, E.: "Fingering Instability in Combustion: An Extended View," *Physical Rev. E* (1999) **60** 1518-1531.

[27] Yortsos, Y.C. and Gavalas, G.R.: "Heat Transfer Ahead of Moving Condensation Fronts in Thermal Oil Recovery Processes," *Int. J. Heat Mass Transfer* (1982) **305** No.3 305-316.

[28] Martin, W.L., Alexander, J.D. and Dew, J.N.: "Process Variabes of In Situ Combustion," *Petroleum Trans.* AIME (1958) **213** 28-35.

IV. HETEROGENEITY AND UPSCALING

The effect of macroscale heterogeneity on displacements, including those of heavy oil is an important consideration. Key issues include the identification of the heterogeneity, and its upscaling. In this section we report on two studies, one on the continuation of a previous effort on the identification of permeability using a passive tracer, and another on the development of a model equation to incorporate heterogeneity effects in both stable and unstable displacements. The work on the identification of permeability is an extension of our previous study for direct inversion to anisotropic porous media. This technique is the first, to our knowledge, that in principle allows to identify the heterogeneity of permeability along the principal axes of anisotropy. The second study provides a new model equation to capture the effect of heterogeneity (noise) on lrge-scale front propagation, by proposing an extension of the so-called KPZ equation. We describe an approach, in which stable and unstable effects can be incorporated using a non-local formalism. The properties of this equation are examined in detail, both for stable and unstable processes. The formalism is generic enough and encompasses processes as diverse as acidization, viscous fingering, combustion front propagation and others.

A DIRECT METHOD FOR THE IDENTIFICATION OF THE PERMEABILITY FIELD

Lang Zhan and Yanis C. Yortsos

Introduction

Permeability heterogeneity is an important feature of natural porous media, as it affects significantly flow and fluid displacement properties. Two main approaches exist for its identification, one based on pressure transients and another on production data. The first approach makes use of the diffusion equation, which governs transient single-phase flow, the second requires the solution of convective flow equations.

The estimation of the heterogeneity from flow displacements, of interest to this chapter, makes use of production data, for example using tracers or produced fluids [*McLaughlin and Townley,* 1996; *Sun,* 1994; *Yeh,* 1986]. Particularly in the field of hydrogeology [*Dassargues,* 2000], permeability estimation is based on the analysis of arrival times in the injection of a passive tracer (namely of tracer that does not affect the fluid viscosity and density) [*Datta-Gupta et al.,* 1998; *Harvey and Gorelick,* 1995; *Vasco and Datta-Gupta,* 1999; *Wagner,* 1992]. The approach relies on the indirect tuning of the permeability heterogeneity at individual points in space to match production data, subject to various available constraints. These techniques are indirect, based on optimizing arbitrary (or constrained) initial guesses to match data at various, usually

sparse, locations. As a result, they suffer from *non-uniqueness*. Nonetheless, useful information can be extracted, which can be used to constrain images of the permeability field.

When knowledge of the displacement front at successive time intervals is available, for example through visual, tomographic or seismic techniques, arrival time methods should in principle be able to provide direct maps of the heterogeneity. Brock and Orr [*Brock and Orr,* 1991] reported such an attempt, based on the visualization of displacements in a 2-D heterogeneous bead pack. Withjack et al. [*Withjack et al.,* 1991] proposed a model to infer the heterogeneity of laboratory samples from concentration contours obtained from X-ray Computerized Tomography (CT). Their model is based on a number of simplifying assumptions, the main of which is that flow streamtubes have constant (but unknown) permeability and porosity, which is tantamount to an assumption of a layered structure. Although restrictive, the work of *Withjack et al.* [1991] was the first to point out the potential of CT in identifying the permeability heterogeneity. CT techniques are now routinely applied to monitor displacement fronts in porous media at the laboratory scale. Advances in the field, for example by seismic methods or cross-hole tomography, are also likely to lead to analogous results at the field scale [*Lumley and Behrens,* 1998]. Yet, well-defined methods to invert this information to determine the permeability heterogeneity are currently lacking.

In a recent publication [*Zhan and Yortsos,* 2000] we proposed a direct method for the inversion of the permeability field of an isotropic porous medium based on the analysis of the displacement of a passive tracer. By monitoring the front at successive time intervals, the permeability can be directly obtained from the solution of a non-linear boundary-value problem. Well-posedness requires knowledge of the pressure profile or the permeability at the boundaries of the system, however. This may restrict the applicability of the method to laboratory applications. The method was tested using synthetic data in 2-D (and some 3-D) geometries for a variety of heterogeneous fields and found to work well when the permeability contrast is not too large.

In this chapter, we extend the direct approach to infer the permeability

heterogeneity of anisotropic porous media, which constitute a large fraction of natural rocks. Identifying anisotropic permeability tensors is difficult. In the homogeneous case, approaches for laboratory applications were summarized by *Scheidegger* [1974]. Estimation on the field relies on interference or pulse tests. Based on research by *Papadopoulos* [1965], Ramey proposed an interference testing method to estimate properties of anisotropic but homogeneous media [*Ramey,* 1975]. Earlier, Earlougher and Kersch applied an automatic regression method for a similar problem [*Earlougher and Kersch,* 1972; *Earlougher,* 1975]. To our knowledge, the identification of the heterogeneity of anisotropic porous media is currently an open problem. This chapter provides a direct method, based on the injection of a passive tracer, which represents an extension of our previous work. When the principal axes of anisotropy are known and fixed, a procedure is proposed, in which the tracer is injected two (or three) consecutive times along the two (or three) principal directions (for the case of a 2-D (or 3-D) problem, respectively). The diagonal components are obtained from the solution of two (or three) coupled boundary-value problems involving the experimentally obtained arrival times. When the permeability tensor is full and the principal axes vary in space, we propose a procedure involving injection in three different directions (for the case of a 2-D problem). In principle, the components of the permeability tensor can be determined from the solution of three coupled boundary-value problems.

The chapter is organized as follows: The first section provides the theoretical background. We summarize the approach for isotropic media described in [*Zhan and Yortsos,* 2000] and propose an extension for the anisotropic case, in two different cases, when the tensor is diagonal and when it is not. Then, we provide numerical examples to illustrate the applicability of the method. We show examples for both isotropic [*Zhan and Yortsos,* 2000] and anisotropic media. Although the theory is in principle applicable to 3-D, we restrict the examples only to two-dimensional problems (a 3-D isotropic problem was solved in [*Zhan and Yortsos,* 2000]).

Theory

Consider the injection of a passive tracer in a heterogeneous porous medium. In the following, we will assume that all quantities are appropriately normalized, so that they can be considered as dimensionless. In this notation, all injection problems correspond to injection pressure of 1 and production pressure of 0. In the absence of dispersion, the concentration $C(\mathbf{x}, t)$ satisfies the equation

$$\phi(\mathbf{x})\frac{\partial C}{\partial t} + \mathbf{v} \cdot \nabla C = 0 \tag{1}$$

where $\phi(\mathbf{x})$ is the porosity of the medium and $\mathbf{v}$ is the superficial fluid velocity. The smallness of molecular dispersion in favor of dispersion due to the permeability heterogeneity is expected to be satisfied in most cases. Under slow, viscous flow conditions, the latter satisfies Darcy's law

$$\mathbf{v} = -\mathbf{K} \cdot \nabla \Phi \tag{2}$$

and the continuity equation

$$\nabla \cdot \mathbf{v} = 0 \tag{3}$$

assuming incompressible fluids. Here, $\mathbf{K}(\mathbf{x})$ is the (symmetric) permeability tensor, and Φ is a flow potential, $\nabla\Phi = \frac{1}{\mu}(\nabla p - \rho \mathbf{g})$, where μ is viscosity, taken as a constant; p is pressure, ρ is density, also assumed constant, and $\mathbf{g}$ is the acceleration of gravity. For isotropic media $\mathbf{K}(\mathbf{x}) = k(\mathbf{x})\mathbf{I}$, where $\mathbf{I}$ is the identity tensor. In the anisotropic case, the tensor is full in general. In the absence of dispersion, we define a front location by the equation

$$\mathcal{F}(\mathbf{x}, t) \equiv t - f(\mathbf{x}) = 0 \tag{4}$$

where, assuming constant or monotonic injection rates, the function $f(\mathbf{x})$ is single-valued, thus associated with a given point $\mathbf{x}$ is a single arrival time.

Consider, first, a diagonal permeability tensor, which in 2-D reads

$$\mathbf{K} = \begin{pmatrix} k_{xx} & 0 \\ 0 & k_{yy} \end{pmatrix} \tag{5}$$

Upon projection of the velocity $\mathbf{v}$ to the front normal $\mathbf{n}$, we obtain

$$v_n = -(\mathbf{K}\nabla \cdot \Phi) \cdot \frac{\nabla \mathcal{F}}{|\nabla \mathcal{F}|} \tag{6}$$

where we used Darcy's law and the expression for the normal at the front,

$$\mathbf{n} = \frac{\nabla \mathcal{F}}{|\nabla \mathcal{F}|} \tag{7}$$

¿From kinematics, we also know that the front normal velocity, v_n, is given by

$$v_n = -\phi(\mathbf{x}) \frac{\mathcal{F}_t}{|\nabla \mathcal{F}|} \tag{8}$$

This equation can be derived simply by taking the following solution of (1)

$$C = H(\mathcal{F}) \tag{9}$$

where $H(z)$ is the Heaviside step function. Then, by inserting in (1), one obtains

$$\mathcal{F}_t \phi(\mathbf{x}) \delta(\mathcal{F}) + \mathbf{v} \cdot \nabla \mathcal{F} \delta(\mathcal{F}) = 0 \tag{10}$$

where $\delta(z)$ is the delta function. Integrating across the front and using (7), equation (8) follows.

¿From the two expressions (7) and (8) and using (4), we find that the permeability of the anisotropic porous media satisfies the following equation

$$(\mathbf{K}\nabla \cdot \Phi) \cdot \nabla f = -\phi(\mathbf{x}) \tag{11}$$

The potential is to be obtained by substituting *Darcy's* law (2) into the mass balance equation (3), hence

$$\nabla \cdot (\mathbf{K} \cdot \nabla \Phi) = 0 \tag{12}$$

In the isotropic case, equations (11) and (12) reduce to

$$k(\mathbf{x}) = -\frac{\phi(\mathbf{x})}{\nabla \Phi \cdot \nabla f} \tag{13}$$

and

$$\nabla \cdot \left[\frac{\phi(\mathbf{x}) \nabla \Phi}{\nabla \Phi \cdot \nabla f} \right] = 0 \tag{14}$$

respectively. The latter can be solved given the porosity and the arrival time function f (both from CT measurements). Then, one can obtain a direct expression for the permeability [*Zhan and Yortsos,* 2000].

The two equations (11) and (12) constitute the keys of the direct inversion method for anisotropic porous media. However, in contrast to the isotropic case, the two equations form a system of two equations in three unknowns (k_{xx}, k_{yy} and Φ), thus requiring additional information for their solution. One approach by which this information can be obtained, is by conducting two tracer displacements, one in the x-direction with no-flow boundaries perpendicular to the y-axis, and another in the y-direction with no-flow boundaries perpendicular to the x-axis. If we denote the arrival time functions and the potentials of the two displacements by f^1 and f^2, and Φ^1 and Φ^2, respectively, application of Eq. (11) twice gives

$$k_{xx} \frac{\partial \Phi^1}{\partial x} \frac{\partial f^1}{\partial x} + k_{yy} \frac{\partial \Phi^1}{\partial y} \frac{\partial f^1}{\partial y} = -\phi \tag{15}$$

$$k_{xx} \frac{\partial \Phi^2}{\partial x} \frac{\partial f^2}{\partial x} + k_{yy} \frac{\partial \Phi^2}{\partial y} \frac{\partial f^2}{\partial y} = -\phi \tag{16}$$

for the respective displacements. Then, the permeability components can be determined from

$$k_{xx} = -\frac{\phi}{A}\left[\frac{\partial \Phi^2}{\partial y}\frac{\partial f^2}{\partial y} - \frac{\partial \Phi^1}{\partial y}\frac{\partial f^1}{\partial y}\right] \tag{17}$$

and

$$k_{yy} = -\frac{\phi}{A}\left[\frac{\partial \Phi^1}{\partial x}\frac{\partial f^1}{\partial x} - \frac{\partial \Phi^2}{\partial x}\frac{\partial f^2}{\partial x}\right] \tag{18}$$

where

$$A = \frac{\partial \Phi^1}{\partial x}\frac{\partial f^1}{\partial x}\frac{\partial \Phi^2}{\partial y}\frac{\partial f^2}{\partial y} - \frac{\partial \Phi^2}{\partial x}\frac{\partial f^2}{\partial x}\frac{\partial \Phi^1}{\partial y}\frac{\partial f^1}{\partial y} \tag{19}$$

given the data f^1 and f^2, and the calculated potentials Φ^1 and Φ^2. The latter are obtained by solving equation (12), with k_{xx} and k_{yy} given by (17)-(19), and with the appropriate boundary conditions corresponding to the two different displacements. The resulting coupled system was solved using the following iterative algorithm:

1. Based on the ν-level estimates for the potentials $\Phi^{1,\nu}$ and $\Phi^{2,\nu}$, use Equations (17) and (18) to estimate the ν-level iterates k_{xx}^{ν} and k_{yy}^{ν}. At the initial level ($\nu = 0$), an initial guess, typically in the form of a linear variation, was supplied for the potentials.

2. Based on explicit (ν-level) estimates for k_{xx}^{ν} and k_{yy}^{ν}, integrate (12) twice, using finite differences to calculate the potentials at the next iteration level, $\Phi^{1,\nu+1}$ and $\Phi^{2,\nu+1}$.

In the above index ν denotes the level of iteration in the iterative solution of the coupled problem. A similar construction applies for the 3-D case.

This algorithm was found to work well for the various cases tested in which the permeability variation is small to moderate. For example, in correlated permeability fields in the isotropic case, the algorithm was found to be successful when the standard deviation did not exceed 0.6 for a dimensionless correlation length (compared to the total system length) smaller than 0.25. Larger variances and/or smaller correlation

lengths lead to increasing errors. For cases with sharp permeability contrast, errors in the calculation of the derivatives of the arrival time may cause significant errors in the estimation of the permeability, as well. In the isotropic case, we used forward and backward displacements and inversions, *kriging* interpolation, and optimization to improve the direct inversion results. Such an approach is also needed here for the case of sharp contrasts. The hybrid algorithm is an extension of the isotropic case and is described as follows:

1. Carry out two tracer displacements in the positive x and y directions (where the convention of positive or negative is arbitrary); directly invert to obtain a first pair of permeability estimates, $k^1_{xx}(\mathbf{x})$ and $k^1_{yy}(\mathbf{x})$, from the anisotropic inversion equations (17) and (18) or from the isotropic inversion equations (14) and (13).

2. Carry out two tracer displacements in the reverse (negative) directions; directly invert to obtain a second pair of permeability estimates, $k^2_{xx}(\mathbf{x})$ and $k^2_{yy}(\mathbf{x})$ from the anisotropic inversion equations (17) and (18) or from the isotropic inversion equations (14) and (13).

3. Retain the estimates of k_{xx} and k_{yy} in those places, where they differ in absolute value by no more than a prescribed value, and discard in all others. Assign estimates in these regions by a *kriging* interpolation algorithm.

4. Use an optimization algorithm to fine-tune the so obtained composite permeability estimates.

In typical applications, the fraction of discarded permeability values was of the order of 10% of the total. The optimization algorithm is based on standard gradient methods [*Tarantola,* 1987] and its details are provided in [*Zhan,* 2000]. The objective function can be exactly formulated as that for the isotropic case

$$\mathcal{J} = \frac{1}{2}\{[\mathbf{f}(\mathbf{k})-\mathbf{f}^m]^T\mathbf{W}_1[\mathbf{f}(\mathbf{k})-\mathbf{f}^m]+[\mathbf{k}-\mathbf{k}^p]^T\mathbf{W}_2[\mathbf{k}-\mathbf{k}^p]+[\mathbf{\Phi}_b-\mathbf{\Phi}_b{}^p]^T\mathbf{W}_3[\mathbf{\Phi}_b-\mathbf{\Phi}_b{}^p]\} \quad (20)$$

where the first term on the right-hand side denotes the weighted square errors between the front arrival time from the simulator output, $\mathbf{f}$, and the measured data $\mathbf{f}^m$, and the third term is the analogous term for the differences between the potential at the no-flow boundaries obtained from the simulator, $\mathbf{\Phi}_b$, and the measured data, $\mathbf{\Phi}_b^m$. The second term is a regularization term (for example, see [*Tarantola,* 1987]). It represents the mismatch between the current permeability estimate $\mathbf{k}$ and its prior information $\mathbf{k}^p$. $\mathbf{W_1}, \mathbf{W_2}$, and $\mathbf{W_3}$ are weighted coefficient matrices. The "fine-tuning" of the directly inverted results using the optimization algorithm is typically beneficial and should be used whenever possible. The reduction in the overall estimation error will be illustrated below with a specific example.

Sometimes, a practical alternative to the above algorithm was considered. For example, in some cases we found that adequate estimates of the components along the principal directions can be obtained by applying the isotropic inversion method, given in equations (14) and (13), namely by neglecting the y- or x- components in equations (15) and (16), respectively. This decouples the equations for k_{xx} and k_{yy}, reduces the complexity of the problem and contains smaller numerical errors, particularly when the permeability variations are large. Examples will be shown in a later section.

Before we proceed, we should also briefly mention the case of a full permeability tensor, which in 2-D reads

$$\mathbf{K} = \begin{pmatrix} k_{xx} & k_{xy} \\ k_{xy} & k_{yy} \end{pmatrix} \tag{21}$$

and where a symmetric tensor was implied. Equations (11) and (12) still hold. Now, however, we have an additional component, the determination of which requires that a displacement in a third direction is carried out. In principle, one can conduct three displacements, along say the horizontal, the vertical and the diagonal directions. If we denote arrival times and potentials by f^1, f^2, f^3, Ψ^1, Ψ^2 and Ψ^3, respectively, equation (11) reads

$$k_{xx}\frac{\partial\Phi^i}{\partial x}\frac{\partial f^i}{\partial x}+k_{xy}(\frac{\partial\Phi^i}{\partial y}\frac{\partial f^i}{\partial x}+\frac{\partial\Phi^i}{\partial x}\frac{\partial f^i}{\partial y})+k_{yy}\frac{\partial\Phi^i}{\partial y}\frac{\partial f^i}{\partial y}=-\phi \tag{22}$$

where $i = 1, 2, 3$. From this set of equations, the three permeability components can be expressed in terms of the three potentials and their derivatives. The latter solve equation (12) for each respective displacement with k_{xx}, k_{xy} and k_{yy} calculated from (22). An iteration algorithm is required, the details of which can be found in [*Zhan,* 2000].

Numerical Examples

Isotropic Permeability

We first show some results illustrating the applicability of the direct method. We consider tracer displacement in a log-normally distributed permeability field, with a (dimensionless) logarithmic mean of 2.0, a standard deviation of 0.5 and a dimensionless correlation length (with respect to the total system length) of 0.25 (Figure 1). Arrival times as a function of position and pressure profiles at the boundaries were calculated using a finite-difference simulator with a flux limiter (see [*Zhan and Yortsos,* 2000] for details). In the 2-D case, a square lattice of size $L \times L$ was used for the calculation of the arrival times and the boundary pressures, and the same lattice was used for the direct inversion. Values of L equal to 8, 16, 32 and 64 were used in various applications. In the example shown in Figure 1 the lattice used was 16× 16. In this example, the permeability contrast is sufficiently large and requires the use of the hybrid algorithm. Application of the direct inversion method for displacement in two directions (back-and-forth), as described above, followed by kriging leads to the results shown in Figure 1. We note that although this step captures general long-wavelength features

of the permeability field, notably the places of relatively large and relatively small permeabilities, the estimated values are generally coarser and smoother than the actual. For fine-tuning, we applied the optimization algorithm. The results after 40 iterations are shown in Figure 1. Although the algorithm does not fully reproduce the actual field, the improvement is notable. A statistical analysis of the results (not shown here) indicates that histograms and semi-variograms are also well reproduced. Scatter plots also show good agreement, with the exception of large values of permeabilities where the scatter is larger. As pointed out by *Zhan and Yortsos* [2000], the successful matching reflects the good initial guess given to the optimization algorithm at the completion of the kriging step. By contrast, the estimates obtained by directly using optimization with a uniform initial guess for the permeability field were quite poor, even though arrival times and potential matched quite well with the data. Additional results for the isotropic case can be found in [*Zhan and Yortsos,* 2000].

Anisotropic Permeability

Consider, next, the applicability of the direct method to an anisotropic permeability field. We will focus mostly on the diagonal tensor case. For the latter, the permeability field shown in Figures 2 and 3 was used as a numerical example. Here, the principal directions of the permeability are assumed to be known and to coincide with the x and y axes. The statistics of k_{xx} and k_{yy} correspond to a log-normal, spatially correlated distribution with logarithmic means equal to 2.0 (for k_{xx}) and 3.0 (for k_{yy}), respectively, standard deviation of 0.2 and correlation length of 0.25. A 16$\times$ 16 lattice was used. By simulating a forward tracer displacement in the two directions, left-to-right and top-to-bottom, respectively, we obtained arrival time functions (solid lines, panels (a) and (c) of Figure 4) and potentials (solid lines, panels (b) and (d) of Figure 4). The arrival times in all locations and the potentials at the no-flow boundaries were subsequently used for inversion according to the scheme described above. The full anisotropic inversion equations (17) and (18) were used in the calculation.

The directly inverted permeability fields (in the *absence* of optimization or kriging) are shown in the panels in the right in Figures 2 and 3. Corresponding arrival times and potentials (dash-dotted lines) compared to the actual values (solid lines) are shown in Figure 4. Given the coupled nature of the problem, the reconstruction of the two permeability components can be considered generally good. The method reproduces well the regions of high and low permeability, although some additional fine-tuning would be desirable. Compared to the isotropic case under the same permeability contrast, the reconstruction is not as sharp, and the projections of the inverted images appear slightly "blurry" in certain places. This inaccuracy reflects the underlying mismatch between the actual (solid lines) and the inverted potential profiles (dash-dotted lines) in Figures 4 (b) and (d). There is also some mismatch in the arrival time contours between the actual (solid lines) and the directly inverted fields (dash-dotted lines) in Figures 4 (a) and (c). Relative errors of the inverted fields for this example are plotted in Figure 5. Most blocks have relative error less than 15% and the largest is about 28%. For further improvement we applied optimization. In this particular example, the resulting improvement was not major. Figure 6 shows the permeability fields along the principal axes, after the application of optimization. Corresponding arrival time and pressure contours (dotted lines) are shown in Figure 4. The dotted lines almost coincide with the dash-dotted lines, reflecting some improvement. Relative errors in the permeability fields are shown in Figure 7. The largest relative error of the optimized results is still about 27%, although the estimate of the permeability of some blocks has improved to some extent. However, the improvement does depend on the realization, as will be shown below, as well as on the size of the grid. For example, substantial improvement following the application of the hybrid method and after the optimization step was found when the grid was coarser (8×8).

To illustrate the benefit of optimization following the direct inversion method, and to also compare against the results in which optimization was applied to a uniform initial guess (namely without using the direct algorithm), we estimated the permeability field in ten different realizations obeying the same statistics. Figure 8 shows the

estimation error for the three different cases, namely using direct inversion (circles), using optimization following direct inversion (crosses) and using optimization based on a uniform initial guess (stars). It is apparent that the relative improvements depend on the realization of the permeability field. The optimization following direct inversion outperforms the other two in almost all cases. On average, the direct method seems to be the least successful in the estimation of the x-permeability component, although this is not the case in the estimation of the y-permeability component, where on average it does about as well as the optimization with a uniform initial guess.

We must note that in all these examples, only step 1 and step 4 of the hybrid algorithm were used. Back-and-forth displacements were not used. As the permeability contrast increases, the solution of equations (17) and (18) is subject to increasing errors. Then, the other pairs of displacement and inversion (step 2) as well as kriging interpolation (step 3) must also be used. Alternatively, in same cases the isotropic inversion method may be utilized to decouple the solutions of the two diagonal permeability elements, as described above. The underlying reason is that in displacements along the respective principal directions with no-flow boundary conditions along the other direction, the pressure profiles are almost vertical, suggesting a small contribution to the transverse flow (see for example equation (4)). Figure 9 shows the results of such an inversion approach assuming an isotropic medium, for the anisotropic medium shown in the left panels of Figures 2 and 3. The largest relative error was found to be about 30%. In general, we note a quite good agreement with the true distributions, despite the fact that here the isotropic inversion method was used.

Before closing, we mention briefly the application of the technique to the estimation of the full permeability tensor. For this, we considered a log-normal anisotropic permeability field with correlation length 0.5, and natural logarithmic means of about 3.0, 2.0 and 1.0, and standard deviations of about 0.2, 0.3 and 0.3, for k_{xx}, k_{yy} and k_{xy}, respectively. The three components of the actual field are shown in panels (a)-(c) in Figure 10. Left-to-right, top-to-bottom and diagonal displacements were conducted. The diagonal displacement consisted of injecting at one of the corners of the sample

and producing at the opposite corner, with no-flow boundary conditions imposed on all other boundaries, in essence resembling a quarter of a five-spot geometry. Because of significant numerical difficulties, associated with the solution of the process of diagonal injection in anisotropic systems, however, we used alternative isotropic inversion method, applied consecutively to the left-to-right and top-to-bottom displacement data. This method takes advantage of the fact that when the off-diagonal component is relatively small, the displacement problem in each direction can be approximated as that in an isotropic medium (see [*Zhan,* 2000] for details).

Inverted diagonal permeability components are shown in Figure 10. The estimated fields, k_{xx} and k_{yy}, have features similar to those of the directly inverted results in previous examples, namely, they miss high-frequency variations, being smoother than the actual, but they preserve those of large-wavelength. The inverted field for the diagonal component has the correct high values in the upper-right corner and the middle of the sample, but is in error in the lower-left corner, in which the inverted values are too high. This demonstrates the difficulty in the accurate inversion of the full anisotropic permeability tensor. It must be pointed out, however, that although not accurate in various places, the inverted permeabilities provide good arrival time and potential responses in comparison with the actual in the diagonal displacement [*Zhan,* 2000].

An application of the direct inversion method to real systems was not attempted due to the lack of data of spatially variable anisotropic systems. As the method was described, it is obviously better suited for the estimation of the permeability tensor in laboratory applications, where displacements in various directions can be conducted without much difficulty. For the diagonal tensor case, field applications would require carrying out displacements in two directions that are not parallel. With the use of vertical wells, the inversion algorithm should be suitably modified, to account for the different geometry, compared to the rectilinear geometry used in this chapter. In addition, the technique requires the availability of boundary pressure data. We acknowledge that these can be more easily available in the laboratory rather than in

the field. In the absence of such data, one alternative would be to use a linear (or the appropriate to the particular geometry) pressure drop, as an approximation. How would this affect the estimation error is currently being investigated.

Conclusions

In this chapter, we extended a direct inversion method presented in [*Zhan and Yortsos,* 2000], based on the injection of a passive tracer, to estimate the components of the permeability tensor in anisotropic and heterogeneous porous media. For a 2-D medium, the proposed extension requires for a 2-D medium carrying out two (or three) displacements, when the tensor is diagonal (or full). These displacements provide the arrival times and boundary pressure profiles, which are needed for the solution of appropriate boundary value problems, from which the permeability components are computed.

For the diagonal tensor case, numerical examples show that the algorithm works well for small to moderate permeability variations. In general, the technique captures well variations corresponding to larger permeability wavelengths, but not as well the fine-scale details. For the latter, as well as for larger permeability variations, a hybrid algorithm that includes conducting additional displacements in the reverse direction, subsequent kriging interpolation and optimization, can be used to improve the accuracy of the estimates. It was also found that application of the isotropic inversion method to the two displacements along the two principal directions in anisotropic systems, even though in theory inappropriate, does provide good estimates of the diagonal permeability components in cases where the permeability contrast is not too large.

For the case of a full permeability tensor, an inversion approach based on three different displacements was proposed (right-to-left, top-to-bottom, diagonal). It was found to be sensitive to numerical errors due to the difficulty of accurate solving the

diagonal injection problem in an anisotropic system. Implementing a more practical method based on isotropic inversion gives reasonably good results that reproduces the large correlation features of the actual field. These examples show that the accurate inversion of the permeability heterogeneity of a fully anisotropic medium from arival time data remains a difficult task. Additional research is under way to improve on the technique presented and on its application in 3-D.

Notations

A	expression in (19)
C	concentration
f	arrival time distribution
$\mathcal{F}$	tracer front function
$\mathcal{F}_\sqcup$	derivative of tracer front function with respect to time
$\mathbf{I}$	identity tensor
$\mathcal{J}$	objective function
k_{xx}	x component of absolute permeability tensor
k_{yy}	y component of absolute permeability tensor
k_{xy}	diagonal component of absolute permeability tensor
$\mathbf{K}$	permeability tensor
t	time
$\mathbf{v}$	fluid velocity
v_n	front normal velocity
$\mathbf{W_i}$	weight coefficient matrices
$\mathbf{x}$	spatial coordinate
μ	fluid viscosity
ν	iteration index
ρ	fluid density
ϕ	porosity
Φ	potential
Φ_b	boundary potential

References

Brock, D. C. and F. M. Orr, Flow visualization of viscous fingering in heterogeneous porous media, SPE 22614 presented at 66th SPE Annual Technical Conference and Exhibition, Dallas, Texas, October 6-9, 1991.

Dassargues, A. (Eds.), *Tracers and modeling in Hydro-geology*, Proceedings of conference TRAM 2000, Liege, Belgium, May 23-25, 2000.

Datta-Gupta, A., S. Yoon, I. Barman and D. W. Vasco, Streamline-based production data integration into high resolution reservoir models, *JPT 50(12)*, 72-77, 1998.

Earlougher, R. C., Further discussion of interference analysis for anisotropic formations - A case history, *JPT 27(12)*, 1525, 1975.

Earlougher, R. C. and K. M. Kersch, Field examples of automatic transient test analysis, *JPT 24(10)*, 1271-1277, 1972.

Harvey, C. F. and S. M. Gorelick, Mapping hydraulic conductivity: sequential conditioning with measurements of solute arrival time, hydraulic head, and local conductivity, *Water Resource Res. 31(7)*, 1615-1626, 1995.

Lumley, D. E. and R. A. Behrens, Practical issues of 4-D seismic reservoir monitoring: What an engineer needs to know, *SPEREE 1*, 528-538, Dec. 1998.

McLaughlin, D. and L. R. Townley, A reassessment of the groundwater inverse problem, *Water Resource Res. 32(5)*, 1131-1161, 1996.

Papadopoulos, I. S., Non-steady flow to a well in an infinite anisotropic aquifer, Proceeding of 1965 Dubrovnik Syposium on Hydrology of Fractured Rocks., International Assoc. of Sci. Hydrology, 1965.

Ramey, H. J., Interference analysis for anisotropic formations - A case history, *JPT 27(10)*, 1290-1298, 1975.

Scheidegger, A. E. *The Physics of Flow Through Porous Media*, University of Toronto Press, Toronto, Canada, 1974.

Sun, N. Z. *Inverse Problems in Groundwater Modeling*, Kluwer Academic Publishers, Netherlands, 1994.

Tarantola, A. *Inverse Problem Theory: Methods for Data Fitting and Model Parameter Estimation*, Elsevier Science Publishers, Amsterdam, 1987.

Vasco, D. W. and A. Datta-Gupta, Asymptotic solutions for solute transport: A formalism for tracer tomography, *Water Resource Res. 35(1)*, 1-16, 1999.

Wagner, B. J., Simultaneous parameter estimation and contaminant source characterization for coupled groundwater flow and contaminant transport modeling, *J. Hydrology 135* 275-303, 1992.

Withjack, E. M., S. M. Grahamand and C-T. Yang, CT determination of heterogeneities and miscible displacement characteristics, *SPEFE 7*, 447-52, Dec. 1991.

Yeh, W. G., Review of parameter identification procedures in groundwater hydrology: The inverse problem, *Water Resources Res. 22(2)*, 95-108, 1986.

Zhan, L. *Identification of the Permeability Heterogeneity of a Porous Medium by Passive Tracer Displacement*, Ph. D. Disseration, University of Southern California, Los Angeles, CA., August, 2000.

Zhan, L. and Y. C. Yortsos, Identification of the permeability field of a porous medium from the injection of a passive tracer, *Physical Review E. 62(1)*, 863-879, 2000.

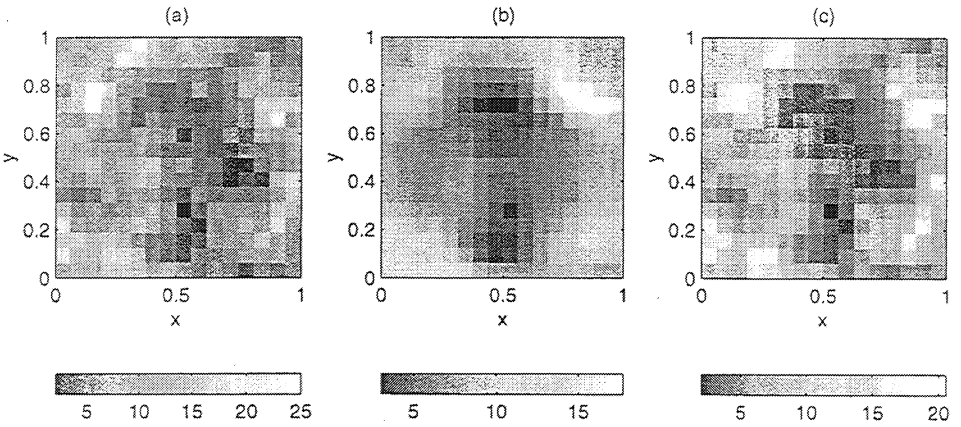

Figure 1. Application of the direct inversion method to an isotropic field: (a)-(b) plots of the actual permeability component values; (c)-(d) plots of the inverted permeability estimates after steps 1-3 (kriging); (e)-(f) plots of permeability estimates after step 4 (optimization).

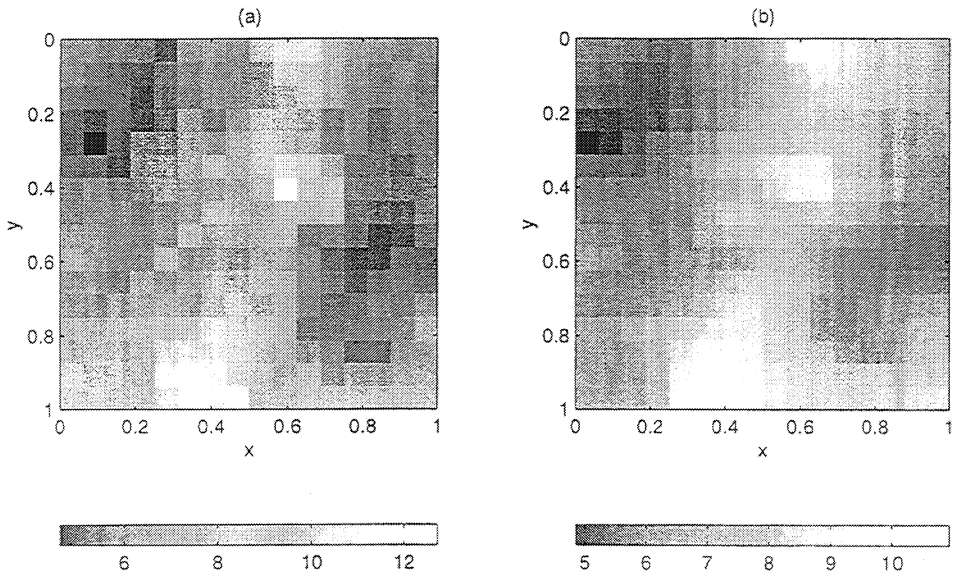

Figure 2. Application of the direct inversion method to an anisotropic field with known and fixed principal axes of anisotropy. Results for k_{xx}: (a) actual permeability component values; (b) inverted permeability after step 1.

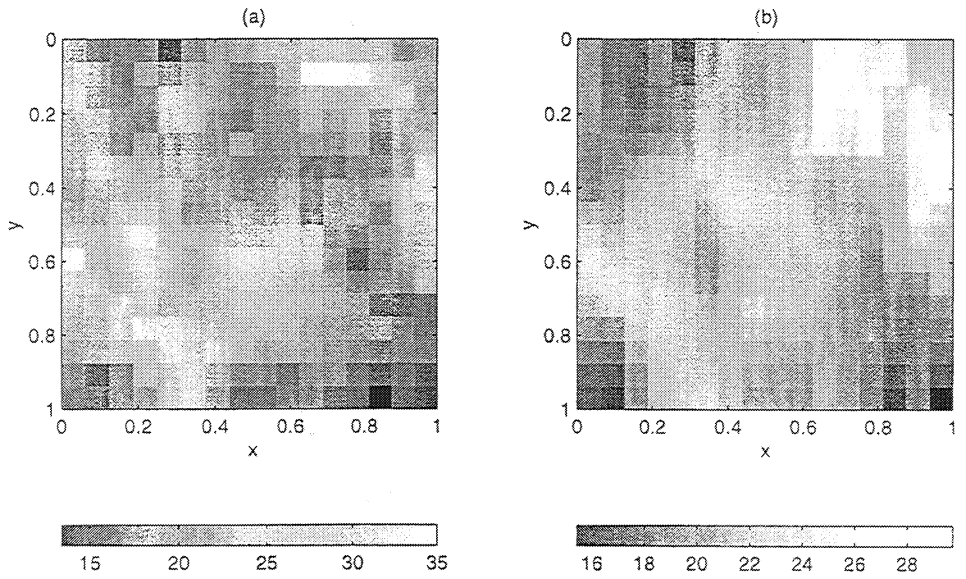

Figure 3. Application of the direct inversion method to an anisotropic field with known and fixed principal axes of anisotropy. Results for k_{yy}: (a) actual permeability component values; (b) inverted permeability after step 1.

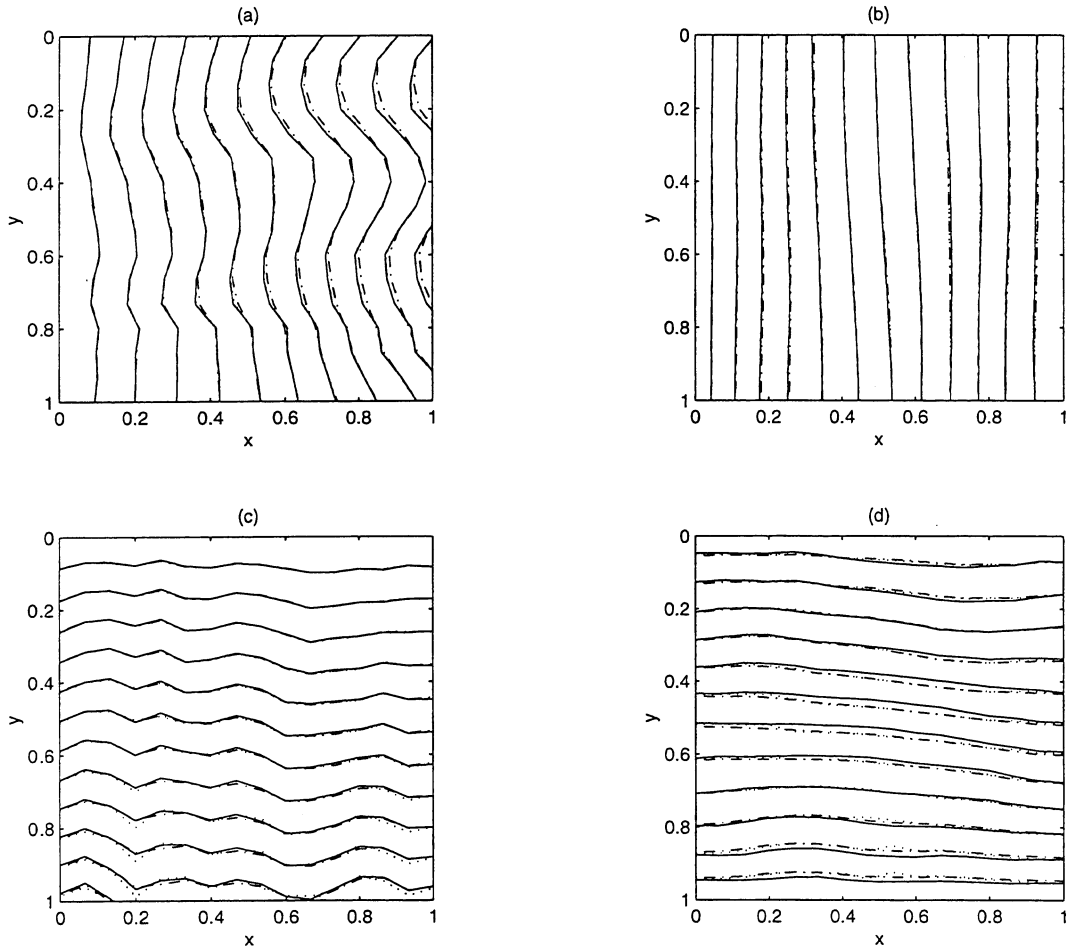

Figure 4. Arrival time and potential contours corresponding to the actual (from numerical simulation) (solid lines), directly inverted (dash-dotted lines) and optimized (dotted lines) results: (a) arrival time of left-to-right displacement; (b) potential of left-to-right displacement; (c) arrival time of top-to-bottom displacement; (d) potential of top-to-bottom displacement.

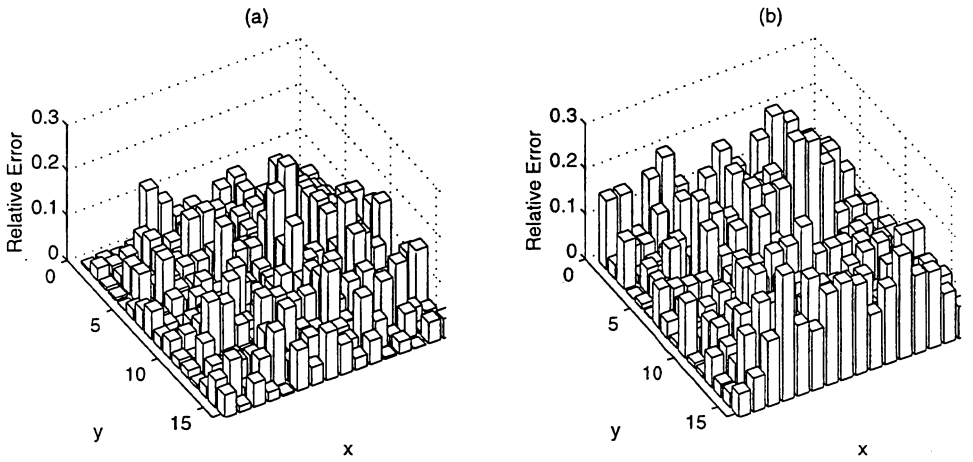

Figure 5. Errors obtained during direct inversion: (a) relative errors of estimated k_{xx}; (b) relative errors of estimated k_{yy}.

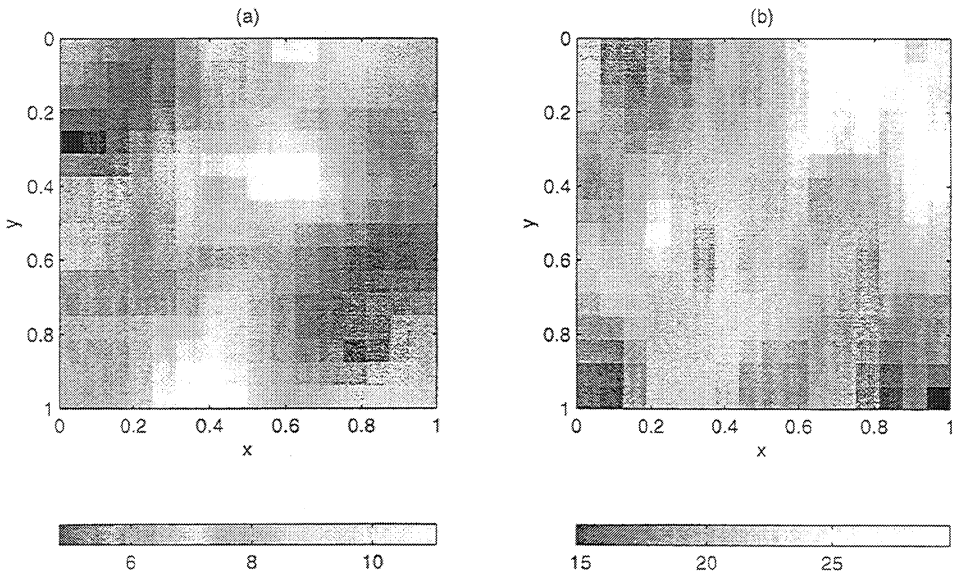

Figure 6. Application of the direct inversion method to an anisotropic field with known and fixed principal axes of anisotropy, after step 4 of the hybrid algorithm. (a) optimized k_{xx}; (b) optimized k_{yy}.

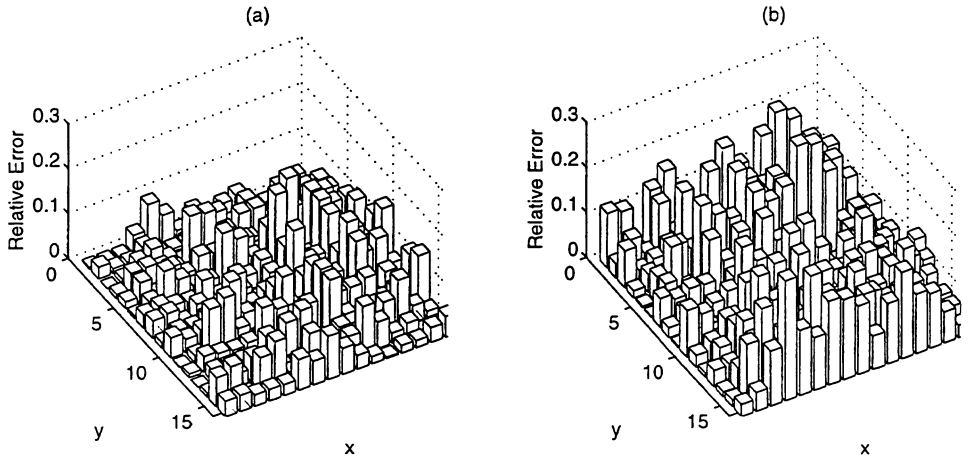

Figure 7. Errors obtained after optimization: (a) relative errors of estimatedk_{xx}; (b) relative errors of estimated k_{yy}.

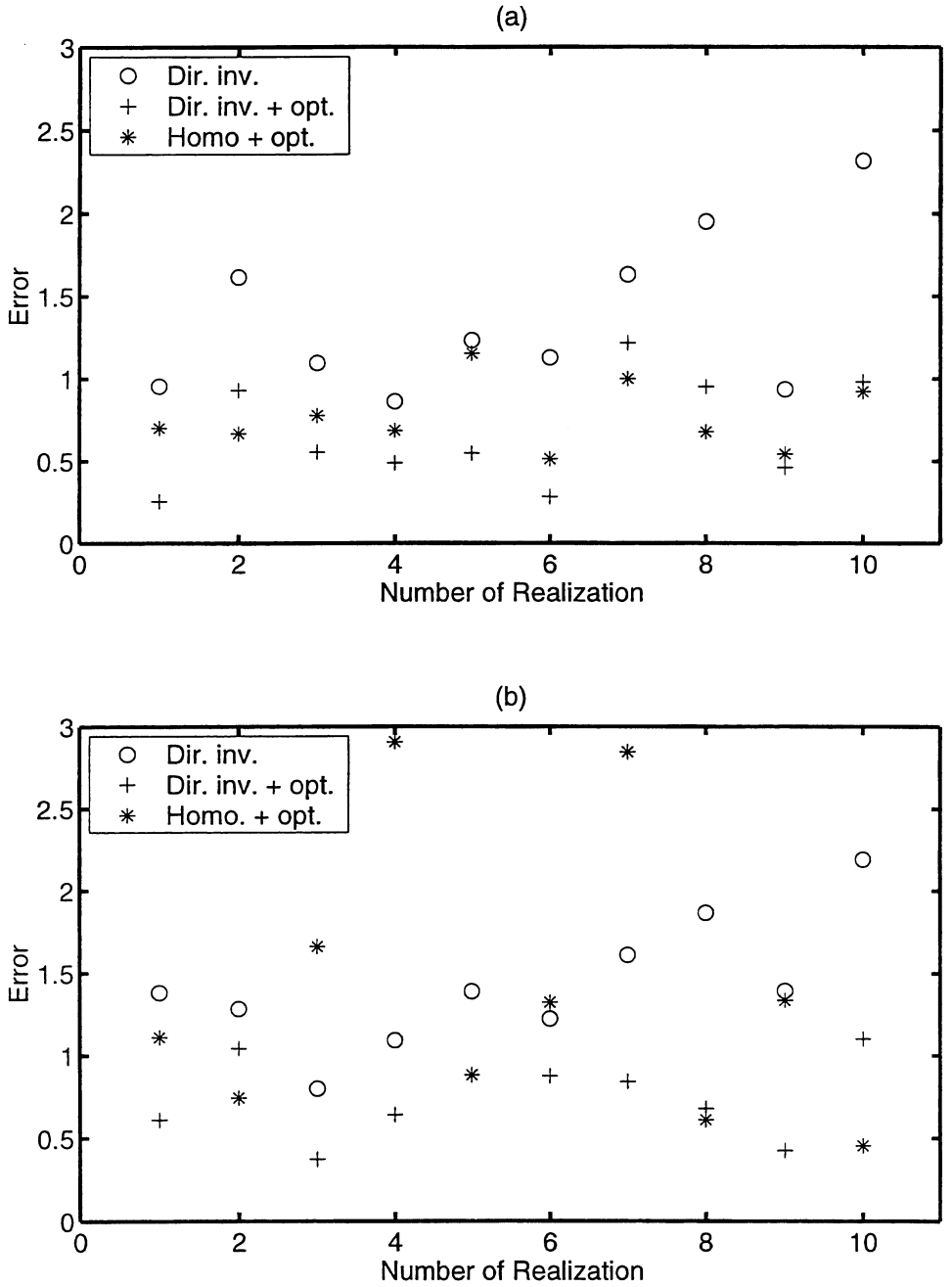

Figure 8. Absolute errors using direct inversion (circles), optimization following direct inversion (crosses) and optimization based on a uniform initial guess (stars) for ten different realizations of a permeability field: (a) estimated k_{xx}; (b) estimated k_{yy}.

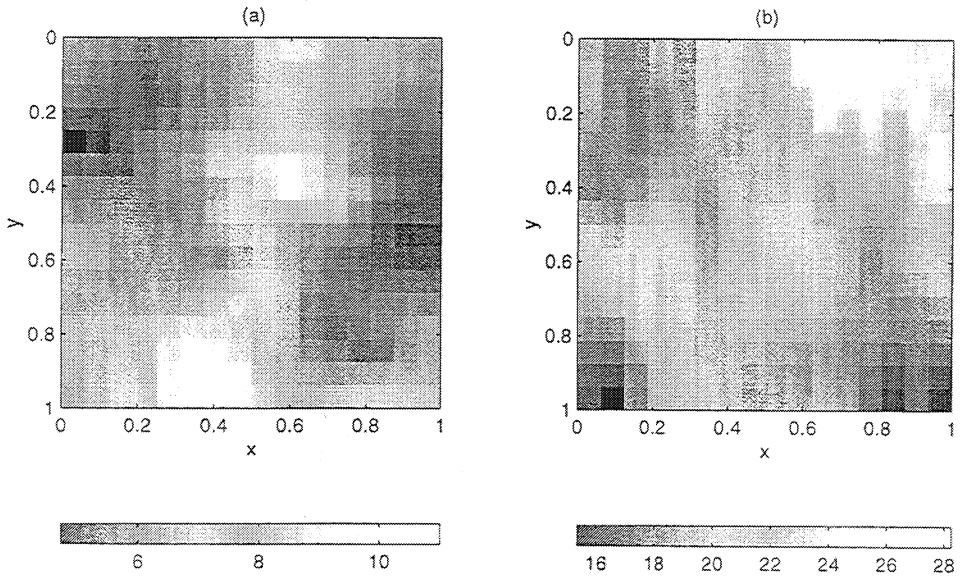

Figure 9. Results obtained from the isotropic inversion method: (a) inverted component k_{xx}; (b) inverted component k_{yy}.

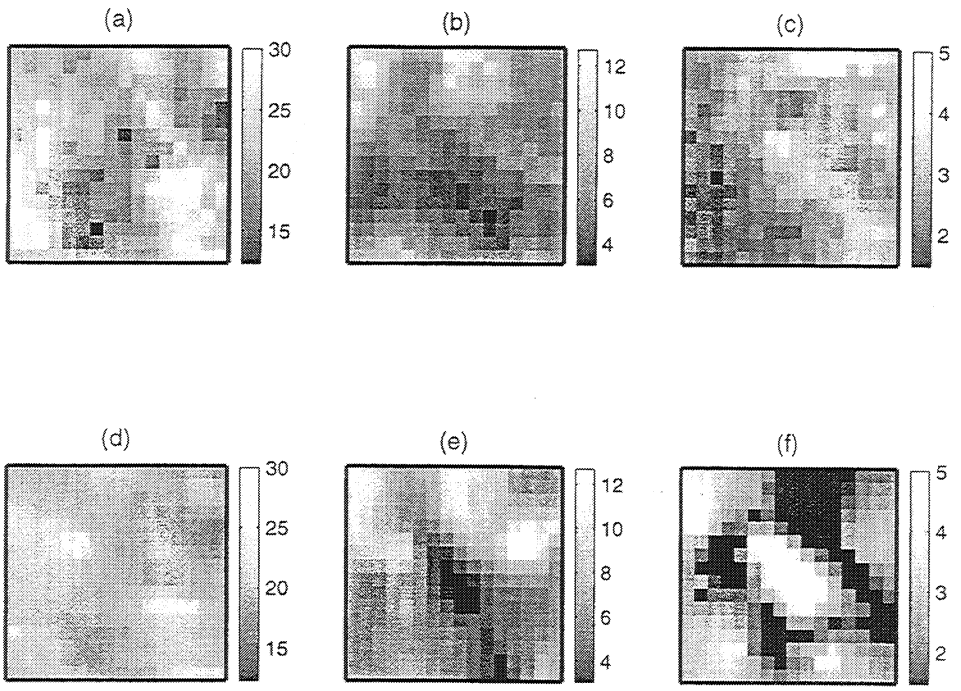

Figure 10. Application of the direct inversion method to an anisotropic permeability field with a full permeability tensor. Results for k_{xx}: (a)-(b) the actual distribution; (c)-(d) the directly inverted distribution using isotropic inversion.

A NON-LOCAL KARDAR-PARISI-ZHANG EQUATION TO MODEL INTERFACE GROWTH

by

Persefoni Kechagia and Yanis C. Yortsos

I. Introduction

The evolution of interfaces growing in a direction normal to themselves, in the presence of noise and interfacial smoothing, was described in a pioneering paper by Kardar, Parisi, and Zhang [1]. These authors proposed a Langevin-type equation

$$\frac{\partial h}{\partial t} = \nu \nabla^2 h + \frac{\lambda}{2} (\nabla h)^2 + \eta(\mathbf{x}, t) \tag{1}$$

commonly known as the KPZ equation, for the evolution of the fluctuation, $h(\mathbf{x}, t)$, of the height of the interface from its mean. In this equation, the first term on the right-hand side describes interfacial smoothing by a surface tension ν in a direction lateral to the main growth, and the second is the leading-order term for growth in a direction normal to the interface, where λ is the growth velocity. The noise $\eta(\mathbf{x}, t)$ is an uncorrelated Gaussian with zero mean and amplitude D, satisfying $< \eta(\mathbf{x}, t) >= 0$ and $< \eta(\mathbf{x}, t)\eta(\mathbf{x}', t') >= 2D\delta^d(\mathbf{x} - \mathbf{x}')\delta(t - t')$, where d is the dimension of the interface and δ^d is the d-dimensional delta function.

The properties of the KPZ equation have been studied in great detail. Its considerable interest stems from the fact that equation (1) is prototypical of self-affine growth with exponents that are universal (for example see [2] and references therein). Methods such as the dynamic renormalization group [1], have been used to obtain insight into its scaling properties and exponents. Equation (1) is also the weakly non-linear expansion in the presence of noise of a linear equation with the spectral relationship

$$\omega = -\nu \mathbf{k}^2 \tag{2}$$

where ω is the rate of growth corresponding to wavenumber $\mathbf{k}$ (and where we have assumed $h \sim \exp(\omega t + i\mathbf{k} \cdot \mathbf{x})$). Dispersion relation (2) shows that the process described by the KPZ equation is linearly stable ($\omega < 0$) for all $\mathbf{k}$.

The KPZ equation and its variants have been used to describe a variety of processes, from ballistic deposition [3] to the formation of cell colonies in bacteria or tissue cultures (Eden Model) [4], [5], randomly stirred fluids [6] and directed polymers in random media [7]. Of interest to this work, however, has been a more recent observation by Aharonov and Rothman [8], who suggested that the KPZ equation can also describe the evolution of the pore-grain interface in sedimentary rocks when the process is reaction-controlled. In the particular approach in [8] the relative height (asperity), h, of the grain surface, grows due to a chemical reaction involving the pore fluid. The process is kinetically controlled, and the growth is at a constant velocity, determined from the reaction kinetics. For example, if the reaction occurs everywhere at the constant rate λ, then the normal velocity, v_n, of the front $z = F(t, \mathbf{x})$, in the absence of interfacial smoothing and noise, would be constant

$$v_n \equiv \frac{F_t}{|\nabla F|} = \lambda \tag{3}$$

For a KPZ-like equation, one takes the weakly non-linear limit, in which case equation (3) leads to

$$F_t = \lambda(1 + \frac{1}{2}|\nabla F|^2 + \cdots) \tag{4}$$

By defining the relative asperity height $h = F - \lambda t$, one then obtains

$$h_t = \frac{\lambda}{2}|\nabla h|^2 + \cdots \tag{5}$$

which constitutes the non-linear part of the KPZ equation. Addition of a diffusion term and noise, then leads to the KPZ equation.

In many processes involving reaction-induced morphology changes in porous media, however, reaction rates are not necessarily slow, while the growth process may be controlled by (non-local) transport, for example by diffusion or convection. Indeed, this would be also the

case for the process in [8], in which diffusion towards the interface constitutes the non-local transport. We cite other examples from dissolution or precipitation processes [9], gas-solid reactions [10], and a variety of reaction engineering processes [11]. Here, diffusive or convective transport operates in the bulk of the fluid, or of the porous medium, and towards the grain interface, rather than only along the interface, as in the interfacial process envisioned in [8]. Two other examples obeying similar dynamics, but in a slightly different context, involve the displacement of one fluid by another of different viscosity in a random porous medium [12] and the propagation of laminar flames [13], [14]. In the latter cases, the pressure fields governing fluid flow obey the Laplace equation (due to Darcy's law in the first case and to Euler's equations in the second), as in the case of steady-state diffusion, giving rise to a non-local term. Finally, a similar situation occurs in the acidization of a porous matrix [9, 15], and more generally in reactive infiltration in porous media, an example for which will be analyzed in detail below. Changes in the mobility of the flowing phases, the expansion of fluids at the flame fronts and the pore structure of the matrix (permeability), in the respective cases, affect the transport towards the front and in turn its evolution. These changes may result in stable or unstable fronts. Under these circumstances, the KPZ equation cannot capture the growth and coarsening dynamics, which now become non-local.

To account for problems in which non-local transport is dominant and cannot be neglected, we propose in this chapter an extension of the KPZ equation, by adding to (1) a term of the form $\mathcal{H}(h_x)$, where $\mathcal{H}$ is the Hilbert transform, to obtain, in the case of 1+1 dimensions, the equation

$$h_t = \nu h_{xx} - m\mathcal{H}(h_x) + \frac{\lambda}{2}(h_x)^2 + \eta(\mathrm{x}, t) \tag{6}$$

For simplicity, we will refer to (6) as the HKPZ (Hilbert-KPZ) equation. In the various applications mentioned, this modification accounts for non-local transport in the weakly non-linear limits, as will be shown below. Recall that the Hilbert transform is defined as the principal value of the following integral [16]:

$$\mathcal{H}(f) = \frac{1}{\pi}\mathcal{P}\int_{-\infty}^{\infty} \frac{f(t)}{x-t}\,dt \tag{7}$$

and also satisfies the following property

$$\hat{\mathcal{H}}(h_x) = -|k|\hat{h} \tag{8}$$

where superscript hat denotes Fourier Transform. We note that the somewhat similar equation

$$v_t = \nu v_{xx} - \mathcal{H}(v_x) + vv_x + \eta(\mathbf{x}, t) \tag{9}$$

was proposed by Olami et al. [17] to investigate the propagation of combustion fronts in the presence of noise. This equation was obtained from a normalized version of Sivashinsky's equation [13], which is equation (6) without noise and with $\lambda = -1$, by differentiating with respect to x and subsequently adding noise. Thus, in Olami et al. [17] the noise is added to the growth of the slope of the front, rather than the growth of the front itself, contrary to the case in the HKPZ (and the KPZ) equation. Note also that (9) corresponds to unstable growth ($m = 1 > 0$).

In this chapter we will study the properties of the general equation (6) by proceeding as follows: First, we provide a derivation of the HKPZ equation, first by using general physical arguments and subsequently by focusing on the specific problem of reactive infiltration under fast kinetics. Its solution in one-space dimension is considered next. We develop a numerical scheme using finite-differences and a Fast Fourier Transform, which is tested against available analytical results in the absence of noise. Then, the linearized version of HKPZ, which is the counterpart of the Edwards-Wilkinson (EW) [18] equation, is analyzed. We develop asymptotics for early and late times, which allow for the roughness exponents (if any) of the linearized HKPZ to be derived. Results are presented for both the stable and unstable cases. Then, the full HKPZ equation is solved numerically in one spatial dimension. The scaling behavior of the results is investigated in the small and large time limits.

II. Derivation of the HKPZ equation

In this section we provide a derivation of the HKPZ equation, first, by using general arguments and subsequently, by considering a specific example from reactive infiltration in a porous medium. We also discuss briefly the process envisioned in [8] and show that it must also belong to the general problem described by HKPZ.

In general, deriving an HKPZ equation corresponding to the processes described above consists of the following steps: defining a base-state corresponding to a planar interface, conducting a linear stability analysis, deriving the linear dispersion relation, which must correspond to the linearized HKPZ, considering a long-wave expansion near the onset of the non-local behavior, taking the weakly non-linear limit, and adding noise. For example, all but the last steps were taken by Sivashinsky [13] in his long-wave hydrodynamic stability of flames. Olami et al. [17] added noise as explained above and studied the evolution of unstable fronts.

As noted previously, for the result to be of the HKPZ type, the linear dispersion relation must include a non-local term of the form

$$\omega = m|k| - \nu k^2 + \dots \tag{10}$$

(e.g. compare to (2)). Then, the linear process is unconditionally stable if $m < 0$, and conditionally unstable if $m > 0$. The term involving $|k|$ reflects non-local transport, arising from the solution of a Laplace equation at long wavelengths, and corresponds in the HKPZ to the Hilbert transform. The fact that the latter represents the flux at the interface at $y = 0$, arising from the solution of the Laplace equation, can be seen simply by writing a conservation equation of the type

$$h_t - mh_y = \nu h_{xx} \quad \text{at} \quad y = 0 \tag{11}$$

and by extending the function h to be a harmonic function in the upper half plane ($y > 0$), namely by taking

$$h_{xx} + h_{yy} = 0 \quad \text{for} \quad y > 0 \tag{12}$$

Then, if we introduce the analytic function $w = h + i\mathcal{H}(h)$, use of the Cauchy-Riemann conditions shows that $h_y|_{y=0} = -\mathcal{H}(h_x)$, as postulated. In such an interpretation, for example of the process of [8], the flux $-\mathcal{H}(h_x)$, arriving at $y = 0$, is used partly for the growth of the interface, and partly to satisfy the lateral diffusion along the interface (compare with (11) and also see below). The Laplace equation (12) may describe transport either by diffusion or by advection, when the latter is controlled by potential flow, as for example in the case of flow in porous media. A more rigorous derivation for the case of reactive infiltration will be described below. For future reference, we also note that in 1-D and for $m > 0$ there exists a cut-off mode, $k_c = \frac{m}{\nu}$, and a fastest growing mode, $k_{max} = \frac{m}{2\nu}$, with growth rate $\omega_{max} = \frac{m^2}{4\nu}$.

We must note that not all processes whose linear spectral relationship is (10) lead to HKPZ. The converse is true, however. In addition, if the linear limit is (10), then the non-linear version of the process cannot evidently be of the KPZ type. Specifically, we will show below that such is the case with the model considered in [8].

Parameter m expresses a contrast in transport properties across the growing interface, with stable or unstable displacement corresponding to negative or positive m, respectively. As discussed above, long-wave dispersion relations of the type (10) arise in a variety of problems. In displacements in porous media, m is a normalized viscosity difference upstream (subscript 1) and downstream (subscript 0) of the front, $m = \frac{\mu_0 - \mu_1}{\mu_0 + \mu_1}$, as pointed out by Saffman and Taylor in Hele-Shaw flows [19] or by Yortsos and Hickernell [20] in general displacements in porous media. When the pore structure changes, as a result of flow and reaction, for example in acidization, then $m = \frac{K_1 - K_0}{K_1 + K_0}$, where K is the flow permeability [21, 22]. In such applications, non-local growth is driven by advection which is controlled by Darcy's law. In the case of flame propagation, Sivashinsky showed that $m = (1 - \sigma)$, where σ is the coefficient of thermal expansion [13]. Here, the non-local transport results from Euler's equations, which also give rise to potential flow. In interfacial growth problems, such as in [8], non-local transport is due to diffusion in the bulk. That transport problem is similar to

directional solidification [23, 24], where $m \sim v$ and v is the undisturbed interface velocity. The latter is positive in the case of solidification or in the case of deposition/precipitation, hence indicating instability, but negative in the case of melting or in the case of dissolution, indicating stability.

The stabilizing coefficient $\nu > 0$ reflects an effective interfacial tension. In displacements in porous media it expresses capillarity, in reactive infiltration it expresses diffusion in the bulk (see below), in flame propagation it is related to the Lewis number of the component limiting the reaction, and in the process analyzed in [8] it describes interfacial diffusion along the interface. Interestingly, in the latter process, diffusion acts in two different ways: in the bulk, in order to supply the necessary flux to the interface (and to destabilize or stabilize the interface depending on whether or not the interface grows or recedes, respectively) and along the interface, in order to stabilize the latter. We must point out that in problems, such as solidification [23, 24], where the relaxation of the interface is controlled by the Gibbs-Thomson condition, or in Hele-Shaw cell displacements [12], where the interfacial tension acts in proportion to the effective curvature of the interface, the resulting stabilization enters at order $|k|^3$. Therefore, such problems do not have the linear dispersion relation (10) and will not lead to an HKPZ equation. The dots in (10) reflect the existence of additional terms in the general problem (for example in displacements in porous media, in flame propagation, etc.) which are of higher order and do not contribute in the long-wave limit.

Taking the weakly non-linear limit has been done in the context of flame propagation. Specifically, Sivashinsky [13] obtained the following weakly non-linear equation,

$$h_t + \epsilon\nabla^2 h + \frac{1}{2}(\nabla h)^2 = \frac{(1-\sigma)}{8\pi^2}\int_{-\infty}^{\infty} |\mathbf{k}|\hat{h}(t,\mathbf{k})e^{i\mathbf{k}\cdot(\mathbf{x}-\mathbf{z})}\,d\mathbf{k}dz \tag{13}$$

valid at large wavelengths (in this notation $\epsilon < 0$). For $1 - \sigma > 0$, equation (13) describes long-wave instability. Including only the non-linear part, namely by taking

$$h_t + \frac{1}{2}|\nabla h|^2 = 0 \tag{14}$$

describes the propagation of a front of a constant normal velocity, as noted before. In the

general case, we can write

$$h_t = \nu \nabla^2 h - m\mathcal{H}(h_x) + \frac{\lambda}{2}(h_x)^2 \tag{15}$$

An equation of this type was also proposed by Yortsos [25] to describe the weakly non-linear propagation of displacement fronts in porous media. Theoretical work performed by Thual et al. [26] has shown that equation (15) admits a polar decomposition. This property is useful for analytical purposes and will be used later below to check the numerical results. The final step is to add noise to (15), leading to the HKPZ equation

$$h_t = \nu h_{xx} - m\mathcal{H}(h_x) + \frac{\lambda}{2}(h_x)^2 + \eta(x,t) \tag{16}$$

The random noise reflects heterogeneity and is typically an uncorrelated, in space and time, Gaussian with zero mean.

In the remaining of this section we will provide a derivation of the HKPZ equation for a model problem corresponding to reactive infiltration, for example the acidization of a porous rock. To derive equation (15) we will apply first a linear and then a weakly non-linear stability analysis.

A Specific Example from Reactive Infiltration

Consider the injection in a porous medium of a chemical at concentration c_1 and constant rate q. The chemical does not affect the fluid viscosity but it reacts with a mineral at the pore surface, of initial concentration M_0, and results in a change of the permeability of the porous medium, so that a permeability contrast, $\kappa \equiv \frac{K_1}{K_0}$, develops. We assume that as a result of the reaction, the mineral and the injected chemical are completely consumed. In this notation, subscripts 0 and 1 refer to the initial and injected states, respectively. We further assume that the reaction kinetics are fast, so that the reaction occurs over a surface (front). This requires large Damkholer numbers (see [27] for more details). Under this assumption, the reacting surface separates a downstream region, where the chemical concentration is identically zero and the mineral is at concentration M_0, from an upstream

region, where the chemical concentration is variable due to diffusion and advection, while the mineral concentration is identically zero (see schematic in Fig. 1). One example for this problem could be the oxidation of minerals, like pyrite or uraninite (UO_2). Although such a reaction usually leads to the formation of secondary mineral products, the oxygen is consumed at a redox front as the mineral dissolves. Other examples, for instance involving the dissolution of quartz, can be readily formulated as well. For the reaction we will take the simple scheme

$$\{Chemical\} + \theta\{Mineral\} \rightarrow \{Products\} \tag{17}$$

where θ is the stoichiometric coefficient of the reaction. In dimensionless notation (subscript D), the problem is described by the following.

Define the reacting front by the equation $\mathcal{F}(x_D, y_D, t_D) = 0$. Downstream of the front, $\mathcal{F} > 0$, we have

$$c_D = 0; \quad M_D = 1; \quad K_D = 1; \quad \mathbf{u}_D = -\nabla p_D \tag{18}$$

where the characteristic variables for the chemical concentration, the mineral concentration, the permeability, the velocity and the pressure were taken as c_1, M_0, K_0, q and $\frac{\mu(1+A)\mathcal{D}}{K_0}$, respectively. Here, μ is the fluid viscosity, $\mathcal{D}$ is the diffusion-dispersion coefficient and A is a dimensionless constant expressing the capacity of the reactive process

$$A = \frac{\phi\theta c_1}{M_0} \tag{19}$$

where ϕ is upstream porosity. Implicit in the above is the use of the characteristic length $l = \frac{(1+A)\mathcal{D}}{q}$ and the use of Darcy's law for fluid flow in the porous medium. Upstream of the front, $\mathcal{F} < 0$, we have

$$M_D = 0; \quad K_D = \kappa; \quad \mathbf{u}_D = -\kappa\nabla p_D \tag{20}$$

and

$$\frac{\partial c_D}{\partial t_D} + \mathbf{u}_D \cdot \nabla c_D = \frac{1}{(1+A)} \nabla^2 c_D \tag{21}$$

where time was made dimensionless by $\phi l/q$. In either region, the continuity equation applies, namely

$$\nabla \cdot \mathbf{u}_D = 0 \tag{22}$$

where, it was assumed that the mineral capacity is sufficiently large. The problem is completed by interface conditions: Across the front, the concentration of the chemical is continuous,

$$c_D = 0 \quad \text{at} \quad \mathcal{F} = 0 \tag{23}$$

but the mineral concentration undergoes a jump from 0 to 1. In addition, conservation of mass leads to the following condition for the normal component of the front velocity,

$$v_{Dn} = -\frac{A}{(1+A)} \frac{\partial c_D}{\partial n} \tag{24}$$

where n denotes the direction of the unit normal $\mathbf{n}$ at the front (see Fig. 1).

We will consider, in sequence, the existence of a planar traveling wave under steady-state conditions, its linear stability and its weakly non-linear stability. For simplicity, and to be consistent with the rest of the text, the analysis is restricted to a 2-D geometry.

The base state

The base-state, denoted by superscript bar, is a planar front traveling at the dimensionless velocity $\bar{v}_D$. In the limit of fast kinetics, the base-state concentration $\bar{c}_D$ is given upstream by

$$\bar{c}_D = 1 - \exp(\xi) \quad \xi < 0 \quad \text{and} \quad \bar{c}_D = 0 \quad \xi > 0 \tag{25}$$

where we introduced the moving coordinate $\xi = y_D - \bar{v}_D t_D$. The base-state velocity $\bar{v}_D$ is found using (24)

$$\bar{v}_D = \frac{A}{(1+A)} < 1 \tag{26}$$

For the stability analysis, it is convenient to introduce a coordinate system moving with the front

$$\rho = \xi - F(\tau, \zeta); \quad \zeta = x_D; \quad \tau = t_D \tag{27}$$

where F is the front perturbation relative to the moving coordinate (compare also with (4) and (5)), based on which (21) becomes

$$\begin{aligned} &\frac{\partial c_D}{\partial \tau} + (u_{D\rho} - \bar{v}_D - F_\tau - u_{D\zeta} F_\zeta)\frac{\partial c_D}{\partial \rho} + u_{D\zeta}\frac{\partial c_D}{\partial \zeta} \\ = \; &\frac{1}{(1+A)}\left[\frac{\partial^2 c_D}{\partial \rho^2} + \frac{\partial^2 c_D}{\partial \zeta^2} - F_{\zeta\zeta}\frac{\partial c_D}{\partial \rho} - 2F_\zeta \frac{\partial^2 c_D}{\partial \rho \zeta} + F_\zeta^2 \frac{\partial^2 c_D}{\partial \rho^2}\right] \end{aligned} \tag{28}$$

Darcy's law reads as

$$u_{D\rho} = -\kappa \frac{\partial p_D}{\partial \rho}; \quad u_{D\zeta} = -\kappa\left[\frac{\partial p_D}{\partial \zeta} - F_\zeta \frac{\partial p_D}{\partial \rho}\right] \tag{29}$$

in the upstream region, and as in (29) but with 1 replacing κ in the downstream region. The continuity equation becomes

$$\frac{\partial u_{D\rho}}{\partial \rho} + \frac{\partial u_{D\zeta}}{\partial \zeta} - F_\zeta \frac{\partial u_{D\zeta}}{\partial \rho} = 0 \tag{30}$$

and the interface condition reads

$$\bar{v}_D + F_\tau = -\frac{A}{(1+A)}\left[\frac{\partial c_D}{\partial \rho}(1 + F_\zeta^2) - F_\zeta \frac{\partial c_D}{\partial \zeta}\right] \quad \text{at} \quad \rho = 0 \tag{31}$$

Subscripts τ and ζ denote differentiation with respect to these variables.

Linear stability analysis

Consider, next the linear stability analysis of the above system. We will take the general expansion

$$\psi_D = \bar{\psi}_D(\rho) + \Psi' \approx \bar{\psi}_D(\rho) + \epsilon\Psi(\rho)\exp(\omega\tau + ik\zeta) \tag{32}$$

Here Ψ' is the perturbation of the variable ψ, which in the linear stability limit is expressed in terms of normal modes, with ω being the rate of growth of a disturbance with wavenumber k and i is the imaginary variable. Here, we have assumed that k is positive. More strictly speaking, one should use $|k|$ instead. Analogously, we will take $F \sim \exp(\omega\tau + ik\zeta)$. Substitution in the governing equations and linearization gives after considerable manipulations the eigenvalue condition for the determination of ω. Details are omitted and can be found in [27]. We obtain

$$\begin{aligned} & (A + A\sqrt{1 + 4(\omega^* + k^2)})((\kappa + 1)(k - \omega^*) + k(\kappa - 1)(A + 1)) \\ = \; & 2(A - \omega^*)(k - \omega^*)(\kappa + 1) + 2A(A + 1)k(k + 1)(\kappa - 1) \end{aligned} \tag{33}$$

where we defined for simplicity $\omega^* = \omega(1 + A)$. A plot of the admissible solution of (33) for ω as a function of k and for different values of κ is given in Fig. 2. As expected, the problem is unstable in a region of large wavelengths (small wavenumbers) if $\kappa > 1$, and stable otherwise. The instability is driven by the change in permeability, which focuses flow towards the fingers and accentuates small disturbances. It is mitigated at smaller wavelengths by the diffusion of the chemical, which in this case acts to stabilize the system. We must note that (33) also accepts the trivial solution $\omega^* = 1$, which is not admissible, however, as the derivation was based on the assumption $\omega^* \neq 1$ (see [27]).

For the particular application in this chapter, we must consider the roots of $\omega = 0$, which in addition to the trivial solution $k = 0$, can be readily shown to occur at the value k_c, where

$$k_c = \frac{(\kappa - 1)(\kappa + 1 + (\kappa - 1)(1 + A))(1 + A)}{(\kappa + 1)(\kappa + 1 + 2(\kappa - 1)(1 + A))} \tag{34}$$

As expected, k_c vanishes as $\kappa \to 1$. Then, an asymptotic expansion of (33) in this limit shows [27] that

$$\omega = \frac{A}{(A+1)}\frac{(\kappa-1)}{(\kappa+1)}k - \frac{2A\kappa(\kappa+1+A(\kappa-1))}{(1+A)^2(\kappa+1)^2}k^2 + \cdots \tag{35}$$

Thus, in the region of the onset of instability we have $k \sim \kappa - 1$ and $\omega \sim (\kappa-1)^2$. It follows that if we were to consider long-time and large-wavelengths in this limit, the problem will become quasi one-dimensional, like in [13]. This particular scaling will be considered in the non-linear analysis to follow. Before we proceed, we also note that at this limit, we have the following scaling [27]

$$C' \sim C(\rho) \sim O((\kappa-1)^2); \quad U'_\rho \sim U_\rho(\rho) \sim O((\kappa-1)^2); \quad U_\zeta = -F_\zeta \tag{36}$$

for the leading-order expansion of the perturbations of the concentration and of the components of the two velocities.

Weakly non-linear stability analysis

Consider, now, a weakly non-linear analysis near the long-wave limit, which from (35) is meaningful when $\kappa \sim 1$. We remark that a weakly non-linear analysis of a similar problem was done in [28], but in a different context. In that analysis, the width of the system was finite, the marginal state such that the cut-off wavelength $\sim 1/k_c$ is precisely equal to the width, and the system was weakly perturbed to an unstable state, ultimately leading to a Landau equation. An analogous approach for two-phase flow in porous media was done earlier in [29].

To proceed with our analysis we take again the expansion

$$c_D = \bar{c}_D(\rho) + C'; \quad \mathbf{u}_D = \bar{\mathbf{u}}_D + \mathbf{U}' = \mathbf{i}_y + \mathbf{U}'; \quad p_D = \bar{p}_D(\rho) + P' \tag{37}$$

where $\mathbf{i}_y$ is the unit vector in the main flow directiom and recognize that the perturbations have the order indicated in (36) in this limit. The equation for the perturbation in concentration reads

$$\frac{\partial C'}{\partial \tau} + (1 - \bar{v}_D - F_\tau - U'_\rho - U'_\zeta F_\zeta)\frac{\partial C'}{\partial \rho} - (F_\tau - U'_\rho - U'_\zeta F_\zeta)\frac{\partial \bar{c}}{\partial \rho} + u'_\zeta \frac{\partial C'}{\partial \zeta}$$

$$= \frac{1}{(1+A)}\left[\frac{\partial^2 C'}{\partial\rho^2}(1+F_\zeta^2)+F_\zeta^2\frac{\partial^2\bar{c}}{\partial\rho^2}+\frac{\partial^2 C'}{\partial\zeta^2}-F_{\zeta\zeta}\frac{\partial\bar{c}}{\partial\rho}-2F_\zeta\frac{\partial^2 C'}{\partial\rho\zeta}\right] \tag{38}$$

In the large-time (of $O(\kappa-1)^{-2}$)) and large-wavelength (of $O(\kappa-1)^{-1}$)) limits, recognizing the scaling (36) and assuming that $F = O(1)$, the disturbance of the concentration satisfies the following equation to order $(\kappa-1)^2$,

$$\frac{1}{(1+A)}\frac{\partial^2 C'}{\partial\rho^2}-\frac{1}{(1+A)}\frac{\partial C'}{\partial\rho}=\left[U'_\rho-F_\tau-F_\zeta^2+\frac{F_{\zeta\zeta}}{1+A}\right]\frac{\partial\bar{c}}{\partial\rho}-\frac{F_\zeta^2}{1+A}\frac{\partial^2\bar{c}}{\partial\rho^2} \tag{39}$$

Subsequent integration of (39) gives

$$\frac{1}{(1+A)}\frac{\partial C'}{\partial\rho}-\frac{1}{(1+A)}C'=-\int_0^\rho\exp(\rho)\left[U'_\rho-F_\tau-F_\zeta^2-\frac{F_\zeta^2}{1+A}+\frac{F_{\zeta\zeta}}{1+A}\right]d\rho+\frac{1}{(1+A)}\frac{\partial C'}{\partial\rho}|_0 \tag{40}$$

where we used the continuity condition $C'(\rho=0)=0$. The last term in the right-hand side of the above can be calculated using the interface condition (31). We find

$$\frac{1}{(1+A)}\frac{\partial C'}{\partial\rho}|_0=\frac{F_\zeta^2}{1+A}-\frac{F_\tau}{A} \tag{41}$$

Then, evaluating (40) at $\rho=-\infty$ and requesting that the disturbance and its derivative vanish upstream, we obtain the following equation for F,

$$\frac{(A+1)}{A}F_\tau+F_\zeta^2-\frac{1}{(1+A)}F_{\zeta\zeta}+\int_0^{-\infty}\exp(\rho)U'_\rho d\rho=0 \tag{42}$$

The final step is to evaluate the disturbance for the velocity, U'_ρ, and insert it in (42). For this, we need to find the solution for the pressure disturbance in the limit taken, $\kappa\to 1$. The latter can be shown [27] to be equal to

$$\begin{aligned} P' &= -\frac{F}{\kappa}+\Pi(\rho,\zeta,\tau);\quad \rho<0 \\ P' &= -F+\Pi(\rho,\zeta,\tau);\quad \rho>0 \end{aligned} \tag{43}$$

where Π satisfies the Laplace equation in the respective regions, along with continuity of pressure and mass at the front, $\rho = 0$. By taking a Fourier Transform on the variable ζ, we obtain the solution

$$\hat{\Pi}(\rho, k, \tau) = -\frac{(\kappa - 1)}{\kappa(\kappa + 1)} \hat{F} \exp(|k|\rho); \quad \rho < 0 \tag{44}$$

which may then be used for the evaluation of $\hat{U}'_\rho = -\kappa \frac{\partial \hat{\Pi}}{\partial \rho}$. After some calculations we find

$$F.T.\{\int_0^{-\infty} \exp(\rho) U'_\rho d\rho\} = -\frac{(\kappa - 1)}{(\kappa + 1)} \frac{|k| \hat{F}}{(|k| + 1)} \tag{45}$$

which, in the limit of small k, can be inverted to the following

$$\int_0^{-\infty} \exp(\rho) U'_\rho d\rho = \frac{(\kappa - 1)}{(\kappa + 1)} \mathcal{H}(F_\zeta) \tag{46}$$

Finally, substituting back in (42) we find the desired equation

$$F_\tau + \frac{A}{(A+1)} F_\zeta^2 + \frac{A}{(A+1)} \frac{(\kappa - 1)}{(\kappa + 1)} \mathcal{H}(F_\zeta) - \frac{A}{(A+1)^2} F_{\zeta\zeta} = 0 \tag{47}$$

which is the HKPZ equation in the absence of noise, equation (15), with $h = F$, $t = \tau$, $x = \zeta$, $\lambda = -\frac{A}{2(A+1)}$, $m = \frac{A}{(A+1)} \frac{(\kappa-1)}{(\kappa+1)}$ and $\nu = \frac{A}{(A+1)^2}$.

In the sections to follow, we will consider the general properties of HKPZ. It must be recalled, however, that its validity for a physical process, e.g of the reactive infiltration type, is subject to the restrictions of large wavelengths near the onset of instability (namely, when the destabilizing contrast is weak, $\kappa - 1 \ll 1$, or small $m > 0$). In the more general case of strong instability, HKPZ does not generally apply and cannot capture Laplacian growth, which must be modeled instead by processes of the Diffusion-Limited-Aggregation (DLA) type (e.g. see [15] and related references). In a sense, in the destabilizing case HKPZ corresponds to the weak-instability limit, with DLA being its strong-instability counterpart.

Before closing this section, we must note that a similar analysis also applies for the diffusion-reaction system studied in [8]. In that application, there is no bulk flow, the chemical diffuses in the bulk and precipitates (or leads to a dissolution of the solid) at

the reacting interface. In the schematic of Fig. 1 only the upstream region needs to be considered for this process. A first-order reaction is assumed to occur at the interface with kinetic constant $\mathcal{K}$ (units of velocity). The interface moves in the negative direction, in the case of precipitation, and in the positive direction, in the case of dissolution. One can then show by a linear stability analysis, that the case of precipitation is long-wave unstable for the growing surface, the slope in the $\omega - k$ curve at the origin vanishing as the base-state velocity of the interface equals the kinetic velocity $\mathcal{K}$. The analysis is very similar to that for directional solidification [23, 24]. Now, interface instability is driven by the non-local transport due to bulk diffusion. The process is stabilized by lateral diffusion along the interface, an interface condition for which can be postulated by partitioning the incoming flux partly to the interface growth along the normal (as in (31)) and partly to interfacial diffusion along the interface. For an equation of the KPZ type to result, the latter must be taken proportional to the curvature. For lack of space, this analysis will not be detailed here. If one proceeds along lines similar to the above, however, an equation similar to (15) would then be derived. Thus, the process studied in [8] appears to also fall in the HKPZ class (in fact, in its unstable version, $m > 0$).

In the remaining of this chapter we will consider the solution of equation (16) and its linear counterpart in one space dimension. For this, we will first present the numerical scheme and then compare results against analytical solutions in the absence of noise. Then, the linearized HKPZ equation will be solved analytically. Finally, the full HKPZ equation will be solved numerically.

III. Numerical Scheme

Equation (16) was discretized numerically using standard methods. For spatial derivatives we used forward-backward finite differences of lattice constant Δx. The Hilbert transform was evaluated using a Fast Fourier Transform algorithm. The equation was marched in time using an Euler scheme with time increments Δt. Periodic boundary conditions were used for its solution. If grid points are labeled by integer n, the discretized version of (16) reads

$$h_n(t+\Delta t) = h_n(t) + \frac{\Delta t}{\Delta x^2}\left(\nu[h_{n+1}(t) - 2h_n(t) + h_{n-1}(t)] + \frac{1}{8}\lambda[h_{n+1}(t) - h_{n-1}(t)]^2\right) + m\Delta t I_n(t) + \Sigma\sqrt{12\Delta t}R_n(t) \quad (48)$$

where $I_n(t)$ is the discretized Hilbert transform calculated using a Fast Fourier Transform routine and we defined $\Sigma^2 = 2D/\Delta x$ (recall that D is related to the noise amplitude). The random numbers R_n are taken from a uniform distribution between $-\frac{1}{2}$ and $\frac{1}{2}$. The prefactor $\Sigma\sqrt{12\Delta t}$ guarantees that the noise has the same second moment as the Gaussian noise integrated over the time interval Δt [30]. In our simulations we have typically taken $\Delta x = 1$, $\nu = 0.5$, $\Sigma = 0.1$, and $\Delta t = 0.05$, while we varied λ and m. In all simulations, the initial condition is a flat interface, $h = 0$ at $t = 0$.

The accuracy of the numerical scheme was tested by comparing the numerical results against the analytical solution of a related equation in the absence of noise, namely the extended Burgers equation [31]

$$v_t - 2vv_x + m\mathcal{H}v_x = v_{xx} \quad (49)$$

which, as noted before, admits a polar decomposition [26]. This equation describes the evolution of the slope of the interface of (16), $v = h_x$, in the absence of noise and where $\nu = 1$ and $\lambda = 2$. For the periodic case of interest here, analytical results are possible for the one-"lump" solution

$$v = n\left(\cot(n(x+a)) + \cot(n(x+a^*))\right) \quad (50)$$

where $2n$ is the wavenumber, the pole is described by the time-dependent complex variable, $a = \phi + i\psi$, with $\psi > 0$, and a^* denotes complex conjugate. Substitution of (50) in (49) shows that ϕ is a constant, which we can take as $\phi(0) = 0$, without loss in generality. We find

$$v = \frac{2n\sin(2nx)}{\cosh(2n\psi(t)) - \cos(2nx)} \quad (51)$$

where $\psi(t)$ solves the equation

$$\psi'(t) = \frac{2n\sinh(4n\psi)}{\cosh(4n\psi) - 1} - m \tag{52}$$

and has the implicit solution

$$\frac{1}{(1+\gamma)}\ln\left|\frac{\exp(4n\psi) + \frac{1+\gamma}{1-\gamma}}{\exp(4n\psi(0)) + \frac{1+\gamma}{1-\gamma}}\right| - \left(\frac{1-\gamma}{1+\gamma}\right)2n(\psi - \psi(0)) = 4n^2(1-\gamma)t \tag{53}$$

where $\gamma \equiv \frac{m}{2n}$. For v to reach a non-trivial steady-state requires $\gamma > 1$ (i.e. $m > 2n$) which, in this case ($\nu = 1$), is identical to the condition for the existence of an unstable mode in the linear problem (dispersion relation (10)).

Analytical and numerical results are shown in Fig. 3 for the cases $\psi(0) = 1$, $m = 0.2$ and $n = 2\pi/L$, where $L = 128$ is the lattice size. Comparison is shown for two different times. The agreement between the solutions is very good, except near the end points of the simulation interval, where there is a small discrepancy that increases somewhat at larger times. Fig. 3 implies the existence of a "wrinkled" front, the slope of the front increasing rapidly at the ends of the interval. This was noted in the simulations reported in [14], [31] and [32]. The results of Fig. 1b essentially correspond to an asymptotic steady state, which, as expected from the theory, is reached in this case of $\gamma > 1$. Here, the non-linearity acts to stabilize the fastest growing mode. By constrast, if $\gamma < 1$, the slope of the front eventually vanishes, all modes being stable. Excellent agreement between theory and numerical simulations was found for that case as well. Good agreement between theory and simulations was also found in testing more complex profiles that included more poles. From these examples it was concluded that the computational scheme would lead to accurate solutions of the HKPZ equation.

IV. The Linearized HKPZ Equation

Insight in the behavior of the HKPZ equation can be obtained by considering its linearized version

$$h_t = \nu h_{xx} - m\mathcal{H}(h_x) + \eta(x,t) \tag{54}$$

For its analysis, we follow previous work on the KPZ equation by Natterman and Tang [33]. Consider a process with periodic boundary conditions, initiated at $t = 0$ (and in which case $\eta(x,t) = 0$ for $t < 0$). By applying a double Fourier transform in space and time, defined as

$$\hat{h}(k,\omega) = \int_{-\infty}^{\infty}\int_{-\infty}^{\infty} e^{-i(kx-\omega t)} h(x,t)dxdt \tag{55}$$

equation (54) becomes

$$\hat{h}(k,\omega) = \frac{1}{(\nu k^2 - m|k|) - i\omega}\hat{\eta}(k,\omega) \tag{56}$$

Equivalently, given that $\eta = 0$ for $t < 0$, we may take a Laplace transform in time. Proceeding as in [33] and noting that

$$\langle \hat{\eta}(k,\omega)\hat{\eta}(k',\omega')\rangle = 2D(2\pi)\delta(k+k')\int_0^{\infty} e^{i(\omega+\omega')\tau}d\tau \tag{57}$$

we find using (56) the result

$$\langle \hat{h}(k,t)\hat{h}(k',t)\rangle = \frac{2\pi D}{(\nu k^2 - m|k|)}\left[1 - e^{-2(\nu k^2 - m|k|)t}\right]\delta(k+k') \tag{58}$$

based on which we can calculate the mean-square width of the interface over the lattice

$$w^2(L,t) = \langle [h(x,t) - \langle h(x,t)\rangle]^2\rangle = \frac{1}{4\pi^2}\int_{2\pi/L}^{\pi/\Delta x}\int_{2\pi/L}^{\pi/\Delta x}\langle \hat{h}(k,t)\hat{h}(k',t)\rangle dkdk' \tag{59}$$

Note that the lower and upper limits of the integrals are $2\pi/L$ and $\pi/\Delta x$, respectively. Substitution of (58) and carrying out one integration yields

$$w^2(L,t) = \frac{1}{\pi}\int_{\frac{2\pi}{L}}^{\pi/\Delta x}\frac{D}{(\nu k^2 - m|k|)}\left[1 - e^{-2(\nu k^2 - m|k|)t}\right]dk \tag{60}$$

which can be further rearranged to read

$$w^2(L,t) = \frac{DL}{\pi\nu}\int_{2\pi}^{N\pi}\frac{1}{(z^2+cz)}\left[1-e^{-2b(z^2+cz)}\right]dz \tag{61}$$

Here, we introduced the notation $N = \frac{L}{\Delta x}$, $z = kL$, $c = -\frac{mL}{\nu} = -k_c L$ and the dimensionless time $b = \frac{t\nu}{L^2}$. The effect of the non-local transport enters through parameter c, which is also proportional to the lattice size L. Note that the denominator in (61) is singular, when $c < 0$ (which corresponds to the destabilizing case), however the singularity is removable. Equation (61) can be expressed in a compact form as

$$w^2(L,t) = \frac{DL}{\pi\nu}f(b;c,N) \tag{62}$$

where

$$f(b;c,N) = \int_{2\pi}^{\pi N}\frac{1}{z^2+cz}\left[1-e^{-2b(z^2+cz)}\right]\,dz \tag{63}$$

We note that the existence of two dimensionless variables c and b, containing different t and L dependences, breaks the similarity scaling $\frac{t\nu}{L^2}$ applicable in the EW equation (where $c = 0$), thus one expects a different scaling behavior.

In the following, we will consider the behavior of $f(b;c,N)$ in the two asymptotic limits of large and small times, respectively, for the two different cases, a stabilizing case, $c > -2\pi$, and a destabilizing case, $c < -2\pi$ (and where we took into account the dispersion relation (10)). For each case, we will consider the two different limits of large and small times.

i. The stabilizing case, $c > -2\pi$.

In the stabilizing case, and at large times ($b \gg 1$), the function $f(b;c;N)$ approaches the limit

$$f(b;c,N) \approx \frac{1}{c}\int_{2\pi}^{\pi N}\left(\frac{1}{z}-\frac{1}{z+c}\right)\,dz \tag{64}$$

Due to the condition $c > -2\pi$, the above integral converges. Then, substitution in (62) gives the large-time result

$$w^2(L,t) \to w^2_\infty(L) = -\frac{D}{\pi m}\ln\left(\frac{1-\frac{mL}{2\pi\nu}}{1-\frac{m\Delta x}{\pi\nu}}\right) \tag{65}$$

Thus, in the stabilizing case the mean-square width saturates to a value which, for sufficiently large L, has a logarithmic dependence on L. This is to be contrasted to the power-law scaling, $w^2 \sim L$, which applies in the 1-D EW equation. The latter scaling can also be derived from (65) in the limit $m \to 0$. The saturation width decreases with increasing $|m|$, reflecting the more compact nature of the front at increasing stabilization. The analytical results were confirmed using numerical simulations. Fig. 4 shows a plot of $w^2_\infty(L)$ versus $\ln\left(\frac{1-\frac{mL}{2\pi\nu}}{1-\frac{m\Delta x}{\pi\nu}}\right)$, obtained numerically, for $m = -0.5$, $\nu = 0.5$ and various lattice sizes up to $L = 512$. In the simulations, the width was averaged over 100 realizations. The theoretical calculations predict a straight line with a slope equal to $-\frac{D}{\pi m} = 0.0032$. The figure shows very good agreement between theory and simulations.

In the opposite limit of small times ($b \ll 1$), the integral in (63) can be manipulated to read as

$$f(b;c,N) = A(b;c,N) - \frac{1}{c}\ln\left(\frac{2\pi}{2\pi+c}\right)\left[1 - e^{-2b(4\pi^2+2\pi c)}\right] - \frac{2b}{c}I \tag{66}$$

where we introduced the function

$$A(b;c,N) = \frac{1}{c}\ln\left(\frac{\pi N}{\pi N+c}\right) - \frac{1}{c}\ln\left(\frac{\pi N}{\pi N+c}\right)e^{-2b(\pi^2N^2+c\pi N)} \approx -\frac{1}{\pi N} + O(e^{-2b\pi^2N^2}) \tag{67}$$

and the integral

$$I = \int_{2\pi}^{\pi N} \ln\left(\frac{z}{z+c}\right)(2z+c)e^{-2b(z^2+cz)}\,dz \tag{68}$$

Note that the right-hand-side of (66) is well-defined in the limit $c \to -2\pi$, which is the point of transition from the stabilizing to the destabilizing case. This also suggests that the early-time scaling applies equally well to the destabilizing case. For sufficiently large discretization, $b \gg N^{-2}$, parameter A tends to $-\frac{1}{\pi N}$, as in the EW equation, and where we implicitly assumed that $|m|\Delta x \ll \nu$. Thus, the first term in (66) (and the expansion for w^2)

is infinitesimally small at large N. The contribution from the second term in (66) is $O(b)$, hence the leading-order term arises only from the integral I. For sufficiently large N, this becomes

$$I \approx \frac{2b}{c} \int_{2\pi}^{\infty} \ln\left(\frac{z}{z+c}\right)(2z+c)e^{-2b(z^2+cz)}\,dz \tag{69}$$

the asymptotic behavior of which at small b can be evaluated. After several manipulations, we obtain the result

$$I = \sqrt{2\pi b} + 2b \int_{4\pi^2+2\pi c}^{\infty} \left(\ln\left[1 - \frac{2c}{c+\sqrt{c^2+4t}}\right] + \frac{c}{\sqrt{t}}\right) dt + \cdots \tag{70}$$

Thus, the leading-order term is $O(\sqrt{b})$, which when substituted in (62) gives the following small-time asymptotic result

$$w^2(L,t) = -\frac{D\Delta x}{\pi^2\nu} + \frac{DL}{\pi\nu}(\sqrt{2\pi b} + O(b) + O(e^{-2b\pi^2N^2})) \tag{71}$$

It follows that in the range $N^{-2} \ll b \ll 1$, the width of the front scales as a power law of time with exponent $\beta = 1/4$. This scaling is identical to the EW equation, suggesting that in the small-time limit the non-local contribution does not enter to leading-order. This regime is preceded by a linear scaling regime, the interval of which, $b \ll N^{-2}$, decreases with increasing N, and where the corresponding exponent is $\beta = 1/2$. This interval and exponent also apply in the EW case.

The above were confirmed using numerical simulations. Fig. 5 shows a log-log plot of $w(L,t)$ vs. time. The width is again averaged over 100 realizations of the noise, while the parameters in the simulations take the values $L = 256$, $m = -0.5$, and $\nu = 0.5$. Agreement between theory and simulation is good, the two different regimes at small times having the theoretical slopes of $1/2$ and $1/4$, respectively.

ii. The destabilizing case, $c < -2\pi$.

In the destabilizing case, equation (10) shows that m must satisfy the constraint $m > \frac{2\pi\nu}{L}$, or, equivalently, $c < -2\pi$. Now, the denominator in (63) vanishes in the range of integration.

however, the singularity is removable. The asymptotic properties of the solution in the two limits of large and small times, respectively, can be obtained by proceeding as follows.

To obtain the behavior of the solution at large times, we decompose the integral into two parts

$$f(c;b;N) = \int_{2\pi}^{-c} \frac{1}{z^2+cz}\left[1-e^{-2b(z^2+cz)}\right]\,dz + \int_{-c}^{\pi N} \frac{1}{z^2+cz}\left[1-e^{-2b(z^2+cz)}\right]\,dz \qquad (72)$$

In the limit of large b, the second integral remains bounded, since $z^2+cz>0$, however the first integral does not. Thus, at large times, the dominant contribution arises from the first term only

$$f(b;c,N) \sim \int_{2\pi}^{-c} \frac{1}{z^2+cz}\left[1-e^{-2b(z^2+cz)}\right]\,dz \qquad (73)$$

By further manipulating this integral using Watson's lemma [34], leads to

$$f(b;c,N) \sim \frac{2\sqrt{2\pi}\exp\left(\frac{bc^2}{2}\right)}{c^2\sqrt{b}} \qquad (74)$$

and final substitution in (62) yields the asymptotic behavior of w at large times

$$w \sim \left(\frac{2\pi\nu}{t}\right)^{1/4}\frac{\sqrt{2D}}{m}\exp\left(\frac{m^2t}{4\nu}\right) \qquad (75)$$

As expected, the linearized equation results in exponential growth at large times. The unbounded growth reflects the absence of any stabilizing influence due to non-linearity, which was demonstrated in the corresponding equation (49) (see also Olami et al. [17, 32]). Equation (75) indicates that $\ln(w^2t^{1/2})$ is a linear function of time, with slope $m^2/2\nu$. Fig. 6 shows the corresponding numerical results for the parameters $L=256$, $m=0.5$, and $\nu=0.5$. In agreement with the theory, the slope of the plot on Fig. 6 is very close to the theoretical, $m^2/2\nu=0.25$. The scaling at early times for the destabilizing case is identical to that for the stabilizing, given that the non-local effect does not enter to leading-order, hence a power-law scaling applies at early times.

The lack of simultaneous power-law scalings in the two limits (small and large times) is a consequence of the fact that the linear HKPZ does not admit a self-affine solution. Indeed, a scaling approach in which $x \to lx$, $h \to l^{\alpha}h$, and $t \to l^{z}t$ [2], cannot be simultaneously satisfied for the HKPZ due to the presence of the non-local term.

iii. The correlation function

For completeness, we also present results for the correlation function (the semivariogram)

$$C(r,t) = \langle |h(r,t) - h(0,t)|^2 \rangle \tag{76}$$

for the case of an infinitely large lattice. Working similarly and following closely reference [33], we find the result

$$C(r,t) = \frac{2Dr}{\pi\nu} \int_0^{\infty} \frac{1 - \exp(-2x(y^2 + \lambda y))}{y^2 + \lambda y}(1 - \cos y)dy \tag{77}$$

where we introduced the variables $\lambda = -\frac{mr}{\nu}$ and $x = \frac{\nu t}{r^2}$. The behavior of $C(r,t)$ in the various asymptotic limits follows closely that of w^2. For either stabilizing and destabilizing cases, the expansion at small r is linear

$$C(r,t) \sim \frac{Dr}{\pi\nu} \tag{78}$$

The correlation function increases with r and saturates at large r to a value increasing with time

$$C(r,t) \to \frac{2D\sqrt{t}}{\pi\sqrt{\nu}} \int_0^{\infty} \frac{1}{z^2 + \rho z}\left[1 - \exp(-2z^2 - \rho z)\right] dz \tag{79}$$

and where we introduced the time variable $\rho = -m\sqrt{\frac{t}{\nu}}$. In the stabilizing case, $\rho > 0$ and $C(r,t)$ approaches a limiting value at large times. In the destabilizing case, $\rho < 0$, the large-time limit can be manipulated in the same manner as above to lead to an exponentially growing function

$$C(r,t) \sim \exp\left(\frac{\rho^2}{2}\right) = \exp\left(\frac{m^2 t}{2\nu}\right) \tag{80}$$

As before, the scaling behavior is affected by the presence of the non-local transport term m, which breaks the self-similarity and introduces additional dependences.

V. Numerical Solution of the HKPZ Equation

The preceding analysis suggests that the behavior of the HKPZ equation would also depend on whether the process is stabilizing or destabilizing. We used the numerical scheme described above to simulate the solution of the nonlinear equation in these two cases. Typically, the simulations were carried out starting from an initially flat interface. However, results were also obtained, particularly for the destabilizing case of the noiseless equation (15), starting from a random initial position.

Results corresponding to the stabilizing case are shown in Fig. 7. The figure shows snapshots of the front at early and late times. Both the front and its width increase with time and eventually approach a mean steady-state, which fluctuates in both space and time. The presence of noise results in the constant fluctuation of the front around its mean value, in contrast to the flat front obtained asymptotically in the corresponding noiseless case, equation (51). In addition, and in contrast to the linearized case, the asymptotic mean position of the front is not zero, reflecting the effect of the non-linear contribution. The variation with time of the width averaged over 100 realizations is shown in Fig. 8 for $L = 128$, $m = -0.5$, and $\lambda = 7$. For comparison purposes, also shown is the ensemble-averaged width corresponding to the KPZ equation with the same parameters. The scaling behavior of the width appears to be the same in the two equations at early times. However, as time proceeds the width of the HKPZ grows slower and saturates earlier and to smaller values, compared to those of the KPZ equation. This difference reflects the more compact front expected in the stabilizing HKPZ, compared to the KPZ. We recall that in the KPZ equation, the front has self-affine characteristics, with the interface width satisfying the dynamic scaling

$$w(L,t) \equiv \left\langle [h(x,t) - \langle h(x,t) \rangle]^2 \right\rangle^{1/2} \sim L^{\alpha} f(t/L^{\alpha/\beta}) \tag{81}$$

where $f(c) \sim c^{\beta}$ for $c \ll 1$, and $f(c) \to$ const. as $c \gg 1$. The growth exponent $\beta = 1/3$ characterizes the time-dependent dynamics of the roughening process, while the roughness exponent $\alpha = 0.5$ characterizes the roughness of the saturated interface [2]. Fig. 8 suggests that the HKPZ also has an early-time power law scaling similar to KPZ, namely with exponent $\beta = 1/3$. The independence from the parameter m and the non-local character of the process, at early times, is consistent with the linearized HKPZ findings, where the early-time scaling is identical to the EW equation. The sensitivity of the early-time scaling to changes in various parameters was tested by varying L, m and λ. Fig. 9 shows that the behavior of the ensemble-averaged width is practically unaffected by variations in λ. This was also the case for small values of λ. A similar effect was found for the KPZ equation, as well. The effect of the non-local term is more important (Fig. 10) and affects the range of the validity of the early-time power-law regime and the overall extent. As $|m|$ increases, the power-law scaling at early times lasts for a shorter period, and the width is smaller overall. As before, this reflects the stabilizing influence of non-local transport.

The dependence of the saturation width at large times to parameter m and the lattice size L is shown in Fig. 11. As before, larger values in the absolute magnitude of m lead to smaller asymptotic widths. The dependence on size is rather weak. If, in an attempt to satisfy (81), the curves were fitted with a power law, a small exponent α would result, estimated from the plot as $\alpha = 0.19$. This exponent is quite smaller than the corresponding roughness exponent of the KPZ, where $\alpha = 0.5$. In analogy with the linearized HKPZ, we then elected to test the late-time results with a logarithmic function, of the form $w^2 \sim \ln L$. The results are shown in Fig. 11 and demonstrate a good match for the three different values of m tested. The slope of the straight line is of the same order of magnitude as in the linearized case and decreases inversely proportionally to $|m|$, as $|m|$ increases. This is consistent with the findings from the linearized HKPZ. We are led to conjecture, therefore, that the scaling behavior of the HKPZ is not of the self-affine form (81), but that the early-

time power law scaling is followed at late times by a logarithmic dependence of the front width on the lattice size.

Subsequently, we studied the behavior of the HKPZ under destabilizing conditions, where $m > 0$. As noted before, a rigorous analysis of the similar equation (9), which is the extended Burgers equation in the presence of noise, was undertaken by Olami et al. [17]. These authors examined a number of issues, including the evolution of the solution of (9) in the absence of noise but with noisy initial conditions, and the effect of noise. Although equation (9) is not the same as the HKPZ, we anticipate similar results. In the following we will discuss the solution of the destabilizing HKPZ in two cases, first in the absence of noise forcing term, but with noisy initial conditions, and second in the presence of a noise forcing term.

The results of a simulation of the noiseless HKPZ equation (15) in 1-D, but with noisy initial conditions, are shown in Fig. 13 for different values of time. At early times, the front evolves in terms of well-defined fingers, the number of which decreases as time increases (Fig. 13a). At later times the shape of the front changes to a few dominant fingers and the development of a "giant" cusp (Fig. 13b). These features are very similar to those observed by Olami et al. [17], who explained the attraction to a giant cusp by using polar decomposition. We expect that similar arguments will hold here as well. The evolution of the width of the front as a function of time is plotted in Fig. 14. Following an initially slow variation, the width enters a regime which can be approximated as a power law, $w \sim t^{\zeta_1}$ with an exponent estimated to be $\zeta_1 = 1.2$. This value is similar to that reported by Olami et al. [17] for the different equation they studied. Fig. 14 also shows that the width stabilizes asymptotically to a value, expected to be size-dependent.

Results for the simulation of the full HKPZ in the presence of noise and for the destabilizing case are shown in Fig. 15. Comparison with Fig. 13 shows a qualitatively different behavior. The number of fingers does not decrease significantly, as time increases, while it does not appear that an attracting cusp actually exists. The additive noise present in the HKPZ continuously adds new poles altering the dynamics of the noiseless equation (15). As explained in [17], the asymptotic state of the noiseless equation is nonlinearly unstable,

thus leading to a qualitatively new regime. The behavior in Fig. 15 has features similar to those in regime II of Olami et al. [17], where noise is of sufficiently large amplitude. Fig. 16 shows the variation of the ensemble-averaged width with time for this case. It indicates a continuous growth, with the late time behavior resembling a power-law regime, $w \sim t^{\zeta_2}$, with the exponent estimated at $\zeta_2 \approx 1.1$.

VI. Conclusions

In this chapter, we derived a new equation that extends the well-known KPZ equation in order to capture non-local transport effects, through a Hilbert transform term. The new equation, termed the HKPZ equation, can be used to describe the long-wave dynamics, near the onset of the non-local transport and in the weakly nonlinear limit, of various physical processes, where the non-local transport is governed by the Laplace equation, and the stabilizing term is a second-order diffusion process. The non-local term may lead to processes that can be linearly stable or unstable, depending on the parameter values. A specific example from reactive infiltration was studied and was shown to lead in the weakly non-linear limit to the noiseless HKPZ. The solution of the HKPZ equation in one dimension was considered by developing an appropriate numerical scheme, the accuracy of which was asserted by comparison with the extended Burgers equation in the absence of noise. An analytical solution to the latter is possible through a pole decomposition method.

Then, the linear version of the HKPZ was investigated. Asymptotics for small and large times were developed and the appropriate scaling behavior was obtained analytically in these limits. The early-time behavior was found to be independent of the non-local transport term, hence identical to that for the EW equation, for either the stabilizing or the destabilizing cases. This behavior is a power law with exponent $\beta = 1/4$. In the stabilizing case, the width saturates at large times to a value which has a logarithmic dependence on lattice size, reflecting the non-local character of the process. This is different from the EW equation, where a power law regime applies. In the destabilizing case, the late-time behavior is exponential growth with a rate corresponding to the fastest growing mode of the linear dispersion relation, as expected.

Subsequently, the full HKPZ equation was solved numerically in one spatial dimension. For the stabilizing case, the dynamical exponent was found to be identical to that of the KPZ, hence to not be affected by the non-local term. On the other hand, the long-time behavior appears to obey a logarithmic scaling with respect to the lattice size. The large-time scaling is also sensitive to the non-local transport parameters. For the destabilizing case, we found results similar to Olami et al. [17]. The noiseless equation, but with noisy initial condition, showed attraction to a giant cusp. However, the solution of the HKPZ in the presence of noise showed continuous fluctuations, and the absence of a dominant giant cusp. The width at late times was found to obey a power-law growth.

These results should find direct applications to the dynamics of growing interfaces, where the flux to the interface is controlled by a non-local Laplacian transport. Such applications are many and cover a broad range of physical processes. For example, they may include the displacement of viscous fluids in porous media, convection-reaction in porous media with permeability changes, reaction-diffusion processes on pore surfaces with morphological changes, and flame propagation. We also believe that the process studied in [8] falls in the same class. The effect of the non-local term becomes important at large times, the early-time behavior being controlled by the KPZ dynamics. In the stabilizing case ($m < 0$), the width asymptotically stabilizes, however, the power-law prediction of the KPZ equation must be now replaced by a logarithmic dependence on the lattice size. This dependence breaks down the spatiotemporal self-affinity of the KPZ interfaces, and also leads to more compact fronts. The development of more compact fronts is a result of the stabilizing influence of non-local transport. Under such conditions, therefore, one should use caution before applying the scalings derived from the KPZ equation. In the destabilizing case, the evolution of interfaces at large times also shows behavior significantly different than KPZ. Specifically, the front width does not saturate at large times but rather increases as a power-law of the latter, reflecting the frontal instability. We must note that for a physical application, for example in reactive infiltration, the validity of this scaling is subject to the restrictions of large wavelengths near the onset of instability (namely, when the destabilizing contrast is weak,

$\kappa - 1 \ll 1$, or small $m > 0$). In the more general case of strong instability, HKPZ does not apply and cannot capture Laplacian growth, which must be modeled instead by processes such as Diffusion-Limited-Aggregation (DLA) (e.g. see [15] and related references). In a sense, in the destabilizing case HKPZ corresponds to the weak-instability limit, with DLA being its strong-instability counterpart.

References

[1] M. Kardar, G. Parisi, and Y. Zhang, "Dynamic scaling of growing interfaces", Phys. Rev. Lett. **56**, 889 (1986).

[2] A. L. Barabasi, and H. E. Stanley, *Fractal concepts in surface growth* (Cambridge University press, Cambridge, 1995).

[3] P. Meakin, P. Ramanlal, L. M. Sander, and R. C. Ball, "Ballistic deposition on surfaces", Phys. Rev. A **34**, 5091 (1986).

[4] R. Jullien, and R. Botet, "Surface thickness in the Eden model", Phys. Rev. Lett. **54**, 2055 (1985).

[5] R. Jullien, and R. Botet, "Scaling properties of the surface of the Eden model in d=2, 3, 4", J. Phys. A.: Math. Gen. **18**, 2279 (1985).

[6] A. R. Kerstein, and W. T. Ashurst, "Propagation rate of growing interfaces in stirred fluids", Phys. Rev. Lett. **68**, 934 (1992).

[7] M. Kardar, and Y. C. Zhang, "Scaling of directed polymers in random media", Phys. Rev. Lett. **58**, 2087 (1987).

[8] E. Aharonov, and D. H. Rothman, "Growth of correlated pore-scale structures in sedimentary rocks: a dynamical model", J. Geophys. Res. **101**, No. B2, 2973, (1996).

[9] P.C. Lichtner, C.I. Steefel, and E.H. Oelkers (eds.) "Reactive transport in porous media", Reviews in Mineralogy **34**, 438 pp. (1996).

[10] T. Dogu, "The importance of pore structure and diffusion in the kinetics of gas-solid non-catalytic reactions: reaction of calcined limestone with SO2", Chem. Engng. J. **21**, 213 (1980).

[11] G. F. Froment, *Catalyst Deactivation* (B. Delmon and G. F. Froment (eds.), Elsevier, 1980).

[12] G. M. Homsy, "Viscous fingering in porous media", Ann. Rev. Fluid Mech. **19**, 271 (1987).

[13] G. I. Sivashinsky, "Nonlinear analysis of hydrodynamic instability in laminar flames - I. Derivation of basic equations", Acta Astronautica **4**, 1177 (1978).

[14] D. M. Michelson, and G. I. Sivashinsky, "Nonlinear analysis of hydrodynamic instability in laminar flames - II. Numerical experiments", Acta Astronautica **4**, 1207 (1978).

[15] G. Daccord, and R. Lenormand, "Fractal patterns from chemical dissolution", Nature **325**, 41 (1987).

[16] A. Erdelyi, F. Oberhettinger, and F. G. Tricomi, *Tables of integral transforms* (Bateman Manuscript Project, McGraw-Hill, New York, 1954).

[17] Z. Olami, B. Galanti, O. Kupervasser, and I. Procaccia, "Random noise and pole dynamics in unstable front propagation", Phys. Rev. E **55**, 2649 (1997).

[18] S. F. Edwards, and D. R. Wilkinson, "The surface statistics of a granular aggregate", Proc. R. Soc. London, Ser. A **381**, 17 (1982).

[19] P. G. Saffman, and G. I. Taylor, "The penetration of a fluid into a porous medium or Hele-Shaw cell containing a more viscous liquid", Proc. R. London, Ser. A. **245**, 312 (1958).

[20] Y. C. Yortsos, and F. J. Hickernell, "Linear stability of immiscible displacement in porous media", SIAM J. Appl. Math. **49**, 730 (1989).

[21] E. J. Hinch, and B. S. Bhatt, "Stability of an acid front moving through porous rock", J. Fluid Mech. **212**, 279 (1990).

[22] J. D. Sherwood, "Stability of a plane reaction front in a porous medium", Chem. Engng. Sci. **42**, 1823 (1987).

[23] J. S. Langer, "Instabilities and pattern formation in crystal growth", Rev. Mod. Phys. **52**, 1 (1980).

[24] P. Pelce, *Dynamics of curved fronts* (Academic, Boston, 1988).

[25] Y. C. Yortsos, "Instabilities in displacement processes in porous media", J. Phys.: Condens. Matter **2**, SA443 (1990).

[26] O. Thual, U. Frisch, and M. Henon, "Application of pole decomposition to an equation governing the dynamics of wrinkled flame fronts", J. Physique **46**, 1485 (1985).

[27] P. Kechagia, Ph.D. Thesis, University of Southern California, expected (2001).

[28] J. Chadam, P. Ortoleva, and A. Sen, "A Weakly Nonlinear Stability Analysis of the Reactive Infiltration Interface", SIAM J. Appl. Math. **48**, 1362 (1988).

[29] E.D. Chikhliwala, and Y.C. Yortsos, "Investigations on Viscous Fingering by Linear and Weakly Nonlinear Stability Analysis", SPE Reservoir Engineering 1268 (1988).

[30] K. Moser, J. Kertesz, and D. Wolf, "Numerical solution of the Kardar-Parisi-Zhang equation in one, two, and three dimensions", Physica A **178**, 215 (1991).

[31] H. V. McConnaughey, G. S. S. Ludford, and G. I. Sivashinsky, "A calculation of wrinkled flames", Comb. Sci. and Tech. **33**, 113 (1983).

[32] O. Kupervasser, Z. Olami, and I. Procaccia, "Geometry of developing flame fronts: analysis with pole decomposition", Phys. Rev. Lett. **76 (1)**, 146 (1996).

[33] T. Nattermann, and L.-H. Tang, "Kinetic surface roughening I: The Kardar-Parisi-Zhang equation in the weak-coupling regime", Phys. Rev. A **45**, 7156 (1992).

[34] G. F. Carrier, M. Krook, and C. Pearsosn, *Functions of a complex variable* (McGraw-Hill, New York, 1966).

[35] D. Forster, D. R. Nelson, and M. J. Stephen, "Large-distance and long-time properties of a randomly stirred fluid", Phys. Rev. A **16**, 732 (1977).

[36] A. D. Fowler, H. E. Stanley, and G. Daccord, "Dissequilibrium silicate mineral textures: fractal and non-fractal features", Nature **341**, 134 (1989).

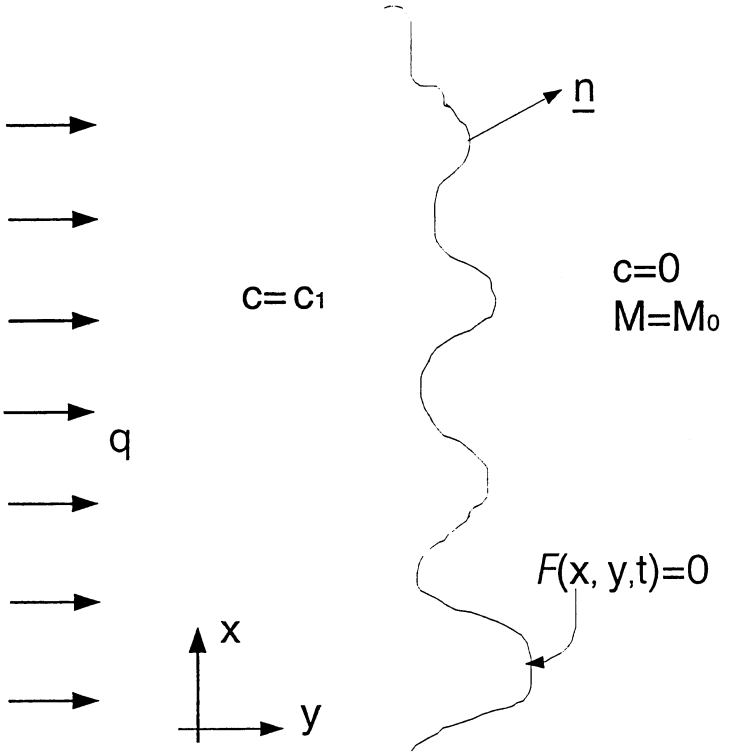

Figure 1: Schematic of a reactive infiltration interface. Chemical injected upstream at concentration c_1 and rate q reacts infinitely fast at the reactive interface (front), with a mineral of initial concentration M_0. Both chemical and mineral are consumed completely at the interface. As a result of the reaction, the permeability changes in the two regions. The normal vector at the interface is indicated.

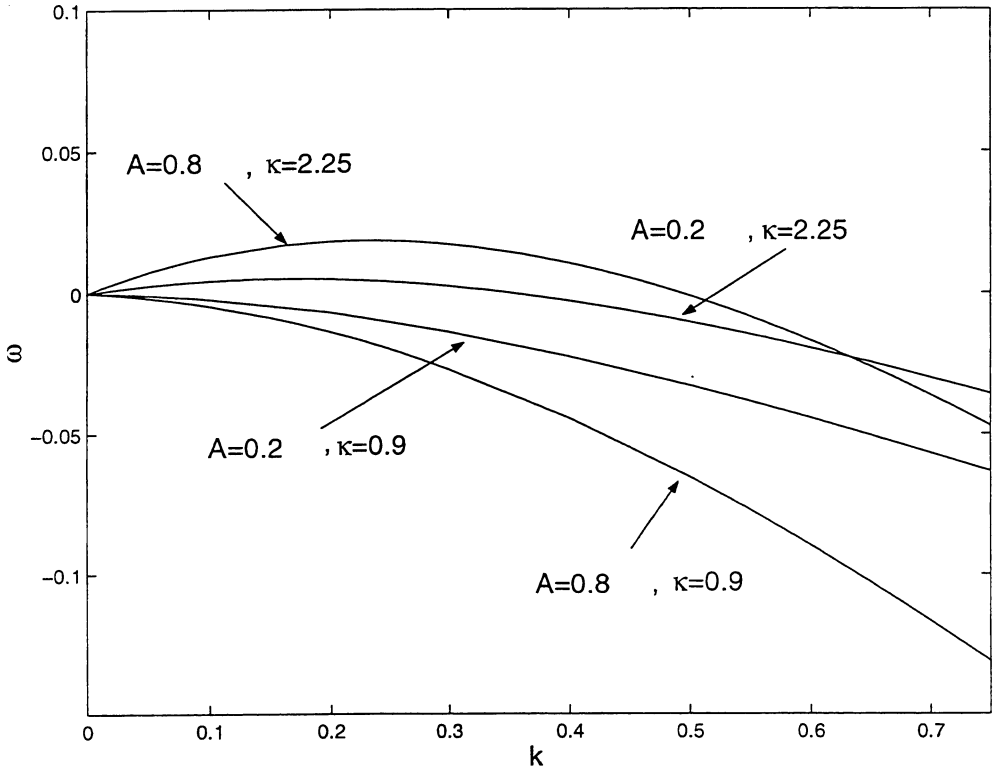

Figure 2: The eigenvalue ω plotted as a function of the wavenumber k for different values of the permeability contrast κ. Long-wave instability is predicted for $\kappa > 1$, the process being stabilized at smaller wavelengths due to diffusion. Unconditional stability exists for $\kappa < 1$. The effect of parameter A is to affect the numerical values of ω, but does not change the qualitative nature of the instability.

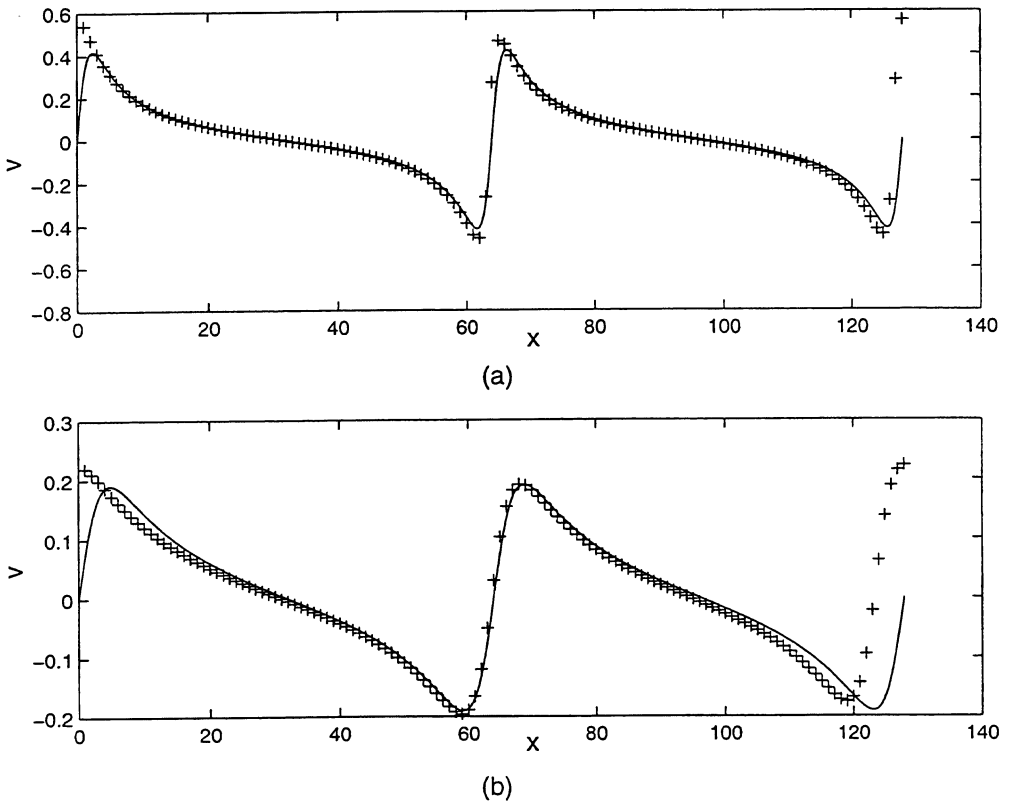

Figure 3: Comparison of the analytical solution of the extended Burgers equation, denoted with a solid line, and the numerical solution, denoted with crosses, for two different times: (a) $t = 3.57$, (b) $t = 51$. The latter time corresponds effectively to a steady-state solution. Here $L = 128$, $n = \pi/64$ and $m = 0.2$.

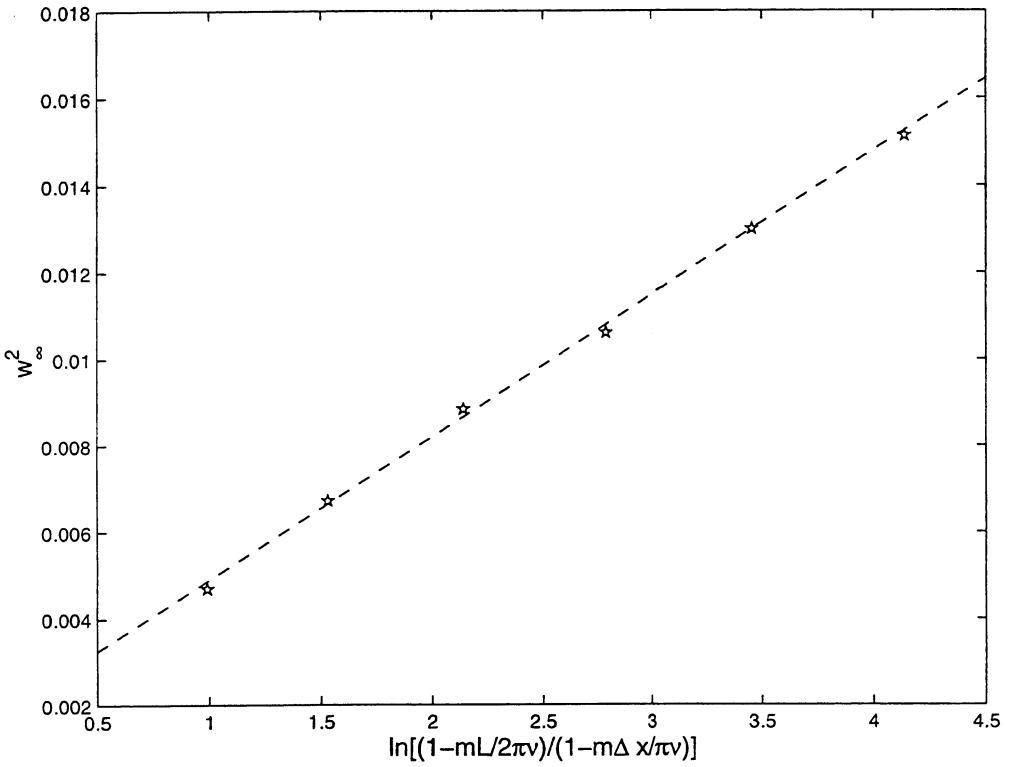

Figure 4: Dependence of the saturation width on the lattice size for the linearized HKPZ equation in the stabilizing case and for large times. The numerical results are denoted by stars and correspond to $L = 16, 32, 64, 128, 256, 512$, respectively. Here, $m = -0.5$, and $\nu = 0.5$. The width in the vertical axis is the ensemble average over 100 realizations. The dashed line corresponds to the analytically calculated slope $-\frac{D}{\pi m} = 0.0032$.

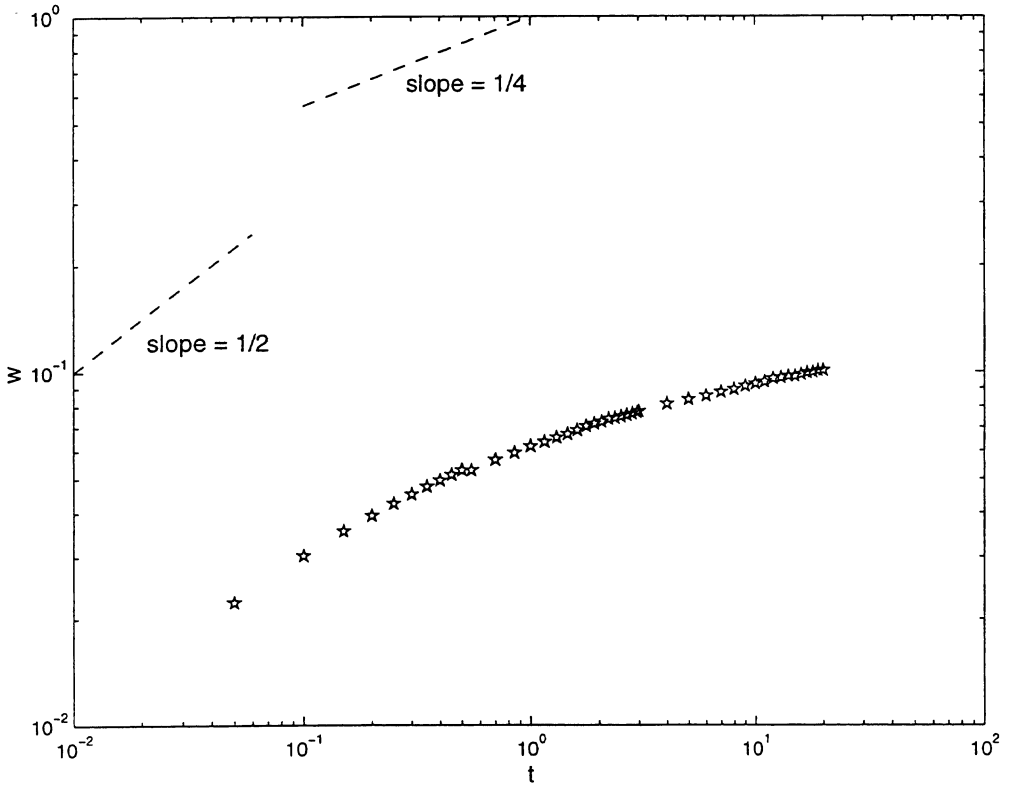

Figure 5: Dependence of the ensemble-averaged width on time for the linearized HKPZ equation for the stabilizing case and at early times. The numerical results are denoted by stars. Here $L = 256$, $m = -0.5$, and $\nu = 0.5$. The dotted lines indicate the theoretically calculated slopes. The width is averaged over 100 realizations.

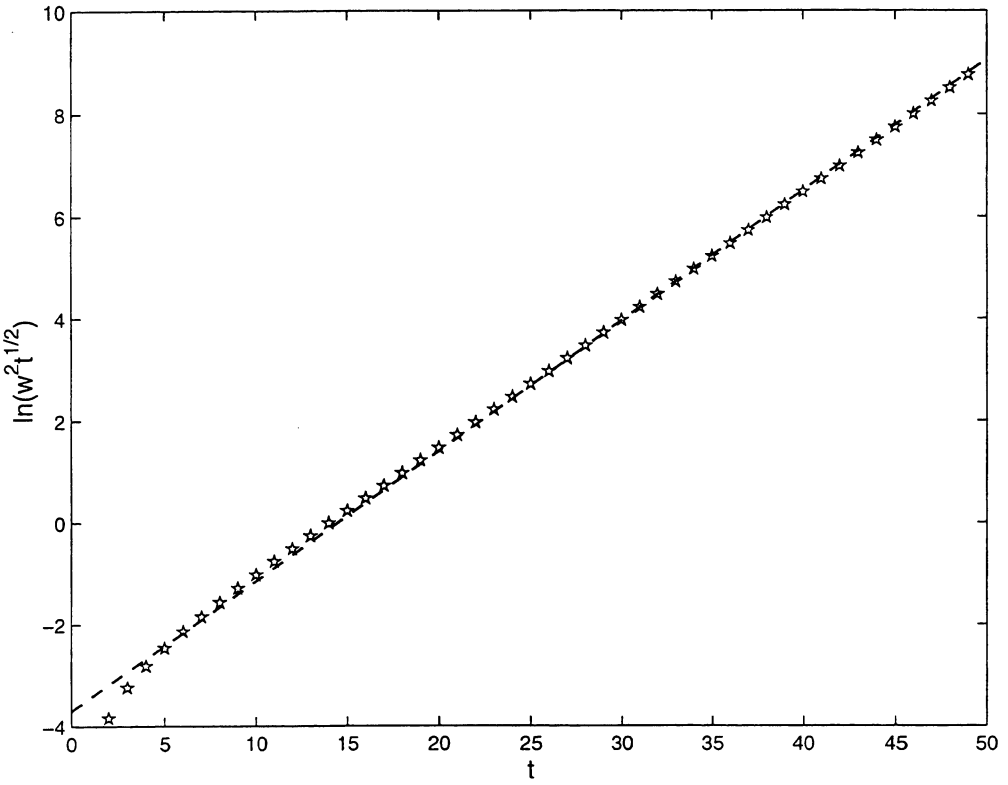

Figure 6: Dependence of the ensemble-averaged width on time for the linearized HKPZ equation for the destabilizing case at large times. The numerical results are denoted by stars, where $L = 256$, $m = 0.5$, and $\nu = 0.5$. The width is averaged over 100 realizations. The dashed line is the analytical calculation with slope $m^2/2\nu = 0.25$.

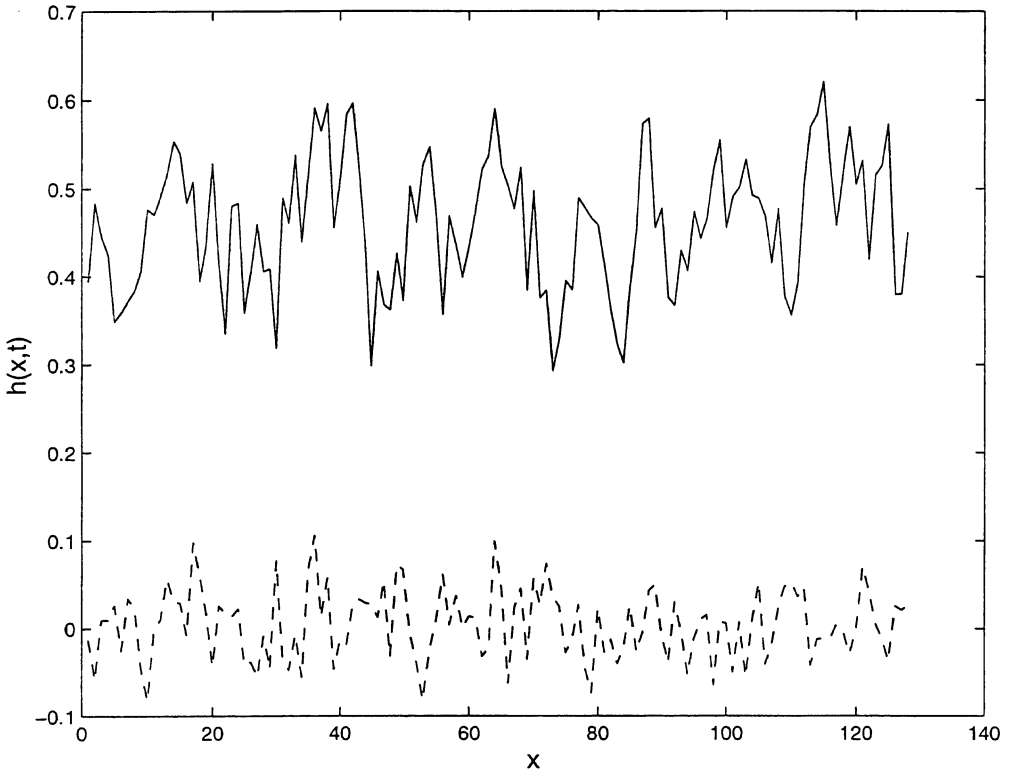

Figure 7: Snapshots of the height $h(x,t)$ of the front of the HKPZ under stabilizing conditions for two different times: $t = 0.25$ (dotted line) and $t = 50$ (solid line). Here $L = 128$, $m = -0.5$, $\nu = 0.5$, $\lambda = 7$.

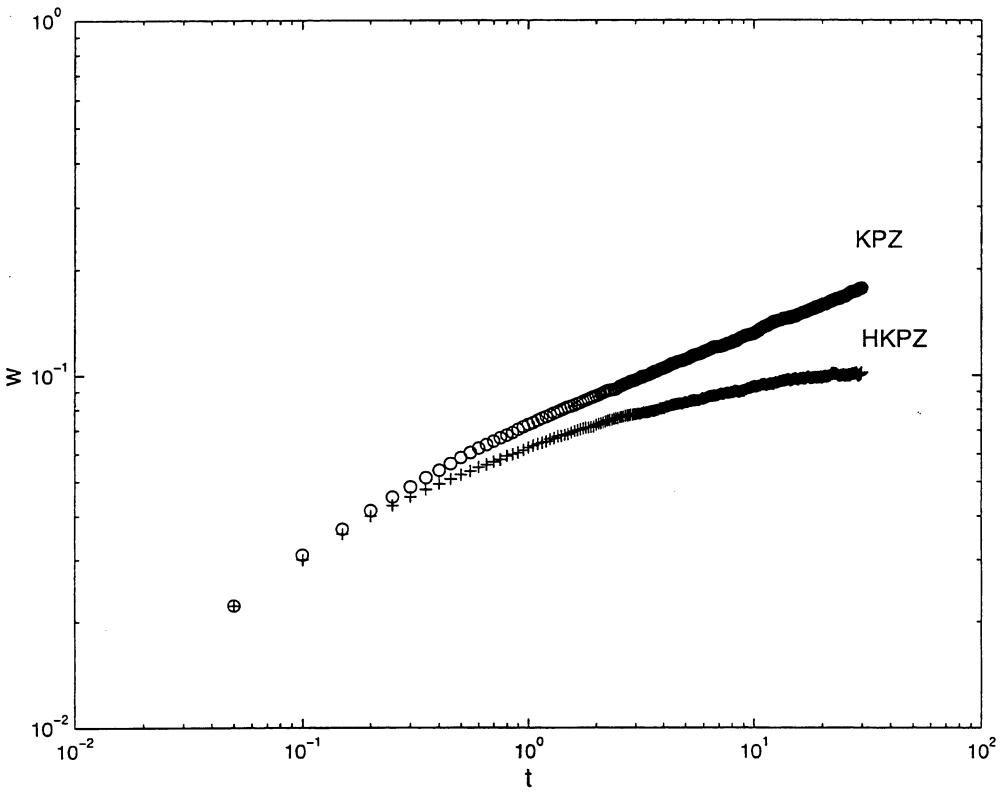

Figure 8: Early-time behavior of the ensemble-averaged width for the KPZ (represented by circles) and the HKPZ under stabilizing conditions (represented by crosses) . Here $L = 128$, $m = -0.5$, $\nu = 0.5$, and $\lambda = 7$.

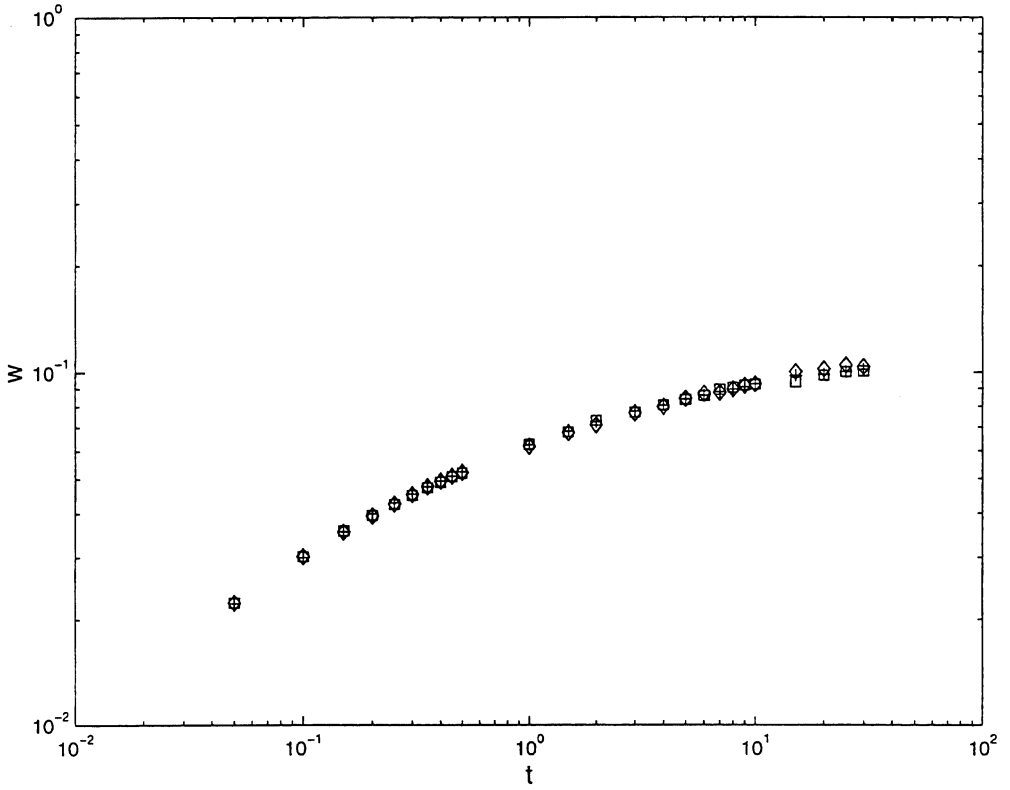

Figure 9: Effect of λ on the dependence of the ensemble-averaged width of the HKPZ equation under stabilizing conditions, at early times and for three different values of λ, ($\lambda = 1$ (squares) $\lambda = 7$ (crosses), $\lambda = 17.58$ (diamonds)). Here $L = 128$, $m = -0.5$, and $\nu = 0.5$.

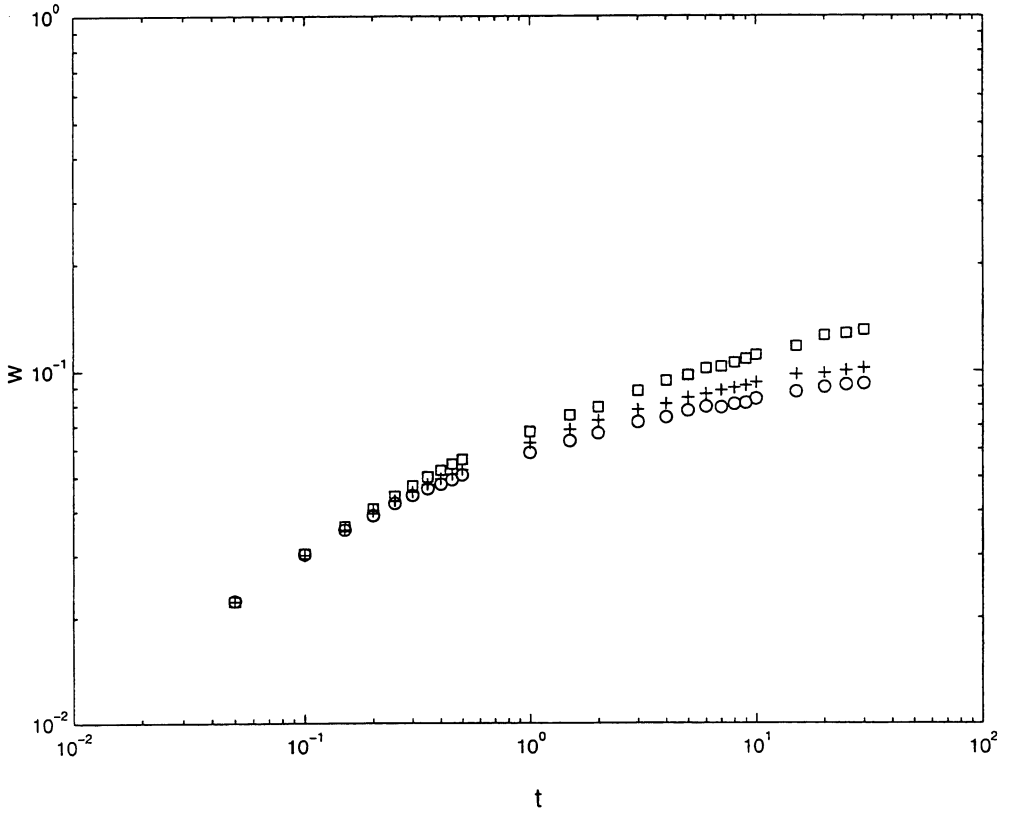

Figure 10: Effect of m on the dependence of the ensemble-averaged width of the HKPZ equation under stabilizing conditions, at early times and for three different values of m ($m = -0.2$ (squares), $m = -0.5$ (crosses), $m = -0.7$ (circles)). Here $L = 128$, $\lambda = 7$ and $\nu = 0.5$.

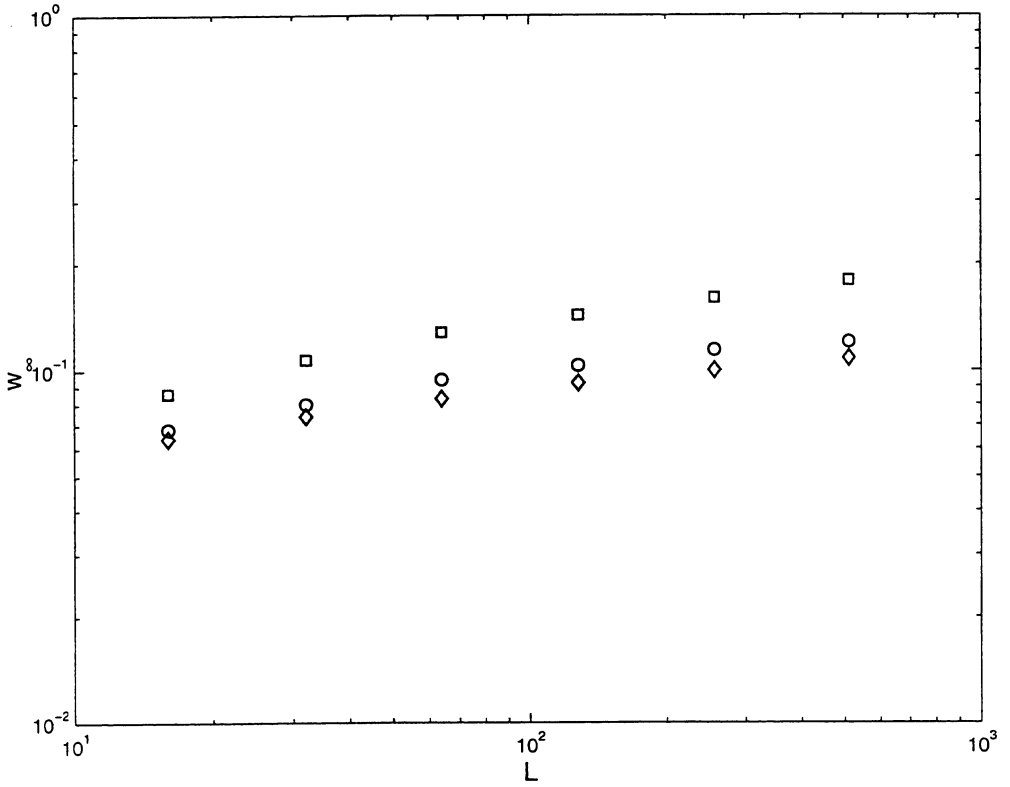

Figure 11: Effect of m on the dependence of the ensemble-averaged width of the HKPZ equation under stabilizing conditions at late times ($m = -0.2$ (squares), $m = -0.5$ (circles), $m = -0.7$ (diamonds)). Here $\lambda = 7$ and $\nu = 0.5$.

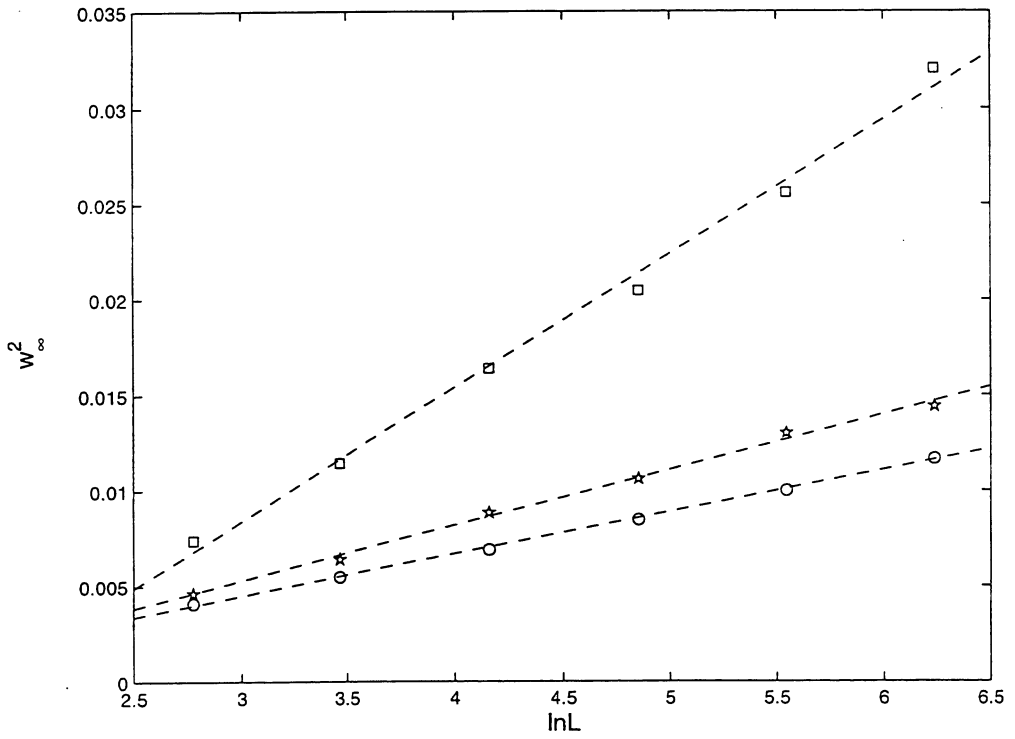

Figure 12: Long-time behavior of the HKPZ equation under stabilizing conditions. The ensemble-averaged width shows logarithmic scaling with the lattice size L (where $L = 16, 32, 64, 128, 256, 512$). Numerical results are indicated by squares for $m = -0.2$, by stars for $m = -0.5$, and by sircles for $m = -0.7$. Here $\nu = 0.5$ and $\lambda = 7$. The dotted lines indicate a least squares straight-line fit.

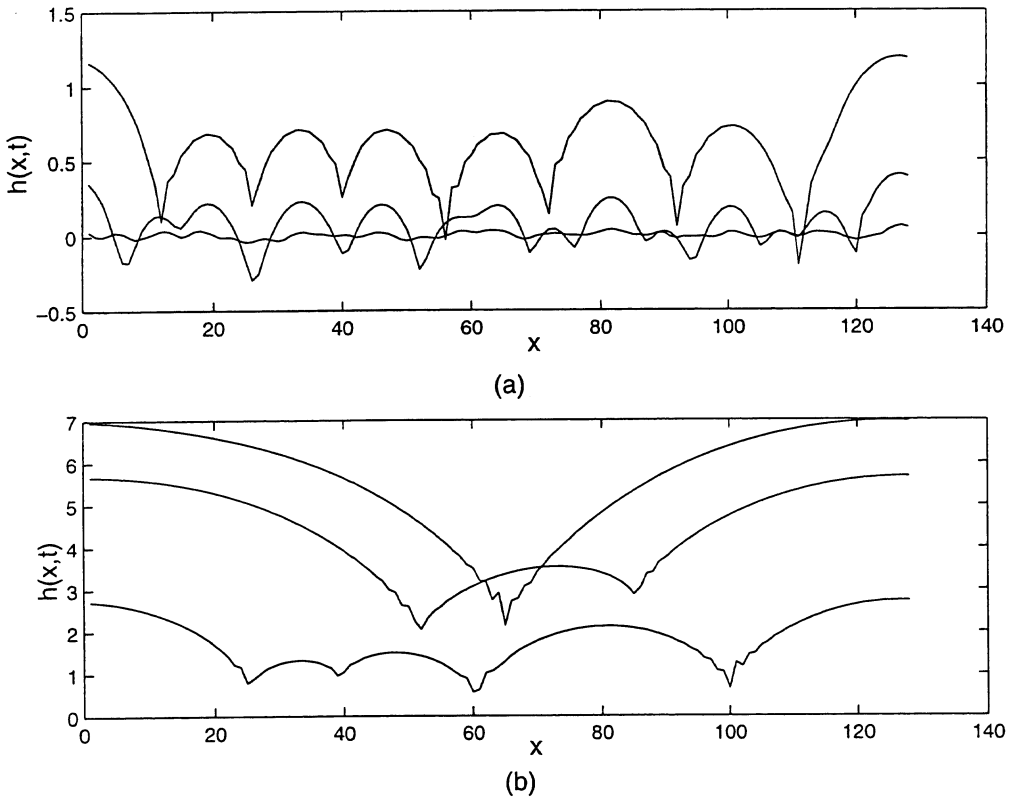

Figure 13: Snapshots of the height of the interface of the noiseless HKPZ equation under destabilizing conditions starting from a noisy initial condition. In plot (a) the time is $t = 5, 25, 50$ from bottom to the top. In plot (b) the time is $t = 100, 200, 250$ from bottom to the top. Here $L = 128$, $m = 0.5$, $\nu = 0.5$ and $\lambda = 7$.

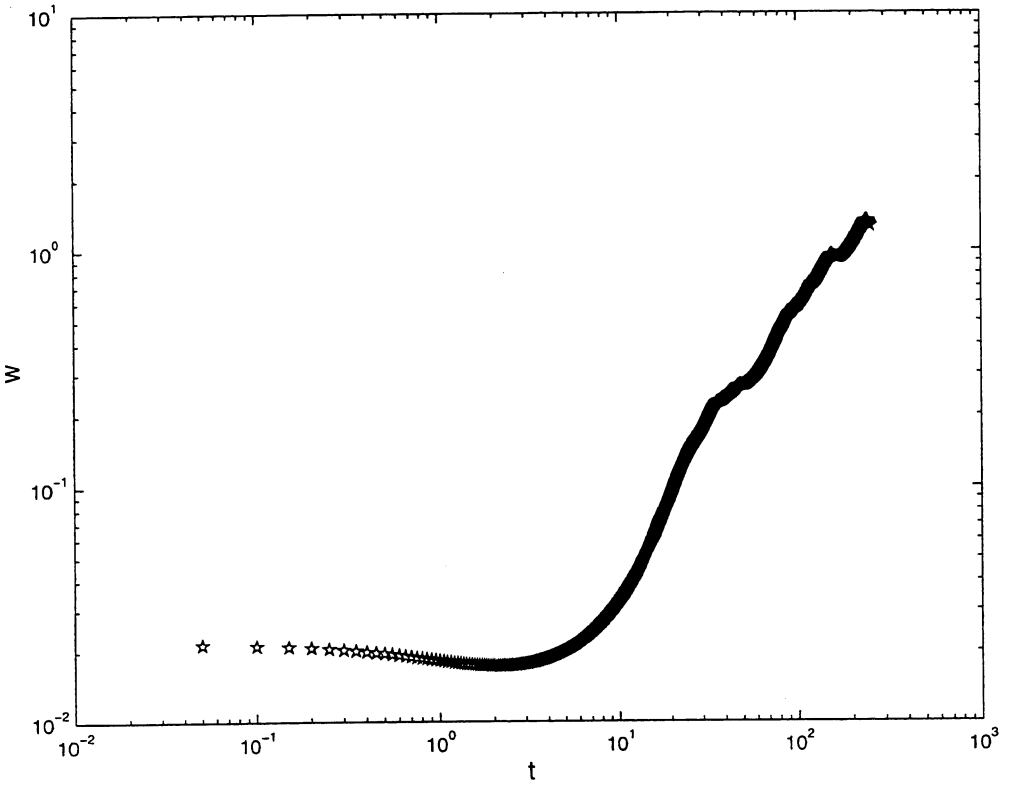

Figure 14: Ensemble-averaged width for the noiseless HKPZ equation under destabilizing conditions starting from a noisy initial condition, corresponding to Fig. 13. Here $L = 128$, $m = 0.5$, $\nu = 0.5$ and $\lambda = 7$.

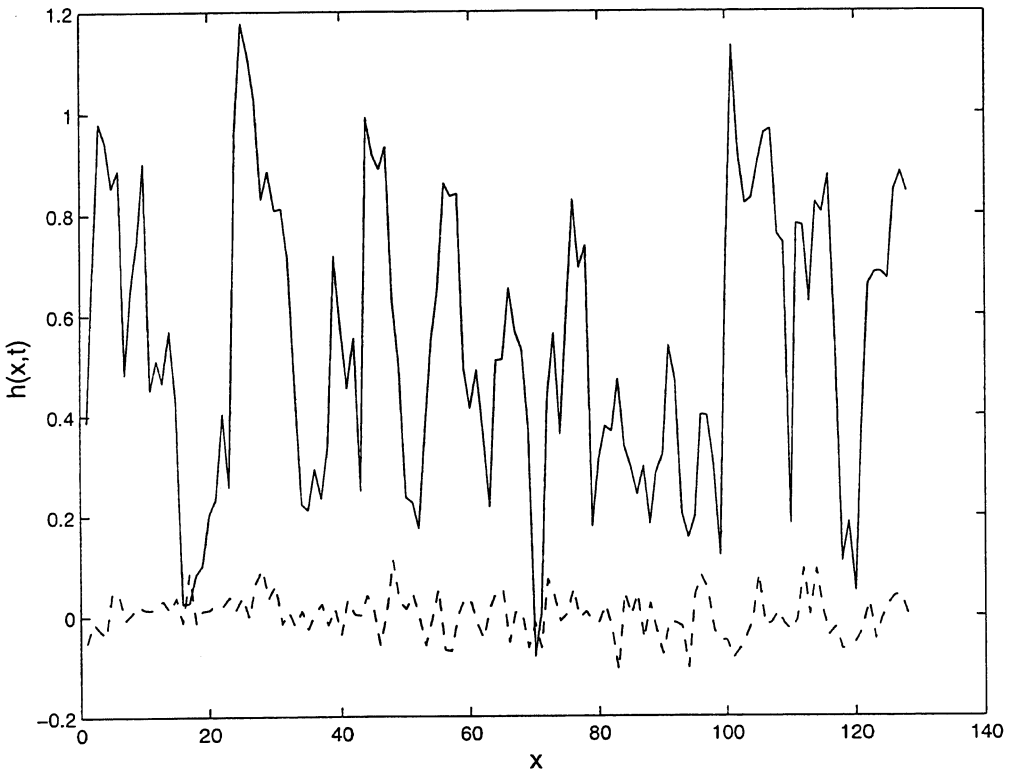

Figure 15: Snapshots of the height $h(x,t)$ of the front of the HKPZ under destabilizing conditions starting with a flat initial condition. Dotted line: $t = 0.25$, solid line: $t = 10$. Here $L = 128$, $m = 0.5$, $\nu = 0.5$ and $\lambda = 7$.

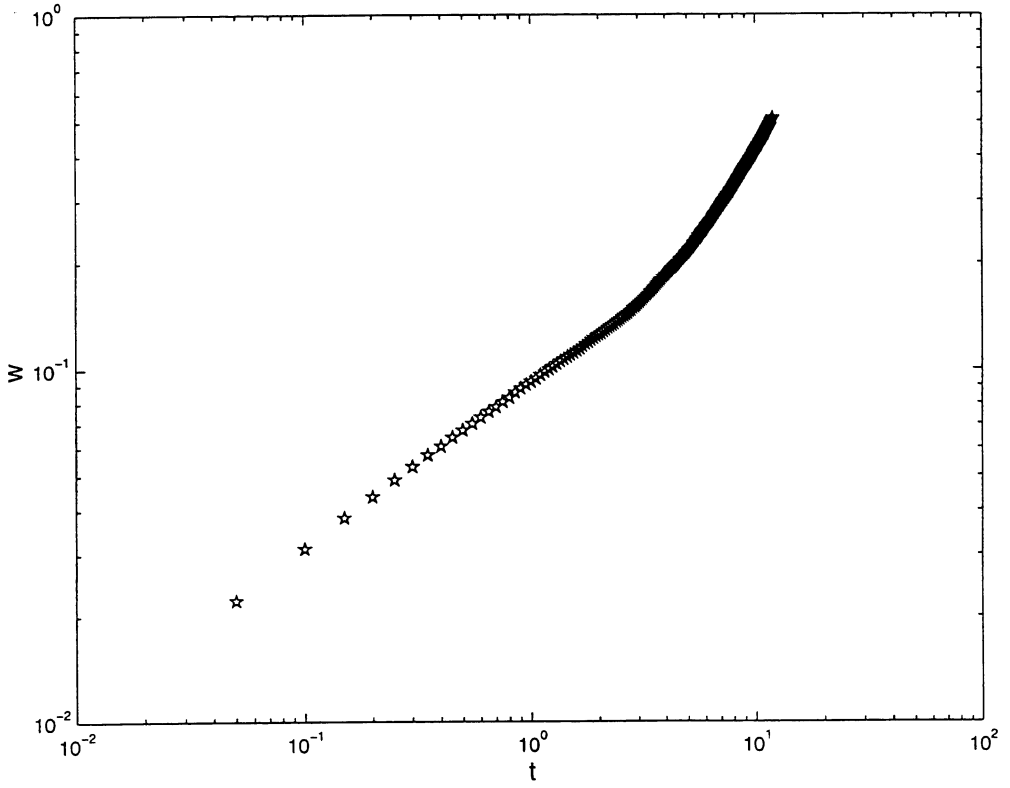

Figure 16: The ensemble-averaged width of the HKPZ equation under destabilizing conditions as a function of time. Here $L = 128$, $m = 0.5$, $\nu = 0.5$ and $\lambda = 7$.